

UNIVERSITY OF COPENHAGEN  
FACULTY OF SCIENCE



## Doctoral Thesis

# A Search for Tau Neutrino Appearance with IceCube-DeepCore

Michael. J. Larson

Advisor: Dr. D. Jason Koskinen

Handed in: March 17, 2018



Submitted in fulfilment of the requirements  
for the degree of  
Doctorate in Philosophy  
at  
the Niels Bohr Institute, University of Copenhagen.

## Abstract

Neutrino have been known to oscillate between the three flavors since the first discoveries two decades ago. Over that time, our knowledge of the parameters which govern these oscillations has improved significantly. The largest remaining uncertainties in the measurement of neutrino oscillations are those that govern the tau neutrino. In this thesis, a direct measurement of tau neutrino oscillations is performed with the IceCube Neutrino Observatory located in the ice deep beneath the South Pole.

The measurement of atmospheric tau neutrino appearance requires a precise understanding of backgrounds. In order to perform the measurement, improvements to the modeling of the detector noise have been performed, reducing the uncertainties in the noise model used in IceCube significantly. Additional improvements to the simulation efficiency investigated during this thesis reduce the computational requirements of atmospheric muon background events by more than three orders of magnitude. These improvements allow, for the first time, the use of simulation of background events in oscillation measurements performed by IceCube.

Using the DeepCore detector, a densely instrumented infill of IceCube located in the clearest ice of the Antarctic glacier, a new selection of events has been created in the search for tau neutrino appearance from atmospheric oscillations. Tau neutrino appearance and muon neutrino disappearance were measured simultaneously with the new sample from 5.6 to 56 GeV from data collected over a period of 968 days. The best fit values,  $N_{\tau}^{CC} = 0.566_{-0.303}^{+0.356}$  for the charged current exclusive channel and  $N_{\tau}^{NC+CC} = 0.733_{-0.243}^{+0.305}$  for the neutral current inclusive channel, improve upon previous measurements set by other experiments.



## Resumé

Siden de første opdagelser af fænomenet for tyve år siden, har vi vidst at neutrinoer oscillerer mellem deres tre familier. Siden da er vores viden om neutrinoernes oscillationsparametre vokset betragteligt. De største tilbageværende usikkerheder i målingen af neutrino oscillationer, vedrører tau-neutrinoen. I denne afhandling præsenteres resultaterne af en direkte måling af oscillationen af atmosfæriske neutrinoer til tau-neutrinoer, udført med IceCube Neutrino Observatoriet, beliggende dybt i isen ved Sydpolen.

Målingen af atmosfæriske tau-neutrinoer kræver overordentligt godt kendskab til de systematiske baggrundssignaler. For at kunne gennemføre målingen af tau-neutrinoer, udvikledes en forbedret model for detektorens støj niveau, hvilket resulterede i en kraftig reduktion i usikkerheden for denne baggrund i IceCube. Yderligere forbedringer i effektiviteten af simuleringen af den atmosfæriske muon baggrund reducerede kravene til computerressourcer med mere end tre størrelsesordner. Disse forbedringer tillader, for første gang, brugen af simulerede baggrundsbegivenheder i en oscillationsmåling med IceCube.

Ved at bruge DeepCore detektoren, en tæt instrumenteret del af IceCube placeret i den klareste is i gletcheren ved Sydpolen, kunne en ny klasse af begivenheder udvælges, med det særlige mål for øje at måle tilsynecomsten af atmosfæriske tau-neutrinoer via neutrino oscillationer. Både andelen af atmosfæriske neutrinoer der oscillere til tau-neutrinoer og muon-neutrinoer der oscillere til en anden af de tre familier, er blevet målt i energiområdet 5.6 til 56 GeV med denne nye udvælgelse af data, indsamlet over 968 dage.

Det bedste fit til data giver at  $N_{\tau}^{CC} = 0.566_{-0.303}^{+0.356}$  når der kun kigges på charged current interaction kanalen og  $N_{\tau}^{NC+CC} = 0.733_{-0.243}^{+0.305}$  når der kigges på kanalen der også inkluderer neutral current begivenheder. Begge værdier er bedremålinger end andre eksperimenter tidligere har kunne offentliggøre.



## Acknowledgements

I have now spent a total of nine years of my life working in IceCube. Over that time, I've had a number of amazing opportunities and met some incredible people.

I'd like to thank Jason (and the rest of the Koskinens) without whom I would quite literally not be here. You've been the closest I've had to a family here for years and I can't think you enough for the kindness and patience you've shown me. Thank you for letting me be a part of your lives for these last nine years.

And to you in particular, Jason: somehow you've managed to put up with me all of these years and haven't yet killed me. I can only imagine the patience you've had to master as I've fumbled my way through one deadline after another on the road through this PhD. Thanks for always being around and willing to help me through it all. I hope you feel as happy as I do to finally get this analysis over with.

The people in my office over the years have come and gone, but I'll always remember the general tone of barely concealed chaos. I think that may have been mostly Joakim and Eva, although maybe Morten also got a little bit of that action sometimes. I think I'll always have great memories of sitting in the office making beers.

IceCube people not at NBI: you've been an incredible bunch over the years and I look forward to working together again in the future! That goes doubly for Samuel, Lisa, Elim, Martin, Sarah, and Melanie. You five have been my closest friends in the collaboration over the last few years and I can't wait to see what we can do together once we don't have theses to worry about any more!

And finally: my actual family. I think my mother would kill me if I didn't mention her somewhere, so here goes: Hi Mom! Hi Dad! Hope you're happy that my stress and white hairs might actually let up now! I mean, maybe. Possibly. Probably shouldn't get my hopes up.

Okay, they're not reading anymore. Almut: you have been the greatest thing to happen to me since I moved to Copenhagen. I cannot begin to explain to you how much I appreciate your support through the last few years. You've been around for every failure, every frustration, and every victory I've had and you're still with me after those rollercoasters. I can't image a better person to have in my life every day.

And finally, Henning. You can't read and, frankly, you can't really even sit yet. You may never see this statement. But I want you to know that seeing you smile when I get home every night has kept me going for the last four months. I can't wait to show you the world.



# Author's Contributions

This thesis covers a wide range of topics related to the search for tau neutrinos in DeepCore. While I have personally accomplished much of the work of Chapters 5, 6, 7, and 8, I cannot claim sole credit for every task described. Instead, I will outline my own contributions here.

In order to study backgrounds for my analysis, I spent a significant amount of my time working on simulations. As part of my Master's degree at the University of Alabama, I studied the detector noise of IceCube in detail. Chapter 5 represents a continuation of this work. The creation and fitting of the Vuvuzela V2 noise model was performed by me at the Niels Bohr Institute during the winter of 2014-2015 without outside contributions.

The work described in Chapter 6 is less clear. I am not the primary author of the MuonGun or CORSIKA software packages in IceCube. Instead, my work producing MuonGun simulation began as a partnership with Melanie Day, a postdoctoral researcher at the University of Wisconsin who started preliminary tests with the generator in the spring of 2015. My contributions to the DeepCore MuonGun sets (Section 6.2) consisted of tuning the simulation scheme to more efficiently use the collaboration's GPU resources. I also chose the energy range and produced all MuonGun sets of Table 8.3. As of the time of this writing, these are the only MuonGun simulation sets designed for oscillation analyses.

My work further improving the atmospheric muon simulation, described in Section 6.3, was completed more recently. The coding and testing were performed in the summer and fall of 2017. I was able to combine the MuonGun code written by the IceCube collaboration with a general-purpose kernel density estimator from the SciPy python software package. I am not the author of either of these projects, although the novel work presented in Section 6.3 was performed solely by me.

The GRECO event selection, discussed in Chapter 7, consists of a number of levels. The DeepCoreFilter, described in Section 7.2, is my own project, but was written many years prior to my employment at the Niels Bohr Institute during my undergraduate degree at Penn State University. The NoiseEngine project mentioned briefly in Section 7.3.1 is a contribution of mine from my master's degree work at the University of Alabama. Neither of these algorithms was changed by me during the course of my PhD work.

The cuts included in the GRECO selection up to Level 3 (Section 7.3) were original written for the low energy working group in IceCube and I did not modify these. The cuts performed at Level 4 (Section 7.4) were written originally by Jason Koskinen for a previous incarnation of this analysis which suffered from poor modeling of backgrounds. I took over the analysis when I joined the Niels Bohr Institute in January of 2014 and chose to use Jason's cuts and BDT without retraining on newer simulation sets.

The GRECO Levels 5 (Section 7.5) and 6 (Section 7.6) are my own work, although the algorithms described were not written by me. Instead, my contribution consisted of the choice and optimization of variables for these levels with the goal of reducing the

---

atmospheric muon and accidental trigger rates in the sample. This process occurred concurrently with the calibration of the Vuvuzela V2 model from the summer of 2014 until the spring of 2015 .

The PegLeg reconstruction described in Section 7.7 is the work of Martin Leuermann, a PhD student at RTWH Aachen. Likewise, the cuts described in Section 7.7.3 were also discovered by Martin and added to the standard GRECO processing. Martin’s work investigating disagreement between data and simulation during his analysis led to the discovery of the flaring DOMs described in Section 7.8.3. The discovery of disagreement in the simulated SPE template (Section 7.27) was informed by investigations performed by me, although the new templates were found through the work of Martin Rongen at RTWH Aachen and Spencer Axani at MIT. I do not claim credit for the hard work performed by these collaborators. The remaining work described in Section 7.7 was performed by me.

The analysis work presented in Chapter 8 was part of a collaborative effort amongst many PhD students. The choice of binning for the appearance analysis was informed by work done by Elim Cheung of the University of Maryland. Martin Leuermann, Elim, and I performed analyses of the GRECO dataset in parallel to measure the neutrino mass hierarchy, muon neutrino disappearance, and tau neutrino appearance respectively. We have worked together continuously for nearly three years. The analyses performed have many similarities and have benefited from the regular dialog between the three of us.

The OscFit software used to perform the fits for the appearance analysis was originally written by Juan Pablo Yanez for his PhD thesis work at Humboldt-Universität zu Berlin with later updates by Andrii Terliuk at DESY and Joshua Hignight at Michigan State University. Martin and I have worked together to further upgrade this software, implementing additional systematics and other improvements for oscillation measurements. Elim developed an independent fitter and performed checks of the OscFit code, finding and eliminating numerous minor errors previously included in the fitter implementation.

The final measurements of Martin’s, Elim’s, and my searches were performed simultaneously, but independently. The checks described in Sections 8.3.1 through 8.9.2 were performed by me specifically for the tau appearance analysis. Results from each were checked across all three analyses to improve our understanding of the sample.

My work has been varied over the course of my time at the Niels Bohr Institute. This thesis exists as a partial record of my involvement in IceCube. I regret that timing constraints prevent me from remarking upon my contributions to trigger development, background and signal simulation, and reconstruction work for a planned upgrade of the IceCube detector that I have performed during my time at the Niels Bohr Institute. Despite the omissions, I hope that this record provides a useful description for my own efforts during the last four years and context for this thesis.

# Contents

<b>1</b>	<b>Introduction</b>	<b>1</b>
1.1	The History of the Neutrino . . . . .	1
1.2	History of Cosmic Rays . . . . .	2
1.3	Atmospheric Neutrinos . . . . .	4
1.4	The Standard Model . . . . .	4
1.5	Methods of Detection . . . . .	8
<b>2</b>	<b>Neutrino Oscillations</b>	<b>12</b>
2.1	Solar Neutrinos: A Hint of Multiple Flavors . . . . .	12
2.2	Super-Kamiokande and Atmospheric Neutrinos . . . . .	13
2.3	Oscillation Theory and the PMNS Matrix . . . . .	14
2.4	Unitarity of the Mixing Matrix . . . . .	17
<b>3</b>	<b>The IceCube Detector</b>	<b>25</b>
3.1	The DOM: The Basic Unit of IceCube . . . . .	25
3.2	Pulse Extraction . . . . .	28
3.3	The Geometry of the Detector . . . . .	29
3.4	The Bulk Ice Model . . . . .	32
3.5	The Hole Ice . . . . .	33
<b>4</b>	<b>Simulation of the IceCube-DeepCore Detector</b>	<b>36</b>
4.1	Monte Carlo Generators . . . . .	36
4.2	Propagation of the Particles and Light . . . . .	40
4.3	Simulating the Detector Electronics . . . . .	41
<b>5</b>	<b>Updates to the Noise Simulation</b>	<b>44</b>
5.1	A Summary of Previous Fits . . . . .	44
5.2	Limitations and Disagreement with Previous Fits . . . . .	45
5.3	Low-dt Noise from Vuvuzela . . . . .	46
5.4	Updating the Fitting Code . . . . .	47
5.5	Results of New Noise Fits . . . . .	52
<b>6</b>	<b>Low-Energy Muon Simulation</b>	<b>57</b>
6.1	CORSIKA Generation In DeepCore . . . . .	57
6.2	MuonGun for DeepCore . . . . .	58
6.3	Simulation Efficiency with KDE Prescales . . . . .	59
<b>7</b>	<b>GRECO: An Event Selection at the Limits of DeepCore</b>	<b>64</b>
7.1	Hit Cleaning . . . . .	64
7.2	Level 1: The DeepCoreFilter . . . . .	66
7.3	Low-En Level 3 Cuts . . . . .	67

---

7.4	GRECO Level 4 Cuts . . . . .	69
7.5	GRECO Level 5 Cuts . . . . .	74
7.6	GRECO Level 6 Cuts . . . . .	80
7.7	GRECO Level 7: Final Level . . . . .	86
7.8	Calibration Discoveries with GRECO . . . . .	90
7.9	The Properties of the GRECO Event Selection . . . . .	101
<b>8</b>	<b>A Search for Tau Neutrinos from Oscillations</b>	<b>106</b>
8.1	Parametrizing the Tau Neutrino Appearance . . . . .	106
8.2	Binning of the Appearance Analysis . . . . .	109
8.3	Parametrization of Systematic Uncertainties . . . . .	112
8.4	Effects of Systematic Uncertainties . . . . .	118
8.5	The Test Statistic for the Analysis . . . . .	132
8.6	Expected Sensitivity to Appearance . . . . .	137
8.7	Feldman-Cousins vs Wilk's Theorem . . . . .	138
8.8	Impact of Systematic Uncertainties . . . . .	141
8.9	Fitting Data . . . . .	143
8.10	Results from the Search for Appearance . . . . .	146
8.11	Complementary Measurements from This Analysis . . . . .	151

# List of Figures

1.1	The number of neutrinos coupling to the Z from ALEPH . . . . .	2
1.2	The cosmic ray spectrum as a function of energy . . . . .	3
1.3	Expected neutrino flux as a function of energy . . . . .	5
1.4	Expected neutrino flux as a function of direction . . . . .	5
1.5	The Standard Model . . . . .	6
1.6	Feynman diagrams for W, Z interactions of neutrinos . . . . .	6
1.7	QE, RES, and DIS cross sections for neutrinos . . . . .	7
1.8	A Feynman diagram of a charged current DIS neutrino interaction . . . . .	8
1.9	Energy losses of a muon in matter . . . . .	10
2.2	Global best fit neutrino oscillation parameters from Nu-Fit.org . . . . .	18
2.3	Oscillation probabilities between 1 and 300 GeV . . . . .	19
2.4	The MINOS and NO $\nu$ A NC oscillation search results . . . . .	20
2.5	Unitarity normalization tests of the PMNS matrix . . . . .	22
2.6	Constraints on PMNS matrix terms from unitarity . . . . .	23
3.1	The IceCube DOM . . . . .	25
3.2	Afterpulsing calibrations in IceCube . . . . .	26
3.3	Examples of IceCube digitized waveforms . . . . .	27
3.4	The timing structure of noise in the IceCube detector . . . . .	28
3.5	An overview of the subdetectors in the IceCube Neutrino Observatory . . . . .	29
3.6	The IceCube and DeepCore string geometry . . . . .	30
3.7	Event signatures above 1 TeV in IceCube . . . . .	31
3.8	Event topologies of 50 GeV events in DeepCore . . . . .	32
3.9	Dust concentration measurements from deployment of strings . . . . .	33
3.10	The absorption and scattering properties of the ice . . . . .	34
3.11	The measurement of anisotropy in the ice . . . . .	35
4.1	Energy losses for a muon in ice . . . . .	40
4.2	Angular acceptance models for IceCube hole ice . . . . .	42
4.3	The SPE template used in IceCube simulation . . . . .	43
5.1	Examples of noise distributions from Vuvuzela V1 calibrations . . . . .	45
5.2	Noise trigger rates with Vuvuzela V1 . . . . .	46
5.3	HLC and SLC number of hit DOMs with Vuvuzela V1 . . . . .	47
5.4	HLC and SLC charge with Vuvuzela V1 . . . . .	48
5.5	The effect of low-dt Vuvuzela in the charge distribution . . . . .	48
5.6	Schematic diagram of Vuvuzela V2 calibration fit . . . . .	49
5.7	Examples of Vuvuzela V2 noise fits . . . . .	50
5.8	Vuvuzela V2 likelihood values as a function of fit parameters . . . . .	54
5.9	Vuvuzela V2 fit parameters as a function of string and DOM number . . . . .	55

5.10	Vuvuzela V2 log-likelihood vs string and DOM number . . . . .	56
6.1	The CORSIKA distribution at L5 used to select MuonGun's simulation range	59
6.2	Inefficiency in energy and zenith of the MuonGun generation spectrum . . .	60
6.3	Inefficiency in zenith and azimuth of the MuonGun generation spectrum . .	61
6.4	The MuonGun generation energy and zenith spectrum using the KDE Prescale	62
6.5	The MuonGun generation energy and azimuthal spectrum using the KDE Prescale . . . . .	62
7.1	Hit cleaning algorithms in IceCube . . . . .	65
7.2	The distribution of effective particle speeds used by the DeepCoreFilter to identify and reject muons. Because muons interact first outside of DeepCore, a large peak is visible at speeds around 0.3 m/ns, the speed of light. Figure from [72] . . . . .	67
7.3	The FirstHit Z position . . . . .	70
7.4	Number of Hits Above Z=-200 . . . . .	71
7.5	QR6 and C2QR6 . . . . .	71
7.6	Tensor-of-Inertia Eigenvalue Ratio . . . . .	72
7.7	The improvedLineFit Speed . . . . .	72
7.8	The L4 BDT Score . . . . .	73
7.9	Time to 75% Charge . . . . .	75
7.10	A schematic diagram showing the regions of the VICH algorithm. VICH returns the number of hit DOMs in the shaded region, corresponding to the pulses that are both causally connected with the trigger and entering DeepCore. . . . .	75
7.11	Veto Identified Causal Hits . . . . .	76
7.12	First Hit $\rho$ Position . . . . .	76
7.13	Quartile Distance . . . . .	77
7.14	Quartile Z-Travel . . . . .	77
7.15	SPE Reconstruction Zenith Angles . . . . .	78
7.16	The L5 BDT Score . . . . .	79
7.17	Fill-Ratio . . . . .	81
7.18	The number of hit DOMs at GRECO Level 6 . . . . .	83
7.19	Number of hit DOMs found by CorridorCut . . . . .	84
7.20	Example of Corridors into DeepCore . . . . .	85
7.21	The FiniteReco Containment Cuts . . . . .	86
7.22	Diagram Describing the FiniteReco Method . . . . .	86
7.23	The FiniteReco containment cut applied at GRECO Level 6 . . . . .	87
7.24	The Pegleg containment cuts applied at Level 7 . . . . .	89
7.25	The 2D cuts applied to the time and energy variables at Level 7 . . . . .	91
7.26	The effect of the data SPE correction applied in 2015 . . . . .	92
7.27	A comparison if the old and new SPE templates for simulation . . . . .	93
7.28	A comparison of the charge extraction in data and simulation at GRECO L7. Both the time and charge are shown for individual pulses on all DOMs. The time is measured relative to the largest pulse observed on each DOM during an event. The data and simulation histograms are independently normalized to 1.0. While the two show broad agreement, notable differences occur at low charge. . . . .	94

7.29	The reconstructed Z position plotted against the reconstructed distance from string 36. The L7 cuts from GRECO have been removed for this plot. The colorbars in both plots have been normalized to be identical. The data and simulation show good agreement except for two points in the data, near $\rho_{36} = 75$ at depths of -310 and -490. . . . .	95
7.30	The reconstructed X position and Y position of events in the detector. The L7 cuts from GRECO have been removed for this plot. The colorbars in both plots have been normalized to be identical. Once again, reasonable agreement is observed in most regions, although data events have a clear excess near $x=110$ m, $y=-60$ m. This position corresponds to string 83. . . . .	96
7.31	The RMS of the charges showing the events with flaring DOMs . . . . .	97
7.32	The reconstructed Z position using Pegleg. The GRECO L7 cuts have not been applied in order to show discrepancies below the detector. Noticeable disagreement is seen below the detector at a depth of -500 m. Additional disagreements are also visible at the top of DeepCore, a region dominated by atmospheric muons. . . . .	98
7.33	The NuGen and GENIE true energy spectra at Final Level . . . . .	98
7.34	The NuGen and GENIE interaction depths at Final Level . . . . .	99
7.35	The reconstructed azimuthal direction from Pegleg . . . . .	100
7.36	GRECO rates at each cut level . . . . .	101
7.37	GRECO Final Level zenith and energy spectrum . . . . .	103
7.38	The reconstructed energy and zenith of the GRECO sample at Final Level. Events in data reconstruct to both relatively high energies ( $E_R > 100$ GeV) and very low energies ( $E_R \approx 2$ GeV). Using the NuFit 2.2 oscillation parameters and the flux model from Honda, the $\nu_\tau$ events are observed in the very upgoing region around $10^{1.4} = 25$ GeV. . . . .	103
7.39	Reconstructed zenith resolutions . . . . .	104
7.40	Reconstructed zenith resolutions . . . . .	105
8.1	A tau neutrino event observed at OPERA . . . . .	108
8.2	Signal and background in the Super-Kamiokande analysis . . . . .	109
8.3	Cumulative distributions of two PID variables in GRECO . . . . .	110
8.4	Comparison of separating power between PID variables . . . . .	111
8.5	Neutrino histograms for appearance analysis . . . . .	114
8.6	Background and data histograms for appearance analysis . . . . .	115
8.7	Effect of $\Delta m_{31}^2$ in the analysis histogram . . . . .	119
8.8	Effect of $\theta_{23}$ in the analysis histogram . . . . .	119
8.9	Effect of $\delta\gamma_\nu$ in the analysis histogram . . . . .	120
8.10	Effect of $N_{\nu_e}$ in the analysis histogram . . . . .	121
8.11	The neutrino flux shape uncertainties . . . . .	121
8.12	Effect of $\nu/\bar{\nu}$ in the analysis histogram . . . . .	122
8.13	Effect of Up/Horizontal in the analysis histogram . . . . .	122
8.14	Effect of $\delta\gamma_{CR}$ in the analysis histogram . . . . .	123
8.15	Effect of $M_a^{QE}$ in the analysis histogram . . . . .	124
8.16	Effect of $M_a^{RES}$ in the analysis histogram . . . . .	125
8.17	Effect of the neutrino DIS uncertainty in the analysis histogram . . . . .	125
8.18	Effect of the neutrino DIS uncertainty in the analysis histogram . . . . .	126
8.19	Effect of the neutral current normalization in the analysis histogram . . . . .	127
8.20	Effect of the coincident events in the analysis histogram . . . . .	128

8.21	Effect of the DOM efficiency in the analysis histogram . . . . .	128
8.22	Effect of the absorption in the analysis histogram . . . . .	129
8.23	Effect of the scattering in the analysis histogram . . . . .	130
8.24	Effect of the hole ice parameter in the analysis histogram . . . . .	131
8.25	Effect of the forward scattering parameter in the analysis histogram . . . . .	131
8.26	The sensitivity of this analysis in the (a) NC+CC and (b) CC-only channel. The top plot shows the Asimov expectation (black dotted line) and the Brazilian flag (green, yellow bands). The significances assuming Wilk's theorem (gray horizontal lines) and Feldman-Cousins (red horizontal lines) are also shown. The bottom plot shows the expected $1\sigma$ and 90% ranges for Wilks theorem and Feldman-Cousins compared to the most recent results from the OPERA and Super-Kamiokande analyses. . . . .	137
8.27	$\Delta\chi_{FS}^2$ distributions for 11 points in $N_{\nu\tau}^{True}$ . . . . .	140
8.28	The N+1 parameter tests . . . . .	142
8.29	The N-1 redundancy tests . . . . .	143
8.30	The hidden potential tests . . . . .	144
8.31	The goodness of fit in the appearance search . . . . .	145
8.32	The "signed" $\chi_{FS}^2$ values for the CC-only fit . . . . .	145
8.33	The "signed" $\chi_{FS}^2$ values for the NC+CC fit . . . . .	146
8.34	The final result of the CC-only fit . . . . .	147
8.35	The final result of the NC+CC fit . . . . .	147
8.36	The best fit value of each systematic with priors . . . . .	148
8.37	The CC-only posterior distributions expected compared to final fit values . . . . .	148
8.38	The NC+CC posterior distributions expected compared to final fit values . . . . .	149
8.39	The results of a disappearance fit with GRECO . . . . .	152
8.40	Neutrino mass ordering measurement with GRECO . . . . .	152

# List of Tables

1.1	Branching ratios for the tau lepton decay . . . . .	9
6.1	The computational requirements needed for the production of standard CORSIKA sets in IceCube. The number of events reaching Final Level of the appearance search (Section 7.7) are shown. CORSIKA simulations are computationally intensive, but inadequate for low energy analyses in IceCube.	58
6.2	The computational requirements needed for the production of MuonGun simulation for DeepCore. The MuonGun simulation is nearly two orders of magnitude more efficient at producing statistics at Final Level in the appearance analysis. . . . .	59
6.3	The computational requirements and number of events for each muon generation scheme. The use of the KDE prescale improves the simulation efficiency by a factor of 50x compared to the DeepCore MuonGun simulation method described in Section 6.2. . . . .	61
7.1	The event rates after the Level 3 cuts in GRECO. The total simulated rate is calculated using CORSIKA events and ignoring MuonGun. The data is estimated from a burn sample of 14 days. Rates are given in mHz. . . . .	69
7.2	The event rates after the Level 4 cuts in GRECO. The total simulated rate is calculated using CORSIKA events and ignoring MuonGun. The data rate is estimated from a burn sample of 14 days. Rates are given in mHz. . . . .	74
7.3	The event rates after the Level 5 cuts in GRECO. The total simulated rate is calculated using CORSIKA events and ignoring MuonGun. The data rate is estimated from a burn sample of 14 days. Rates are given in mHz. . . . .	80
7.4	The event rates after the Level 6 cuts in GRECO. The total simulated rate is calculated using CORSIKA events and ignoring MuonGun. Rates are given in mHz. . . . .	85
7.5	The event rates at each cut level in the GRECO selection. Note that the MuonGun events are included in this table, but do not contribute to the total Monte Carlo expectation to prevent double-counting of muon events from the CORSIKA sample. All rates are given in millihertz. . . . .	102
7.6	Simulation uncertainties at GRECO Level 7 . . . . .	102
8.1	The rates expected for each of the neutrino types in the Super-Kamiokande search for tau neutrino appearance . . . . .	109
8.2	Available systematics simulation sets for GENIE . . . . .	116
8.3	Available systematics sets for MuonGun . . . . .	117
8.4	Total $\chi^2$ impact of each of the oscillation parameters . . . . .	118
8.5	Priors and allowed ranges for each systematic included in this analysis. . . . .	135
8.6	The numerical values of the systematics parameters . . . . .	150



Measurements of atmospheric neutrino oscillations, such as those performed in this thesis, require a background of understanding of both atmospheric neutrinos as well as neutrino oscillations. A history of neutrinos (Section 1.1) is used to explain the discovery of the three known flavors of neutrinos as well as the difficulties inherent in the study of these elusive particles. A discussion of the history of cosmic rays (Section 1.2) explains the source of both the neutrinos (Section 1.3) used as signal in this thesis as well as the muons, which form one of the primary backgrounds in the search for atmospheric neutrino oscillations.

The detection of neutrinos is described in two parts. A discussion of the neutrino interactions (Section 1.4.1), explains the interactions of neutrinos with matter. The detection of these interactions through electromagnetic emission is then covered (Section 1.5).

## 1.1 The History of the Neutrino

In 1896, Henri Becquerel discovered radioactivity in uranium [1]. Measurements over the following decades showed various types of nuclear decays based on the penetration depth of the ionizing emissions. Measurements of one type of radioactivity, beta decay, over the following 30 years showed that the production of two observed particles from one parent nucleus: a daughter nucleus and an outgoing electron. A single body decay of this type produces a known energy spectrum of the daughter nucleus and the electron determined by conservation of energy and momentum, leading to a narrow line emission spectrum.

Contrary to expectations, however, the measurement of energies of the two resulting particles showed wide, continuous spectra [2]. The spectrum provided a major puzzle for physicists due to the contradiction with the simple theoretical expectations. A conundrum for many years, one possible solution was suggested in 1930 by Wolfgang Pauli. In his letter, Pauli suggested that the conservation of energy and momentum could be saved if "... there could exist in the nuclei electrically neutral particles... which have spin  $1/2$  and obey the exclusion principle, and additionally different from light quanta in that they do not travel with the velocity of light" [3]. The solution to the beta decay puzzle was, then, that this additional "neutron" particle was emitted simultaneously with the observed daughter particles.

Pauli's suggestion provided a way to save the beloved conservation laws in physics, but at the expense of the assumption of a new particle. The particle, called the "neutron" in Pauli's letter and later renamed the "neutrino" by Fermi, was proposed to be electrically neutral and, therefore, completely undetectable at the time. Later work [4] proposed that the neutrinos interact only via the weak nuclear force, with an interaction strength many orders of magnitude smaller than electromagnetic and strong nuclear forces. Experimental measurements, sensitive only to electromagnetic forces, therefore could not be used to study neutrinos directly in the same way that other particles may be measured.

It was not until nearly 20 years later, in 1956, that this mystery particle was first detected [5]. In a groundbreaking work, Cowen and Reines performed an experiment at the Savannah River Plant, a nuclear power plant, demonstrating detection of the neutrino. The experiment, made up of layers of scintillation detectors around polyethylene boxes, yielded a signal-to-background rate of about 3 to 1 with a rate of  $2.88 \pm 0.22$  counts/hour

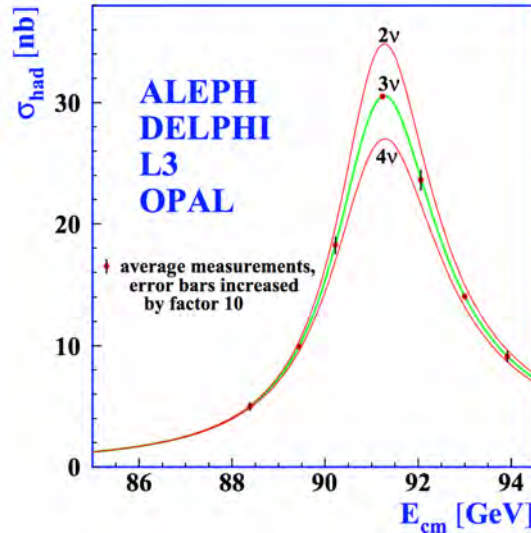


**Figure 1.1** – The number of active neutrinos with a coupling to the Z boson as measured by ALEPH, DELPHI, L3, and OPAL. The data from the four experiments strongly favors only three neutrinos coupling to the Z boson. Image taken from [11].

with a total livetime of 1371 hours, including time during which the nearby nuclear reactor was offline. For the discovery of the first neutrinos, Frederick Reines was granted a shared Nobel Prize in Physics for the year 1995 [6].

Since the neutrino was first observed, additional measurements have discovered two new flavors of neutrinos: the muon neutrino [7] and the tau neutrino [8, 9].

Searches for additional neutrinos beyond the discovered three have been performed by investigating the decays of the Z boson. The Z boson, a particle of 91 GeV [10], couples both to the neutrinos and to more easily observed hadrons and charged leptons making it a useful probe of neutrino interactions. The width of the Z decay to hadrons, for instance, is affected by the number of active, light neutrino species [11]. Additional flavors of neutrinos coupling to the Z boson would lead to a smaller decay rate to hadrons observed in accelerator searches for hadrons as shown in Figure 1.1. The number of neutrinos may be calculated by comparing the best-fit ratio of "invisible" decays of the Z boson (ie, those involving two neutrinos) to the measured width expected from charged leptons in the standard model.

$$R_{inv} \equiv \frac{\Gamma_{inv}}{\Gamma_l} = N_\nu \left( \frac{\Gamma_{\nu\nu}}{\Gamma_l} \right)_{SM} \quad (1.1)$$

Here the number of neutrinos is extracted by assuming that all active neutrinos have the same coupling to the Z boson, which has been verified experimentally. A precision measurement of the Z resonance completed at the LEP collider found the best fit value of  $N_\nu = 2.9840 \pm 0.0082$ , in good agreement with only three active neutrinos.

## 1.2 History of Cosmic Rays

In the early years of the 20th century, scientists began investigating previously-unknown ionizing radiation in the atmosphere. Scientists using electroscopes, early instruments designed to measure electric charge and radiation, discovered low levels of radiation in the air. This new radiation was observed to be reduced when the electroscope

was shielded by metal free of radioactivity, indicating that the signal was not an artifact of the detector itself and was, instead, coming from an external source.

Following just a few decades after the discovery of radioactivity by Becquerel, many scientists believed that the electroscope was detecting radiation from the Earth itself. The rate would be expected to decrease with increasing altitude above sea level and, to increase with increasing depth in the sea. Early measurements by Domenico Pacini in 1910 showed that the radiation rate decreased by 20% at a depth of 3 meters underwater compared to the rate at the surface [12], implying an origin independent of the Earth's crust. Measurements were performed with electroscopes by Victor Franz Hess in 1912 of the rate of ionizing radiation up to an altitude of 5 km [13].

Hess showed that the observed rate decreased until an altitude of around 1 km, but at a slower rate than expected from theory. Above 1400 meters, however, the rate of ionizing radiation increased again, rising substantially up to the maximum altitude reached at 5300 meters [14]. Hess's work, later confirmed by Henri Millikin, showed definitively that there exists a source of radiation of extraterrestrial origin, earning him the Nobel Prize in Physics for 1936 [15]. This radiation was later dubbed "cosmic rays" by Millikan in reference to their extraterrestrial origin.

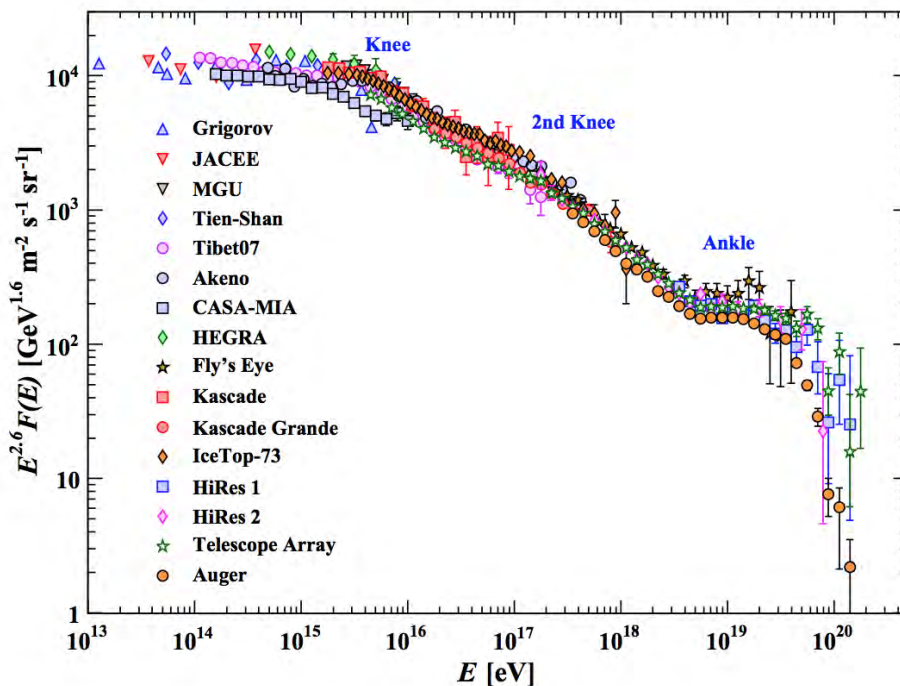


**Figure 1.2** – The cosmic ray spectrum covers many orders of magnitude in energy and has been verified by many experiments to high precision. The various features are thought to be caused by multiple sources at different scales. Image taken from [10]

The cosmic rays originally observed by Hess are now known to be primarily composed of protons and helium nuclei reaching the atmosphere from beyond the Earth. Modern measurements have shown that the cosmic ray spectrum primarily consists of protons with a small contribution from helium and heavier elements [10]. These ions are accelerated in astrophysical sources up to extremely high energies. The cosmic ray spectrum extends over many orders of magnitude, with the highest energy observations reaching  $10^{20}$  electronvolts - far higher than any Earth-based accelerator. The spectrum, shown in

Figure 1.2, has multiple features that are believed to arise from different accelerator sources at different scales, each of which has been verified by multiple experiments.

Work on cosmic rays has led to numerous discoveries. In 1937, the first *hadronic showers* were observed [16]. Hadronic showers of particles created by interactions of cosmic rays were shown to produce large numbers of daughters [17, 13]. These showers may result in the production of  $5 \times 10^6$  to over  $10^9$  particles each [18]. These showers begin with a cosmic ray primary particle, often a single proton accelerated to high energies, which interacts with particles of the Earth's atmosphere. The interaction leads to the creation of various daughters, including muons, pions, kaons, and other hadrons and neutrinos.

### 1.3 Atmospheric Neutrinos

Air showers from cosmic rays provide a useful natural source of neutrinos in the GeV energy range and above that may be used for fundamental physics research. The hadronic shower produces pions and kaons which decay to produce neutrinos

$$\pi^+ \rightarrow \mu^+ \nu_\mu \rightarrow e^+ \nu_e \bar{\nu}_\mu \nu_\mu \quad (1.2)$$

from the pions and from the kaons

$$K^+ \rightarrow \pi^+ \nu_\mu \rightarrow e^+ \nu_e \bar{\nu}_\mu \nu_\mu \nu_\mu \quad (1.3)$$

The resulting neutrino flux depends on a number of parameters, including the Earth's magnetic field and temperature profile, the cosmic ray flux, and the details of hadronic interactions in air showers [19]. The calculation of the neutrino flux predictions requires significant, dedicated simulation work, producing fluxes as both a function of energy (Figure 1.3) and direction (Figure 1.4).

### 1.4 The Standard Model

Muons and neutrinos form just a small part of the Standard Model of particle physics. The Standard Model, with fundamental particle types and properties shown in Figure 1.5, consists of six quarks (up, down, strange, charm bottom, and top), three charged leptons (electron, muon, and tau), three uncharged leptons (electron neutrino, muon neutrino, and tau neutrino), and the five bosons related to interactions (photon, Z, W, gluon, and Higgs). The Standard Model, developed over the last half century, elegantly encapsulates the range of phenomena known to occur in particle physics and has been verified repeatedly over decades by many experiments, yielding precise checks on a wide range of parameters.

The three charged leptons and neutrinos form three "families" or "flavors". Each charged lepton is associated with a coupled neutrino which shares a lepton number that is conserved in interactions mediated by the W boson. The electron, the lightest of the charged leptons at 511 keV [10], is a key ingredient of the atoms that make up the world, is the only stable charged lepton. The muon, with a mass of 105.7 MeV, is the middle of the three charged leptons, often appearing in particle interactions accompanied by the muon neutrino. The muon has a relatively long lifetime of 2.197 microseconds, far longer than many unstable hadrons. The tau lepton is the heaviest of the leptons, and with a mass of 1.777 GeV, it is heavier than the proton and appears only in relatively high energy interactions. The tau has an extremely short lifetime, at 290.6 femtoseconds, and

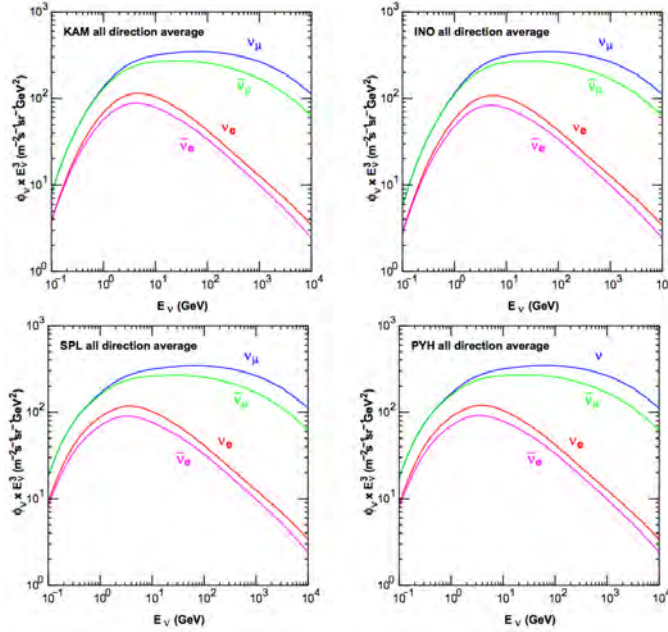


**Figure 1.3** – The expected neutrino flux at Kamioka mine, Japan (Super-Kamiokande, top left), Ino Peak, India (India-based Neutrino Observer, top right), the South Pole (IceCube, bottom left), and Pyhasalmi mine, Finland (EMMA experiment, bottom right) as a function of energy. Note that the neutrino and anti-neutrino fluxes are characterized separately. The differences in the flux at each site is due to differences in the Earth’s magnetic field and temperature profile. Figure taken from [19].

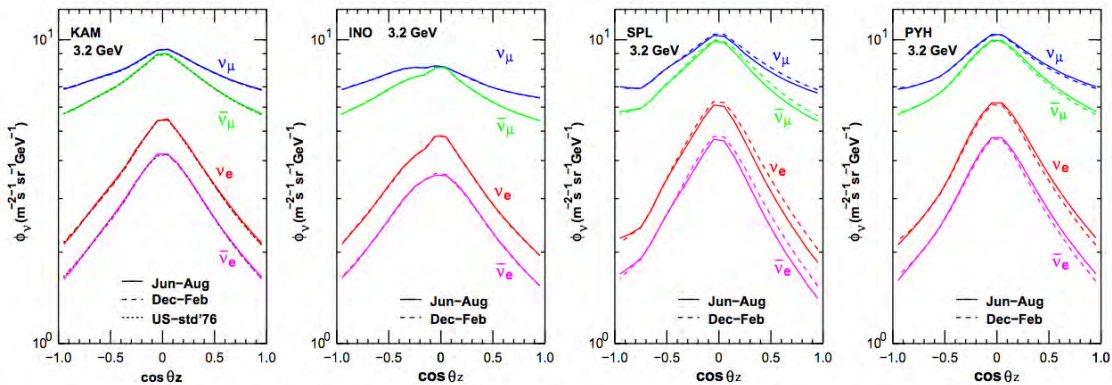


**Figure 1.4** – The expected flux of 3.2 GeV neutrinos at Kamioka mine, Japan; Ino Peak, India; the South Pole; and Pyhasalmi mine, Finland as a function of the cosine of the zenith angle. A value of  $\cos\theta_z = -1$  indicates neutrinos passing through the entire Earth and entering the detector from below while a value of  $\cos\theta_z = +1$  indicates neutrinos coming from the atmosphere directly above the detector. The differences in the flux at each site are due to differences in the Earth’s magnetic field and temperature profile. Figure taken from [19].

a rich variety of decay products. This extremely short lifetime and high mass make the tau difficult to produce and study.

For the purposes of this work, the most significant parts of the Standard model are the neutrinos, which will be defined to be signal events; the up and down quarks, which will make up the protons and neutrons upon which the neutrinos will interact; the W and

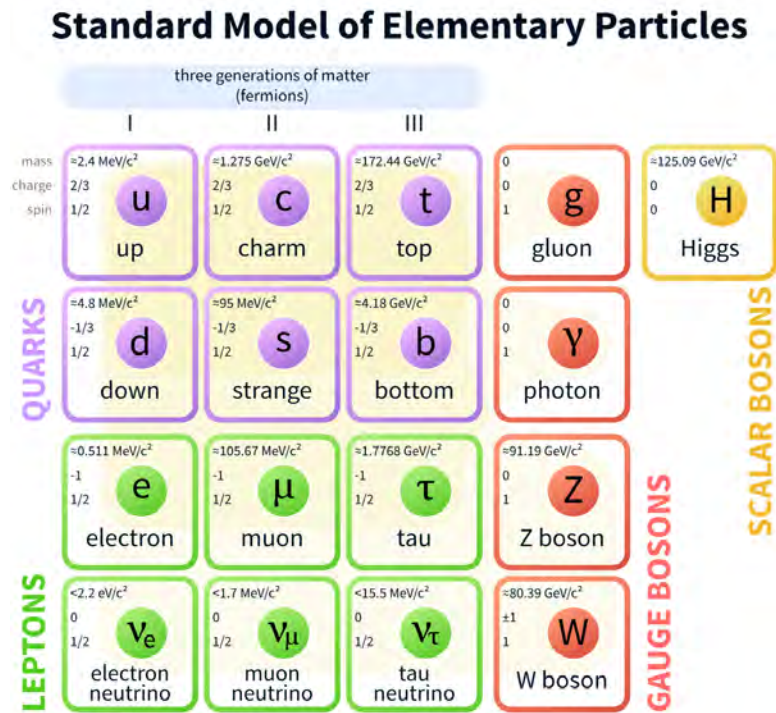


**Figure 1.5** – The Standard Model of particle physics is made up of charged and uncharged leptons, quarks, and the various bosons. Image taken from [20].

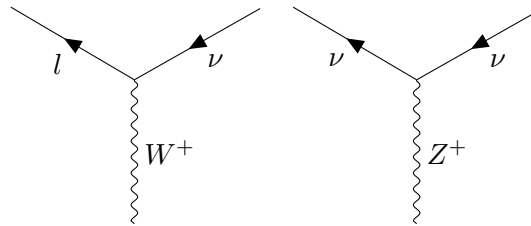


**Figure 1.6** – Feynman diagrams showing the interaction vertex of the neutrino with the W and Z boson.

Z bosons, which mediate the weak interactions via which the neutrinos may be observed; and the photon, which gives a method of observation of the interactions.

### 1.4.1 Neutrino Interactions

In the Standard Model, neutrinos are assumed to be massless, left-handed spin- $1/2$  leptons which interact solely via the weak force. The neutrinos may also interact gravitationally, although gravity has no known representation in the Standard Model. Neutrinos, therefore, are only visible via indirect effects, such as scattering or production of charged particles that may, in turn, give off their own visible signature. An understanding of the methods by which neutrinos are detected therefore forms an important basis for the study of these elusive particles. Two basic Feynman diagrams, shown in Figure 1.6, represent the two major interaction vertices available for neutrinos.

These two vertices describe the interactions relevant for the work presented in this thesis. During *charged current* (CC) interactions, a  $W^\pm$  boson is exchanged between a neutrino and target particle(s), in the process converting the uncharged neutrino to

the corresponding charged lepton. The *neutral current* ( $NC$ ) interactions are those in which the uncharged  $Z$  boson is exchanged with the target and the neutrino. Although the neutrino can change energy and momentum, it does not get converted to a charged lepton.

Detectors used to study particle properties rely on electromagnetic interactions and photons in order to detect particles. Because the neutrino itself does not interact via the electromagnetic force, charged leptons and hadrons must be used to indirectly study the properties of the incident neutrinos. Outgoing charged leptons in charged current interactions may be detected, although the direction will not necessarily correspond to that of the incident neutrino. The average angle between the incident neutrino and outgoing lepton may be approximated following Equation 1.4,

$$\langle \bar{\theta}_{\nu l} \rangle \approx \frac{1.5^\circ}{\sqrt{E_\nu [TeV]}}. \quad (1.4)$$

There exist three further classifications of neutral current and charged current neutrino interactions in the energy range used in this work: the quasi-elastic, resonant, and deep inelastic interactions [21]. A fourth type, coherent neutrino scattering, may also occur, although the energies involved are too low to impact this work. The three types of interactions contribute to the total cross section with peaks at different energies, as shown in Figure 1.7.

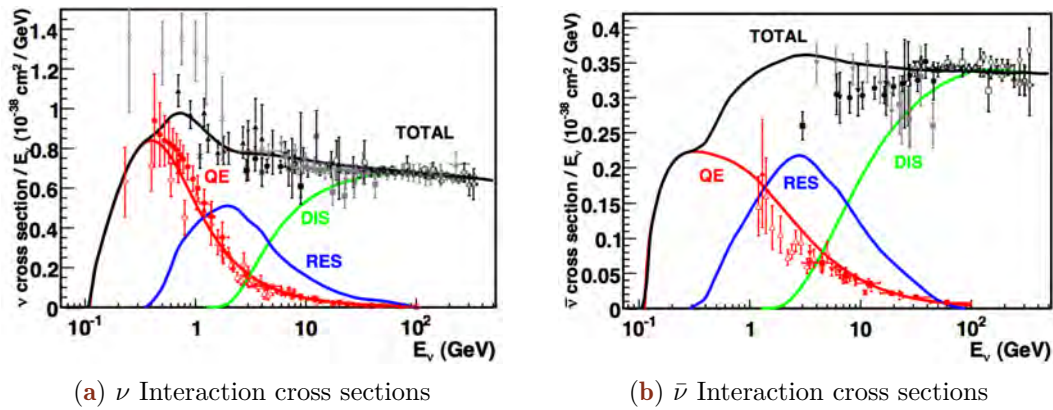


**Figure 1.7** – The relative contributions to the cross section for  $\nu$  (left) and  $\bar{\nu}$  (right). The QE events dominate below 1 GeV while the DIS events dominate above 10 GeV. Note the different scales for the neutrino and antineutrinos. Images taken from [21].

## Quasi-Elastic and Resonant Interactions

At low energies of approximately 100 MeV to around 2 GeV, the neutrinos predominantly interact via *quasi-elastic scattering* ( $QE$ ) interactions. In the  $QE$  interaction, the neutrino scatters off an entire nucleon instead of the individual quarks. In a charged current  $QE$  neutrino (anti-neutrino) interaction, the target neutron (proton) is converted to a proton (neutron) while the neutrino is converted to a charged lepton.

The cross section for  $QE$  interactions depends on various nuclear form factors that must be fit to experimental data. Many of these form factors may be fit to electron

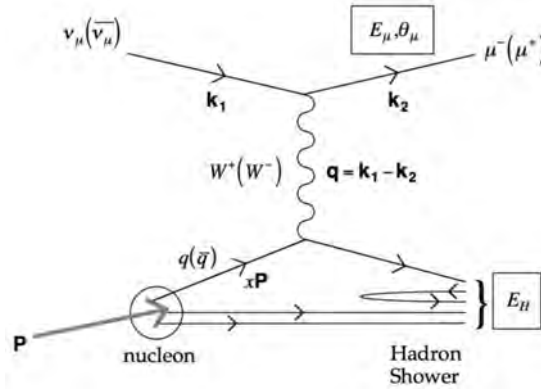


**Figure 1.8** – A Feynman diagram showing an example of a charged current neutrino DIS interaction. An incident muon neutrino interacts with a quark inside of a proton. The result is a hadronic shower as well as a charged muon. Diagram taken from [21]

scattering data, leaving only the axial vector nuclear form factors to be measured in the neutrino sector [21]. This form factor is normally assumed to have the dipole form

$$F_A(Q^2) = \frac{g_A}{\left(1 + \frac{Q^2}{M_A^2}\right)^2} \quad (1.5)$$

where  $g_A$  is a constant fit to experimental data,  $Q^2$  is the 4-momentum transferred in the interaction, and  $M_A$  is the "axial mass". This last term is fit to experimental data with a value of  $M_A = 0.999 \pm 0.011$  GeV [21].

*Resonant scattering* interactions (*RES*), which result in the excitation of a nucleon followed by decay via emission of (typically) pions, occur for neutrinos of slightly higher energies of around 500 MeV to 10 GeV. Resonant interactions are modeled in a similar way as the quasi-elastic interactions, with an associated axial mass term used to describe nuclear uncertainties.

## Deep Inelastic Interactions

Above a few GeV, the neutrino cross section rises approximately linearly with energy and is dominated by *deep inelastic scattering* (*DIS*) interactions. An example of a DIS interaction is shown in Figure 1.8. In DIS events, the exchange of the  $Z$  or  $W$  boson probes the internal structure of the nucleons, leading to a scattering off of the individual nucleons. This results in disruption of the nucleon and the larger nucleus and a collection of daughter particles forming a *hadronic shower*.

As seen in Figure 1.7, the DIS process dominates the neutrino cross section above 10 GeV and form the only significant interaction above 100 GeV [21].

## 1.5 Methods of Detection

Neutrinos may be detected through the QE, RES, and DIS interaction channels. The interaction of neutrinos at the GeV energy ranges relevant for this thesis lead to the emission of hadrons in a hadronic shower. The QE interactions at low energies convert neutrons into protons (neutrino) or protons into neutrons (antineutrino) and emitting a charged lepton. RES interactions excite a nucleon, leading to a deexcitation and emission

Decay	Branching Ratio	Background
$\tau \rightarrow e^- \nu_e \nu_\tau$	$17.83 \pm 0.04 \%$	$\nu_e$ CC
$\tau \rightarrow \mu^- \nu_\mu \nu_\tau$	$17.41 \pm 0.04 \%$	$\nu_\mu$ CC
$\tau \rightarrow \text{hadrons}$	Otherwise	$\nu$ NC

**Table 1.1** – The branching ratios for the decay of tau leptons. Two-thirds of the time, the tau lepton decays hadronically.

of particles that can be detected. DIS interactions produce larger hadronic showers containing many charged particles.

In addition to the hadronic shower, charged current interactions result in an outgoing charged lepton, the result of which depends on the flavor of the incident neutrino. Outgoing electrons quickly scatter in interactions with the surrounding media, ionizing atoms and producing a secondary *electromagnetic shower* of particles. Muons, on the other hand, travel longer distances before scattering or decaying in the medium, leading to an extended track.

The signature of a tau neutrino charged current interaction varies depending on the specific decay channels, shown in Table 1.1. Because the tau lepton has a very short lifetime, outgoing taus from charged current tau neutrino interactions tend to decay immediately.

Each of the three decay modes mimic interactions of the electron and muon neutrinos. The decay to an electron or hadrons produces electromagnetic or hadronic showers respectively. The secondary electromagnetic or hadronic cascade is theoretically distinguishable from the primary hadronic cascade produced by a tau neutrino charged current interaction, although the distance traveled by the tau lepton at the energies used in atmospheric oscillation measurements, around 10 GeV, is on the order of millimeters.

In each case, the charged particles deposit energy into the interaction medium through a series of stochastic and continuous emissions. It is through the detection of these stochastic and continuous losses that daughter particles may be identified in the study of neutrinos.

### 1.5.1 Stochastic Emission Mechanisms

A total of five major stochastic emission mechanisms are important for the energy losses in neutrino experiments [22]: ionization, bremsstrahlung, pair production,

The decay of the particle splits the energy of the parent into multiple, lower energy daughters. Decays of daughter leptons can often be important in the identification of the neutrino flavor, particularly for tau neutrino candidates occurring above 10 TeV when the primary and secondary hadronic interactions become well-separated.

Ionization losses occur when the charged lepton interacts with electrons in the medium, transferring enough energy to liberate the electrons from bound states. At energies below 1 TeV, these losses are the most significant form of energy loss for charged particles, producing a significant source of additional electrons. Ionization losses occur roughly independently of the energy of the charged lepton.

Above energies of a few hundred GeV, radiative processes dominate the energy losses for muons in matter [10]. Bremsstrahlung, photon emission from charged particles accelerating in a magnetic field, pair production, in which a particle and antiparticle (typically electron and positron) are created, and hadronic interactions of photons all dominate the energy losses of muons above 1 TeV.

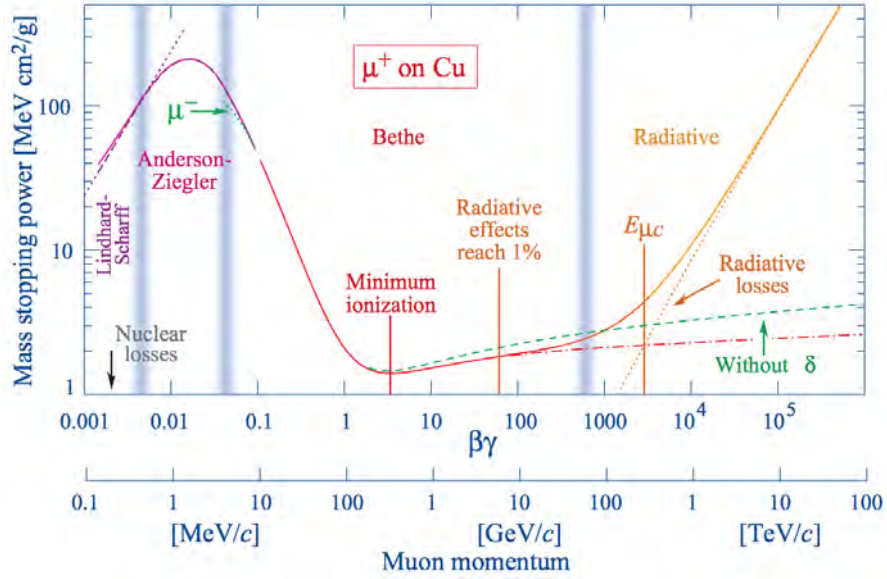


**Figure 1.9** – An example of the energy loss ( $-\frac{dE}{dx}$ ) calculated for muons incident on copper. The radiative losses due to bremsstrahlung, pair production, and photonuclear interactions are dominant above 1 TeV. Note the labeled minimum of the curve showing the energy losses of a minimum ionizing particle. Image taken from [10].

There exists a minimum in the energy loss rates. Particles emitting near this minimum rate are known as *minimum-ionizing* particles [10].

Stochastic emissions result in additional particles in the detector, leading to improved light yield. In addition, some detectors use photosensitive emulsions [23, 8], scintillators [24, 25, 26, 27], or time projection chambers [28] in order to track ionization losses. These emulsions yield precise characterization of particle decays, allowing experimentalists to uniquely determine the flavor state of the interacting neutrino.

## 1.5.2 Cherenkov Emission

When a charged particle passes through a dielectric medium with a speed larger than the local phase velocity of light, it will emit *Cherenkov radiation*[29]. The effect, first reported by Pavel Cherenkov in 1934 [30] remained unexplained theoretically until work done by Ilya Frank and Igor Tamm in 1937 [31].

For a dielectric medium, the electric field of charged particle will polarize atoms, inducing a small dipole moment in atoms in the medium [32]. The resulting disturbance of the medium propagates with the phase velocity of light, given by the speed of light,  $c$ , and the index of refraction as a function of the frequency of light,  $n(\omega)$ . If the charged particle is traveling faster than the local phase velocity, the electromagnetic disturbance propagates with constructive interference, resulting in a planar wavefront of emission known as *Cherenkov emission*. The angle of the wavefront relative to the propagation direction is given by the ratio of the distance traveled by the particle and photons in a given time,

$$\cos(\theta_C) = \frac{\frac{c}{n(\omega)}t}{vt} = \frac{c}{n(\omega)v} \quad (1.6)$$

where  $\theta_C$  is the *Cherenkov angle*,  $v$  is the speed of the particle. The energy threshold for Cherenkov emission is set by a combination of the particle mass and the local phase velocity for light,  $\frac{c}{n}$ . Using the relativistic kinetic energy [33],

$$E_C \geq mc^2 \sqrt{\frac{n^2}{n^2-1}}. \quad (1.7)$$

For ice with a index of refraction of 1.32 at 400 nanometers [34], this works out to a minimum energy of 270 keV for electrons and 56.2 MeV for muons. The number of photons emitted increases with photon energy, with approximately 50% more photons produced in blue visible light than in red[33] The full emission spectrum, first worked out by Ilya Frank and Igor Tamm in 1937 [31], depends on a number of parameters, including the energy and charge of the emitting particle as well as the properties of the medium. In the case of a particle traveling a distance  $L$  much larger than the photon frequency of interest,  $\lambda$ , the number of emitted photons may be approximated by

$$\frac{dN}{d\lambda} = \frac{2\pi\alpha}{\lambda^2} L \sin^2\theta_C \quad L \gg \lambda \quad (1.8)$$

where  $\alpha$  is the fine structure constant.

Cherenkov emission is not limited to a single charged lepton. All charged particles emit Cherenkov radiation, including any hadrons and charged daughter particles. While the total amount of energy lost via Cherenkov emission is small relative to losses due to stochastic processes, this emission type is both continuous and results directly in photons which may be observed by photodetectors. This technique is used by multiple experiments, including SNO [35], Super-Kamiokande [36], ANTARES [37], and IceCube [38].

The search for oscillation events requires an explanation of neutrino oscillations. Experimental evidence for the neutrino oscillations and current constraints on the oscillation parameters is presented in Sections 2, 2.2, and 2.3.4. The theory of neutrino oscillations is included here with broad descriptions of oscillations in vacuum (Section 2.3.2) and in matter (Section 2.3.3). Finally, a description of unitarity in the PontecorvoMakiNakagawaSakata (*PMNS*) mixing matrix is given in Section 2.4 with particular emphasis placed on the search for additional neutrino flavors (Section 2.4.1). The motivation for this thesis as well as the purpose behind joint fits between appearance and disappearance data is discussed in Section 2.4.3.

## 2.1 Solar Neutrinos: A Hint of Multiple Flavors

Early searches for neutrinos focused primarily on the Sun. The first major experiment, proposed by Ray Davis and John Bahcall, was designed to verify that fusion was the primary energy source of the Sun [39, 40]. While the core of the sun is not directly visible to conventional telescopes, neutrinos produced via nuclear fusion could escape the sun relatively unchanged and be observed at Earth.

The Homestake experiment, named for Homestake mine in South Dakota, used 615 tons of perchloroethylene to measure neutrinos via the inverse beta decay reaction



The production rate was well-measured, with a rate of 0.48 counts per day and a background of 0.09 counts per day due to interactions from cosmic ray induced muons [41]. In the typical units of the solar neutrino experiments, this worked out to

$$(\sigma\phi) = 2.56 \pm 0.16 \pm 0.16 \text{ SNU} \quad (2.2)$$

where the solar neutrino unit, SNU, is equal to  $10^{-36}$  captures/nucleus/second. The expected rate of neutrino interactions from the sun, however, was predicted to be  $8.00 \pm 0.97$  SNU given the solar models at the time. The Homestake experiment, therefore, was only observing approximately 30% of the predicted interaction rate. New measurements from other experiments, such as SAGE [42], GALLEX [43], and GNO [44] confirmed the results, although with a reduction of around 50% instead of 70% compared to theoretical expectations.

The disagreement between the number of neutrinos expected and the number predicted was not definitively solved until the Sudbury Neutrino Observatory (SNO) experiment came online. SNO was a detector located 2 km underground in the Sudbury mine in Canada [35]. The detector consisted of a large tank filled with heavy water surrounded by photo-multiplier tubes for the detection of Cherenkov emission. By introducing heavy water, SNO was sensitive to not only the charged current interactions of previous experiments, but also to neutral current interactions invisible to the inverse beta decay experiments.

SNO detected the neutral current and charged current interactions via two distinct channels. The charged-current interactions caused a deuterium atom to break down into two separate protons while also transforming the neutrino into an electron. The electron

would be produced with an energy high enough to emit Cherenkov radiation and could, therefore, be observed directly, with the energy of the electron used to constrain the incident neutrino spectrum. The primary charged current interaction at SNO was only sensitive to electron flavor neutrino interactions.

The neutral current interactions, with a threshold energy of 2.22 MeV, were able to separate the deuterium in the heavy water, leading to a free neutron in the detector. The detection of the free neutron posed initial challenges for the same fundamental reason that neutrino detection is difficult: neutrons are not charged and therefore do not emit electromagnetic radiation. Instead, early detections of these neutrons relied on the emission of a high energy gamma ray when the neutron was captured on a deuterium atom. The gamma ray could then, in turn, be absorbed on an electron, accelerating the charged particle and producing Cherenkov radiation.

Measurements at SNO were divided between these two channels in order to investigate one possible solution to the missing solar neutrinos: neutrino oscillations [45]. Because the three known neutrino states all have the same neutral current interaction cross section, the neutral current rate is expected to be constant in the presence of oscillations. The charged current rate is, however, expected to change due to the different couplings of each neutrino flavor to the  $W^\pm$  boson. Measuring both the neutral current and charged current rates therefore provided a direct test of neutrino oscillations, allowing researchers to identify the effect independent of the solar model.

SNO expected a rate of neutral current interactions from solar neutrinos of  $5.05 \times 10^6 \text{ cm}^{-2} \text{ s}^{-1}$  and an equivalent observed

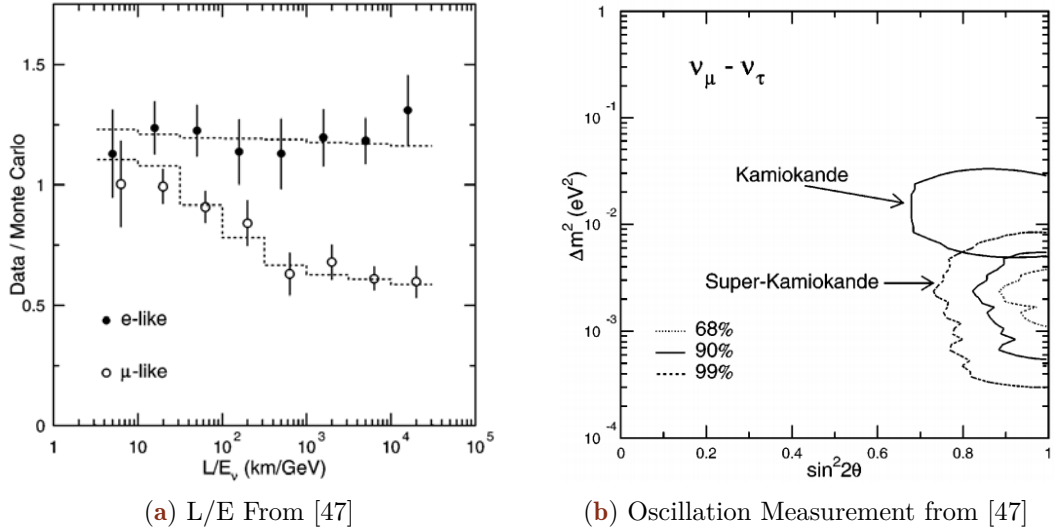
$$\phi_{NC}(\nu \text{ active}) = 5.25 \pm 0.16(\text{stat})_{-0.13}^{+0.11} \times 10^6 \text{ cm}^{-2} \text{ s}^{-1} \quad (2.3)$$

a result consistent with expectations. The charged current interaction was measured to be only 30% of the expected rate, clearly indicating that the number of electron neutrinos was well below expectations. The combination of these two results gave the first clear indication of neutrino oscillations, a result which earned the director of the experiment, Art McDonald, a Nobel Prize in 2015 [46].

## 2.2 Super-Kamiokande and Atmospheric Neutrinos

While the SNO experiment was working to identify the source of the solar neutrino deficit, the Kamioka Nucleon Decay Experiment (KamiokaNDE) and its successor, Super-Kamiokande (Super-K), were using a similar water Cherenkov detector to search for proton decay. The primary background for this rare process is neutrino interactions. Unlike SNO, however, Super-Kamiokande was sensitive to both MeV solar neutrinos and GeV neutrinos produced in the atmospheric showers from cosmic ray interactions.

While investigating backgrounds, Super-Kamiokande observed an interesting deficit in the atmospheric neutrino signal. Unlike the case in the solar neutrinos, the deficit observed by Super-K was observed solely in the muon neutrino events with no effect seen in the electron neutrinos [47]. Using the reconstructed energy and direction of events, Super-K was able to show that the number of fully contained events of  $\nu_\mu$ -like interactions changed as a function of  $L/E$  - a clear signature of neutrino oscillations in the atmospheric neutrinos. The figure, reproduced in Figure 2.2, was used, in part, with an  $2 \times 2$  approximation to the PMNS matrix to produce the first measurements, shown in Figure 2.2, of the atmospheric oscillation parameters. For the discovery of atmospheric neutrino oscillations at the same time as SNO's discovery of solar neutrino oscillations, Takaaki Kajita was awarded the 2015 Nobel Prize [46].



(a) L/E From [47]

(b) Oscillation Measurement from [47]

The first atmospheric neutrino oscillation measurements from the Super-K experiment. (a) The  $\nu_e$ -like events show no shape in L/E, as expected from a lack of electron neutrino oscillations at these L/E scales. The  $\nu_\mu$ -like interactions, however, show a clear drop, indicating the presence of oscillation effects. (b) Using the two-neutrino approximation, Super-K produced contours of the best-fit oscillation parameters for  $\nu_\mu \rightarrow \nu_\tau$  oscillations. Both figures from [47]

## 2.3 Oscillation Theory and the PMNS Matrix

In 1968, Bruno Pontecorvo suggested a process, known as *neutrino oscillation*, by which neutrinos could change flavors [48]. The theory of neutrino oscillations was further developed for the neutrino sector by Ziro Maki, Masami Nakagawa and Shoichi Sakata in 1962 [49].

### 2.3.1 The PMNS Mixing Matrix

We now understand there to be three distinct flavors of neutrinos. Neutrinos interact via the weak force and are created in flavor eigenstates ( $\nu_e, \nu_\mu, \nu_\tau$ ) describing the fields of the left-handed neutrinos. These flavor states couple via the weak charge to the electron, muon, and tau respectively.

The three weak eigenstates are related to three known neutrino mass eigenstates,  $\nu_1$ ,  $\nu_2$ , and  $\nu_3$ , via the Pontecorvo-Maki-Nakagawa-Sakata (*PMNS*) lepton mixing matrix.

$$\begin{pmatrix} \nu_e \\ \nu_\mu \\ \nu_\tau \end{pmatrix} = U_{PMNS} \begin{pmatrix} \nu_1 \\ \nu_2 \\ \nu_3 \end{pmatrix} = \begin{pmatrix} U_{e1} & U_{e2} & U_{e3} \\ U_{\mu 1} & U_{\mu 2} & U_{\mu 3} \\ U_{\tau 1} & U_{\tau 2} & U_{\tau 3} \end{pmatrix} \begin{pmatrix} \nu_1 \\ \nu_2 \\ \nu_3 \end{pmatrix} \quad (2.4)$$

This may be written in the shortened form

$$\nu_\alpha(x) = \sum_i U_{\alpha i} \nu_i(x) \quad (2.5)$$

where  $\alpha = e, \mu, \tau$  and  $i = 1, 2, 3$ .

As a  $3 \times 3$  unitary matrix, the PMNS matrix may be parametrized in terms of three mixing angles and six phases. Of these phases, five may be removed by rephasing the lepton fields with no change to the underlying physics, leaving one physical phase related to CP violation.

The PMNS matrix may be written in terms of the product of three smaller unitary matrices, each described by a *mixing angle*  $\theta_{ij}$ :

$$U_{PMNS} = \begin{pmatrix} 1 & 0 & 0 \\ 0 & c_{23} & s_{23} \\ 0 & -s_{23} & c_{23} \end{pmatrix} \begin{pmatrix} c_{13} & 0 & s_{13}e^{-i\delta_{CP}} \\ 0 & 1 & 0 \\ -s_{13}e^{i\delta_{CP}} & 0 & c_{13} \end{pmatrix} \begin{pmatrix} c_{12} & s_{12} & 0 \\ -s_{12} & c_{12} & 0 \\ 0 & 0 & 1 \end{pmatrix} \quad (2.6)$$

where  $c_{ij}$  denotes  $\cos(\theta_{ij})$  and  $s_{ij}$  denotes  $\sin(\theta_{ij})$ .

Note that if neutrinos are Majorana fermions, the additional phases may not be removed without making the masses complex. The Majorana terms form additional diagonal terms in Equation 2.6. While Majorana mass terms are beyond the scope of this work, further information may be found in [50, 51].

The three submatrices of Equation 2.6 have historically been studied by different types of experiments. This history has led to the proliferation of alternative names for the matrices and of the mixing angles.

$$U_{PMNS} = U_{Atmospheric}U_{Reactor}U_{Solar} \quad (2.7)$$

This leads to the alternative names of the mixing angles, with  $\theta_{23}$ ,  $\theta_{13}$ , and  $\theta_{12}$  being referred to as the atmospheric mixing angle, the reactor mixing angle, and the solar mixing angle respectively.

### 2.3.2 Neutrino Mixing in Vacuum

Neutrinos are created in pure flavor eigenstates. To propagate the neutrino, the Hamiltonian must be applied to the state. The flavor eigenstate of the initial neutrino is not an eigenstate of the Hamiltonian, however. Instead, the neutrino state must be written in terms of the mass eigenstates

$$|\nu(t=0)\rangle = |\nu_\alpha\rangle = \sum_i U_{\alpha i} |\nu_i\rangle. \quad (2.8)$$

After propagation for a time  $t \neq 0$ , the state will no longer be a pure flavor state.

$$|\nu(t)\rangle = \sum_i U_{\alpha i} e^{-iE_i t} |\nu_i\rangle \quad (2.9)$$

where  $E_i = \sqrt{p^2 + m_i^2}$  is the total energy of the  $i$ th mass eigenstate. If the neutrino interacts, the flavor eigenstate must again be used to calculate the probabilities of interacting as each of the three known flavors.

$$P(\nu_\alpha \rightarrow \nu_\beta) = |\langle \nu_\beta | \nu_\alpha(t) \rangle|^2 = \left| \sum_i U_{\beta i} U_{\alpha i}^* e^{-iE_i t} \right|^2 \quad (2.10)$$

Proper calculations from this point can be performed by treating each neutrino as a quantum mechanical wave packet [52]. This allows for the full description of neutrino oscillation in the context of decoherence of the mass states during propagation, allowing each mass state to possess separate momenta.

In practice, the description of neutrino oscillations necessary for this work is adequately described by making a few simplifying assumptions. In particular, this work assumes that all mass eigenstates propagate as plane waves possessing identical, well-defined momenta [50]. Neutrinos are further assumed to be extremely relativistic at the energies

of interest, an assumption well-justified by cosmological fits to the sum of the three neutrino masses, which give an upper limit of around 0.2 eV [10]. The total neutrino energy is also assumed to be unchanged during propagation. The resulting calculation of the oscillation probabilities is identical in both the simplified version and the full derivation.

To begin, equation 2.10 is expanded by explicitly including the complex conjugate,

$$P(\nu_\alpha \rightarrow \nu_\beta) = \sum_i^3 U_{\beta i}^* U_{\alpha i} \sum_j^3 U_{\beta j} U_{\alpha j}^* e^{i(E_i - E_j)t} \quad \alpha, \beta = e, \mu, \tau. \quad (2.11)$$

In the highly relativistic limit,  $E \gg m_i$ , and  $t \approx L$  where  $L$  is the distance traveled during propagation. Using these two approximations, the exponential term in Equation 2.10 may be rewritten using Euler's formula as

$$e^{i(E_i - E_j)t} = 1 - 2 \sin^2 \left( \frac{\Delta m_{ij}^2 L}{4E} \right) + i \sin \left( \frac{\Delta m_{ji}^2 L}{2E} \right) \quad (2.12)$$

where  $\delta_{\alpha\beta}$  is the Kronecker delta function. Note that a new shorthand has been defined,  $\Delta m_{ji}^2 = m_j^2 - m_i^2$ , giving a fundamental parameter of neutrino oscillations. The PMNS terms of equation 2.11 may be expanded further, yielding

$$\left| \sum_j U_{\beta j} U_{\alpha j}^* \right|^2 = \delta_{\alpha\beta} + 2 \sum_{i < j} \sum_i U_{\beta i}^* U_{\alpha i} U_{\beta j} U_{\alpha j}^* \quad (2.13)$$

where the factor of two arises due to the symmetry  $i \leftrightarrow j$ . Putting the terms together, the final oscillation probability formula is

$$\begin{aligned} P(\nu_\alpha \rightarrow \nu_\beta) = & \delta_{\alpha\beta} - 4 \sum_{i < j} \text{Re} \left[ \sum_i U_{\beta i}^* U_{\alpha i} U_{\beta j} U_{\alpha j}^* \right] \sin^2 \left( \frac{\Delta m_{ij}^2 L}{4E} \right) \\ & + 2 \sum_{i < j} \text{Im} \left[ \sum_i U_{\beta i}^* U_{\alpha i} U_{\beta j} U_{\alpha j}^* \right] \sin \left( \frac{\Delta m_{ji}^2 L}{2E} \right). \end{aligned} \quad (2.14)$$

The PMNS matrix terms may be replaced in terms of the mixing angles using Equation 2.6.

This calculation has been derived for neutrinos. To calculate the probabilities for anti-neutrinos, the calculation changes by replacing  $U \rightarrow U^*$ , resulting in a change in sign of the last term of Equation 2.14.

From Equation 2.14, the general form of the oscillation probabilities becomes clear. The PMNS matrix elements yield the amplitude of oscillations, while the frequency of the oscillations is related to three quantities: the squared difference in the masses,  $\Delta m_{ji}^2$ ; the baseline, or distance traveled,  $L$ ; and the energy of the neutrinos. Only one of these three is a fundamental physics parameter. The choices of energy and baseline are used to define characteristics of detectors used for measurements of the various mass splitting parameters and oscillation mixing angles.

Note that the oscillation probability is insensitive to the sign of the mass splitting parameter.

### 2.3.3 Matter Effects in Oscillation

Calculations up to this point have assumed neutrinos oscillating in vacuum. Modifications required for a description of matter effects begin with a modification of the Hamiltonian with a potential,  $V$ , due to coherent forward scattering of neutrino on electrons and nucleons in the medium [53].

$$H = H_0 + V \quad (2.15)$$

The value of  $H_0$  is the value of vacuum Hamiltonian. In the two-flavor case, the Hamiltonian can be shown [50, 54] to be

$$H_0 = \frac{\Delta m^2}{4E} \begin{pmatrix} -2 \cos 2\theta & \sin 2\theta \\ \sin 2\theta & 0 \end{pmatrix}. \quad (2.16)$$

where  $\theta$  is the mixing angle associated with the 2x2 PMNS matrix. The potential includes contributions from both charged current and neutral current interactions, although the charged current interactions arise solely from the electron neutrinos. The potential, expressed in the flavor basis, is then

$$V_{CC,\alpha} = \begin{cases} \sqrt{2} \pm G_F n_e(x) & \alpha = e \\ 0 & \alpha = \mu, \tau \end{cases} \quad V_{NC,\alpha} = -\frac{G_F}{\sqrt{2}} n_e(x) \quad \alpha = e, \mu, \tau \quad (2.17)$$

where a + is used for neutrinos and a - is used for antineutrinos,  $n_e$  is the density of electrons in the medium, and  $G_F$  is the Fermi coupling constant. Note that the angle included here is that of the PMNS matrix in two dimensions. A full description of three flavor neutrino oscillation in the presence of a matter potential may be found in [50, 54]. The full three-flavor oscillation calculation is used for this thesis using the Prob3++ code [55, 56], which includes an implementation of matter effects.

### 2.3.4 Global Fits to Oscillations

Since the initial discoveries of SNO and Super-K, many experiments have measured neutrino oscillations. Global fits are performed and updated regularly [57, 58].

The most recent results are shown in Figure 2.2 and include information from solar, reactor, and atmospheric oscillation experiments. The results explicitly assume unitarity of the PMNS mixing matrix and three neutrino species.

In this thesis, a measurement of atmospheric oscillations at 20 GeV will be performed. Plots of the oscillation probabilities using the global fit values of Figure 2.2 is shown in Figure 2.3.

## 2.4 Unitarity of the Mixing Matrix

While global fits assume three flavors of neutrinos, additional neutrino flavors are theoretically possible. The number of active neutrino flavors is limited to the three known flavors from the measurements of the Z boson invisible decay width (see the discussion of Section 1.1), although such measurements implicitly only measure the number of species with a coupling to the Z boson [11]. Additional flavors with no or very small couplings to the Z boson are not excluded [59]. New neutrino flavors introduced with these properties are known as *sterile neutrinos*.

The effect of sterile neutrinos on the unitarity measurements will be discussed here, although it should be noted that sterile neutrinos aren't the only possible source of non-

NuFIT 3.2 (2018)					
	Normal Ordering (best fit)		Inverted Ordering ( $\Delta\chi^2 = 4.14$ )		Any Ordering
	bfp $\pm 1\sigma$	$3\sigma$ range	bfp $\pm 1\sigma$	$3\sigma$ range	$3\sigma$ range
$\sin^2 \theta_{12}$	$0.307^{+0.013}_{-0.012}$	$0.272 \rightarrow 0.346$	$0.307^{+0.013}_{-0.012}$	$0.272 \rightarrow 0.346$	$0.272 \rightarrow 0.346$
$\theta_{12}/^\circ$	$33.62^{+0.78}_{-0.76}$	$31.42 \rightarrow 36.05$	$33.62^{+0.78}_{-0.76}$	$31.43 \rightarrow 36.06$	$31.42 \rightarrow 36.05$
$\sin^2 \theta_{23}$	$0.538^{+0.033}_{-0.069}$	$0.418 \rightarrow 0.613$	$0.554^{+0.023}_{-0.033}$	$0.435 \rightarrow 0.616$	$0.418 \rightarrow 0.613$
$\theta_{23}/^\circ$	$47.2^{+1.9}_{-3.9}$	$40.3 \rightarrow 51.5$	$48.1^{+1.4}_{-1.9}$	$41.3 \rightarrow 51.7$	$40.3 \rightarrow 51.5$
$\sin^2 \theta_{13}$	$0.02206^{+0.00075}_{-0.00075}$	$0.01981 \rightarrow 0.02436$	$0.02227^{+0.00074}_{-0.00074}$	$0.02006 \rightarrow 0.02452$	$0.01981 \rightarrow 0.02436$
$\theta_{13}/^\circ$	$8.54^{+0.15}_{-0.15}$	$8.09 \rightarrow 8.98$	$8.58^{+0.14}_{-0.14}$	$8.14 \rightarrow 9.01$	$8.09 \rightarrow 8.98$
$\delta_{CP}/^\circ$	$234^{+43}_{-31}$	$144 \rightarrow 374$	$278^{+26}_{-29}$	$192 \rightarrow 354$	$144 \rightarrow 374$
$\frac{\Delta m_{21}^2}{10^{-5} \text{ eV}^2}$	$7.40^{+0.21}_{-0.20}$	$6.80 \rightarrow 8.02$	$7.40^{+0.21}_{-0.20}$	$6.80 \rightarrow 8.02$	$6.80 \rightarrow 8.02$
$\frac{\Delta m_{3\ell}^2}{10^{-3} \text{ eV}^2}$	$+2.494^{+0.033}_{-0.031}$	$+2.399 \rightarrow +2.593$	$-2.465^{+0.032}_{-0.031}$	$-2.562 \rightarrow -2.369$	$\left[ +2.399 \rightarrow +2.593 \right]$ $\left[ -2.536 \rightarrow -2.395 \right]$

**Figure 2.2** – The global best-fit values for the three flavor neutrino oscillation fits as of November 2017. The first column shows results assuming the normal ordering while the second column shows the results for the inverted ordering. Image taken from [58]

unitarity. Any new physics models that include flavor violation, including non-standard interactions or neutrino decay models can also induce apparent non-unitarity in the 3x3 PMNS mixing matrix. For the purposes of this thesis, the sterile neutrinos offer a useful insight into one possible cause.

## 2.4.1 Sterile Neutrinos

Models of sterile neutrinos assume that no weak interactions are available to the new species. Instead, sterile neutrinos are assumed to interact with the three active neutrinos via oscillations. In this model, neutrinos oscillate using a 4x4 (or larger NxN) PMNS matrix [50, 60, 61, 59].

$$\begin{pmatrix} \nu_e(x) \\ \nu_\mu(x) \\ \nu_\tau(x) \\ \nu_s(x) \end{pmatrix} = U_{4 \times 4} \begin{pmatrix} \nu_e(x) \\ \nu_\mu(x) \\ \nu_\tau(x) \\ \nu_s(x) \end{pmatrix} = \begin{pmatrix} U_{e1} & U_{e2} & U_{e3} & U_{e4} \\ U_{\mu1} & U_{\mu2} & U_{\mu3} & U_{\mu4} \\ U_{\tau1} & U_{\tau2} & U_{\tau3} & U_{\tau4} \\ U_{s1} & U_{s2} & U_{s3} & U_{s4} \end{pmatrix} \begin{pmatrix} \nu_1(x) \\ \nu_2(x) \\ \nu_3(x) \\ \nu_4(x) \end{pmatrix} \quad (2.18)$$

The additional terms in  $U_{4 \times 4}$  lead to new mixing angles,  $\theta_{14}$ ,  $\theta_{24}$ , and  $\theta_{34}$ . The new terms may be used in the standard oscillation framework introduced in Section 2.3.2 extended with a fourth flavor state,  $\nu_s$ , and mass state,  $\nu_4$ .

$$P(\nu_\alpha \rightarrow \nu_\beta) = \sum_i^4 U_{\beta i}^* U_{\alpha i} \sum_j U_{\beta j} U_{\alpha j}^* e^{i(E_i - E_j)t} \quad \alpha, \beta = e, \mu, \tau, s \quad (2.19)$$

Unlike the three active neutrinos, sterile neutrinos cannot interact with matter, leading to a deficit in the neutrino rates from oscillations of the form  $P(\nu_\alpha \rightarrow \nu_s)$ . The location and size of the deficit is determined by the oscillation parameters associated with the  $\nu_s$  and  $\nu_4$  states. Sterile neutrinos may be indirectly observed through this deficit by studying the active neutrinos with either charged current or neutral current interactions. The effects of steriles can also be observed through the MSW and resonance effects for neutrinos that pass through the Earth [62].

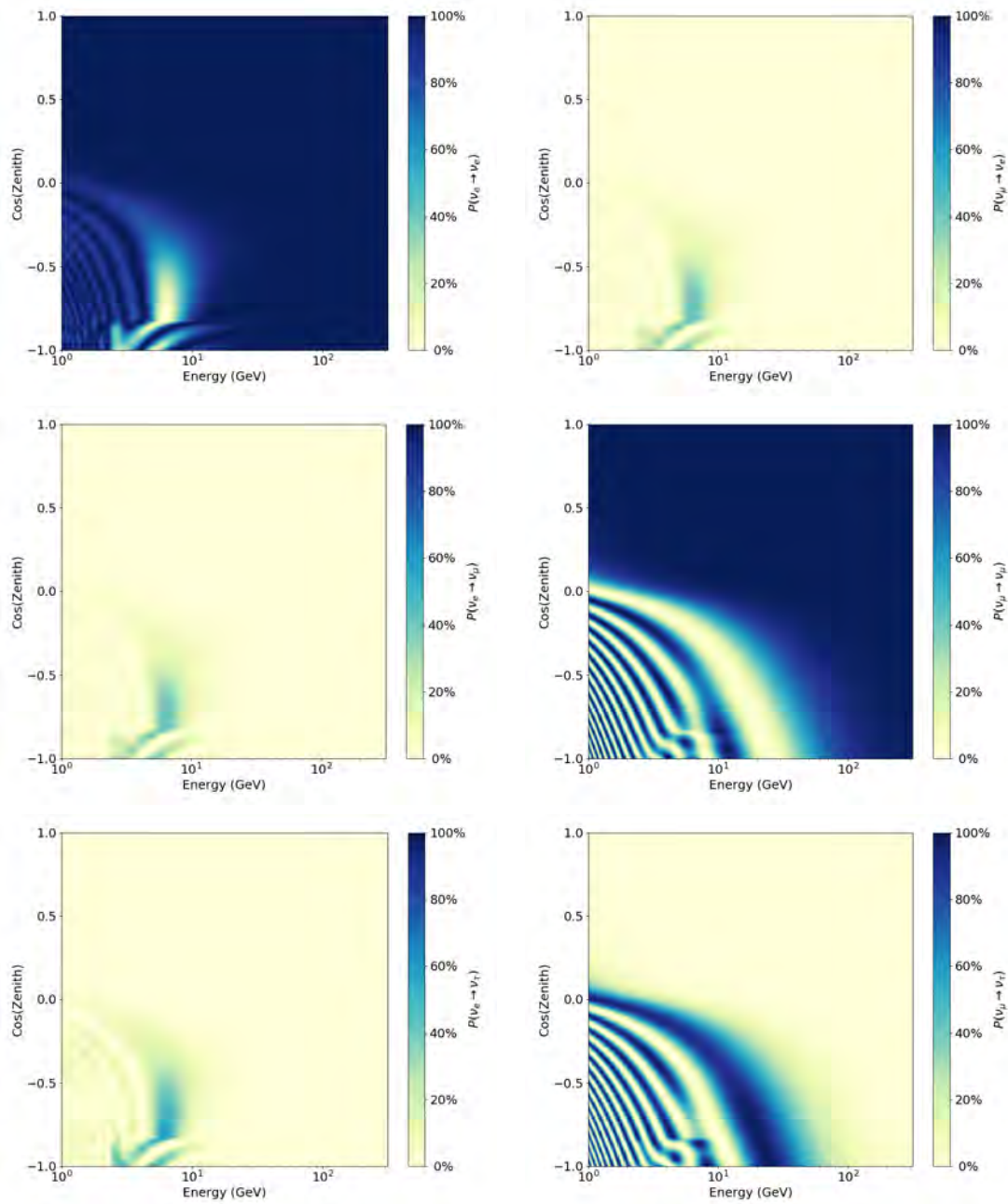


**Figure 2.3** – The oscillation probabilities for (left) electron neutrinos and (right) muon neutrinos from 1 to 300 GeV. The top row shows the oscillation probabilities to electron neutrinos, the middle row shows the oscillation to muon neutrinos, and the bottom row shows the oscillation to tau neutrinos.

### 2.4.2 Direct Searches for Steriles

While oscillation of the three active neutrinos preserves the total neutral current rate, sterile neutrinos do not. This provides a unique experimental signature for sterile neutrinos. Dedicated searches for this disappearance have been performed by MINOS [63, 64] and NO $\nu$ A [65] with assumptions on the new terms of the mixing matrix. The effect of three sterile hypotheses on the MINOS data is shown in Figure 2.4a. Around 15% of the neutral current events disappear in the three hypotheses tested by MINOS. The results of the NO $\nu$ A search are shown in Figure 2.4b.

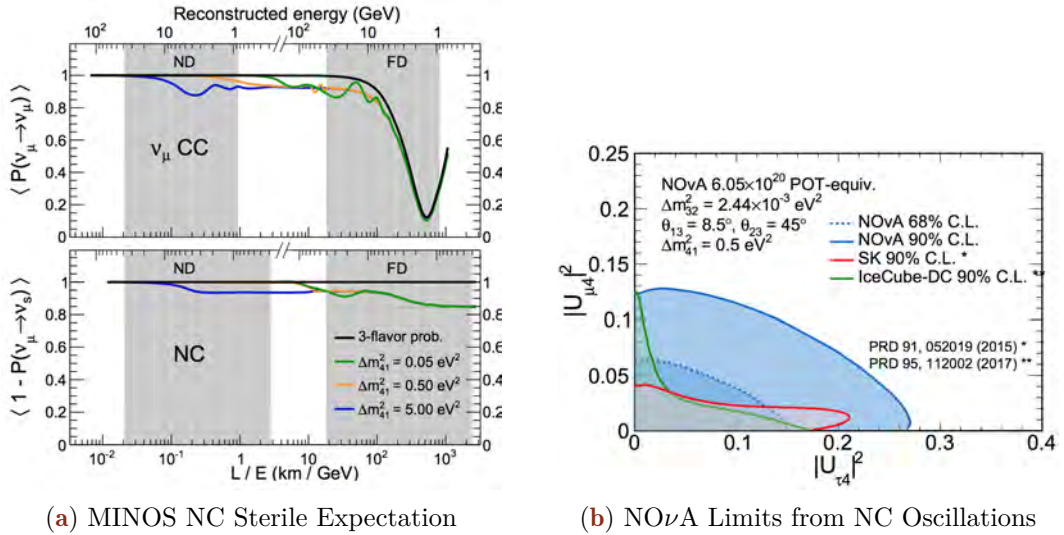


**Figure 2.4** – Expectations (a) and results (b) of searches for sterile neutrinos in the neutral current interactions. (a) Effect of three hypothetical sterile neutrinos on the measurements of the MINOS detector [64]. "ND" and "FD" refer to the near and far detector of MINOS respectively. The sterile neutrinos have a small effect on the main oscillation minimum in the charged current channel, but up to 15% of the neutral current events are lost. (b) The results of the NO $\nu$ A search for sterile neutrinos using neutral current events. The limits are interpreted in terms of the 4 $\times$ 4 PMNS mixing elements in order to compare to searches with charged current interactions in Super-Kamiokande [66] and IceCube [67].

Most experiments attempt to investigate one of the additional terms only, assuming the remainder to be negligible [66, 67, 62]. The results rule out large mixing between a hypothetical sterile neutrino and the three active flavors, although small mixing angles are still allowed by experiments [61, 59].

### 2.4.3 Indirect Searches for Steriles Using Unitarity

The addition of a fourth generation of neutrino would have consequences for neutrino oscillation measurements performed in the 3 $\times$ 3 PMNS framework. Standard 3-flavor oscillation measurements may therefore be used to place limits on sterile neutrinos.

The PMNS matrix gives the change in basis and is assumed to be unitary. The unitary condition imposes summation rules for both the rows and columns of the matrix [68].

$$\sum_i |U_{\alpha i}|^2 = 1 \quad \alpha = e, \mu, \tau \quad (2.20)$$

$$\sum_{\alpha} |U_{\alpha i}|^2 = 1 \quad i = 1, 2, 3 \quad (2.21)$$

If the neutrino mixing matrix consists of more than the three known active neutrinos, however, these unitary relations would only hold in higher dimensions. When projected down to the a 3x3 PMNS matrix, non-unitarity would be observed.

Neutrino oscillation measurements are performed with the assumption of 3x3 unitarity imposed, allowing the PMNS matrix to be rewritten in terms of three mixing angles and a single phase. The appearance and disappearance probabilities in oscillation measurements are typically written in terms of these mixing angles. Using these mixing angles, the disappearance probability for atmospheric oscillations of  $\nu_{\mu} \rightarrow \nu_{\mu}$  is given by

$$\begin{aligned} P(\nu_{\mu} \rightarrow \nu_{\mu}) &= 1 - \left| \sum_i U_{\mu i}^* U_{\mu i} e^{-im_i^2 L/2E} \right|^2 \\ &= 1 - \left( \cos^2 \theta_{13} \sin^2 2\theta_{23} + \sin^4 \theta_{23} \sin^2 2\theta_{13} \right) \sin^2 \left( \frac{\Delta m_{31}^2 L}{4E} \right) \\ &\approx 1 - \sin^2 2\theta_{23} \sin^2 \left( \frac{\Delta m_{31}^2 L}{4E} \right). \end{aligned} \quad (2.22)$$

where the final approximation has been made due to the small value of  $\theta_{13}$ . The atmospheric appearance probability,  $\nu_{\mu} \rightarrow \nu_{\tau}$ , is given by

$$\begin{aligned} P(\nu_{\mu} \rightarrow \nu_{\tau}) &= \left| \sum_i U_{\mu i}^* U_{\tau i} e^{-im_i^2 L/2E} \right|^2 \\ &= \left( \cos^2 \theta_{13} \sin^2 2\theta_{23} \right) \sin^2 \left( \frac{\Delta m_{31}^2 L}{4E} \right) \\ &\approx \sin^2 2\theta_{23} \sin^2 \left( \frac{\Delta m_{31}^2 L}{4E} \right). \end{aligned} \quad (2.23)$$

The form of the oscillation probabilities for appearance and disappearance are very similar when written in terms of the mixing angles. However, the appearance and disappearance probabilities in neutrino oscillation measurements depend on different elements of PMNS mixing matrix. Because of the difference in the elements probed, appearance and disappearance measurements may be interpreted to give limits on the fundamental elements of the mixing matrix without imposing unitarity.

This method of searching for sterile neutrinos may be applied to global fits, reinterpreting standard oscillation measurements to place limits on the size of any non-unitarity. Using the unitarity conditions of Equation 2.20 and 2.21, limits on the size of non-unitarity have been calculated[68]. Experimental constraints from a number of experiments (see reference 26 of [68]) were used to evaluate the best-fit 3x3 mixing matrix. The unitarity constraints were tested by looking at the potential deviation of each row or column

$$\Delta U_{\alpha} = 1 - \left( |U_{\alpha 1}|^2 + |U_{\alpha 2}|^2 + |U_{\alpha 3}|^2 \right) \quad \alpha = e, \mu, \tau \quad (2.24)$$

or

$$\Delta U_i = 1 - \left( |U_{\alpha i}|^2 + |U_{\beta i}|^2 + |U_{\delta i}|^2 \right) \quad i = 1, 2, 3 \quad (2.25)$$



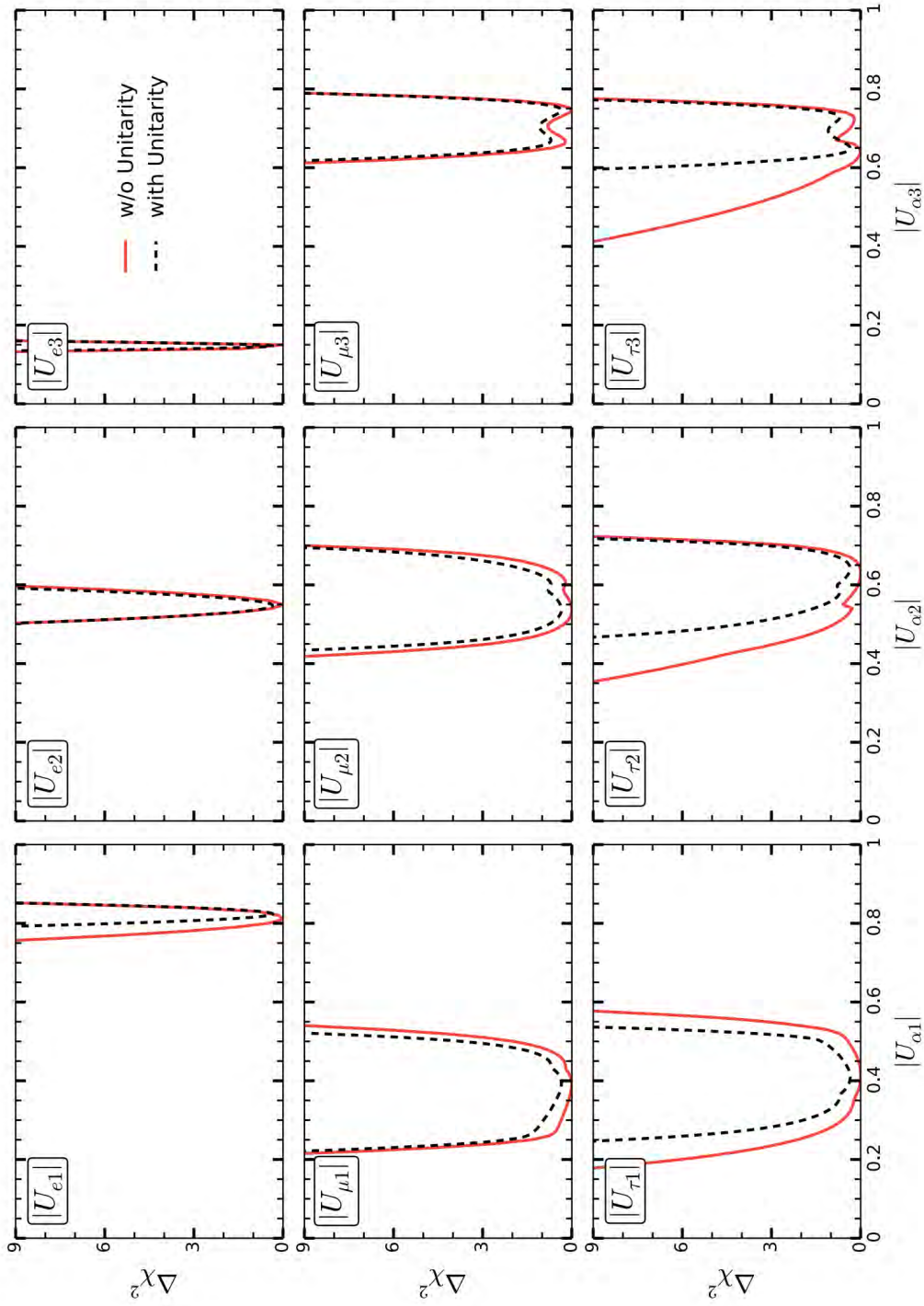


**Figure 2.6** – The constraints from a global fit to neutrino oscillation data[68] with an assumption of unitarity (black dotted) or no assumption of unitarity (red solid). The first two rows show little change from the unitarity assumption, indicating strong constraints from direct measurements. The elements of the third row, related to the  $\nu_\tau$ , show much larger changes, indicating that constraints are obtained from indirect oscillation measurements.

When the individual limits for each element of the 3x3 PMNS matrix are checked in Figure 2.6, it is the tau sector that shows the largest uncertainties. Measurements of  $\nu_\tau$  oscillations therefore can provide valuable information on unitarity in the neutrino sector, leading to indirect constraints on sterile neutrino hypotheses.

There exist two avenues for the measurement of neutrinos. The precise measurements of individual events, used most notably in the OPERA [23] and DONUT [8] experiments to identify individual events, gives unique constraining power with low backgrounds. More common, however, is the use of large experimental volumes to collect high-statistics neutrino samples. For the study of atmospheric neutrinos, volumes on the order of a kiloton are required.

The IceCube Neutrino Observatory is currently the largest neutrino detector in the world, encompassing a volume of  $1 \text{ km}^3$  of glacial ice at the geographic south pole. The design of the IceCube detector is also presented in this chapter, beginning with a description of the DOMs that make up the primary detectors within the IceCube observatory (Section 3.1). The overall geometry of the detector is discussed in Section 3.3 with a focus on the differences between the larger IceCube detector and the DeepCore subarray used for oscillation searches.

## 3.1 The DOM: The Basic Unit of IceCube

The basic unit of the IceCube detector is the *digital optical module*, often referred to simply as the *DOM* [38]. The DOM is designed around a downward-facing 10 inch R7081-02 photomultiplier tube (*PMT*) from Hamamatsu Photonics [69, 70] and includes onboard electronics for standard operation as shown in Figure 3.1. Circuit boards are included for data acquisition, control, calibration, communications and power conversion as well as for high voltage input from the surface. The electronics of the DOM are encased in a spherical glass housing designed to withstand the high pressures associated with operation in the glacier of Antarctica.

The IceCube PMTs are used to detect Cherenkov photons produced by particle interactions in the ice. The PMT of an IceCube DOM sensitive to wavelengths between 300 nm and 650 nm with a peak quantum efficiency of about 25% for standard PMTs [38]. The PMT is optically coupled to a glass pressure housing enclosing the DOM to minimize distortion of incoming light.

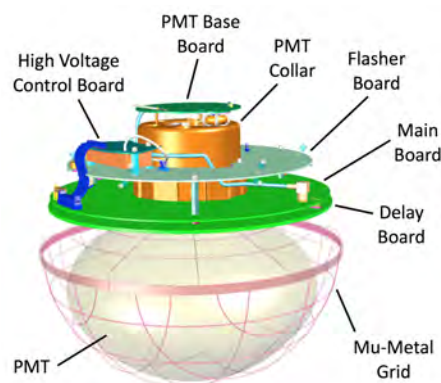


**Figure 3.1** – The IceCube DOM contains multiple components, including the PMT itself, onboard calibration devices, and various electronics necessary for semi-autonomous operation.

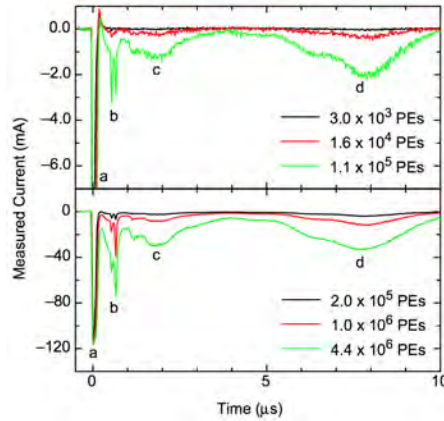


**Figure 3.2** – Afterpulsing calibration measurements performed in the lab. LEDs with known brightness were flashed to test for offtime response of the IceCube PMT. Clear dips, corresponding to detected charge, are visible. Drop (a) corresponds to the initial LED flash while (b), (c), and (d) show prominent afterpulsing peaks. Image taken from [69].

### Pre-, Late-, and Afterpulsing

A PMT amplifies signals of electrons emitted from a photocathode due to incident light, producing a voltage drop at the anode called a *pulse*. Errors in the amplification process can introduce additional pulses reaching the anode. These effects are divided into *pre-pulses*, *late-pulses*, and *afterpulses*.

The pre-pulses, arriving within a few dozens of nanoseconds prior to the main pulse, arise from the small probability of an electron bypassing one of the dynodes. Late-pulses are likewise thought to be produced by electrons which return to a previous dynode, inducing a signal a few dozens of nanoseconds immediately following the main signal. These signals tend to be small and inconsequential for physics measurements.

Afterpulses are produced from ionization of residual gases in the PMT. The ionized atoms tend to travel significantly more slowly than electrons, resulting in a delay between the main signal and the subsequent afterpulses that may be as large as 10 microseconds. The afterpulses require dedicated calibration and mismodeling may affect other measurements as addressed in Section 5.2.

#### 3.1.1 The Discriminator Used for DOM Triggering

A discriminator onboard the DOM is used to identify signals from the PMT with a voltage threshold corresponding to 0.25 photoelectrons (*PE*). Each discriminator crossing begins a *DOM launch*, the lowest level signal available in the IceCube detector containing a digitized representation of the raw PMT output in the form of a *waveform*. Launches are stored in DOM memory while awaiting a decision from the triggering system.

#### 3.1.2 Local Coincidence

If any of the notified DOMs also record a launch within a configurable 1 microsecond window, both launches are said to form a *hard local coincidence (HLC)* pair. Nearby DOMs, here defined to be either of the two DOMs above or below the current DOM, are notified of the launch via a signal sent using the *local coincidence* wiring. Launches which fail to satisfy the local coincidence conditions are referred to as *soft local coincidence (SLC)* launches. Launches recorded as part of an HLC pair receive a flag to record local coincidence status. This flag may be used to later identify only those launches which

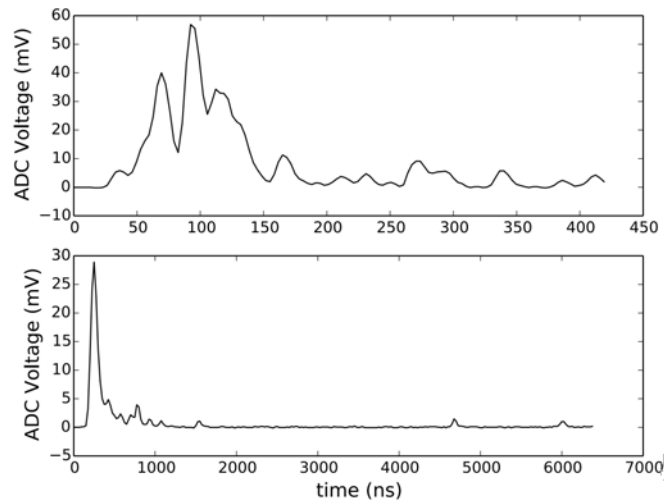


**Figure 3.3** – Examples of the ATWD (top) and FADC (bottom) waveforms output from an IceCube PMT. Taken from [38]

satisfy the local coincident conditions, providing a simple, default method of identifying hits likely to be caused by particle interactions in the detector.

### 3.1.3 Digitization

While awaiting a local coincidence decision, the waveform of a launching DOM is passed to the two onboard digitizers. Information from the PMT is digitized using the fast analog-to-digital converter (*FADC*), which provides binned information at  $40 \times 10^6$  samples/second for the 6.4 microseconds following the initial DOM launch [38]. Simultaneously, the *Analog to Digital Waveform Digitizer*, or *ATWD*, will digitize the waveform using 322 bins with 3.3 nanoseconds per bin.

If a launch satisfies the HLC conditions, the DOM will request the full digitization of the waveforms from both the ATWD and FADC, providing a complete record of the launch. Examples of digitized waveforms from the ATWD and fADC are shown in Figure 3.3.

When digitizing a signal, the ATWD experiences up to 29 microseconds of deadtime [38]. During this time, the secondary ATWD is available to record further pulses, resulting in a total average fractional deadtime per DOM of  $2.2 \times 10^{-5}$  seconds/second. In addition, each of the two ATWDs possesses three channels with separate gains. This provides the ability to accurately measure the waveform, even in cases of saturation of high gain channels. The unsaturated ATWD with the highest gain provides a record for the launch.

If the launch fails the HLC launch criteria, the information in the ATWD ceases the digitization process and the FADC instead digitizes only the three bins associated with the largest peak of the waveform. While this limits the information available for these launches, the lack of associated nearby launching DOMs provides strong evidence that the launch is due to random detector noise.

### 3.1.4 Noise in IceCube DOMS

Dedicated measurements using IceCube DOMs have shown multiple components to the detector noise[71]. A large fraction of the detector noise displays non-Poissonian behavior in time [38]. The model used in IceCube, shown in Figure 3.4, splits the detector noise into *Poissonian* and *non-Poissonian(time-correlated)* noise.

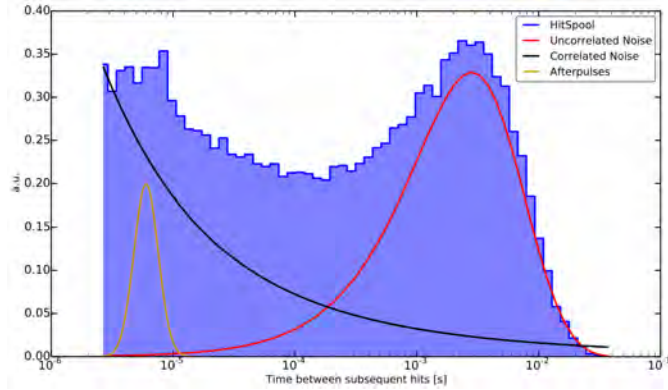


**Figure 3.4** – A histogram of the time between subsequent hits on DOM 15 of string 27. Hitspool data, specialized data collected with no trigger applied, is shown in blue. The "correlated" (non-Poissonian) and "uncorrelated" (Poissonian) features are shown in red and black respectively. The location of a large afterpulsing peak is shown in yellow. Note that the features included are not to scale. Image taken from [38].

The Poissonian noise consists of thermal noise and radioactive decays in the glass of the PMT and DOM. Studies of these radioactive components are ongoing, with some evidence that Potassium-40 and Uranium-238 may be responsible for at least some of the observed decays. Once a decay occurs, a rapid series of pulses occurs in the PMT, leading to a "burst" of noise that continues for up to a few milliseconds [71]. These hits are believed to be due to a scintillation or luminescence process.

The typical averaged noise rate is 560 Hz for standard IceCube DOMs and 780 Hz for high quantum efficiency DOMs. Poissonian noise makes up approximately 250 Hz of this rate with the remainder due to non-Poissonian processes.

### 3.1.5 Triggering in IceCube

Digitized versions of the waveforms are transmitted from the DOM to the IceCube physics data acquisition system (*pDAQ*) for use in trigger and event building. The most common type of trigger used in IceCube analyses is the *Simple Majority Trigger* or *SMT*. This trigger is designed to look for coincidences between DOMs using HLC launches. Each of the SMTs is defined by three fundamental configurations: a DOMSet, which lists the DOMs available for use in the trigger conditions; a threshold number of HLC launches before the trigger fires; and a time window length,  $\Delta t_{trig}$  in which the HLC are required to coexist. The trigger time,  $t_{trig}$  is defined to be the time of the first contributing HLC launch.

Information from the detector is recorded in a *readout window* around each trigger from  $t_{trig} - 4\mu\text{s}$  to  $t_{trig} + \Delta t_{trig} + 6\mu\text{s}$  around each trigger time. Once all triggers are identified, a *global trigger* is defined as the union of all overlapping readout windows.

## 3.2 Pulse Extraction

The extraction of charge and timing information from recorded waveforms is performed using the *wavedeform* module, which accepts and processes the information from the launches in each triggered event. Wavedeform reconstructs the original charge information from the digitized waveform information.

Wavedeform uses a parametrized version of the PMT pulse associated with a single photoelectron describing the timing and charge profile of the PMT amplification process.

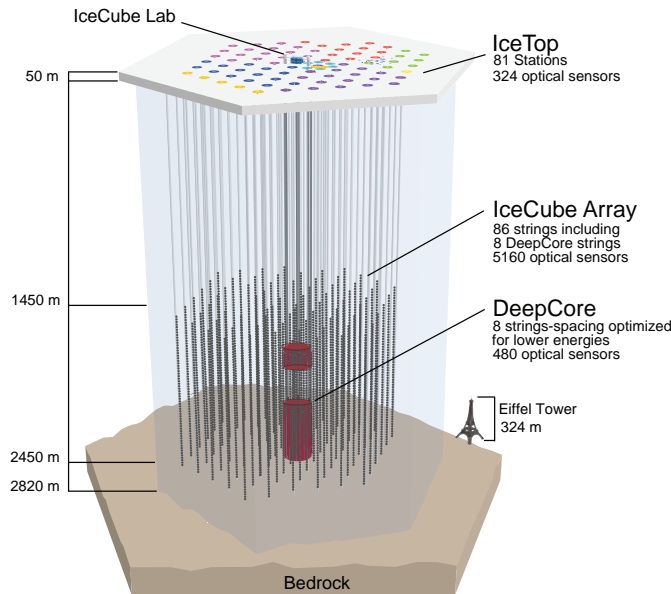


**Figure 3.5** – The IceCube Neutrino Observatory. Three separate subdetectors are shown: IceTop, a cosmic ray air shower detector; IceCube, an array designed to search for astrophysical neutrinos; and DeepCore, a dense subarray used for atmospheric oscillation physics measurements. The detector was deployed over multiple years. Strings deployed in the same year are shown with identical colors at the surface.

Beginning with a single pulse template, a least squares minimization is performed to find the best-fit time of a single pulse in the observed waveform. Additional copies of the pulse template are added and new minimizations are performed until the goodness-of-fit improvement from additional pulses is negligible. The resulting sets of pulses, including associated timing and normalization, are returned as *reconstructed pulses*, often referred to more informally as either *pulses* or *hits*. These pulses represent the best-fit recreation of the analog pulses in the PMT prior to the digitization process.

Both HLC and SLC waveforms are fit, although the limited information in SLC waveforms necessarily results in the loss of information. Information from the ATWD is preferred over information from the FADC for pulse extraction of HLC waveforms.

### 3.3 The Geometry of the Detector

The IceCube detector is located at the geographic south pole in Antarctica. The Antarctic glacier forms a 2.8 km deep surface of clear ice over the bedrock. IceCube uses the Antarctic glacier as both a support structure and as a detection medium for Cherenkov radiation.

The IceCube observatory consists of three distinct subarrays, shown in Figure 3.5, each optimized for separate physics measurements. A total of 5160 DOMs make up the IceCube in-ice array with an additional 324 DOMs used at the surface in the IceTop air shower array [38]. IceCube DOMs are deployed at depths between 1450 m and 2450 m below the surface to shield the detector from atmospheric background muons. The DOMs

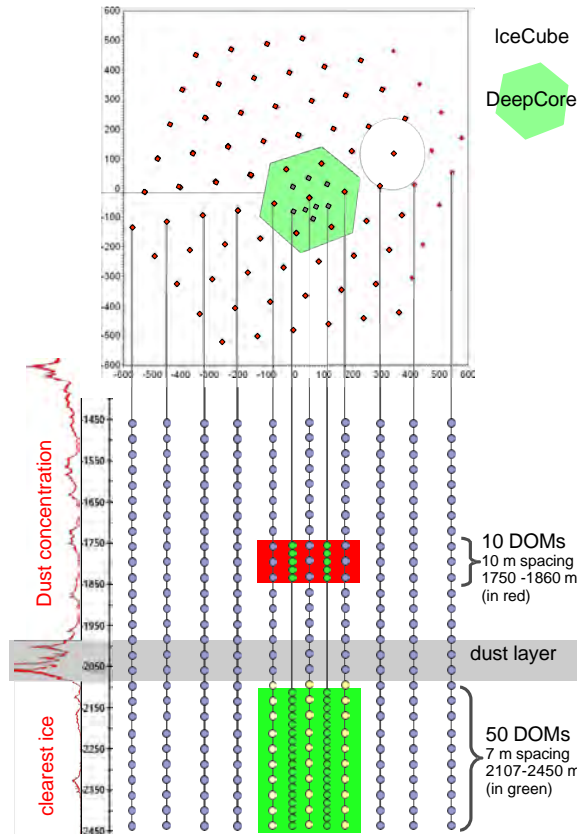


**Figure 3.6** – The layout of the IceCube and DeepCore detectors. DeepCore is installed at the bottom of the IceCube detector in the clearest ice. A subset of DOMs were also deployed above DeepCore to improve muon identification of very-downgoing events.

are deployed in a hexagonal grid in a series of 86 vertical *strings*, each of which provides connections and support for 60 DOMs. Strings are spaced approximately 125 m apart with DOMs space 17 m apart on each string. Each DOM in the IceCube detector is assigned a unique string number (1-86) and DOM number (1-60).

Strings were installed in the glacier annually from 2004 until 2010 with partial detector data collected during construction. During the final years of construction, a denser section of the detector was built, known as DeepCore [72]. The DeepCore subarray consists of 8 strings equipped with high quantum efficiency PMTs 34% more sensitive than the standard IceCube PMT [69]. The DeepCore strings are split between a *fiducial* volume, in which 50 DOMs are spaced 7 m apart on a string, and a *veto plug* of 10 DOMS 10 m apart as shown in Figure 3.6. The DOMs in the DeepCore fiducial volume are located in the clearest ice of the detector at depths between 2100 m and 2450 m below the surface [73]. The veto cap, installed between 1750 and 1850 m below the surface, is used to identify background muons for DeepCore.

### 3.3.1 IceCube: A Detector for TeV Neutrinos

The IceCube detector is a regularly spaced hexagonal grid buried in the glacier with the purpose of measuring astrophysical neutrinos and identify the source of cosmic

rays. The IceCube array has an energy threshold of around 50-100 GeV with an optimal response above 1 TeV [72, 38].

In the standard IceCube detector, an SMT using all DOMs with a threshold of 8 HLC launches within a 5 microsecond trigger time window [38]. This trigger, known as *SMT8* after the number of required launches, is designed for high signal efficiency at energies above 100 GeV with a minimum number of accidental triggers due to detector noise. The IceCube detector records an *SMT8* rate of around 2100 Hz with less than 1 Hz expected from neutrino interactions and the remainder primarily due to muons produced in cosmic ray showers in the Earth's atmosphere.

Events at the TeV scales of the IceCube detector show well-defined topologies, as shown in Figure 3.7. The IceCube detector has performed many measurements, including searches for sterile neutrinos [62], anisotropy in the cosmic ray flux [74], measurements of the neutrino cross section at high energies [75], and the discoveries of an astrophysical neutrino flux [76].

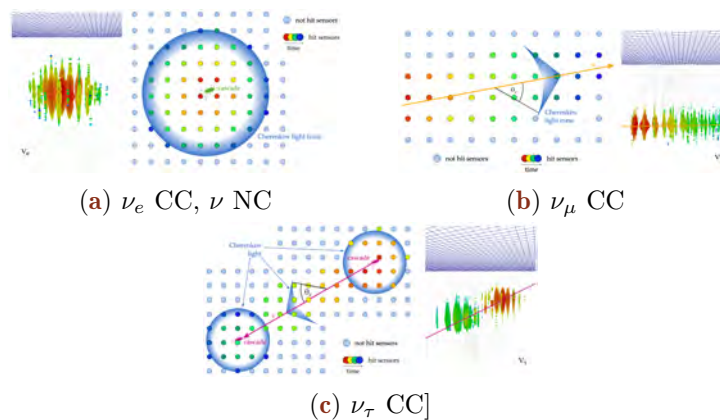


**Figure 3.7** – Examples of event signatures above 1 TeV using the full IceCube array. Event views shown in (a) and (b) are from actual events discovered by IceCube [77]. Images taken from [78]. (a)  $\nu_e$  CC and  $\nu$  NC show similar behavior from electromagnetic and hadronic interactions, which result in a shower of particles that quickly scatter in the ice. Cherenkov emission from these events appears roughly spherical in the detector. These events are known as "cascades". (b)  $\nu_\mu$  CC events begin with a hadronic interaction, then produce Cherenkov light from the outgoing muon. The track of the outgoing muon is clearly visible. (c) Above 1 PeV, the tau lepton from a  $\nu_\tau$  CC interaction may travel a significant distance before decaying. This results in two well-separated cascades in the detector, a tell-tale signature of  $\nu_\tau$  CC interactions. Tau neutrino interactions below 1 TeV are not distinguishable from other cascade-like events.

### 3.3.2 DeepCore: Extending the Reach to GeV Scales

The DeepCore detector was designed to be a smaller, denser detector used in the study of GeV neutrinos. The denser spacing and clear ice of DeepCore lowers the energy threshold to around 10 GeV from IceCube's threshold of around 100 GeV [72], permitting the study of oscillations.

In DeepCore, the desire for lower energy events led to the introduction of a separate trigger, known as *SMT3*. This trigger, using only DOMs within the DeepCore fiducial volume, searches for at least three HLC launches occurring within 2.5 microseconds. This effectively lowers the triggering threshold from roughly 100 GeV with the larger IceCube array to approximately 10 GeV. The *SMT3* rate, at 250 Hz [38, 72], is substantially

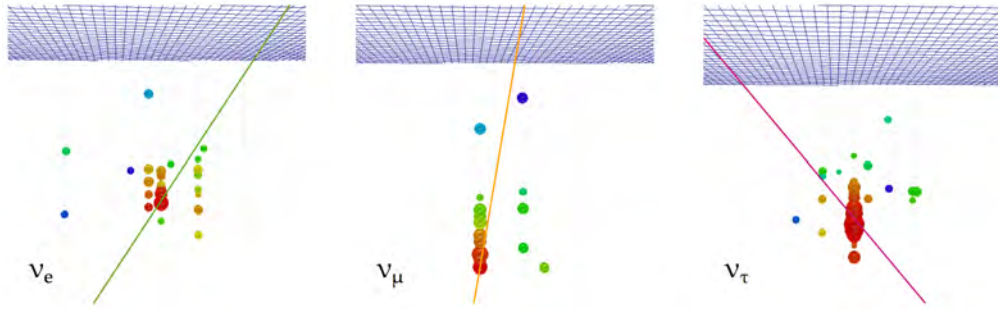


**Figure 3.8** – A selection of 50 GeV simulated events in DeepCore taken from [78]. Unlike the event topologies at high energies, DeepCore events do not show distinct event types.

smaller than the SMT8 rate due to both the increased overburden as well as the smaller number of PMTs included in the SMT3 DOMSet. By placing the detector inside of the larger IceCube array, DeepCore allows analyzers to use the IceCube detector as an active veto, reducing the background rate to 17 Hz.

DeepCore events do not show the clean topological separation of the higher energy IceCube events as seen in Figure 3.7. Events may be separated broadly into *cascade-like* and *track-like* statistically using information contained in the timing of hits in the detector. Such separation techniques are energy-dependent and do not perform well at very low energies.

DeepCore has observed atmospheric neutrino oscillations in the  $\nu_\mu \rightarrow \nu_\tau$  in the disappearance channel [79, 80, 81], with the most recent measurement showing competitive precision to dedicated measurements performed with particle accelerators.

While DeepCore was designed for oscillation physics, the neutrinos may be used for other purposes as well. Recent work with DeepCore has shown sensitivity to studying dark matter interactions in the sun [82] and in the galaxy [83].

### 3.4 The Bulk Ice Model

The Antarctic glacier, with a thickness of 2.8 km at the geographic south pole [73], forms both the support structure and the interaction medium for IceCube. Measurements of the dust concentration of the ice as a function of depth were taken during deployment of the IceCube strings. The IceCube dust logger emitted laser light aimed into the undrilled ice and detected backscattered photons[84, 85]. The results are shown in Figure 3.9.

Peaks are present in the dust logger data due to volcanic events or changes in the climate in the Earth’s past [84]. The most significant peak, a set of features around a depth of 2000 m, form what is known as the *dust layer* of IceCube, a region with significantly higher scattering and absorption properties than the surrounding ice.

To improve the modeling of the photon scattering and absorption in the glacier, dedicated measurements have been performed using light-emitting diodes (LEDs, also known as *flashers* in IceCube) onboard the DOMs [73, 38]. In specialized calibration runs, the LEDs are flashed at a few Hertz for a few minutes while nearby DOMs receive the emitted light. Monte Carlo simulations of the flashers are used with varying ice properties in order to identify the most likely properties of the ice. Each flashing and detecting DOM pair provides a set of known times, positions, and light output in the ice, allowing for the properties of the intervening medium to be determined.

The ice model used for this thesis consists of three main properties: the absorption, the scattering, and the anisotropy of the ice [87]. The measured properties of the

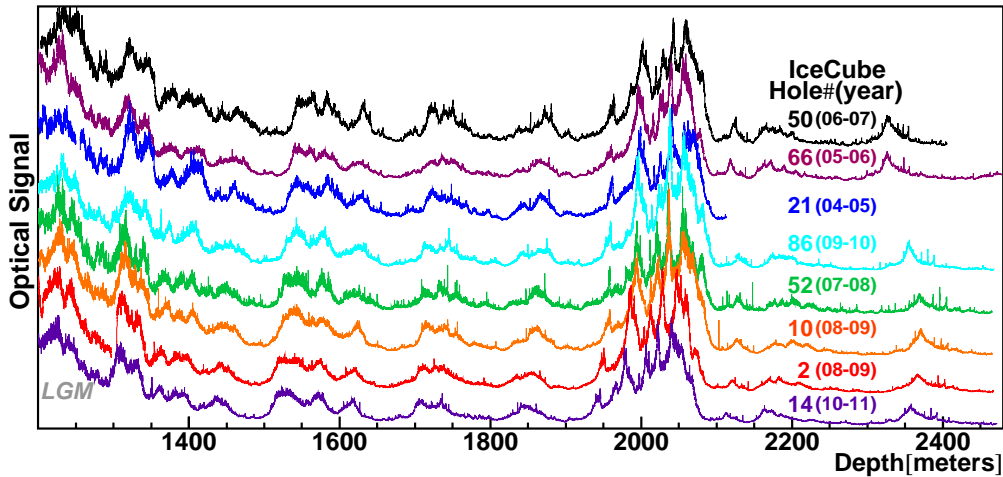


**Figure 3.9** – The data from the dust loggers deployed in various drill holes in IceCube during deployment. Data from individual holes has been offset in the y direction for clarity. Larger relative values of the "Optical Signal" represent more scattering in the ice while smaller values indicate clearer ice. The "dust layer" is visible in all drill holes around 2000 m. Deepcore DOMs are deployed below this layer. Image taken from [86].

absorption and scattering may be seen in Figure 3.10 while the effect of the anisotropy can be seen in Figure 3.11. Scattering photons change direction, losing information about the direction of the emission source. Absorbed photons are not visible to the detector, potentially modifying the observed number of photons and the reconstructed energy of an event.

The anisotropy is an observed azimuthal dependence of the properties of the ice [87]. The microscopic cause of the anisotropy is not currently known, although a model of the effect is included in IceCube simulation. The measurement of anisotropy of the ice consists of a direction and magnitude used to modify the scattering and absorption from each direction in the x-y plane. The effect of the anisotropy has been observed with atmospheric muons due to effects in the azimuthal directions of reconstructions in IceCube.

Uncertainties in the scattering and absorption coefficients are as large as 10% and form a major uncertainty in IceCube experimental measurements. These uncertainties in the context of the DeepCore oscillation measurement performed in this thesis will be discussed in Section 8.4.4. The effects of mismodeled anisotropy in the ice will be discussed in Section 7.8.5

### 3.5 The Hole Ice

After the strings were deployed, each drill hole was allowed to refreeze. The refrozen column of ice around each string is referred to as the *hole ice*. Using a dedicated camera deployed at the bottom of string 80, the refreezing process of the hole ice has been observed over the course of several years [88, 38]. Images obtained from the camera show the refrozen ice divided into three distinct regions.

The outermost region, the *bulk ice*, is the original glacial ice and is unaffected by the deployment of the detector. The outer part of the drill hole shows improved clarity compared to the bulk ice. The central region of the drill hole, a core about 16 cm in diameter, shows significantly worse scattering properties than the bulk ice [38]. This

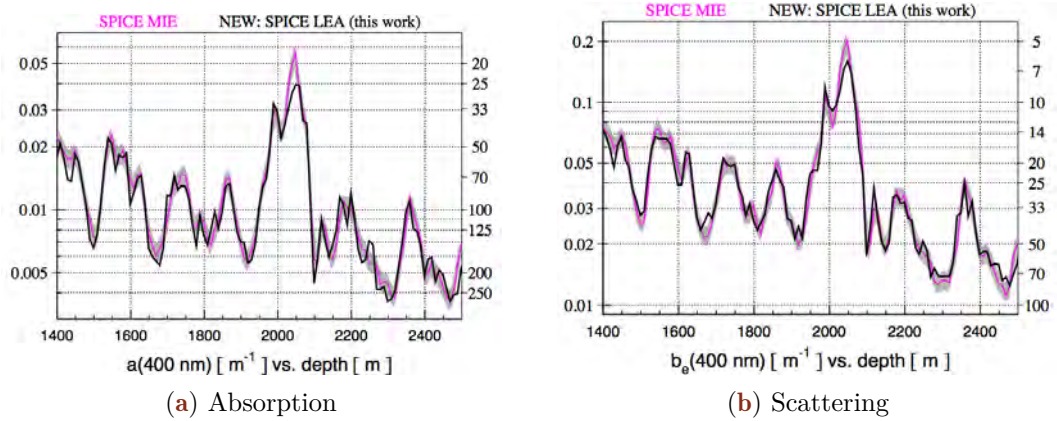


**Figure 3.10** – The absorption and effective scattering properties of the ice as fit to flasher data. Two models are shown representing different generations of ice models used for simulation. The "Mie" model does not include anisotropy while the "Lea" model does. Figure from [87].

central column, referred to as the *bubble column*, affects the photon acceptance of the PMT. Measurements to characterize the hole ice are ongoing.

The properties of the hole ice affect the scattering and absorption of the ice near the DOM, changing the distribution of photon arrival times and leading to changes in the reconstruction. The uncertainties in the hole ice model provide some of the largest uncertainties in oscillation analyses with IceCube [81].

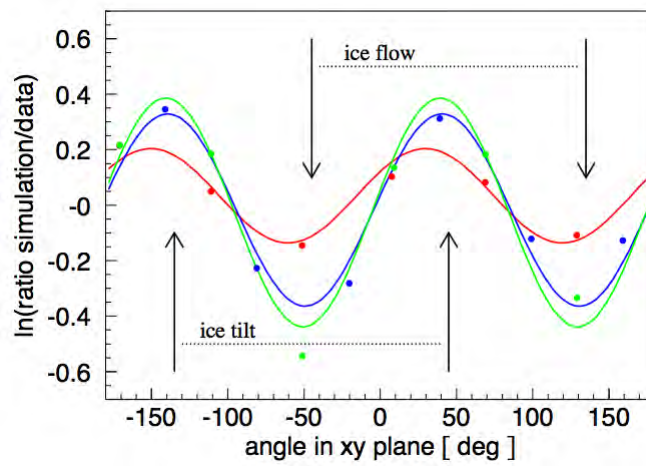


**Figure 3.11** – The effect of the anisotropy on the light output from a flasher on string 63. Measurements (points) are shown for receiving DOMs at three distances: at 125 m (red), at 217 m (blue), and at 250 m (green). A line is included to show the expected effect of anisotropy at each distance. The y-axis shows the ratio of a simulation of the same flasher without including anisotropy to data. A modulation is observed as a function of direction in the x-y plane.

# Simulation of the IceCube-DeepCore Detector

# 4

In order to model both signal and background, *Monte Carlo simulations* of the detector are necessary. In the search for tau neutrinos, this is particularly important due to the low rates and high backgrounds expected, requiring multiple types of simulation for both signal and background.

Simulation in IceCube is broken into three broad stages, each of which will be discussed in turn. The generators used in the appearance analysis are discussed in Section 4.1. The propagation of the charged leptons and photons are then described in Section 4.2. Section 4.3 describes the simulation of the detector, including the PMT electronics and the detector noise.

## 4.1 Monte Carlo Generators

### 4.1.1 Background Generation

#### **CORSIKA**

The primary background for the observation of atmospheric neutrino events is the other particles present in the cosmic ray interactions in the atmosphere. These interactions produce many particles, most of which are stopped before reaching IceCube by the shielding provided by the Antarctic Glacier. In order to correctly account for the interactions and decays of these particles, the *CORSIKA* generator from Karlsruhe Institute of Technology is used [89].

The CORSIKA generator is a collection of code designed to simulate, interact, and propagate a cosmic ray air shower from the interaction point in the upper atmosphere to a user-defined height. Originally designed for use with surface detectors such as Auger, HAWC, and IceTop, the code has been adapted for use in the IceCube collaboration by identifying the muon (and, sometimes, neutrino) components of the air shower.

CORSIKA has many modes of operation and options for configuration. The standard IceCube simulation of air showers uses the SIBYLL 2.1 hadronization mode [90] to follow the interactions through the shower.

IceCube simulation of air showers uses two cosmic ray production modes of CORSIKA: the Polygonato and 5-Component modes.

The "Polygonato" mode generates cosmic rays following the model from [91]. The Polygonato flux parametrized the energy spectra of individual elements of the cosmic ray flux as power laws extrapolated to high energies. In typical IceCube simulation, CORSIKA simulation produced using the Polygonato mode includes a mixture of muons from all seasons, effectively producing an averaged flux useful under the assumption of equal livetime throughout the year. The elemental ratios of the generated cosmic ray primaries follow the Polygonato flux directly, producing a "natural" flux of simulated events [89]. The natural spectrum of the Polygonato CORSIKA simulation has the benefit of allowing a direct physical interpretation of the resulting spectrum without the need for reweighting and simplifies the production of coincident showers, which require a natural spectrum.

The second model, the five-component mode, reduces the full spectrum of cosmic rays to five effective families: hydrogen, helium, nickel, aluminum, and iron. Each of these components is allowed to have a separate normalization and spectral index. The five-component mode is useful due to the ease with which the user can modify and reweight to different primary spectra, allowing the investigation of different cosmic ray compositions without the production of dedicated simulation. The simplicity associated with the reweighting of five-component simulation allows IceCube to produce unphysical spectra in order to optimize the production of simulated events necessary for the various analyses. The five-component simulation may be reweighted to match cosmic ray models, including both the Polygonato model and the newer H3a model, which models the cosmic ray flux using three distinct populations of sources [92]. While this slightly complicates the use of the simulation in analyses, the ability to evaluate the uncertainties in various cosmic ray models has been an invaluable tool for high energy analyses, which can be sensitive to changes in the cosmic ray spectrum above the knee.

About 10% of the muons from cosmic ray air showers which reach the IceCube detector will arrive temporally coincident with muons from other showers. Five-component CORSIKA simulation, due to the unphysical generation spectrum, cannot easily be used in the production of these *coincident* events and are currently supplemented by the Polygonato CORSIKA for this purpose.

In both cases, the particles from the air shower are only propagated to the surface of the ice. For analyses using the in-ice array, we take the muons reaching the surface from a CORSIKA simulation and propagate them through the ice, simulating the continuous and stochastic energy losses along the way. The muons are propagated to a surface in the ice consisting of a cylinder with radius 800 meters and length 1600 m centered on the IceCube detector. In order to reach the detector, a muon must result from a cosmic ray interaction of approximately 600 GeV due to the shielding of the glacier. Because of this, CORSIKA simulations typically have a lower energy cutoff of about this value to avoid simulating events that will not reach the detector.

In principle, neutrinos may also be produced using the CORSIKA generator. In practice, this tends to be extremely inefficient for most searches that are not explicitly looking for muons and neutrinos from the same air showers given the extremely low cross section of the neutrino relative to the muon. For this reason, the background generation with CORSIKA in IceCube typically refers to muon events only, with no accompanying neutrino.

## MuonGun

CORSIKA simulations are computationally costly and offer few ways to directly control the spectrum of events at the detector. Targeted simulations in which particular muon samples are required cannot easily be generated with CORSIKA. In situations where the required muon simulation falls within a relatively narrow phase space, whether that be in energy, angle, or position inside of the detector, it can be beneficial to tailor simulation to the needs of specific analyses. Alternatively, there are situations in which the details of the cosmic ray interactions are an unnecessary complication to the final level IceCube analyses. In these situations, IceCube has developed a tool to bypass the full air shower simulation provided by CORSIKA, producing muons directly at a cylindrical surface inside the ice [93]. This tool, known as *MuonGun*, has the benefit of removing the computationally costly simulation of the full air shower, giving the user more control over the resulting simulated events at the cost of information about the initial cosmic

ray interactions. This allows targeted, high statistics background simulation samples to be produced for analyses.

These features of MuonGun give the generator significant flexibility, allowing for a very focused simulation of muons that would not otherwise be possible with the current implementation of the CORSIKA generator. As with all targeted generation, there are limitations to the generation scheme. For example, the settings described above will provide a good description of muons reaching and triggering the DeepCore array, but will not include the correct contributions of muons in the outer IceCube detector. This can result in disagreement between data and simulation if the limitations are not acknowledged and accounted for.

This abstraction disassociates the muon at the detector from the air shower, and therefore the cosmic ray, that produced it. In order to properly account for the dependence on the cosmic ray spectrum in the muon weights, dedicated simulations must be produced using the full CORSIKA generator. By following the interaction, showering, and propagation to the detector, IceCube is able to produce an effective parametrization of the association between a particular cosmic ray spectrum and the muons reaching the detector. This must only be done once, but requires a substantial number of simulated events in order to produce a clean parametrization in position, energy, zenith angle, and variables associated with shower multiplicities higher than one. The version of MuonGun at the time of writing provides the parametrizations for the Polygonato [91] and H4a [92] cosmic ray spectra. At the time of production for the analyses contained hereafter, all MuonGun simulation is produced assuming a multiplicity of 1, meaning that no bundles are yet produced with this generator. This is a limitation of simulation time: the multiplicity parametrizations vastly extend the parameter space and therefore require significantly more time and effort to handle correctly.

## Accidental Events

While we only observe Cherenkov photons from neutrino and muon interactions in the detector, we also observe a significant component of *accidental triggers* in the DeepCore array. These events, produced by detector noise in the detector, result in about 40 Hz of triggered events in IceCube, primarily in DeepCore due to the low trigger threshold. In these events, no actual particle interactions due to muons or neutrinos are observed. Instead, detector noise alone satisfies the trigger conditions, producing an event.

Production of accidental triggers involves only the noise and electronics simulation. Because the events occur as a result of random HLC launches in the detector, the simulation requires a special mode, here called *long-frame* simulation, which produces continuous detector readout. Breaking the traditional concept of the "simulated event", these simulation sets instead produce a 100 ms long "event" of random detector noise. The photoelectrons from the noise simulation are then run through the simulation of PMT and DOM electronics and triggered as a normal simulated event. After triggering, specialized code is used to divide the long-frame simulation into smaller events similar to standard IceCube experimental readout.

Once the events are generated, weighting the events is relatively straightforward: the weight per event depends on the muon interaction rate and the total simulated time. The latter is straightforward to calculate, depending only on the number of long frame simulation events produced and the time window for each of these events. The former is important due to the definition of the accidental triggers. These events, by definition, may only occur when no muon or neutrino is interacting within the detector.

The weight of the accidental triggers must account for this "deadtime" due to particle interactions. This particle interaction rate in IceCube is dominated by muons with a rate of approximately 2800 Hz, leading to a change in the effective livetime per accidental triggered event of roughly 15%.

Accidental triggers are computationally expensive to produce, given that they rely on a relatively rare property of random detector noise. The production of accidental triggers takes about one hour per minute of simulated livetime, with much of the processing time spent on the simulation of DOMs that do not contribute to final triggered events. This limits the total effective livetime that can be simulated in realistic timescales. Current simulations used in this thesis total approximately two months of effective livetime.

### 4.1.2 Signal Generation

#### GENIE

Background simulation is only part of the Monte Carlo events in IceCube. Studies searching for neutrino candidate events require simulated neutrino signal events to infer properties of the original events.

At energies ranging from approximately 1 GeV to 1 TeV, IceCube has adopted the *GENIE* event generator [94]. This code, used widely throughout the oscillation community, includes information about the various interactions, cross sections, and uncertainties involved in neutrino physics from reactor energies upward.

For IceCube, events in the *GENIE* generator are produced from a power law energy spectrum with a given spectral index. These events are then forced to interact with an electron or nucleon within a specified volume with a target density of ice assumed.

The type of interaction is determined using the cross section for the given flavor and energy. The cross section model, an updated version of GRV98 [95], includes resonant, elastic, quasielastic, and deep inelastic interactions. Particles produced in the interaction are propagated out of the nucleus. *GENIE* includes final state interactions where hadrons produced in neutrino interaction can reinteract before escaping the nucleus. Hadrons with energies less than 30 GeV produced in *GENIE* simulation are propagated individually to obtain the light output using *GEANT4* [96, 97]. Above 30 GeV, the lower event-to-event variability permits the use of parametrized light output for hadrons. *GEANT4* is also used to propagate all muons and tau leptons as well as electrons and photons below 100 MeV.

The *GENIE* code includes tools to reweight events based on uncertainties in eg. the axial masses, cross sections, and various aspects of the interactions themselves [94]. These features are used to model uncertainties in the tau neutrino analysis presented in this thesis.

The code is regularly updated, including both new features and retuning of parametrizations to match the latest data. The events produced in this work use *GENIE* version 2.8.6.

#### Neutrino-Generator

At energies higher than approximately 100 GeV, there are two changes to the simulation code. At these energies, the contribution to the cross section from deep inelastic interactions becomes dominant while the other interactions become negligible, as expected from Figure 1.7 [21]. This allows the simplification of the cross section calculations with no loss in generality. In addition, the cross section continues to rise approximately linearly with the energy. This latter feature requires a detailed simulation of potential interactions

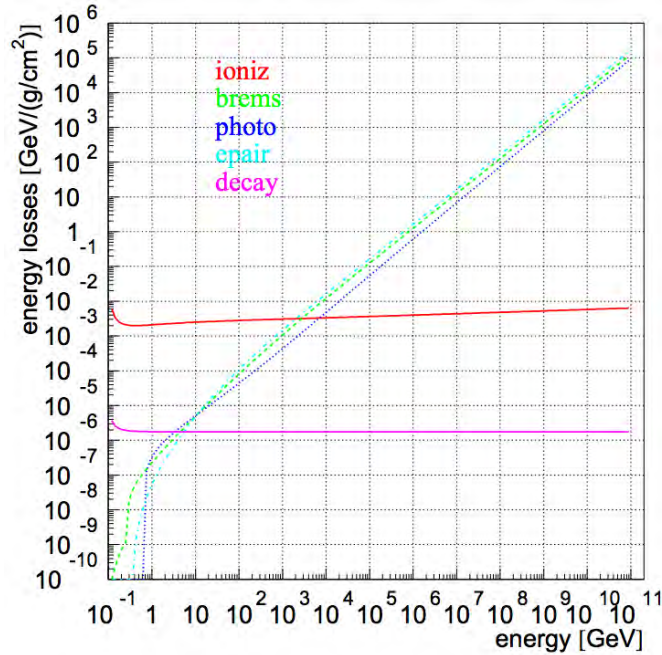


**Figure 4.1** – Average energy losses ( $\frac{dE}{dx}$ ) for a muon in ice. At very low energies, ionization losses dominate. Above approximately 1 TeV, pair production and photonuclear effects become more important. Image taken from [22]

far from the detector: namely, high energy neutrinos have a non-negligible chance of interacting while propagating through the Earth.

The *Neutrino-Generator* code (hereafter, *NuGen*) is designed to handle these higher energy interactions [98]. In this model, neutrinos are no longer produced and forced to interact in the ice directly. Instead, a neutrino is produced from a power law spectrum in the atmosphere surrounding the Earth. The event is then propagated through the planet, using the PREM model of the density layers in the Earth [99] to simulate potential interactions en route. Neutrinos which interact may be lost or may be regenerated following the decay of the daughter particles. Neutrinos arriving at the detector are then forced to interact in the detector fiducial volume, yielding a simulated event.

NuGen can be configured with various Earth models as well as different generation properties. For the studies contained herein, the NuGen files are produced with an  $E^{-2}$  spectrum and interact following the CSMS cross section [100].

## 4.2 Propagation of the Particles and Light

After production of simulated particle interactions, IceCube simulated events require two types of *propagation*. The first, the propagation of charged leptons and individual hadrons below 30 GeV, produces the energy losses in the detector due to continuous and stochastic emissions. These energy losses are then used to produce photons that are propagated through the detector using models of the Antarctic glacier.

### 4.2.1 Lepton Propagation with PROPOSAL

In IceCube, leptons and hadrons not propagated using GEANT4 are propagated by *PROPOSAL*, a software package containing parametrizations of the ionization, electron pair-production, bremsstrahlung, photonuclear interactions, and decay processes of particles in ice [101].

PROPOSAL propagates the charged particles through the detector, simulating these processes to give energy emissions along the path of each particle. The energy losses of particles in the ice is handled by parametrizations as a function of particle energy as shown in Figure 4.1.

### 4.2.2 CLSim for Photon Propagation

Once the energy deposition for each particle simulated with GEANT4 and PROPOSAL, the resulting photons must be produced and propagated. There exist two modules which can handle this: Photon Propagation Code *PPC* and OpenCL Simulation Code *CLSim*. The differences are largely of implementation details and both have been verified to give identical results. Only the latter, CLSim, will be discussed here.

CLSim is a code designed to propagate emitted photons using ray tracing algorithms [102]. The independence of the individual photons is leveraged to perform the propagation of all photons in parallelized calculations using the OpenCL programming language [103]. Photons are then propagated through the ice with the model of the scattering and absorption properties, continuing until they are either absorbed or until they reach a DOM. Photons which reach DOMs are stored to be used in the simulation of the IceCube PMTs.

The propagation of individual photons is efficient at low energies, where the scattering of individual photons is important. At energies above a few hundred GeV, the light yield is large enough that the propagation of individual photons is both excessively costly as well as unnecessary. In those cases, a feature known as *oversizing* is used by setting a *oversize factor*,  $N_{OS}$ . The oversize factor, often set to 5 for IceCube simulations above 1 TeV, allows for the production of *weighted photons*. These weighted photons each represent  $N_{OS}^2$  individual photons, reducing the number of particles to propagate by  $1/N_{OS}^2$ . In order to compensate for the bundling of photons, the effective radius of the DOM is also increased by  $N_{OS}$ .

Oversizing is efficient for the simulation of high energy events with large numbers of photon. This breaks down at GeV energies, where the photon flux from an event is low and scattering or absorption of individual photons matters. Because of the complications associated with oversizing at low energies, most simulations of DeepCore events are done with the oversizing features disabled.

### 4.2.3 Angular Acceptance and Hole Ice

When photons reach the surface of a DOM, the *angular acceptance* is applied in order to model the impact of the hole ice. This acceptance, calculated from a combination of lab and in-situ measurements, represents the PMT efficiency as a function of the photon arrival direction. The acceptance has a negligible efficiency for photons arriving from the back of the PMT and higher efficiency for photons reaching the face of the PMT as shown in Figure 4.2. All other directions follow a curve between these two points. The angular acceptance model used in this thesis uses an empirical form fit to flasher data with two free parameters, as shown in Figure 4.2. The most forward (downward-facing) direction in the PMT, shown with  $\cos(\eta) = -1$ , is most affected by the bubble column (see Section 3.5).

## 4.3 Simulating the Detector Electronics

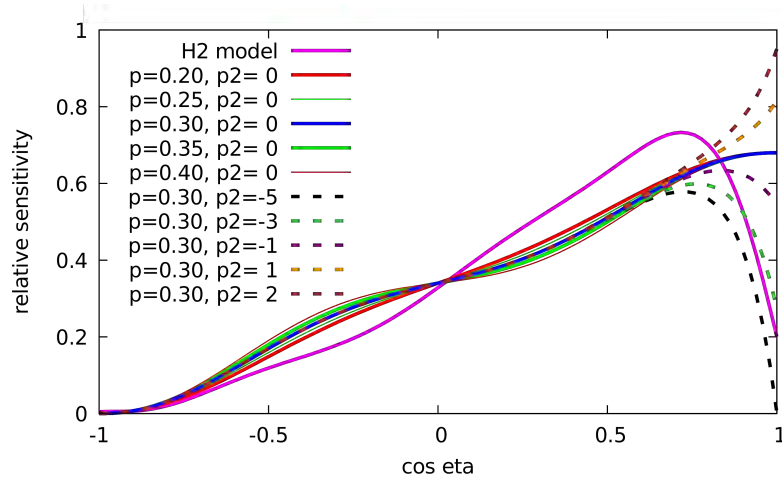


**Figure 4.2** – Examples of the angular acceptance models used by IceCube. The relative sensitivity as a function of arrival direction is shown with  $\cos(\eta)=-1$  indicating the back of the PMT and  $\cos(\eta)=1$  the face. The variation of the acceptance model used for this search is shown by varying two parameters in the model. The ‘p’ parameter primarily controls the acceptance at the side of the DOM while the ‘p2’ parameter controls the acceptance from the forward region. A second model, H2, is also shown.

### 4.3.1 Noise within IceCube-DeepCore

The noise simulation module used in IceCube, known as *Vuvuzela*, models the Poissonian and non-Poissonian detector noise using a set of five parameters, each representing distinct processes [71, 38].

The *thermal noise* and *radioactive decays* are Poisson processes simulated using rates fit to each DOM. The thermal rate is correlated with the temperature and forms a large component of the noise in IceCube DOMs, with a typical rate of 200 Hz while the decay rate has a typical value of 50-100 Hz due to radioactive activity in the DOM glass. The noise model produces photoelectrons at the photocathode of the PMT simulation.

In order to model this bursting behavior described in Section 3.1.4, an effective mode is used which represents the timing of consecutive noise using a log-normal distribution. This introduces three additional parameters to the noise model: the average number of photoelectrons emitted during a "burst", giving the normalization; the mean time between photoelectrons within a burst; and the standard deviation of the timing within a burst. The non-Poissonian component to the noise model produces an additional 400 Hz of noise [71]. Noise photoelectrons in simulation are added as additional charge on each DOM at the face of the PMT.

The *Vuvuzela* model has previously been fit to each DOM in the detector, although with some limitations. Work completed during this thesis, discussed in Chapter 5, improved the calibration of the noise model.

### 4.3.2 PMTResponseSimulator and DOMLauncher

The IceCube detector does not directly measure photoelectrons emitted from the photocathode. Instead, IceCube events record the voltage response from the PMT via the output waveform. The production of simulated waveforms from incident photons is produced by a pair of software modules.

The first module, *PMTResponseSimulator*, simulates the amplification process of the PMT, including the effects of pre-, late-, and afterpulsing. Each of these three effects is modeled using calibration measurements performed in the lab [69]. *PMTResponseSim-*

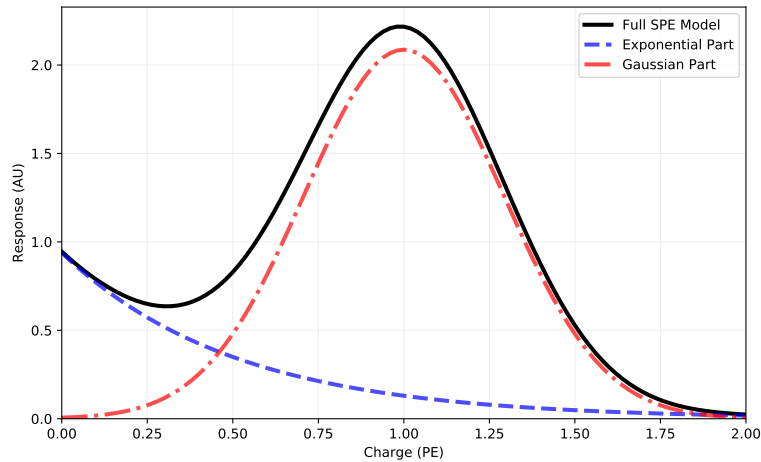


**Figure 4.3** – The SPE template used in Monte Carlo simulation. The gaussian (red, dash-dot) and exponential (blue, dashed) parts of the full model (black) are shown. The SPE template is used as a sampling distribution for each incident photon in order to determine the observed charge. The SPE template is used for all DOMs.

ulator also calculates the amount of charge recorded by the DOM from each incident photon reaching the photocathode by sampling from the *single photoelectron* template (*SPE* template). The SPE template used in simulation generation is calculated from lab measurements of 118 DOMs prior to deployment [104]. The template, shown in Figure 4.3, is represented by the sum of an exponential and gaussian term and is applied identically to all DOMs.

Prepulses, late pulses, and afterpulses are applied in a recursive process, which every incident hit having a probability of 0.3%, 3.5%, and 5.93% to produce each respectively. These probabilities were measured in the lab and are used for all DOMs.

The second module, *DOMLauncher*, handles the local coincidence circuits, simulation of the DOM clock, the discriminator, and digitization. The triggering system is then applied following the description of Section 3.1.5.

The search for tau neutrinos is a search for events near the detector threshold. Under these conditions, the search requires excellent understanding of threshold effects and detector behavior. In order to better model the detector, the noise simulation used in IceCube was updated with improved measurements after the discovery of disagreements in charge variables. This process is described in this chapter.

The chapter begins by describing the process used previously to fit the Vuvuzela noise model for each DOM. The limitations of the previous fitting process and the discovery of new disagreements is discussed in Sections 5.2 and 5.3 respectively. The new fitting procedure is then described in Section 5.4. New results of the fitting procedure are then discussed in Section 5.5.

## 5.1 A Summary of Previous Fits

Detector noise is a nuisance in most physics and astronomy experiments. PMT noise is assumed to be due to random emission of electrons from the photocathode and is affected by the gain of the PMT.

A purely Poissonian noise model was used in the past in IceCube. With the introduction of the looser SMT3 trigger in DeepCore in 2010 it became clear that additional unsimulated sources of noise exist [71]. These additional photoelectrons appeared to occur in 'bursts' on a single DOM extending for up to a millisecond. Due to the time-correlations of these emitted photons, the phenomenon was labeled *correlated noise*.

The Vuvuzela model, described briefly in Section 3.1.4, is now used to model both the Poissonian and non-Poissonian noise in IceCube. The empirical model consists of a Poisson process for electronic noise and radioactive decays and a correlated component modeled with a log-normal distribution. The model contains five free parameters per DOM. Ten minutes of untriggered data from the detector, dominated by noise hits, was used for calibration of the Vuvuzela parameters.

The Vuvuzela noise model is fit using the distributions of the time between subsequent hits, shown previously in Figure 3.4. Fits for each DOM were performed using the Pearson chi-squared test statistic between the data histogram,  $d$ , and the simulated histogram,  $m$ .

$$\chi^2 = \sum_i^{\text{bins}} \frac{(d_i - m_i)^2}{m_i} \quad (5.1)$$

The value of the  $\chi^2$  was minimized using a Metropolis-Hastings algorithm [10]. For each iteration of the algorithm, new parameters were selected and the response of the DOM was resimulated using `PMTResponseSimulator` and `DOMLauncher`. Each fit was computationally intensive, requiring between two and four CPU-weeks for each DOM. Due to the computational requirements of the fits, the stopping condition was intentionally loosely defined, with a goodness-of-fit of 10% used.

Two examples from the original calibration work are shown in Figure 5.1. The Poissonian noise model used previously is shown for comparison. The Vuvuzela model more accurately reproduces the observed data across all timescales than the purely Poissonian noise model used in the past. Distributions of the number of hit DOMs and

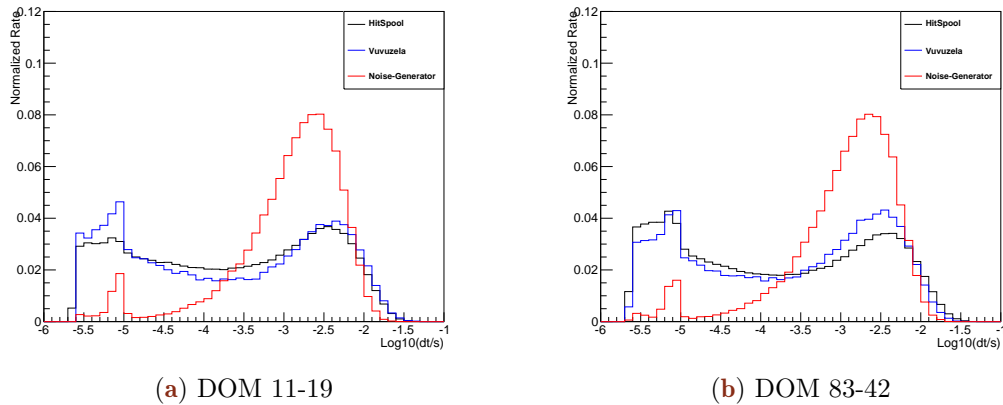


**Figure 5.1** – Two examples of the original calibration work for the Vuvuzela noise model. The x-axis measures the time between consecutive hits on a single DOM ("dt"). Untriggered detector data is given by the black line. In red, a purely Poissonian noise model is shown. An afterpulsing peak is visible at  $10^{-5}$  s. The Vuvuzela mode, in blue, shows better agreement than the purely Poissonian noise model at all timescales.

the number of accidental triggers due to detector noise, shown in Figure 5.2, improve significantly after inclusion of the updated noise model [71].

## 5.2 Limitations and Disagreement with Previous Fits

While accidental triggers with the Vuvuzela model better reproduced the rates observed in data, Figure 5.2 showed disagreement between data and simulation at very low numbers of hits. This region of the parameter space is dominated by accidental noise triggers in simulation.

An evaluation of the previous calibration was performed in 2014, uncovering a number of possible improvements related to various modeling assumptions or omissions. For example, the original Vuvuzela fits excluded the effect of atmospheric muons in the detector under the assumption that the hit rate per DOM due to atmospheric muons (approximately 5 Hz) is significantly smaller than the noise hit rate observed in previous calibration (about 600 Hz). Potential issues may arise from this assumption, which was not tested during original calibrations, including any potential time-correlated hits associated with muons.

Furthermore, some fits resulted in potentially-incomplete minimization. Due to the nature of the fit distributions, there existed significant degeneracy in the parameter space, leading to further difficulties.

During the fitting process, the strength of the afterpulsing peak at 9 microseconds was discovered to differ between DOMs. This effect was unsimulated, leading to convergence problems when fitting this region. In response, fits were artificially limited to timescales longer than 10 microseconds, allowing the minimizer to only observe part of the correlated noise distribution.

Because the noise hits are unlikely to satisfy the HLC conditions, timescales smaller than 6.4 microseconds were unavailable for investigation. No checks were performed for the Vuvuzela model below this limit. However, the noise model was used down to 2 microseconds resulting in uncertainty due to the extrapolation to shorter times. The limit of 2 microseconds was implemented due to the inherent difficulty in characterizing effects at these timescales due to artificial deadtime related to the HLC launch readout.

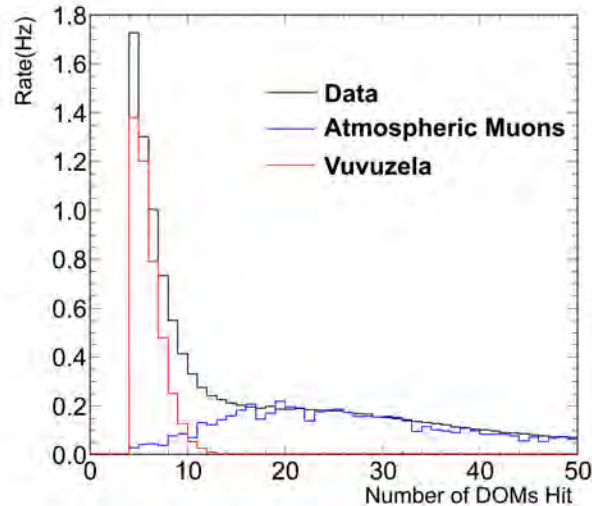


**Figure 5.2** – The rates of events in DeepCore as a function of the number of hit DOMs in a cleaned hit series. The data, shown in black, consists of two components: the accidental triggers (red) and the atmospheric muons (blue). Accidental triggers produced using the Vuvuzela noise model reproduce most of the rate of events below 10 hit DOMs, although a rate disagreement remains. Image from [71].

### 5.3 Low-dt Noise from Vuvuzela

In an attempt to address the imposed simulation limit at 2 microseconds, a new version of the Vuvuzela code was created with this cutoff removed. The resulting noise, labeled *low-dt* noise for the short timescales ( $\Delta t$ ), was used to produce a simulation of accidental noise triggers and CORSIKA muons for testing without further calibration.

The first tests, shown in Figure 5.3, used the number of hit DOMs in DeepCore events to evaluate the effect of the low-dt noise extension. The number of accidental triggers, dominant for events with fewer than 5 HLC hits, increased with the additional noise hits. The number of muons, which make up the majority of events with more than 10 HLC hits, decreased due to the use of the DeepCoreFilter, a veto described in further detail in Section 7.2. Both effects led to improved agreement between data and simulation.

Because the extended noise model adds hits occurring at timescales down to nanoseconds, multiple hits can occur within one waveform, leading to increased observed charge. When the noise distribution is extended below 2 microseconds, the tail of the distribution falls into the ATWD window of 322 nanoseconds, increasing the charge of noise hits in HLC DOMs. Furthermore, some fraction of the hits in a burst of correlated noise occur within the three bins recorded from the FADC for SLC hits. The result is that SLC hits at the start of a noise may appear as an integration of multiple single pulses. Such an effect would be most visible in the charge distribution of SLC DOMs, which are more likely to be due to noise hits than HLC DOMs.

The total charge of DOMs associated with HLC and SLC hits was evaluated to look for this effect due to the extended noise model. The result is shown in Figure 5.4. The change in the charge is observed clearly in the SLC charge distribution, where a systematic shift is visible due to the low-dt extension. Both the original Vuvuzela model and the extended Vuvuzela model show significant disagreement with data in the SLC charge distribution. The strong effect and continuing disagreement in the SLC charge

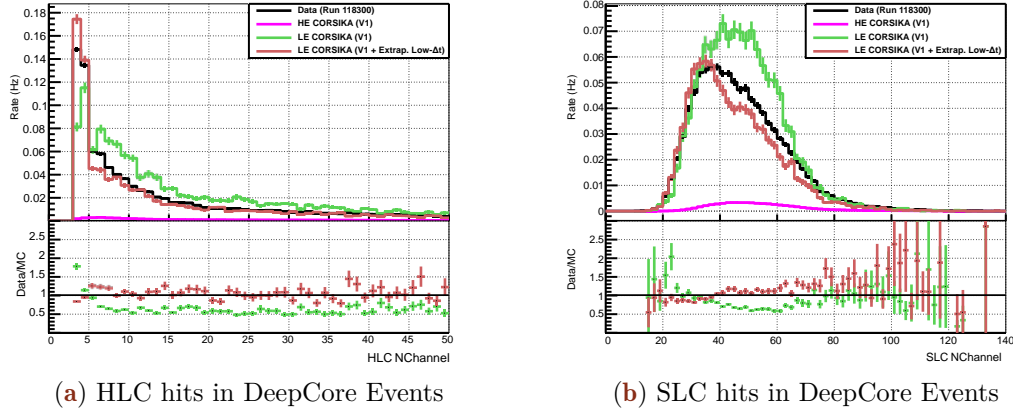


**Figure 5.3** – The number of hit DOMs satisfying the (a) HLC and (b) SLC criteria described in Section 3.1.2. The distribution from 8 hours of data (black) is shown compared to a sample of CORSIKA muons at low-energy ( $600 \text{ GeV} \leq E_{\text{primary}} \leq 100 \text{ TeV}$ ) and high energy ( $100 \text{ TeV} \leq E_{\text{primary}} \leq 100 \text{ EeV}$ ). The addition of the low-dt extension to Vuvuzela improves the agreement between data and simulation in both HLC and SLC distributions.

distribution with data demonstrated that the noise distribution at very short timescales was an important effect that deserved further attention.

The observed effect of the low-dt extension on the SLC charge distribution indicates that the distribution is sensitive to the region below 2 microseconds. The charge distribution of each DOM may therefore be used in the fitting procedure in order to characterize the low-dt end of the noise timing distribution. The effect, demonstrated in Figure 5.5, allows the investigation of a part of the distribution unavailable in previous fits.

## 5.4 Updating the Fitting Code

The effect of the low-dt extension on the charge distributions indicated the potential for improvement in the noise model distribution. New calibration fits for the updated the noise model, referred to as *Vuvuzela V2* fits, were planned to include this extension for all DOMs.

With the opportunity to refit, a number of additional improvements were implemented. The afterpulsing peak at 9 microseconds was explicitly included in the fitting code. To account for the variability in the strength of the peak, a scale factor for the afterpulsing was included in the *Vuvuzela V2* fits.

In order to include the effect of atmospheric muons, a set of Polygonato CORSIKA. The Polygonato model was selected due to the natural weighting scheme of the output files, allowing continuous simulation of the detector. Simulated files were divided into 10 microsecond long events (*long-frame* events), each containing multiple muons. The simulation was halted after photon propagation, giving a collection of muons without detector noise and effects applied.

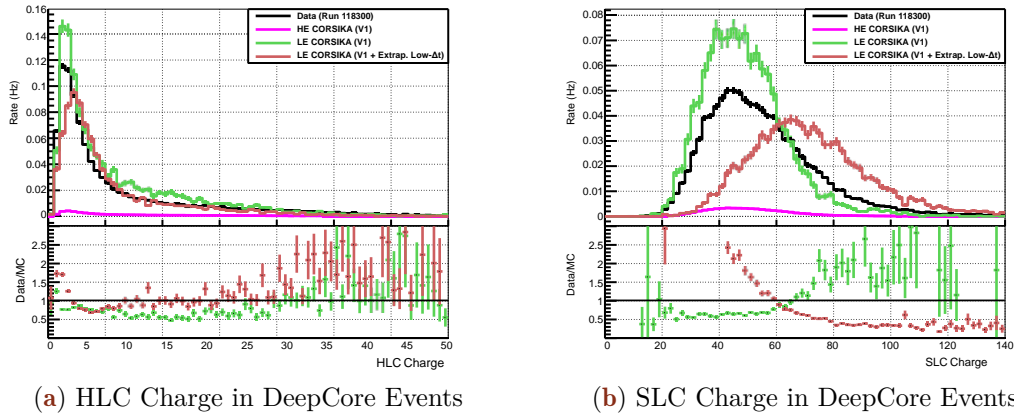


**Figure 5.4** – The total amount of charge on DOMs satisfying the (a) HLC and (b) SLC criteria described in Section 3.1.2. The distribution from 8 hours of data (black) is shown compared to a sample of CORSIKA muons at low-energy ( $600 \text{ GeV} \leq E_{CR} \leq 100 \text{ TeV}$ ) and high energy ( $100 \text{ TeV} \leq E_{CR} \leq 100 \text{ EeV}$ ). Unlike in Figure 5.3, the charge distributions using the low-dt extension to Vuvuzela shows large disagreements with data. This is most visible in the SLC charge distribution.

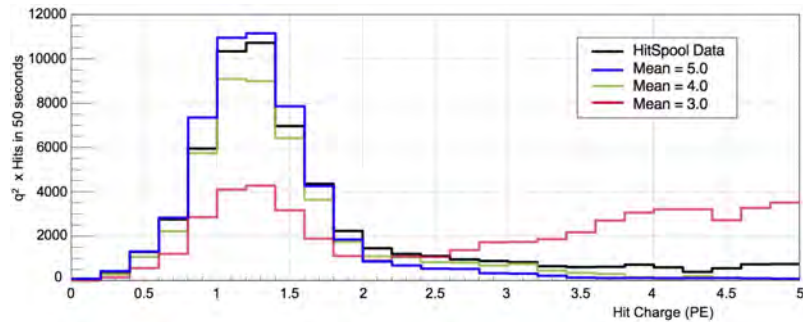


**Figure 5.5** – The effect of changing the Vuvuzela noise model parameters on the charge distribution of observed launches. Note the scale of the y-axis, which is scaled in order to emphasize the effect. Here, the gaussian mean is shifted from "5" (100 microseconds) to "3" (1 microsecond). All other parameters are held constant. By moving the correlated noise distribution to shorter timescales, more of distribution falls into one FADC bin, increasing the charge output for each launch.

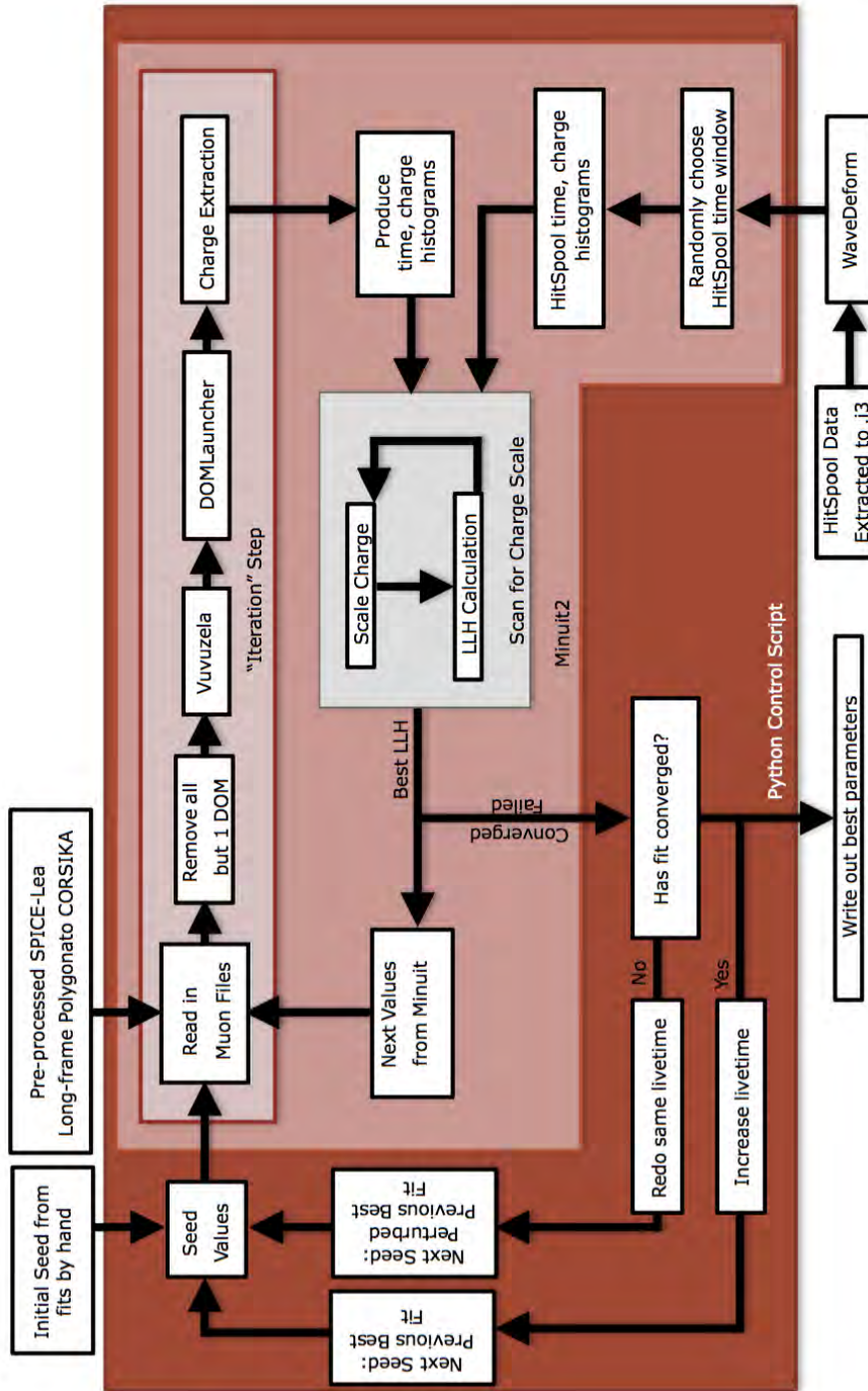
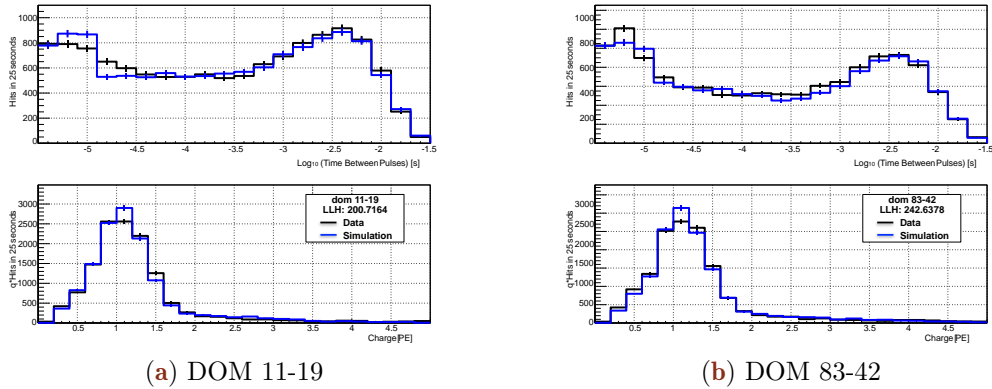


Figure 5.6 – A schematic diagram of the process used in the Vuvuzela V2 calibration fit.

The fitting process, described schematically in Figure 5.6, is divided into several parts. The code started with untriggered detector data as well as the produced long-frame CORSIKA events. The fit included a total of six explicit parameters: the five parameters from the original Vuvuzela model as well as a scale factor for the afterpulsing. Later investigations led to the introduction of a charge scale parameter to account for systematic differences between the data and simulated charge. Seeds for each parameter were taken from the Vuvuzela V1 calibration fits from 2012. Fits were performed for each DOM in parallel.

For each iteration, the long-frame CORSIKA files were filtered to remove information on all DOMs not currently being fit in order to limit the processing power required for DOM simulation. The noise and detector simulation were applied using the current parameter set for the iteration. Charge extraction from the waveforms was performed using standard IceCube tools. After the simulation for a given set of parameters, histograms were produced for untriggered data and simulated launches. As in the previous fits, the time between subsequent hits is used as the primary observable of the noise behavior. In addition, the observed charge on the DOM is used as a second observable for new fits.



**Figure 5.7** – Two examples of the new calibration fits for the Vuvuzela V2 model. The distribution of the time ("dt") between hits and the distribution of charge per launch are shown on top and bottom respectively. The untriggered data, in black, is compared to the Vuvuzela V2 model in blue. The new fits shown good agreement in both time and charge distributions. Note that the y-axis of the charge distribution is scaled by the charge value.

The timing histogram is binned from 6 microseconds until 1 second. Short timescales are measured through the effect on the charge distributions, which are binned from 0 to 5 PE in charge. The distributions for DOMs 11-19 and 83-42 are shown in Figure 5.7.

Using the two distributions, a Poisson binned likelihood is formed. With the simulation in bin  $i$  of histogram  $j$  denoted by  $f_{ji}$  and the data hits in the same bin denoted by  $d_{ji}$  and ignoring normalization constants, the log-likelihood takes the form

$$LLH = \sum_j \sum_i^{nbins_j} d_{ji} (f_{ji}) + f_{ji} \quad (5.2)$$

The negative log-likelihood,  $-LLH$  is minimized as a function of the fit parameters using iMinuit, a python wrapper for the minuit2 package [105, 106].

High values of charge are sensitive to the tail of the noise distribution at low timescales. These high charges from noise hits were rarely produced, limiting the sensitivity to this

region. To provide more weight to high charges, the histogram of the charges was weighted by the value of the observed charge. This reduces the weight of very low charge launches, but increases the weight of higher charges.

Additional work showed disagreement between the charge distributions in data and simulation. This disagreement, due to miscalibration of the SPE peak in data (see Section 4.3), was accounted for by introducing a scale factor applied to the charge in simulation as a free parameter in the fit. The charge scaling was applied to the simulated hits after detector simulation. To limit the computational complexity of the added parameter, the minimization over this charge scale factor is performed independently without resimulation. The form of this charge scale parameter assumes that the difference is a calibration issue in the data rather than a simulation problem.

Further work performed as part of a recalibration in IceCube have led to the production of new SPE templates in data. New SPE templates for Monte Carlo, discussed in Section 7.8, are also now being produced. The updates to the SPE templates were not implemented in the Vuvuzela V2 fitting process.

The previous calibration attempts explicitly avoided fitting the behavior below 10 microseconds due to mismodeled afterpulsing behavior that led to biased results in the noise parameters. The default probability of producing an afterpulse in simulation, assumed to be 5.93% for all PMTs, failed to take into account variations in the effects on each individual DOM. In the updated fit, the afterpulsing behavior has been investigated by including an overall scale factor on the afterpulsing probability for each DOM .

Late pulses, produced by electrons which backscatter to previous dynodes during the multiplication process, were also investigated for their effect on the goodness-of-fit in the noise distributions. These pulses occur at timescales of 50-200 nanoseconds and therefore are outside of both the SLC charge and timing distribution window. The late pulsing behavior was found to have a negligible impact due to both the rarity of late pulses as well as the lack of detailed information to constrain the distribution.

Due to the computational power required to produce large amounts of effective livetime at each iteration of the fitting process, a tiered approach was employed. Initial fits were seeded with the previous noise parameter fit values obtained in 2012. For these events, a coarse binning in both the timing and charge distributions were used. The first tier of the minimization process used one minute of detector data randomly selected from the available untriggered dataset. In addition, a weak tolerance value was used, allowing the minimizer to converge quickly to a reasonable minimum.

When the first tier completes the minimization process, the fit is restarted with a larger effective livetime, more bins, and a stronger tolerance. The best-fit parameters from the first tier are used as seed values for the second tier. The second tier used 5 minutes of data, increasing the simulation time per iteration by a factor of 5.

The third and final tier increased the effective livetime to 10 minutes and again increased the number of bins. The final tier of minimization was the most computationally intensive and required between three and four weeks per DOM.

The fitting process for each tier continued until the minimization either converged or failed. Failure could occur due to electronics issues, such as computing cluster downtime, or due to a limit of 10000 iterations set in the minimizer to prevent exceeding the maximum processing time available on the computing cluster. In the case of a failure, the fitting tier was restarted with a new set of seed values. The new seed values were selected from a gaussian distribution centered on the previous seed with a width of 5%. This process was continued until the third tier was complete for all DOMs.

## 5.5 Results of New Noise Fits

New calibration fits were completed over the course of two months for nearly all DOMs in the IceCube detector. String 25 and DOMs previously disabled due to malfunction are absent from the untriggered data, taken in 2014, and were unable to be fit. The parameters for string 25 were selected using the average of all other fits.

The Vuvuzela V2 fits were checked after convergence in Figures 5.5 and 5.9. One notable feature is the number of DOMs with afterpulsing at the fitter boundary. The likelihood values associated with these fits, however, appear to be consistent with other fits. Due to a planned overhaul of the afterpulsing simulation, the fit values of the afterpulsing probabilities have not been adopted for simulation. Therefore, no further investigation of the probabilities has been pursued.

The likelihood value was checked as a function of string and DOM number in Figure 5.10 to identify outliers. The likelihood values appear to vary as a function of depth and shows at least two notable features: a "band" structure and an overall depth-dependence. This was initially unexpected, given that the noise is an internal property of individual DOMs.

It is worth noting that the noise measurements of each DOM are not fully independent due to the included simulated muons. The fits use long-frame CORSIKA to model the effects of muons in the untriggered data from the detector.

This leads to two subtle limitations in the fitting process. The long-frame CORSIKA is produced with a single flux model, in this case the Polygonato model used in CORSIKA [91]. Disagreement between the Polygonato cosmic ray flux model and the data can lead to disagreement in the fitting of noise parameters. The muon flux decreases with increasing depth, resulting in a lower muon contamination, and consequently smaller effects from mismodeling of the muon background, for deeper DOMs (higher DOM number).

In addition, the long-frame CORSIKA implicitly assumes a single model of the ice for photon propagation. Mismodeling of the scattering and absorption of photons from the CORSIKA simulation may also give rise to disagreement in the noise calibration. While large-scale properties of the ice are believed to be well-reproduced by the chosen ice model, SpiceLea [87], there will inevitably be remaining disagreements. The banding structure of Figure 5.10 corresponds to regions with low scattering and absorption at the top of the detector.

The uncertainties of the ice model and cosmic ray models together explain both features of Figure 5.10. In particular, the best fits occur where the DOM is either well-shielded from the Cherenkov light of muons due to either large overburden or strong absorption in the ice. In both cases, the contamination from light due to muons in the fitted time and charge distributions will be small, leading to a more 'pure' noise distribution that is well-fit by the Vuvuzela V2 noise model.

The sensitivity of the noise calibration procedure to underlying assumptions of both the muon flux and the absorption properties in the detector imply that little further improvement is likely without additional work on one or both issues. Simulation of long-frame CORSIKA is not possible with newer flux models at this time. As the primary uncertainty affecting the goodness-of-fit appears to be related to the muons themselves, merely updating to a newer model of the ice is unlikely to significantly improve the current fit parameters.

The newly calibrated low-dt Vuvuzela was provided to the IceCube simulation group in January of 2015 and quickly integrated into the low-energy simulation chain. New

neutrino, muon, and accidental noise trigger simulations were produced soon thereafter. The updated noise model shows significantly better agreement in both the total charge distribution and the number of hit DOMs for both HLC and SLC+HLC hits. The rate of accidental triggers improved relative to previous calibrations, with the remaining rate disagreement reduced from 50% to approximately 15%. Negligible effect was observed in the low-energy neutrino events at final level for existing samples.

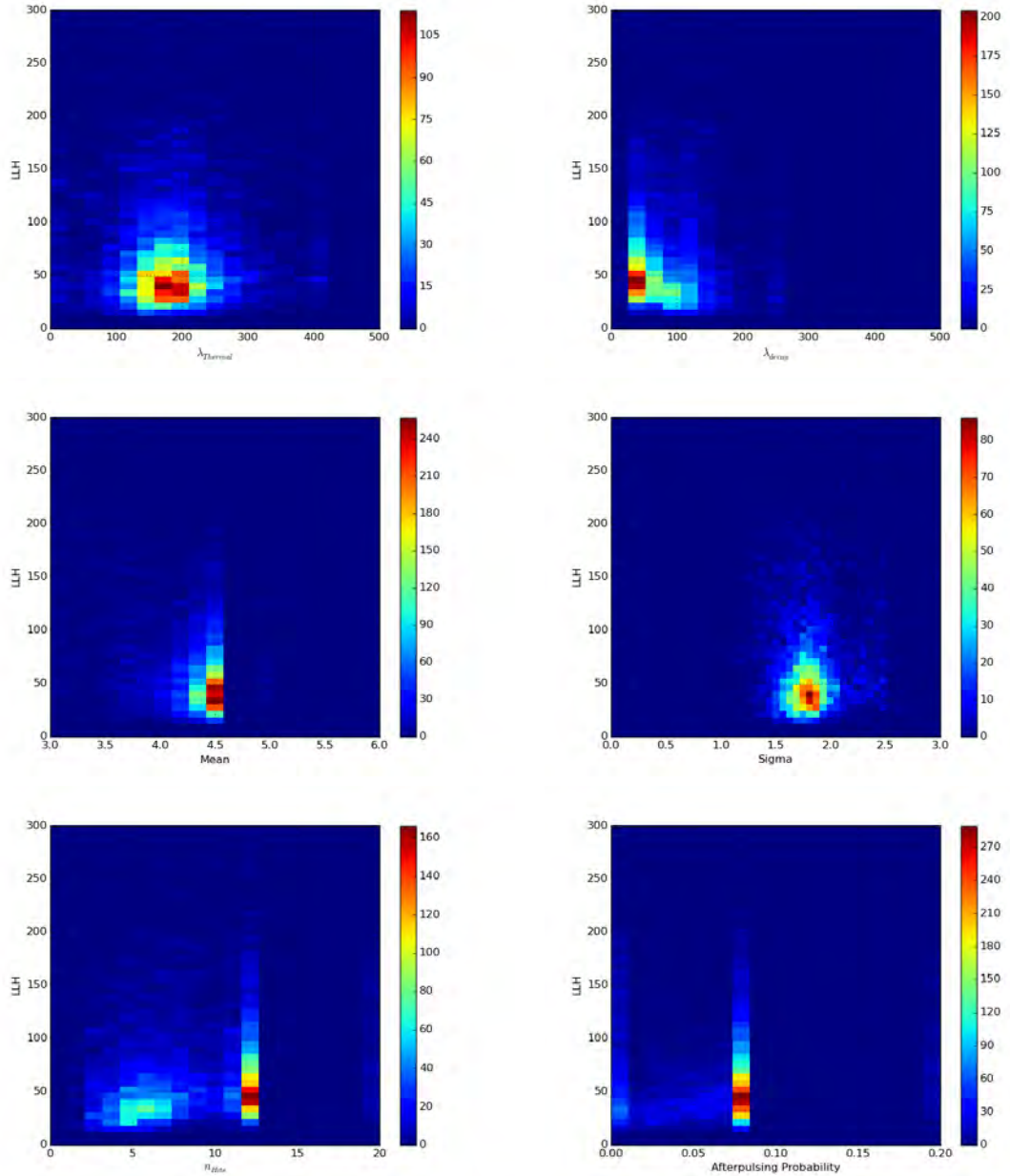


**Figure 5.8 – T** he distributions of each new fit parameter in the Vuvuzela V2 model. The colorbar scale shows the number of DOMs in each bin.

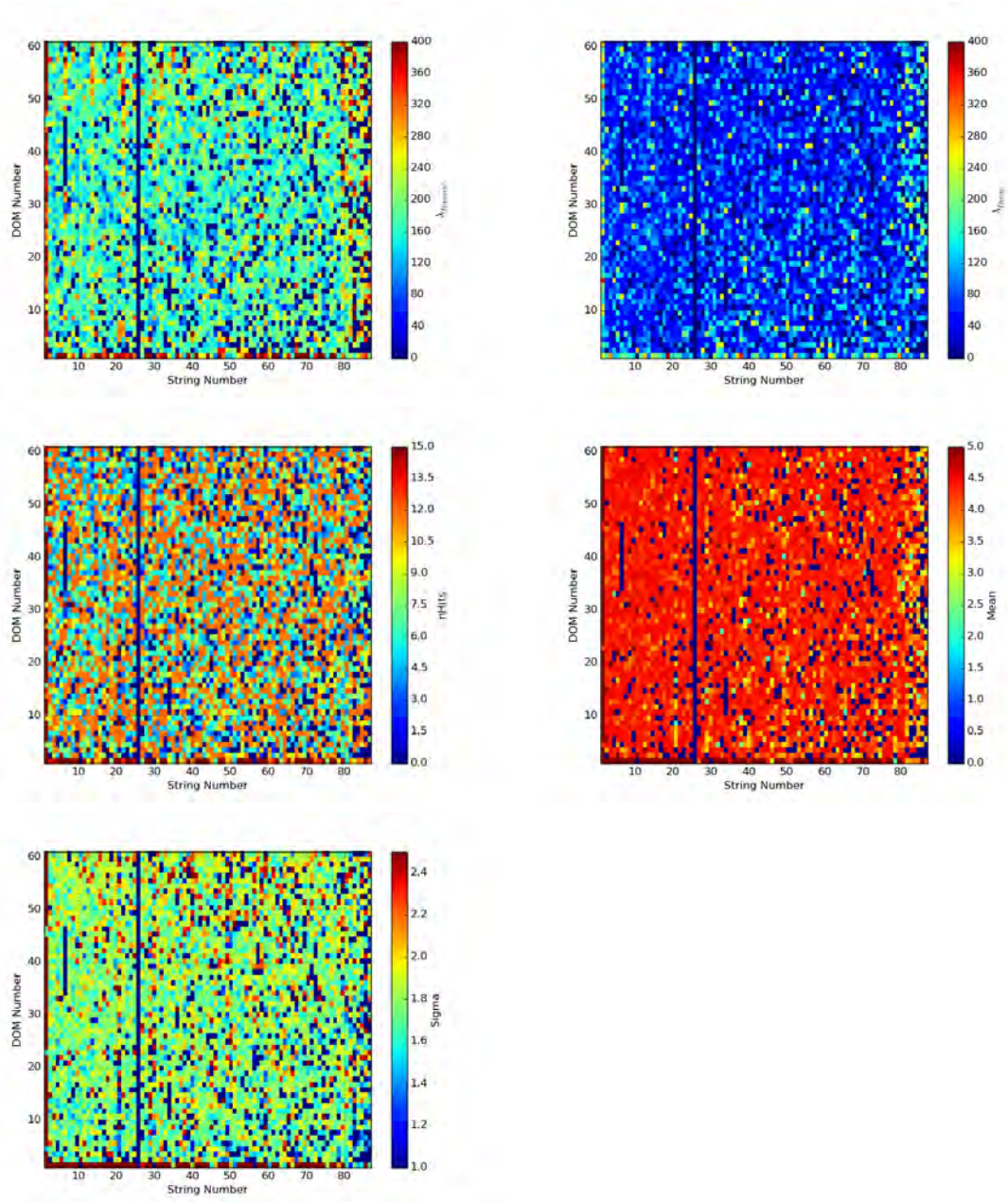


**Figure 5.9** – The distributions of each new fit parameter in the Vuvuzela V2 model as a function of the string and DOM number. Note that the top of the detector is at the bottom of this plot. No parameter appears to be correlated with depth. DOMs on string 25 are missing from the untriggered dataset used here and were not fit. In addition, DOMs which are disabled due to malfunction are also unavailable.

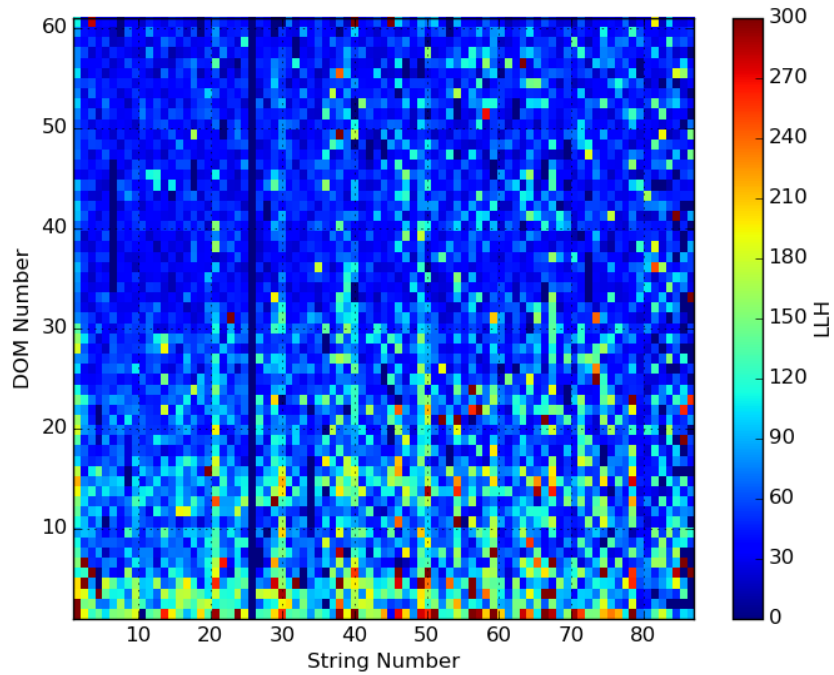


**Figure 5.10** – The log-likelihood as a function of string and DOM number for the Vuvuzela V2 fits. Note that DOM 1 is at the top of the detector and DOM 60 at the bottom. The likelihood value was expected to be independent of depth, but shows some structure. These structures are correlated with both the ice model and the muon flux.

The updates of the noise simulation provide one reduction of background uncertainties in the tau neutrino appearance analysis. Another large uncertainty in the analysis is due to the limited simulation statistics of the atmospheric muon samples.

For low-energy oscillation analyses, the simulation of muons has proven difficult due to the computationally intensive simulation scheme. Large numbers of simulated events are produced for general IceCube analysis use, although the vast majority of these background muons do not reach DeepCore. In response, previous analyses [79, 80, 81, 67] have developed methods to reuse data events which fail the selection as a model of the background at Final Level. Severely limited simulated statistics from the CORSIKA generator precluded strong checks of these samples.

For the search for tau neutrinos, new background generation techniques were used to more robustly model atmospheric muons. Two new generation schemes for low energy IceCube analyses are discussed here. The first, briefly discussed in Section 6.2, provided the final background sample used in the search for tau neutrinos. The second method, discussed in Section 6.3, is more experimental, but shows potential to further improve the background generation efficiency substantially for future analyses.

## 6.1 CORSIKA Generation In DeepCore

In IceCube, most simulation is produced centrally for use by the entire collaboration. This is especially true for background simulation produced with the CORSIKA generator.

CORSIKA simulation, using the 5-component scheme discussed in Section 4.1.1, is the most common background simulation used in IceCube. These simulations are broken into two energy ranges based on the simulated primary particle energy in order to allow efficient generation of rare, high energy events. These are "low energy" CORSIKA, produced with primary energies  $600 \text{ GeV} \leq E_{prim} < 10 \text{ TeV}$ , and "high energy" CORSIKA, with energies  $10 \text{ TeV} \leq E_{prim} < 100 \text{ EeV}$ .

Unlike MuonGun, CORSIKA generation does not currently possess a method to target specific sections of the detector. Instead, CORSIKA muons target a cylinder of radius 800 m and length 1600 m centered on and fully enclosing the IceCube detector. This allows uniform coverage useful for a wide range of analyses.

The centralized CORSIKA simulation in IceCube results in simulated background datasets used by all analyses in the collaboration. The production of these sets is computationally intensive, requiring hundreds of CPU-years and GPU-years worth of processing time in order to reach sufficient statistics for all but the highest energy IceCube analyses. The number of unweighted simulation events and required computational resources required for centralized CORSIKA sets is shown in Table 6.1. Included is the 'simulation efficiency', the average number of events produced per computational year.

$$\epsilon = \frac{N_{final}}{t_{CPU} + t_{GPU}} \quad (6.1)$$

For analyses using DeepCore, the CORSIKA generation scheme results in many muons that are easily rejected during event selections. Events which interact solely outside of the DeepCore fiducial volume are removed early by a veto algorithm discussed in Section 7.2, reducing the background statistics from  $O(10^{12})$  to  $O(10^6)$ . Additional

Generator	Sim. Req.		Number of Events		$\epsilon$
	CPU	GPU	Generation	Final Level	
CORSIKA	188.9 Years	48.75 Years	$8 \times 10^{12}$	284	1.20

**Table 6.1** – The computational requirements needed for the production of standard CORSIKA sets in IceCube. The number of events reaching Final Level of the appearance search (Section 7.7) are shown. CORSIKA simulations are computationally intensive, but inadequate for low energy analyses in IceCube.

cuts reduce this number further, with the GRECO selection described in Chapter 7 removing all but 284 events from an initial sample of  $8 \times 10^{12}$ . These events represent nearly 10% of the Final Level sample after weighting.

The final sample of muons in GRECO is too statistically limited to be of use in oscillation analyses. While previous analyses have used data-driven estimates of the background shape, verification of such techniques is itself limited by the simulated background statistics as well. In order to produce sufficient statistics for use in the appearance analysis, new background simulation techniques were necessary.

## 6.2 MuonGun for DeepCore

As described in Section 4.1.1, the MuonGun generation scheme provides a method to target specific parts of the detector. Doing so allows for *biased generation*, leaving some regions undersimulated while increasing the simulation statistics in the target volume. The limited size of the DeepCore fiducial volume provides an ideal use case for this biased generation.

In MuonGun, the muons are produced on a *generation cylinder* with a radius of 800 meters and length of 1600 meters, matching target volume of standard CORSIKA generation. The muons are pulled from a power law spectrum of the user’s choice. An offset power law distribution is selected for this work in order to align with previous analyses [93].

$$f(E) = (E + E_0)^\gamma \quad (6.2)$$

where  $E$  is the energy of the muon at the generation cylinder,  $E_0$  is an offset energy for generation, and  $\gamma$  is a configured spectral index. For this thesis, a power law is selected with a spectral index of -5, an offset of 700 GeV. Note that the measured cosmic ray spectral index is approximately -2.7. The steep spectral index selected for generation leads to overgeneration of very low energy events. These events are expected to produce little light in the outer detector, making them difficult to identify with vetoing algorithms. Low energy muons are therefore expected to be the dominant component of the muon flux at Final Level of the GRECO sample.

CORSIKA events observed in the GRECO selection at Level 5 (Section 7.5), the last cut level with significant CORSIKA statistics available, are used to select an energy range for MuonGun simulation. These events are shown in Figure 6.1 The lower energy limit, 160 GeV, is selected by using CORSIKA simulation to identify the minimum energy required for a muon at the generation cylinder to reach and trigger the DeepCore detector. A high energy limit on the MuonGun generation was set at 500 GeV, leaving the 5% of the CORSIKA events above 500 GeV unsimulated. The energy range selected, shown in Figure 6.1, includes more than 95% of the distribution of CORSIKA events.

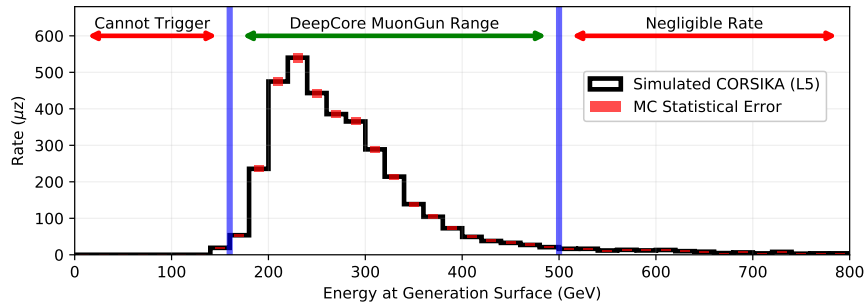


**Figure 6.1** – The distribution of CORSIKA muon energies at the MuonGun generation surface using GRECO Level 5 muon events. Very few events trigger below 160 GeV and less than 5% of events occur beyond 500 GeV. These two energies set the bounds for the MuonGun generation. MuonGun simulation has also been produced and tested above 500 GeV, but no simulated events survived to Final Level in GRECO.

Generator	Sim. Req.		Number of Events		$\epsilon$
	CPU	GPU	Generation	Final Level	
CORSIKA	188.9 Years	48.75 Years	$8 \times 10^{12}$	284	1.20
MuonGun	10.27 Years	12.11 Years	$3 \times 10^9$	2486	111.08

**Table 6.2** – The computational requirements needed for the production of MuonGun simulation for DeepCore. The MuonGun simulation is nearly two orders of magnitude more efficient at producing statistics at Final Level in the appearance analysis.

The angular spectrum of the MuonGun simulation is created by setting a *target cylinder* toward which the generated muon must intersect. For this work, the DeepCore fiducial volume is used as a target, encompassing a cylinder with radius 150 meters and length 500 meters centered on the geometric center of DeepCore at  $x=(46.3, -34.9, -300)$ .

A sample of muons was created using these settings of MuonGun and the resource requirements are shown in Figure 6.2. The efficiency improvement from changing to MuonGun is substantial, increasing from 1.20 CORSIKA events/year to 111.08 MuonGun events/year, an increase of nearly two orders of magnitude.

This simulation scheme has limitations. Because the target volume is small, events which do not enter DeepCore are not included in these MuonGun sets. These events form a substantial background at early selection levels and cannot be ignored. For this reason, CORSIKA muons are required for the development of selections and will be used in the Chapter 7 until Level 5 (Section 7.5).

The generated MuonGun statistics are useful for analyses at or near Final Level, where muons outside of DeepCore are no longer a dominant source of background. The newly produced MuonGun statistics are used to model the muon background after Level 6 (Section 7.6).

### 6.3 Simulation Efficiency with KDE Prescales

After processing to the Final Level of the GRECO event selection (see Chapter 7), the background MuonGun simulation retains 2486 simulated events of the original sample of  $3 \times 10^9$  generated events. The sample is sufficient for the search for tau neutrino appearance, but further improvements are possible.

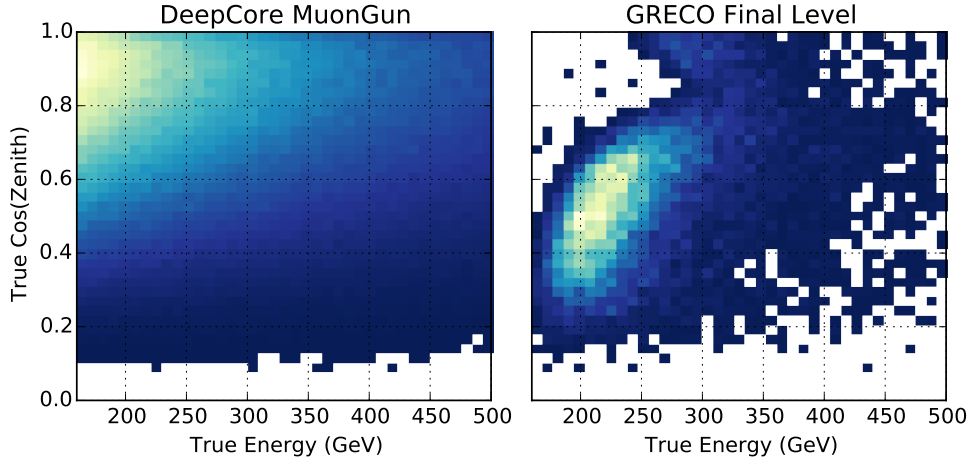


**Figure 6.2** – The generated spectrum from MuonGun in energy and zenith angle compared to the muons reaching the Final Level of the GRECO event selection. Both distributions have been normalized to 1. The majority of events produced by MuonGun are downgoing and low energy. These events do not reach Final Level of the selection.

While the previous section focused on improvements based on the simulation volume using MuonGun, inefficiencies still exist in the energy and zenith angle spectrum of the generated events. This inefficiency is shown in Figure 6.3. The majority of the events produced by MuonGun are very downgoing ( $\cos(\text{zenith}) \approx 1$ ) and low energy. These events are noticeably absent from the Final Level sample.

In addition to the energy- and zenith-dependent effects, the GRECO selection exhibits strong azimuthal selection biases. This arises due to three effects. The first is the offset between the center of IceCube (and therefore the center of the generation volume) at  $(x, y) = (0, 0)$  and DeepCore at  $(x, y) = (46.3, -34.9)$ . Due to this offset, the distance required to reach the DeepCore fiducial volume at an azimuthal angle around 150 degrees is longer than the corresponding distance at 0 degrees. This gives rise to an azimuthal effect appearing as a sinusoidal variation of the minimum generated energy of events at Final Level.

Another cause of azimuthal selection bias is the regular hexagonal structure of the IceCube volume, with long "corridors" through which muons may reach DeepCore without crossing any strings. Cuts designed to look for hits in the veto region produce these azimuthal biases when muons traveling close to strings are more likely to be identified and removed than those further from strings (see Section 7.6).

Finally, the DeepCore detector is not fully surrounded by an evenly distributed layer of strings. This may be seen in Figure 3.6, where a layer of four strings is available for muon identification in the top left, but a layer of only three strings is available on the bottom right. Events entering the detector from this direction are more likely to reach DeepCore without being tagged, resulting in a larger acceptance of events around 300 degrees.

In order to improve simulation statistics at Final Level, the existing MuonGun simulation scheme was modified to include an energy-, zenith-, and azimuthally-dependent prescale factor. This approach, here referred to as a *KDE prescale*, allows simulation to be produced with a known bias matching that of a given set of input files.

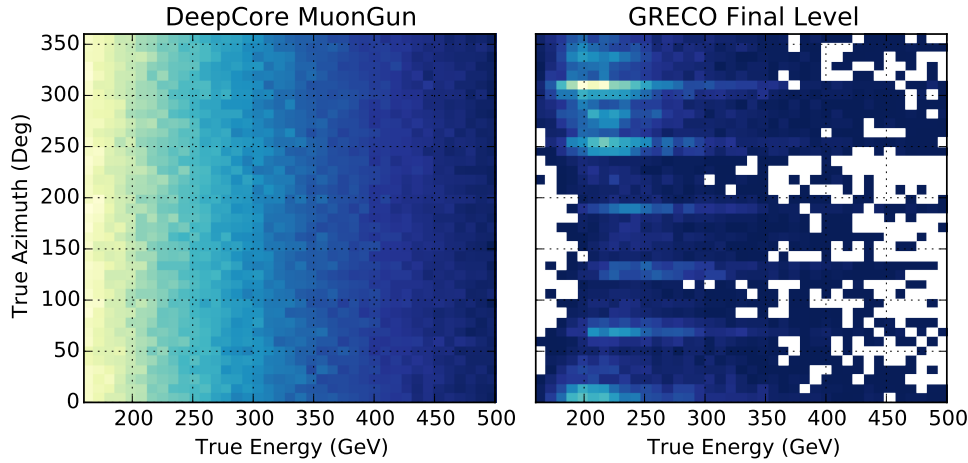


**Figure 6.3** – The generated spectrum from MuonGun in energy and azimuthal angle compared to the muons reaching the Final Level of the GRECO event selection. Both distributions have been normalized to 1. Events in the Final Level sample are strongly biased in azimuth due to the geometry of the detector and the MuonGun production settings.

Generator	Sim. Req.		Number of Events		$\epsilon$
	CPU	GPU	Generation	Final Level	
CORSIKA	188.9 Years	48.75 Years	$8 \times 10^{12}$	284	1.20
MuonGun	10.27 Years	12.11 Years	$3 \times 10^9$	2486	111.08
MuonGun+KDE	1.27 Years	214 Days	$9 \times 10^8$	3588	1933.27

**Table 6.3** – The computational requirements and number of events for each muon generation scheme. The use of the KDE prescale improves the simulation efficiency by a factor of 50x compared to the DeepCore MuonGun simulation method described in Section 6.2.

In this scheme, the *kernal density estimator* (*KDE*) from SciPy [107] is applied to all remaining events at Final Level of the GRECO event selection. The KDE uses a Gaussian kernal to represent each event in energy, zenith, and azimuth. The resulting KDE is used to estimate the selection probability of muons in the Final Level of the GRECO sample.

In the new simulation scheme, shown in Figures 6.4 and 6.5, an event is produced using standard settings for MuonGun generation described in the previous section. Immediately following generation, the probability of the new event reaching Final Level is calculated from the KDE, with typical values of approximately  $10^{-4}$  for a likely event and  $10^{-9}$  or lower for unlikely events. A prescale multiplicative factor of  $10^5$  is used to set the overall probability scale. The product,  $p$ , of the prescale factor and KDE probability is used in order to accept or reject events. The value is interpreted as an acceptance probability and may not exceed 100%. Any values for which this may be the case are directly set to 100%.

Using a random number generator, this  $p$  factor is used to retain or reject the muon event. The simulation then proceeds as normal, with photon propagation, detector simulation, triggering, and filtering.

The results of experimental KDE prescale generation are shown in Table 6.3. By removing unlikely events early in the simulation chain, the required computational

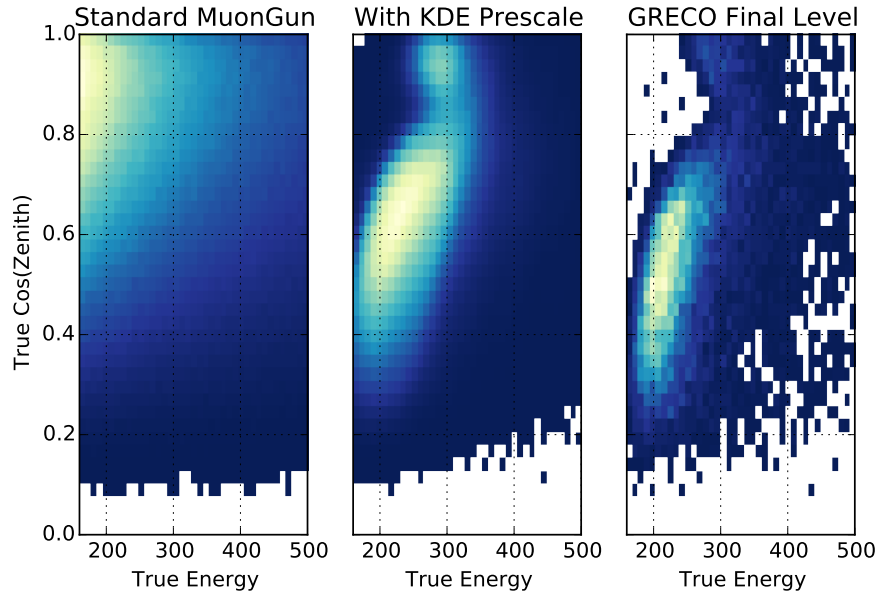


**Figure 6.4** – The generated spectrum from the KDE prescaled MuonGun in energy and zenith angle compared to the muons reaching the Final Level of the GRECO event selection. Both distributions have been normalized to 1. The KDE prescale generation produces events which more closely model the event distributions from Final Level in the GRECO event selection.

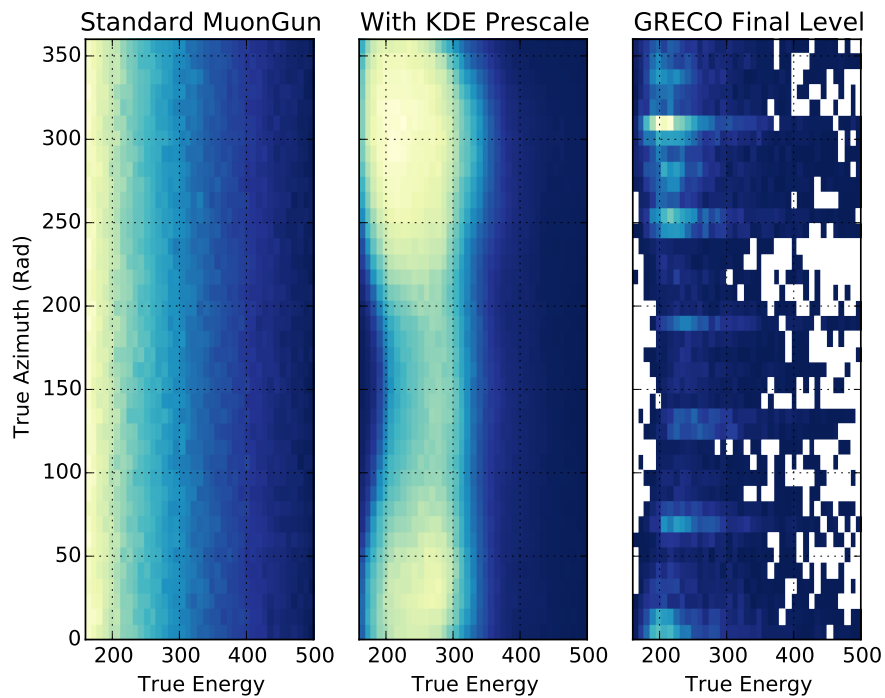


**Figure 6.5** – The generated spectrum from the KDE prescaled MuonGun in energy and azimuthal angle compared to the muons reaching the Final Level of the GRECO event selection. Both distributions have been normalized to 1. The KDE prescale generation produces events which more closely model the event distributions from Final Level in the GRECO event selection.

resources are further reduced compared to the general CORSIKA simulation sets produced by the IceCube collaboration. While the number of events at Final Level is comparable to the MuonGun methods described in Section 6.2, the required time for simulation is reduced to about 2 computation-years.

Further optimizations are possible at the expense of accuracy. For example, the DOM oversizing methods described in Section 4.2.2 may be used to reduce the number of propagated photons. Using  $N_{OS}=3$ , the GPU simulation requirements are further reduced by approximately 8x, leading to a total simulation efficiency of 2671.15. The oversizing is known to cause a small bias in the simulated photon arrival time, potentially leading to bias in particle reconstructions. Oversizing should be used with care in order to minimize or eliminate these biases.

The KDE prescale demonstrated here used only unweighted events due to limitations in the SciPy software. The KDE therefore encodes some bias towards the production of low energy muons due to the soft spectral index of the MuonGun DeepCore generation. Other implementations of multidimensional KDEs can accept event weights [108, 109]. The use of these algorithms would be beneficial and remove some dependence on the generation characteristics of the source events used for building the KDE.

The simulation using KDE prescales is limited by the events used to form the KDE. If too few events are used, the KDE may not adequately represent the shape of the underlying spectrum, leading to little gain in efficiency. Likewise, if a region is underrepresented in the sample, the KDE may not describe the distribution of events in this region. Care should be taken in order to check for unsimulated regions before using the KDE prescale to avoid these situations.

The use of the KDE prescale method shows substantial promise in improving simulation efficiency. Work is ongoing within the IceCube collaboration at the time of this writing to investigate use of the method for DeepCore analyses. If adopted, the improved simulation efficiency may allow future analyzers to significantly reduce the statistical uncertainty in the simulated background samples.

# GRECO: An Event Selection at the Limits of DeepCore

# 7

The search for tau neutrino appearance in atmospheric neutrinos requires a selection of neutrino candidate events. The events passing the SMT3 trigger in DeepCore, however, are dominated by Muons, with a rate of 280 Hz [38] compared to a neutrino rate of about 4 mHz.

In order to remove the atmospheric muons, an *event selection* is necessary. The GeV Reconstructed Events with Containment for Oscillations (*GRECO*) event selection is presented here. This selection was developed for the appearance analysis and reduces the atmospheric muon rate to around 0.07 mHz while retaining around 0.7 mHz of atmospheric neutrino events.

A typical neutrino interaction responsible for only about 10-20% of hits in an event with the other hits recorded by the detector are due to detector noise. These noise hits can affect the behavior of cuts, leading to lower cut efficiency, or can bias reconstructions of particles in the detector. A general discussion of how noise hits are identified and removed in IceCube events will preface this chapter.

The steps of the GRECO selection, known as *cut levels*, are designed to remove the atmospheric muons and accidental triggers while retaining neutrino events for the final analysis of tau neutrino appearance. Each cut level will be described in this chapter.

The GRECO selection provides improved rates compared to other analyses at Final Level. As a result of the high statistics available, the GRECO event selection has identified new miscalibrations, each of which will be described in Section 7.8.

## 7.1 Hit Cleaning

A set of pulses from an event, referred to as a *pulse series*, is stored for each event after running the wavedeform module described in Section 3.2. Not all recorded pulses are the result of muon or neutrino interactions in the detector, however. In a typical neutrino event at 10 GeV in DeepCore, the neutrino interaction may only be responsible for 10-20% of the recorded hits in the detector. These *noise hits* are not useful for understanding the particle interactions and are therefore typically removed during processing by *Hit cleaning* algorithms. These algorithms can increase the purity of a pulse series, defined to be the ratio of *physics hits* due to neutrino or muon interactions. Increased purity is obtained at the expense of efficiency, defined as the number of physics hits retained compared to the total number of physics hits observed. There exist multiple ways to identify pulses likely to be due to detector noise, three of which will be detailed in order from most strict to most accepting.

### HLC Cleaning

The most strict cleaning results from the exclusive use of local coincidence information. This type of cleaning is referred to as *HLC cleaning* and is shown in Figure 7.1. By selecting only pulses that result from DOMs satisfying the HLC criteria discussed in Section 3.1.2, the resulting pulse series can be cleaned of nearly all detector noise. No additional processing is necessary, although cleaning the pulse series based solely on

local coincidence criteria comes at the expense of a potentially significant amount of information about the event, since all SLC hits are removed.

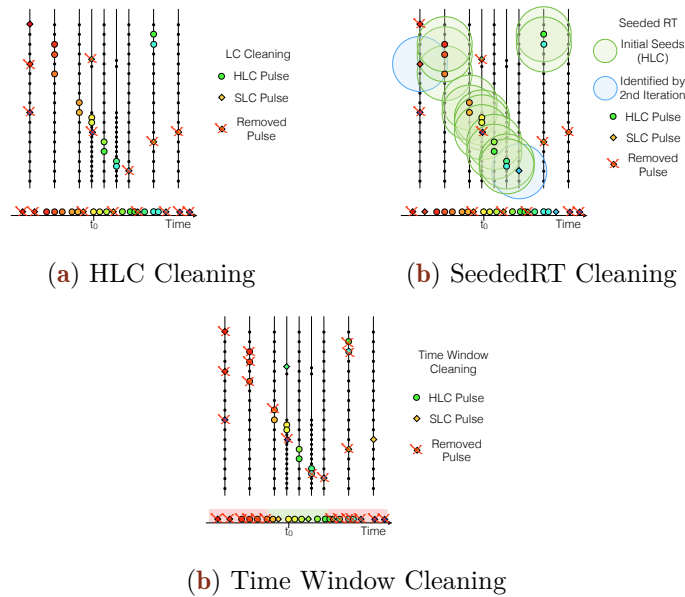


**Figure 7.1** – An illustration of the LC, SeededRT, and time window cleaning methods. (Left) All SLC pulses are removed while all HLC pulses are retained. (Middle) Pulses are removed based on time and distance from nearby HLC DOMs, allowing some SLC pulses to be accepted. (Right) Pulses are removed using the time relative to either the trigger in the static time window (STW) cleaning or the maximum pulse density in time in the dynamic time window (DTW) cleaning algorithms.

### SeededRT Cleaning

Instead of using only HLC hits, additional processing may be used to identify potentially interesting SLC pulses as well. The *SeededRT* (*SRT*) algorithm is one such algorithm, requiring a seed, radius, and time in order to search for additional information in the event as shown in Figure 7.1. SeededRT begins with a subset of "interesting" pulses, often a selection of the HLC pulses, as a seed. Once a seed is selected, a sphere is drawn around each seeded DOM. Any nearby DOMs observing pulses within the sphere and time window are added to the output pulse series. Once all seed DOMs have been checked, a new seed is created composed of the all current output pulse series. The process is repeated until no further pulses are discovered.

The most effective set of parameters is dependent on the detector geometry, since a given radius sphere will contain more DOMs in the DeepCore fiducial than the same sphere outside of DeepCore. Because of this, different settings are chosen for these two regions. In the less dense IceCube detector, a radius of 150 m and time window is 1000 ns is used. In DeepCore, these values are typically halved, with a radius of 75 m and a time window of 500 ns.

The SeededRT algorithm is commonly used in IceCube, allowing for a pulse series with minimal noise contributions while finding most hits due to muon or neutrino interactions.

## Time Window Cleaning

The most permissive pulse cleaning algorithm results in very little loss in pulses due to particle interactions, but allows nearly all noise pulses into the final hit series. This *Static Time Window* cleaning, often referred to using just the acronym *STW* cleaning, looks for pulses near the time of the trigger. For DeepCore processing, any pulses more than 4 microseconds before or more than 6 microseconds after the SMT3 time are removed.

There exists a second type of time window cleaning applied more rarely, but used in the GRECO selection. The *Dynamic Time Window* cleaning, hereafter *DTW* cleaning, is a time window cleaning algorithm that uses the maximum pulse density in time to find a likely interaction time of a muon or neutrino. The timing window is placed around this time instead of around the trigger. DTW cleaning is generally chosen with a significantly tighter window, often consisting of only a few hundred ns compared to the multiple microseconds used in the STW cleaning.

Time window cleaning is typically used in combination with additional cleaning methods, resulting in little loss in useful signal due to the wide time window (in STW cleaning) or in a very pure set of hits likely to be due to unscattered light.

## 7.2 Level 1: The DeepCoreFilter

Triggers are generally designed to be as accepting of the proposed physics signal as possible within processing constraints. Typically, limitations exist solely in the processing and storage capabilities. After triggering, various filters may be applied with the sole purpose of removing the collected background. For the purposes of this document, the only filter considered is the *DeepCoreFilter*.

The DeepCoreFilter proceeds by splitting the first pulse on each DOM identified by the SeededRT cleaning into "veto" and "fiducial" pulses, with each DOM given a designation based on its position in the detector as described in Section 3.3 [72, 71]. All hit DOMs with the first pulse occurring more than one standard deviation away from the mean time are removed from the fiducial pulse series in order to further limit the contributions from noise pulses.

With the updated fiducial pulse series, a center of gravity, or *CoG*, of the remaining hit DOMs is calculated.

$$\vec{x}_{CoG} = \frac{\sum_i^{Hits} \vec{x}_i}{N_{Hits}} \quad (7.1)$$

The "corrected" average time of the fiducial pulses is then calculated by assuming that the pulse is due to light emission at the CoG, as would be the case for a point-like interaction of a cascade event.

$$t_{CoG} = \frac{\sum_i^{Hits} t_i^0 - \frac{\|\vec{x}_i - \vec{x}_{CoG}\|}{c_{ice}}}{N_{hits}} \quad (7.2)$$

where  $t_i^0$  denotes the time of the first observed pulse and  $\vec{x}$  the position of each DOM.

All veto pulses are then compared to this CoG time and position by calculating an effective particle speed,  $v$ .

$$v = \frac{\|\vec{x}_{CoG} - \vec{x}_{hit}\|}{t_{CoG} - t_{hit}} \quad (7.3)$$

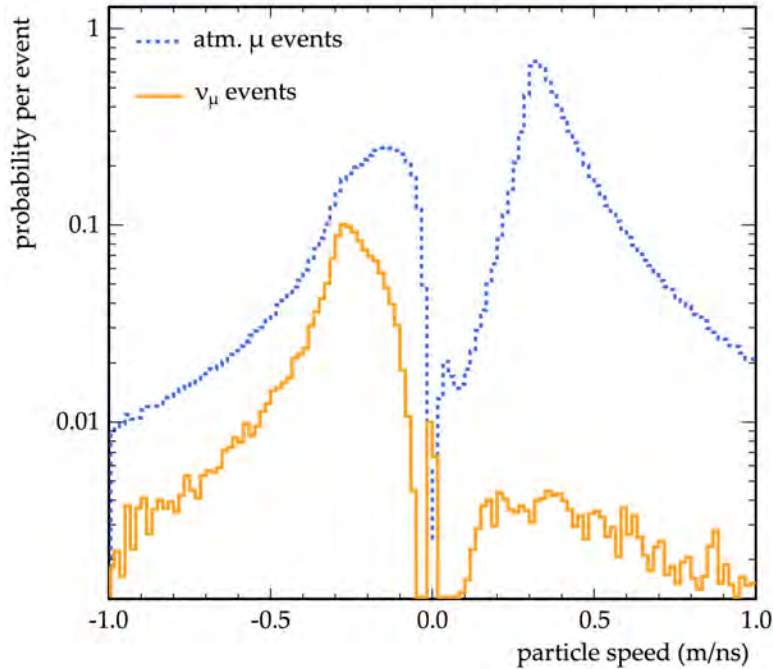


**Figure 7.2** – The distribution of effective particle speeds used by the DeepCoreFilter to identify and reject muons. Because muons interact first outside of DeepCore, a large peak is visible at speeds around 0.3 m/ns, the speed of light. Figure from [72]

Muons passing through the detector will do so at the speed of light, 0.3 m/ns. Unscattered hits left behind in the detector show this peak clearly for muons as shown in Figure 7.2. Low energy neutrino events, on the other hand, typically begin in DeepCore, with hits outside of the fiducial region following hits inside. These neutrino events show a peak at negative speeds. Events with more than one hit with an effective speed  $v$  between 0.25 m/ns and 0.4 m/ns are rejected and are removed from further processing.

The DeepCoreFilter is the first step in a low energy analysis in IceCube and is used in many analyses [71, 78, 79, 80, 81]. The algorithm reduces the atmospheric muon background from 280 Hz to approximately 17 Hz while retaining 99.4% of neutrino events which begin in DeepCore [72].

### 7.3 Low-En Level 3 Cuts

After the DeepCoreFilter is used to remove events, variations of hit cleaning algorithms and reconstructions are used. This processing stage, *Level 2*, does not remove events from the selection and will not be discussed here.

Following the Level 2 processing, the *Low energy Level 3* cuts are introduced. These cuts are standardized and used in all DeepCore oscillation analyses. The Level 3 processing follows the same structure as the following cut levels, consisting of one set of cuts designed to remove atmospheric muons (*muon rejection* cuts) and another set of cuts selected to remove accidental triggered events (*accidentals rejection* cuts).

After the DeepCoreFilter, approximately half of the remaining rate consists of muons. The remainder is due to accidental triggers due to random detector noise due to the low trigger threshold used in DeepCore.

### 7.3.1 Rejection of Accidental Events at L3

Three cuts are introduced at Level 3 in order to reduce the observed number of accidental triggers. Events are required to have at least 3 pulses and a total charge of at least 3 PE in a 250 ns DTW cleaned pulse series in the DeepCoreFiducial region. This removes events which have reached Level 3 processing via random detector noise in the fiducial region.

In addition, the *NoiseEngine* algorithm is used to identify accidental triggers [71]. NoiseEngine uses the relative direction between each pair of hits to search for directionality of the event. Events with fewer than three hit pairs pointing in the same direction are rejected. After the NoiseEngine algorithm, more than 96% of accidental triggers are removed from the analysis.

### 7.3.2 Rejection of Atmospheric Muon Events at L3

The removal of muons relies on some understanding of the characteristics of these events at Level 3. Muons at this level are generally bright enough to be identified by hits in the outer part of the detector, known as the veto region. Because neutrino candidates of interest in this search have energies less than 50 GeV, no light emission is expected in the veto region due to neutrinos. This may be used to identify muons using cuts described here.

#### First Hit Z Position

Because the muon tracks are primarily steeply inclined, most will leave hits in the upper part of the detector. Neutrinos of interest in the search for appearance will primarily emit light within the DeepCore fiducial volume, leading to little or no light emission in the top half of the detector. This difference between neutrino and muon emission veto region is used to identify background muons. The position of the first hit in a STW+SRT cleaned pulse series consisting of DeepCore fiducial hits is used to look for muons using this principle. Any event with a first hit above  $Z=-120$  m is removed.

#### NAbove200

The total charge of recorded hits occurring in the top of the detector is also used in the analysis. This variable, known as *NAbove200*, measure the integrated charge occurring before the SMT3 trigger above a depth of -200 . If more than 12 DOMs are hit above  $Z=-200$  m, then the event is removed.

#### RTVeto

The SeededRT algorithm is useful for removing noise hits in the detector. It may also be used to find clusters of hits due to muons in the outer part of the detector as well. This technique, known as *RTVeto*, uses the SeededRT algorithm to identify the largest cluster of pulses in the veto region. The number of hits in this cluster is used to identify atmospheric muon events. The RTVeto algorithm uses a radius of 250 m and a time window of 1000 ns for both DeepCore and IceCube DOMs.

The cut is used in combination with the total amount of charge observed in the DeepCore fiducial region to define a few separate cut conditions. For the purposes of this search, only the lowest energy version is relevant. In this case, any event with a cluster of 4 or more hit DOMs in the outer detector is removed.

Type	IceCube Processing		
	Any Filter	DC Filter	Low-en L3
CORSIKA	990598	9178	969.818
MuonGun	60669	2982	442.493
Accidentals	35855	8117	283.559
$\nu_e$	1.842	1.721	1.262
$\nu_\mu$	11.317	6.360	4.758
$\nu_\tau$	0.293	0.270	0.206
MC Total*	1026466	17303	1260
Data	1154426	19092	1092

**Table 7.1** – The event rates after the Level 3 cuts in GRECO. The total simulated rate is calculated using CORSIKA events and ignoring MuonGun. The data is estimated from a burn sample of 14 days. Rates are given in mHz.

## C2QR6

Atmospheric muon events at Level 3 tend to leave long tracks and take  $O(3 \mu s)$  to cross the detector. Oscillation neutrino events produce small light patterns due to the low energies involved, with light being deposited quickly. The difference in the light emission profile of the two event types may also be exploited to reject atmospheric muons background events.

To evaluate the deposition time for light in each event, the *charge ratio in 600 ns* ( $QR6$ ) is used.  $QR6$  is defined as the ratio of charge observed in the first 600 ns and the total amount of observed charge.

$$QR6 = \frac{\sum_i q_i}{\sum_i^{hits} q_i} \Bigg|_{0 \leq t_i - t_{first} < 600} \quad (7.4)$$

Here the time is measured relative to the first observed hit in a STW+SRT pulse series. Atmospheric muons will tend to deposit light over a longer timescale, resulting in a charge ratio near 0. Neutrinos will deposit light quickly, with a charge ratio near 1.

The algorithm is sensitive to the first observed hit. Noise hits before the particle interaction can lead to an erroneous definition of the time window. In order to reduce this possibility, the first two hits may be ignored for the calculation. This form, the *cleaned charge ratio in 600 ns* ( $C2QR6$ ) is used in the Level 3 processing to remove atmospheric muon events.

### 7.3.3 Rates at Level 3

The rates after the Level 3 cuts are applied are shown in Table 7.1. The atmospheric muons are reduced by about an order of magnitude. The removal of accidental triggered events forms a large part of the reduction in rate at Level 3, with the rates decreased by more than 96%.

## 7.4 GRECO Level 4 Cuts

The first GRECO-specific cut level is designated *Level 4*, or  $L4$  and was first introduced in 2011 using very similar variables as the Level 3 cuts. This is performed for historical reasons, as the DeepCore Level 3 and GRECO Level 4 were produced in parallel.

As in the DeepCore Level 3 processing, the GRECO Level 4 is divided into two types of cuts: those that remove accidental triggers due to detector noise and those that remove atmospheric muons. The cuts for atmospheric muons are fed into a *boosted decision tree* (*BDT*), a multivariate algorithm designed to separate signal from background [110].

### 7.4.1 Rejection of Accidental Events at L4

Similar to the cuts applied at Level 3, the GRECO Level 4 begins with a cut on the number of observed hits. In this case, static time window cleaning is applied with a range of  $-3500 \text{ ns} \leq t \leq 4000 \text{ ns}$  for hits in the DeepCore fiducial volume. A dynamic time window cleaning is then applied with a window of 200 ns. Any events with fewer than three hits in this stricter pulse series is removed.

### 7.4.2 Rejection of Atmospheric Muon Events at L4

Some cuts used to identify muons in the GRECO Level 4 are similar to those applied in the Level 3 processing. A stricter hit cleaning algorithm is used at this cut level to identify muons missed at Level 3. The reprocessed cuts are then used to train a *boosted decision tree* (*BDT*).

## FirstHit Z

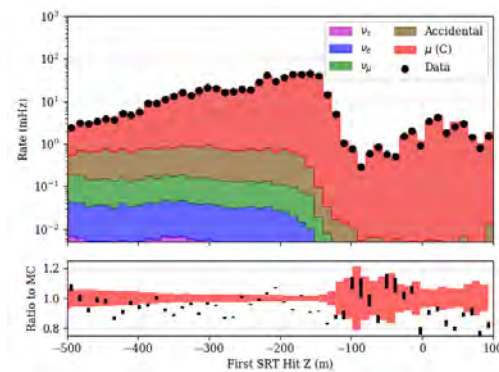


**Figure 7.3** – The Z position of the first hit in a cleaned hit series. Note the shape difference between the atmospheric muons in red and the various neutrino flavors, particularly above -200 m.

The Z position of the first hit DOM in the event is included for the GRECO Level 4. The cut continues to show separation between neutrino events and atmospheric muons with the new hit cleaning.

## NAbove200

Similarly, the number of hit DOMs identified above  $Z=-200$  m is again used with a new hit series. Once again, some separating power remains.

## QR6/C2QR6

Both the QR6 and C2QR6 are used in the GRECO Level 4 processing. The two show some degeneracy, although the BDT shows weaker separation if only one is available. Note that there exists some significant disagreement between data and simulation at low values of C2QR6. This region does not contain much signal and will be removed by the BDT.

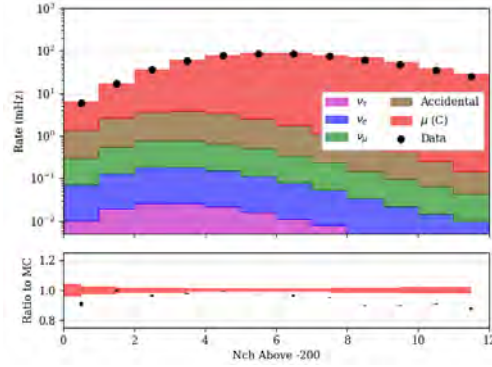


Figure 7.4 – The number of hits above Z=-200 m

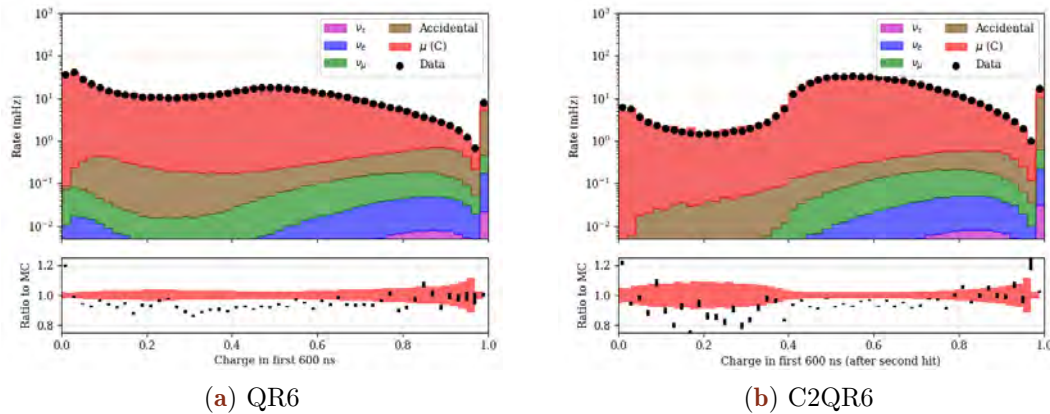


Figure 7.5 – The charge ratio variables used in the GRECO Level 4 cuts.

## Tensor of Inertia

At early cut levels, the muon and neutrino hit patterns appear different spatially in the detector. Many neutrinos with energies in the range of 1-100 GeV will have a compact hit pattern in DeepCore. Muons will have a more elongated hit pattern. The different hit topologies may be measured with the *Tensor of Inertia eigenvalue ratio* (more briefly, *ToI*). This variable is defined analogously to the tensor of inertia from mechanics, with the measured charge taking the place of the mass.

$$\begin{aligned}
 I_X &= \sum_{i=0}^{nhits} (y_i^2 + z_i^2) q_i \\
 I_Y &= \sum_{i=0}^{nhits} (x_i^2 + z_i^2) q_i \\
 I_Z &= \sum_{i=0}^{nhits} (x_i^2 + y_i^2) q_i
 \end{aligned} \tag{7.5}$$

These three moments yield information about the shape of the event. The eigenvalue ratio is defined as

$$e = \frac{\max(I_j)}{I_x + I_y + I_z} \tag{7.6}$$

Events which are very track-like, and therefore muon-like, have eigenvalue ratios near 0 while more cascade-like events have eigenvalue ratios close to  $\frac{1}{3}$ .

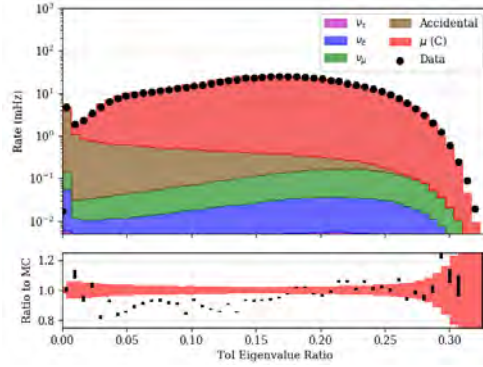


**Figure 7.6** – The eigenvector ratio from a ToI calculation. Larger values indicate more apparent elongation in the event.

## Linefit Speed

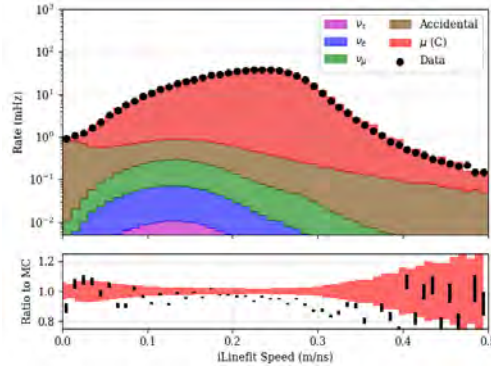


**Figure 7.7** – The effective speed of a plane wave passing through the detector measured in m per nanosecond. Faster speeds are associated with atmospheric muons traveling in ice at speeds  $c$ . Neutrino events below 50 GeV appear more isotropic, with effective speeds close to 0.

*LineFit* is an first-guess reconstruction used in IceCube. The algorithm fits the hits in the detector with a plane wave moving at speed  $v_{LF}$ . The speed of the plane wave may be solved analytically [111].

$$\vec{v}_{LF} = \frac{\langle t_i \cdot \vec{x}_i \rangle - \langle \vec{x}_i \rangle \langle t_i \rangle}{\langle t_i^2 \rangle - \langle t_i \rangle^2} \quad (7.7)$$

where  $\langle t_i \rangle$  denotes the average hit time and  $\vec{x}_i$  is the average hit position in the detector. In cascade-like events, photons have no average preferred direction, resulting in an average velocity close to 0. The relativistic atmospheric muons do have a preferred direction and travel through the detector with speed  $c_{ice} = 0.3$  m/ns.

## The L4 BDT

A Boosted Decision Tree (*BDT*) is trained at L4 to further reduce the atmospheric muon background by a factor of 10x. The variables described above were provided to a BDT training using CORSIKA muon simulation as the background training sample and GENIE simulation as the signal sample. The BDT uses a series of *trees*, collections of

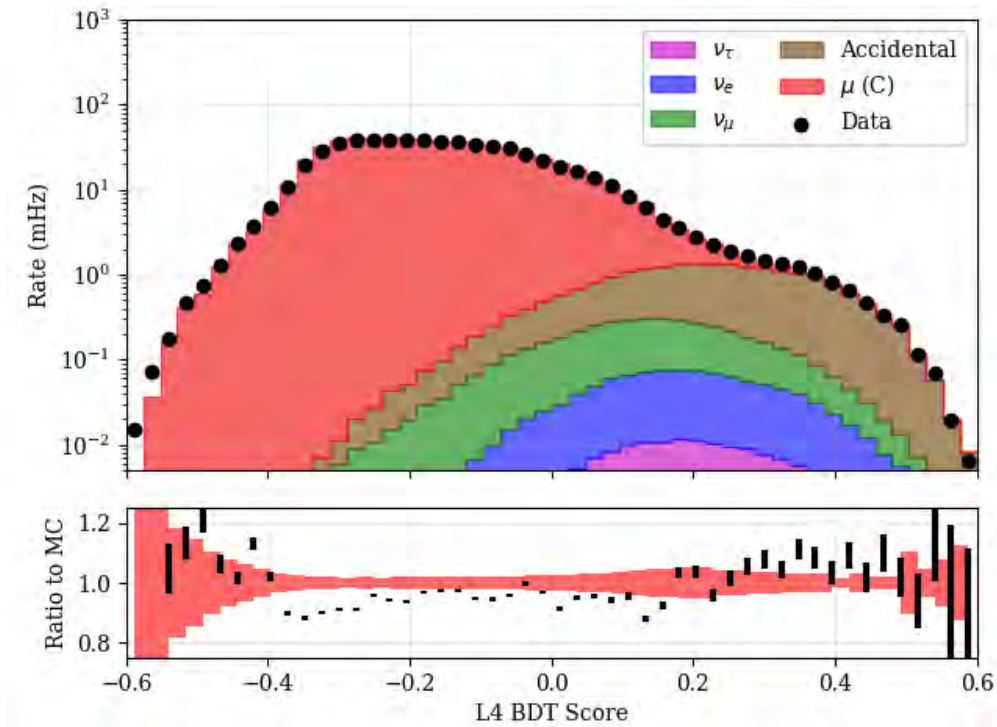


**Figure 7.8** – The distribution of the boosted decision tree decision score used at L4. A cut is applied at 0.04 to remove a significant fraction of atmospheric muon background events. Note the ratio, which shows disagreement in the very muon-like region. The region of disagreement is removed by the cut.

multidimensional cuts, to classify events as either signal-like or background-like [110]. After *boosting*, a process by which event weights are adjusted based on the success or failure of previous classification attempts, the BDT returns a *score* ranging from -1 (background-like) to +1 (signal-like) which may be used as a cut variable in an analysis.

The scores returned by the GRECO Level 4 BDT are shown in Figure 7.8. The distribution ranges from -0.6 to +0.6, indicating that no signal or background events are perfectly identifiable. Separation is observed between the atmospheric muon events, which peak around a score of -0.25, and signal, peaking at +0.15.

Comparisons to MC show mild disagreement between data and Monte Carlo, particularly in the most muon-like regions that get cut away. Its not obvious what causes the disagreement, although it is possible that the cosmic ray flux model is simply an inaccurate model of some part of the spectrum. Alternatively, this may be an artifact of undiscovered mismodeling of the atmospheric muon events. High energy muon events would likely have clear tracks visible in the detector, contributing to the region around -0.5. If the flux or simulation of these events does not reflect data, the BDT score distribution would be expected to show the largest disagreement in the background dominated region below -0.2. No investigation of the disagreement has been performed, as these events are removed from the GRECO selection.

A shoulder attributable to the accidental triggers is visible at high values of the BDT score, peaking around 0.25, indicating that these events appear more signal-like than the nuetrino samples. While initially puzzling, investigation of the training of the BDT showed that the original training sample did not include accidental triggered events. Instead, only CORSIKA and GENIE events were used to train the BDT. Because the

Type	IceCube Processing			GRECO
	Any Filter	DC Filter	Low-en L3	L4
CORSIKA	990598	9178	969.818	50.511
MuonGun	60669	2982	442.493	33.562
Accidentals	35855	8117	283.559	11.963
$\nu_e$	1.842	1.721	1.262	0.783
$\nu_\mu$	11.317	6.360	4.758	2.503
$\nu_\tau$	0.293	0.270	0.206	0.134
MC Total*	1026466	17303	1260	65.893
Data	1154426	19092	1092	68.592

**Table 7.2** – The event rates after the Level 4 cuts in GRECO. The total simulated rate is calculated using CORSIKA events and ignoring MuonGun. The data rate is estimated from a burn sample of 14 days. Rates are given in mHz.

training lacked any accidental triggers, the BDT picked the most obvious feature of the GENIE sets: that the signal events were primarily low energy with lower light deposition than the background muons. These are also key features of the noise triggers.

The GRECO Level 4 places a cut at 0.04 in the BDT score, removing a large fraction of the background sample. A large fraction of the neutrino sample is also removed in order to reduce the muon rates by a factor of 20x.

### 7.4.3 Rates at Level 4

The rates of the selection after the Level 4 cuts are applied are shown in Table 7.2. After the GRECO Level 4 BDT, the number of atmospheric muons is reduced to 50 Hz, a mere 25x the muon neutrino rate. The number of accidental triggers is also reduced in the analysis due to the dedicated cuts applied at this level. The number of accidental triggers is still larger than the number of neutrinos expected, however, indicating that further cuts are necessary.

## 7.5 GRECO Level 5 Cuts

The next stage of cuts, known as the *GRECO Level 5*, or more simply, *L5*, also uses a BDT to remove atmospheric muon background events.

### 7.5.1 Rejection of Accidental Events at L5

Unlike the previous stages, there is no explicit cut introduced at L5 to remove accidental triggers. Instead, an implicit requirement on the number of hit DOMs arises due to the reconstruction used at Level 5.

The STW+SRT pulse series containing DeepCore fiducial pulses is used to fit a total of 6 free parameters: the position (x, y, z), the time (t), and the direction of a muon track (zenith, azimuth). The parameters are degenerate if fewer than five hits are used. In this case, the reconstruction fails to converge and the event is removed. Because of this degeneracy, the GRECO Level 5 requires at least 6 hit DOMs in the hit series.

### 7.5.2 Rejection of Atmospheric Muon Events at L5 Time to 75% Charge

The first variable used to create the L5 BDT is the amount of time required to record 75% of the total charge, the  $t_{75}$ , measured from the start of the event. Similar to the

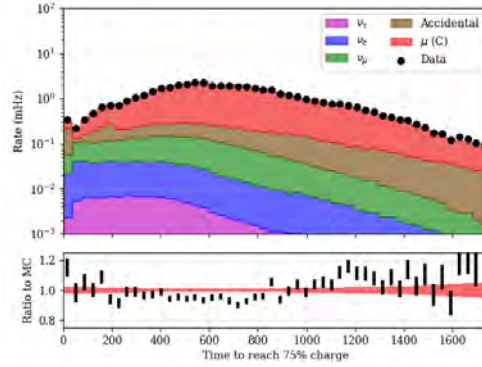


**Figure 7.9** – The time to accumulate 75% of the total charge of the event. Atmospheric muons tend to produce light in the detector over a longer time than the low energy atmospheric neutrinos used in the search for tau neutrino appearance.

QR6 and C2QR6 variables, the  $t_{75}$  is a variable designed to look at the hit distribution in time. However, the variable is now produced in the reverse manner: where the QR6 variable refers to the amount of charge in a given window, the  $t_{75}$  instead attempts to find the amount of time for a given charge level. Figure 7.9 shows the distribution of the  $t_{75}$ .

The neutrino events deposit energy quickly due to the low energies of the sample of interest in this thesis. The muon events take longer to reach 75% of the total charge due to the long travel time of the muons through the detector.

### Veto Identified Causal Hits

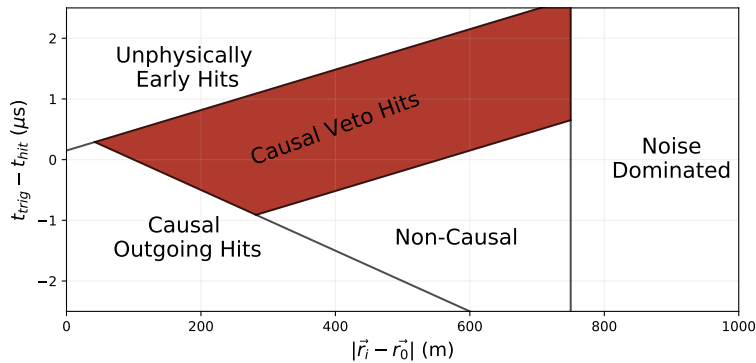


**Figure 7.10** – A schematic diagram showing the regions of the VICH algorithm. VICH returns the number of hit DOMs in the shaded region, corresponding to the pulses that are both causally connected with the trigger and entering DeepCore.

The *Veto Identified Causal Hits (VICH)* algorithm is also used in the GRECO Level 5. This algorithm uses an uncleaned pulse series to search for hits that are causally connected to the trigger [78]. The first DOM to contribute to the DeepCore trigger is used to define the trigger time and position.

Five regions are defined based on the causality criteria shown in Figure 7.10. Hits which are not causally connected to the trigger are ignored. Hits which occur too far away from DeepCore are also ignored to reduce the effect of detector noise. A causal

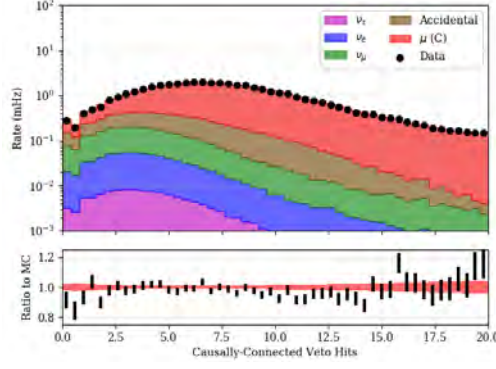


**Figure 7.11** – The amount of causally-connected charge discovered in the veto region.

region which is consistent with light travel outgoing from the trigger position is also ignored.

The VICH algorithm returns the total integrated charge of all pulses in the remaining "causal veto region".

### First Hit $\rho$

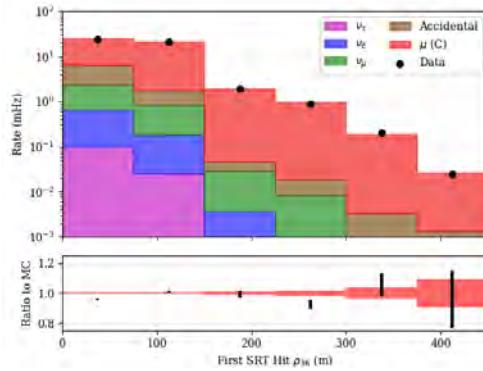


**Figure 7.12** – The radial position of the earliest hit of a cleaned hit series. The radial position is measured relative to string 36, the center of DeepCore.

The Z position of the first hit was used in the GRECO Level 4 cuts in order to identify atmospheric muons coming from above DeepCore. The X and Y position may also be used to identify muons. These are combined to define a *radial distance* ( $\rho_{36}$ ) from the center of DeepCore, here defined to be the position of string 36 at  $(x_0, y_0) = (46.3 \text{ m}, -34.9 \text{ m})$ .

$$\rho_{36} = \sqrt{(x - x_0)^2 + (y - y_0)^2} \quad (7.8)$$

The radial distance is a general parameter and can be used with any event vertex estimator. For the GRECO Level 5, the first hit in the STW+SRT pulse series is used. Atmospheric muons entering DeepCore are more likely to be found at larger values of  $\rho_{36}$  while neutrinos are more likely to be found within the DeepCore fiducial volume, which stops at  $\rho_{36} = 125 \text{ m}$ .

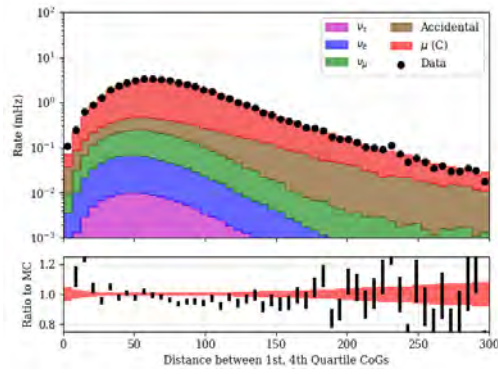


**Figure 7.13** – The distance between the centers of gravity of the first and last quartile in time.

### Quartiles CoG

Atmospheric muons at GRECO Level 5 travel through the detector, leaving an elongated track-like hit pattern. Neutrinos below 100 GeV travel much smaller distances. The apparent distance traveled by a particle is therefore a useful measure of the particle type. In GRECO Level 5, the distance between the CoGs of the first and last quartiles in time are used to characterize the distance traveled by the interacting particle. For atmospheric muon events, this distance is expected to be larger than for low energy neutrino events.

### Z-Travel

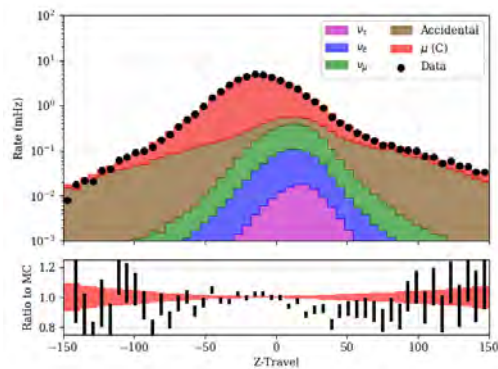


**Figure 7.14** – The distance traveled in Z between the first and last quartile of hits in time.

Because atmospheric muons cannot penetrate the Earth, no background muon events are upgoing. The distance and direction of travel in the Z coordinate can be a useful variable to identify atmospheric muon events. The value, known as the *z-travel*, uses the CoG of the first quartile of hits in time as a starting vertex. Z-travel is the charge weighted average distance in the Z direction of pulses from this vertex

$$\Delta Z = \frac{\sum_i^{pulses} q_i (z_i - z_{CoG})}{\sum_i^{pulses} q_i} \quad (7.9)$$

Atmospheric muons traveling through the detector from above will have a negative z-travel distance and neutrinos may be positive or negative, but is likely to be small due to the small size of neutrino events.

The accidental triggers also are also well-separated from the simulated neutrinos. In the accidental triggers, pulses occur randomly throughout the detector. These events do not have a preferred direction and appear at all values of the z-travel. The accidental events dominate at the tails of the distribution.

## SPE Zenith

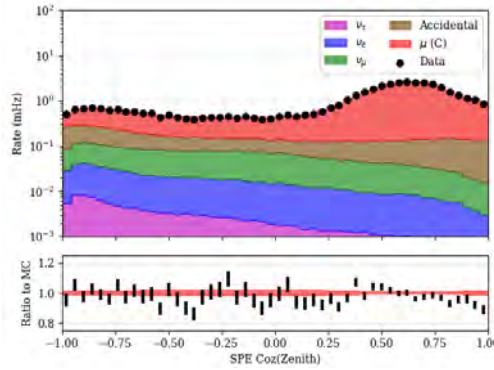


**Figure 7.15** – The zenith angle distribution of events from an 11-iteration SPE fit. The fit assumes an infinite track hypothesis and uses only hit DOMs.

Previous cut levels used the first HLC hit position or various CoG calculations as analytic estimates the properties of particles in each event. These estimators are fast and computationally inexpensive to run on large samples of atmospheric muon background events. At Level 5, the rates are low enough that a *likelihood reconstruction* can be run on the sample, offering additional information about particles in each event.

The *SPE reconstruction* is the first likelihood reconstruction used in the GRECO event selection. This reconstruction includes a model of the effect of scattering in the ice based on the time of the first observed pulse in each DOM.

The minimum time required for a Cherenkov photon to reach a DOM from an emission point is

$$t_{point} = t_{emission} + \frac{n}{c} |\vec{r}| \quad (7.10)$$

where  $|\vec{r}|$  is the distance between the emission point and the DOM. The corresponding time from a muon track is

$$t_{track} = t_{emission} + \frac{\vec{r} \cdot \hat{n} + \rho \tan \theta_C}{c} \quad (7.11)$$

where  $\hat{n}$  is a unit vector pointing in the direction of the muon track,  $\theta_C$  is the Cherenkov angle, and  $\rho = |\vec{r} - (\vec{r} \cdot \hat{n}) \hat{n}|$  is the impact parameter of the track with respect to the DOM [93]. In the absence of scattering, all photons would arrive at the DOM according to these formulae. The addition of scattering delays photons, as they travel a greater distance before reaching the DOM. These delayed photons give a *time residual* distribution.

There is no true analytic form for the timing which includes the effects of scattering, although approximations exist. One such approximation, the Pandel function [112], is used to estimate the time residual distributions as a function of distances between the emission point and the receiving DOM [113].

The Pandel functions may be used to construct a likelihood of the form

$$L(\vec{x}_{vertex}, t_{vertex}, \hat{n}) = \prod_i^{pulses} \frac{dP_{Pandel}(t_i - t_{point} | x_{vertex}, t_{vertex}, \hat{n})}{dt} \quad (7.12)$$

where  $P_{Pandel}$  the Pandel function used to model the distribution of time residuals. This likelihood may be maximized or, equivalently, the negative log-likelihood may be minimized in order to obtain the best-fit values for the position, time, and direction of the track. The likelihood construction assumes an infinite muon track without defined starting and stopping points. Because this construction implicitly assumes that only one photon is received per DOM, this is referred to as the *single photoelectron (SPE)* fit.

The SPE fit is minimized numerically using the simplex method [114]. A total of 11 seeds are used for the SPE fit performed in the GRECO Level 5, each of which differs from the others in direction. The GRECO Level 5 SPE fit uses another SPE fit, performed with only 2 seeds produced during the general IceCube processing at Level 2.

The zenith angle returned by the SPE fit is used in the Level 5 processing. The atmospheric muons are primarily downgoing events. Therefore the direction of the reconstructed track is a useful tool for separating neutrino signal and atmospheric muon background.

## The L5 BDT

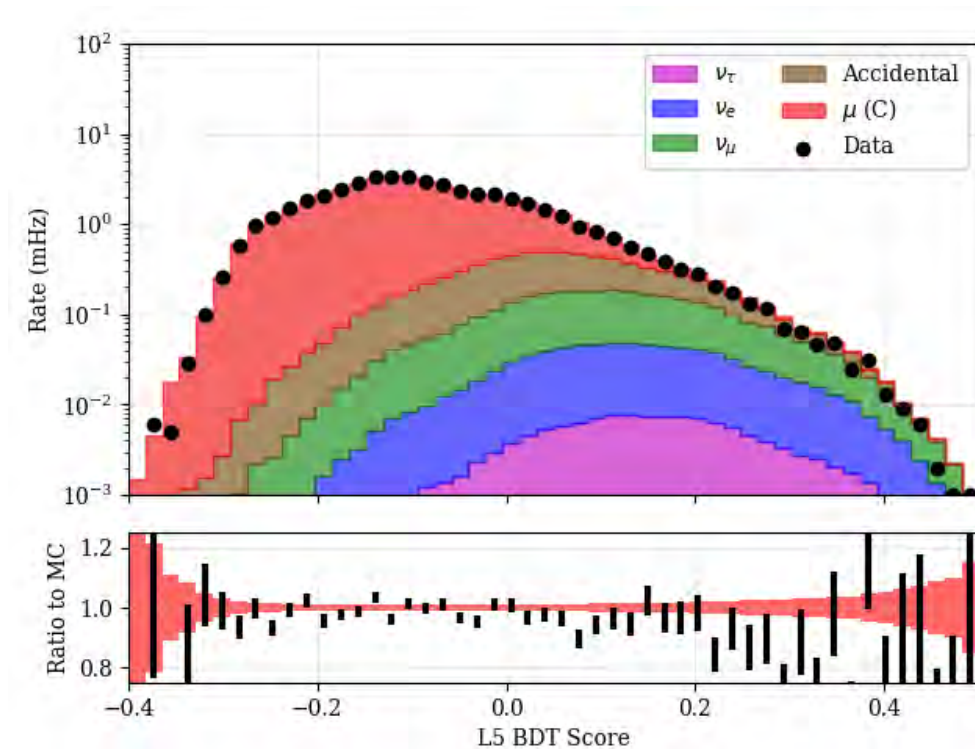


**Figure 7.16** – The distribution of the BDT decision scores used at L5. A burn sample of 14 days is used to test the data. A cut is again applied at 0.04 to remove a significant fraction of atmospheric muon background events.

Type	IceCube Processing			GRECO	
	Any Filter	DC Filter	Low-en L3	L4	L5
CORSIKA	990598	9178	969.82	50.511	4.100
MuonGun	60669	2982	442.50	33.562	3.022
Accidentals	35855	8117	283.560	11.963	1.799
$\nu_e$	1.842	1.721	1.262	0.783	0.544
$\nu_\mu$	11.317	6.360	4.758	2.503	1.629
$\nu_\tau$	0.293	0.270	0.206	0.134	0.103
MC Total*	1026466	17303	1260	65.893	8.176
Data	1154426	19092	1092	68.592	7.422

**Table 7.3** – The event rates after the Level 5 cuts in GRECO. The total simulated rate is calculated using CORSIKA events and ignoring MuonGun. The data rate is estimated from a burn sample of 14 days. Rates are given in mHz.

The six variables described in the GRECO Level 5 are again used to train a BDT. At the time of training, updated versions of both the GENIE and CORSIKA simulations were provided as part of an ongoing upgrade of the IceCube simulation. The L5 BDT was trained using simulation files containing the then-newly available Vuvuzela V1 noise model and an updated version of the GENIE Monte Carlo generator.

A set of fifteen variables were tested. At each step of the training, the least important variable was removed to limit the possible effects of overtraining. The process continued until changes in the cut efficiency larger than 1% were observed, resulting in a BDT containing the six most important variables.

The distribution of BDT decision scores is shown in 7.16. The data and simulation show good agreement in the muon-dominated region. In the signal region, the data statistics is low, but the rates are consistent between data and simulation.

The large number of atmospheric muon events at Level 5 preclude the use of more power likelihood reconstructions. In order to use these additional tools, at least 90% of the atmospheric muon events must be removed from the sample. A cut is placed at a score of 0.04, which gives approximately 95% background rejection with reduction of 30% to all neutrino rates. While this is a significant loss in neutrino events, the reduction in rate reduces the computational burden for the processing at the next cut level.

### 7.5.3 Rates at Level 5

After the GRECO Level 5 cuts, the event rates for the atmospheric muons are a factor of 3x larger than the neutrino flux. The rate from accidental triggers in the detector is comparable to the muon neutrino rate. The tau neutrino rate is more than an order of magnitude smaller than the muon rates, making up less than 2% of the total rate. Additional cuts are needed in order to lower both sets of background below the neutrino rate.

## 7.6 GRECO Level 6 Cuts

Unlike previous levels, the GRECO L6 does not rely on a trained boosted decision tree. The choice was made due to concerns about the significantly limited background simulation. Such a limitation could lead to overtraining, a situation difficult to test with few simulated events.

Two cuts are applied to the sample at GRECO Level 6 for the removal of the remaining accidental triggers. An additional three cuts are applied to reduce the muon background rate.

### 7.6.1 Rejection of Accidental Events at L6

#### Fill-Ratio at L6

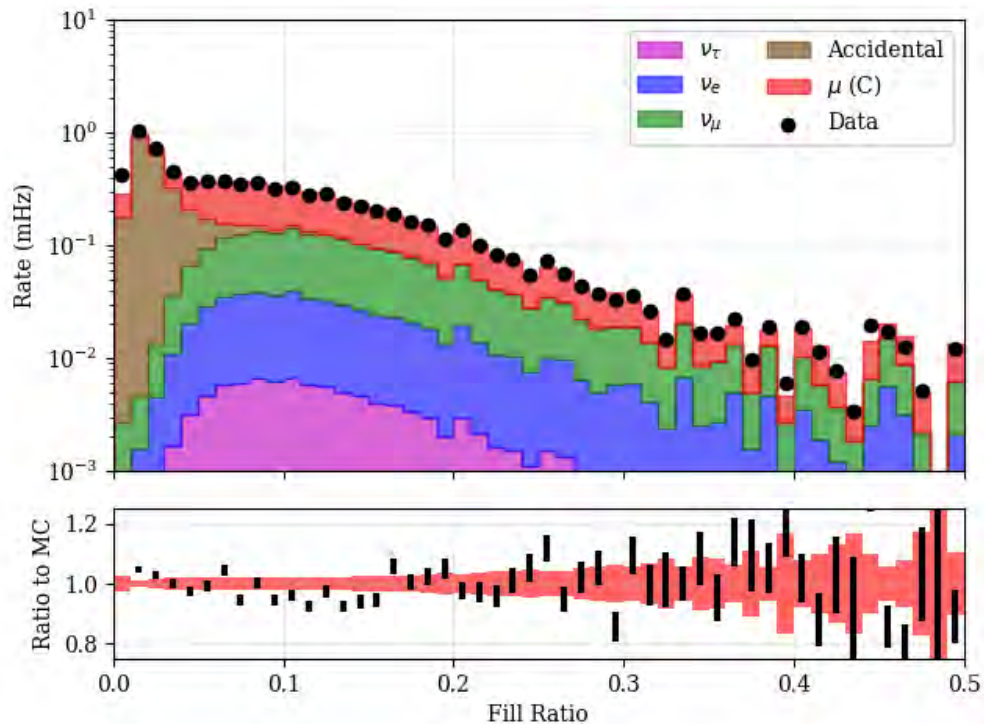


**Figure 7.17** – The fill-ratio distribution. Note the excess of events at low values, a region dominated by the accidental triggers due to detector noise in simulation. A cut is applied at 0.05 to remove these accidental triggers.

After GRECO Level 5, the accidental trigger rate is significantly larger than the expected rate of neutrinos. While the rate of these accidental triggers is low at this stage relative to the rate at L3, they form an important background to the remaining set of neutrino events. In reduce the number of accidental triggers reaching the tau neutrino appearance analysis, two cuts are introduced to separate signal neutrinos from the accidental background.

The first of these cuts, the *fill-ratio*, is a variable typically used in the search for high energy cascades [115, 116] by quantifying the compactness of hits within an event.

Fill-Ratio begins with a reconstructed vertex and pulse series. In the case of the GRECO Level 6, the first hit position in DeepCore within a STW+SRT cleaned pulse series is used as an event vertex. Both the pulse series and the event vertex are used in the fill-ratio calculation.

A radius is computed using the provided information. Many options are available for the calculation of different radii, including calculations using the mean or variance of the distance between the pulses and the vertex, a parametrized radius calculation using the number of hit DOMs, and a calculation using a previously reconstructed energy. Each

configuration was tested in GRECO Level 6 with the calculation using the mean distance from the vertex showing the most promise.

$$r_{Fill-Ratio} = A \left\| \frac{\sum_i^{hits} (\vec{x}_i - \vec{x}_{vertex})}{N_{hitDOMs}} \right\| \quad (7.13)$$

where  $A$  is a configurable scale factor. The algorithm next identifies all DOMs contained within a sphere centered on the provided vertex with a radius of  $\bar{r}_{Fill-Ratio}$ . The fill-ratio value is then given by the ratio of contained DOMs observing a pulse to the total number of contained DOMs.

$$f = \frac{N_{hit}}{N_{DOMs}} \Big|_{\|\vec{r}\| < r_{FR}} \quad (7.14)$$

This results in a measure of the compactness of a hypothetical cascade, where we expect the resulting hit distribution to be approximately spherically symmetric. An approximately spherically symmetric cascade-like event will completely fill the fill-ratio sphere, resulting in a value near 1.0. An extended, track-like event will have hits that are, on average, further from the starting vertex, leading to a large value of  $\bar{f}_{Fill-Ratio}$ , a large number of contained DOMs, and a small value of the fill-ratio.

In the context of high energy events, the fill-ratio provides good separation between cascade-like and track-like events. Fill-ratio has not previously been used in low energy analyses, however, due to the short muon tracks of muon neutrino interactions in the 20 GeV region important for atmospheric oscillations. At GRECO Level 6, fill-ratio has been tested to identify neutrino and atmospheric muon events with no significant separating power observed.

Significant separating power was observed between the neutrino events and accidental triggers, however. The accidental triggers include pulses throughout the detector with no clustering in the event, unlike events caused by muon or neutrino interactions, which typically have some type of clustering of pulses around the interaction position. These events receive a large radius due to this lack of clustering and a correspondingly small value of the fill-ratio. A choice of  $A=1.6$  and the radius calculated using the mean distance between the first hit and all other cleaned pulses gives the separating power shown in Figure 7.17.

The observed separation at a value of 0.05 allows up to one order of magnitude of reduction in the rate of accidental triggers with a relatively small reduction in signal rate of approximately 10%. The use of fill-ratio reduces the number of accidental triggers expected below the neutrino rate.

## The Number of Hit DOMs

The final reconstruction used in this analysis, Pegleg, is discussed in Section 7.7.1. Like the SPE reconstruction used at Level 5, the Pegleg reconstruction requires a minimum number of hit DOMs in order to converge. In order to prepare for the reconstruction performed at GRECO Level 7, events with fewer than 8 hit DOMs in the STW+SRT cleaned DeepCore pulse series are removed from the selection.

The distribution of the number of hit DOMs is shown in Figure 7.18. This removal is performed in order to prepare for the Pegleg reconstruction, but it also removes a significant number of accidental triggers from the selection. The accidental triggers make up about 0.3% of events in the sample following the combination of this cut as and the fill-ratio cut.

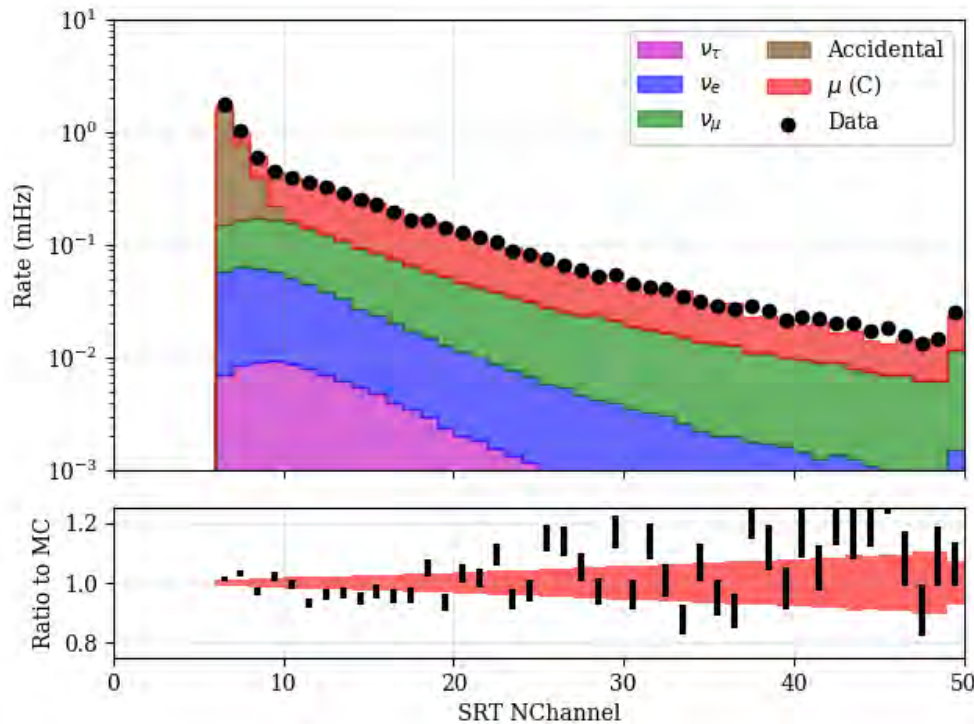


**Figure 7.18** – The number of hit DOMs in the STW+SRT cleaned pulses series at GRECO Level 6. At least 8 hit DOMs are required for the reconstruction performed at GRECO Level 7. Events with fewer than 8 hits are removed during Level 6, coincidentally reducing the number of accidental triggers expected.

## 7.6.2 Rejection of Atmospheric Muon Events at L6 CorridorCut

The remaining atmospheric muon background after the GRECO Level 5 processing show strong selection bias, with few events remaining showing clear tracks in the veto region. In the past, minimum-ionizing muons were discovered to be leaking into the DeepCore fiducial volume along *corridors*, lines connecting the inner part of the detector to the outer edge without crossing any strings. These events pass between strings and leave little trace in the form of identifiable hits in the outer detector. Examples of these corridors are shown in Figure 7.20.

In order to identify these muons, a cut was developed to look along pre-defined corridors for SLC hits correlated with pulses in DeepCore. A CoG of the event is calculated from the STW+SRT cleaned DeepCore pulse series. The string nearest the CoG is used to choose a set of 'corridor' strings to check for the event. The number of hit DOMs found on the corridor strings in an uncleaned pulse series is returned.

Due to the effects of random detector noise, a cut limiting the number of discovered corridor hits to 0 would result in a significant loss of signal events. Instead, one hit is allowed, with two or more discovered DOMs leading to the removal of the event from further processing. At this stage, there are few events due to atmospheric muons with detectable energy in the veto, resulting in the removal of few events. The events removed, however, are dominated by atmospheric muons, as seen in Figure 7.19.

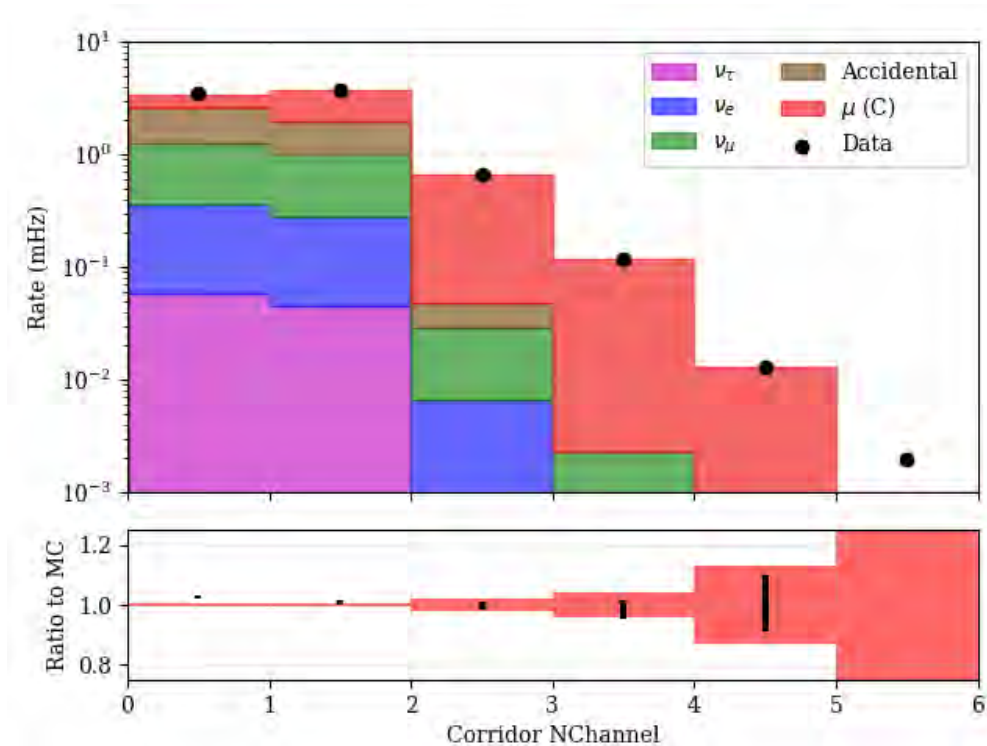


**Figure 7.19** – The number of hit DOMs discovered along one of the various "corridors" in the detector. Events with at least two hit DOMs discovered along a corridor are removed.

### FiniteReco Starting Containment

The SPE reconstruction used in L5 was created using an infinite muon hypothesis. In order to refine this reconstruction, the *FiniteReco* algorithm is employed.

FiniteReco is a module that accepts a previous reconstruction and a given set of pulses [78]. The start and end point of the muon track may be estimated by assuming light is emitted from the track at the Cherenkov angle. FiniteReco does not change the position or direction of the seed track. In the GRECO Level 6 processing, the SPE reconstruction from the Level 5 processing is used as a seed in the FiniteReco reconstruction.

The starting position of the resulting reconstructed particle may be used to estimate the interaction point of the particle. Figure 7.23 shows the position of the reconstructed vertex in terms of depth and distance from string 36. If an event begins outside of the DeepCore fiducial volume, the event is likely to contain a muon and can be removed from the sample. Cuts are applied at the positions shown, resulting in a significant reduction in the number of muon events expected at Final Level.

#### 7.6.3 Rates at Level 6

After the GRECO Level 6 cuts, the sample is dominated by neutrino events. The expected muon rate from CORSIKA simulation makes up 22% of the total sample. The rate from accidental events is also small, with only 5% of events due to random detector noise.

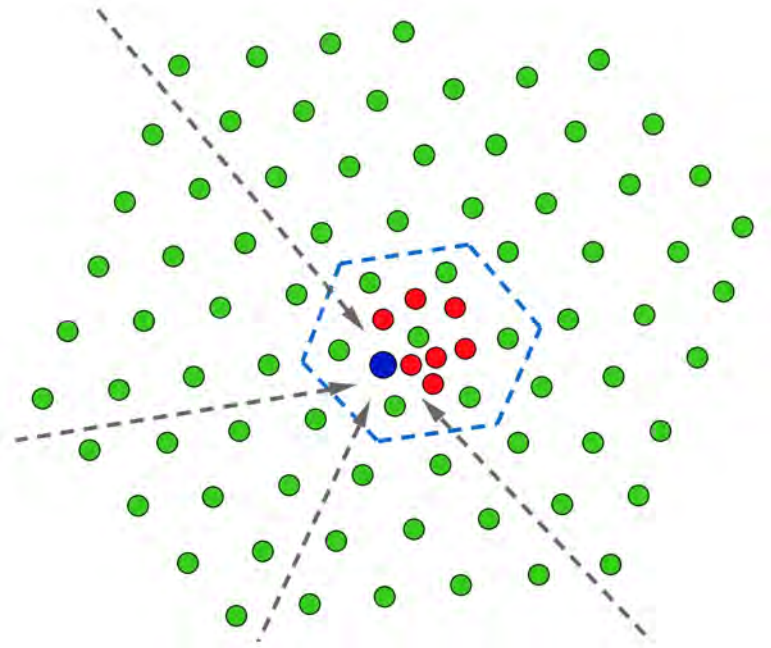


**Figure 7.20** – An example of "corridors" into the DeepCore fiducial volume. Muons may pass into the fiducial volume, outlined in blue, undetected by following the paths indicated by the dashed lines. Image from [117].

Type	IceCube Processing			GRECO		
	Any Filter	DC Filter	Low-en L3	L4	L5	L6
CORSIKA	990598	9178	969.818	50.511	4.100	0.443
MuonGun	60669	2982	442.493	33.562	3.022	0.315
Accidentals	35855	8117	283.559	11.963	1.799	0.102
$\nu_e$	1.842	1.721	1.262	0.783	0.544	0.362
$\nu_\mu$	11.317	6.360	4.758	2.503	1.629	1.011
$\nu_\tau$	0.293	0.270	0.206	0.134	0.103	0.074
MC Total*	1026466	17303	1260	65.893	8.176	1.991
Data	1154426	19092	1092	68.592	7.422	1.841

**Table 7.4** – The event rates after the Level 6 cuts in GRECO. The total simulated rate is calculated using CORSIKA events and ignoring MuonGun. Rates are given in mHz.

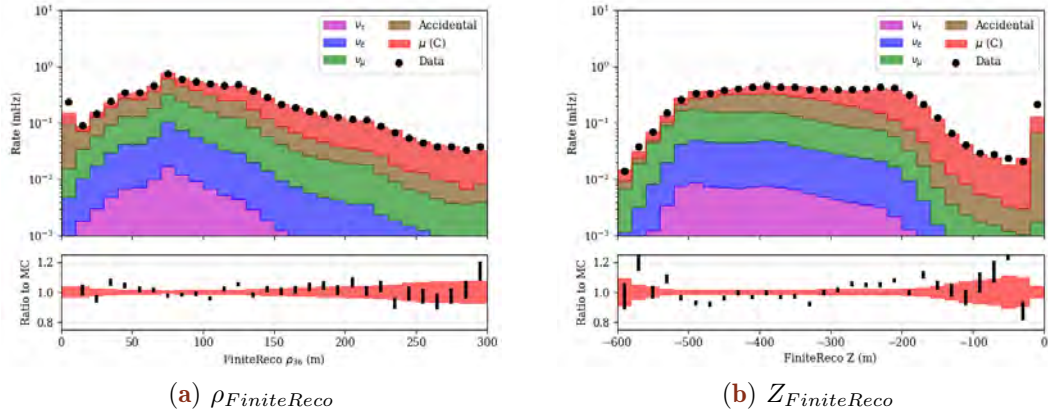


**Figure 7.21** – The FiniteReco containment cuts. Note the excess of muons at the top and outer edge of the DeepCore fiducial volume.

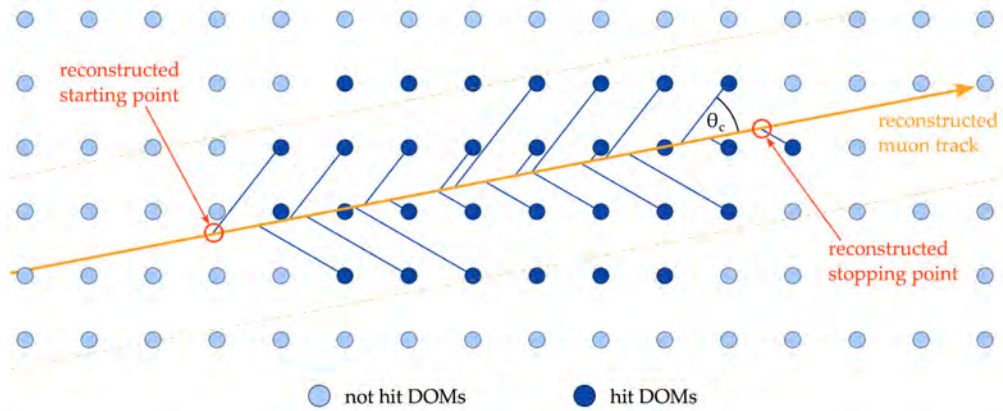


**Figure 7.22** – The FiniteReco starting and endpoint reconstruction method. FiniteReco uses an existing muon track reconstruction and the collection of hit DOMs to estimate the starting and end point of the muon track. Diagram from [78].

## 7.7 GRECO Level 7: Final Level

The Final Level of the GRECO event selection, *GRECO Level 7*, is the most computationally expensive stage of the selection. While previous stages have focused on speed, using cuts based on analytic variables or on fast reconstructions using approximations to the scattering of the ice, the GRECO Level 7 employs the Pegleg reconstruction. This reconstruction is expensive, requiring an average of 10 minutes per event.

The Pegleg reconstruction can be used to define new cuts to further reduce the atmospheric muon rates based on the position of events in the detector.

### 7.7.1 Reconstruction using Pegleg

The *Pegleg* reconstruction [108], a refinement of previous work [117], is a low-energy reconstruction that uses a hybrid cascade+muon hypothesis. The reconstruction returns a total of eight parameters: the position ( $x, y, z$ ), time ( $t$ ), direction ( $\theta, \phi$ ), total energy ( $E_{cascade}$ ) and track length ( $L$ ). The total energy of the event is calculated by assuming the muon track is minimally ionizing with an energy loss of 220 MeV/m in ice [117].

$$E_{total} = E_{cascade} + (220 \text{ MeV/m}) L \quad (7.15)$$

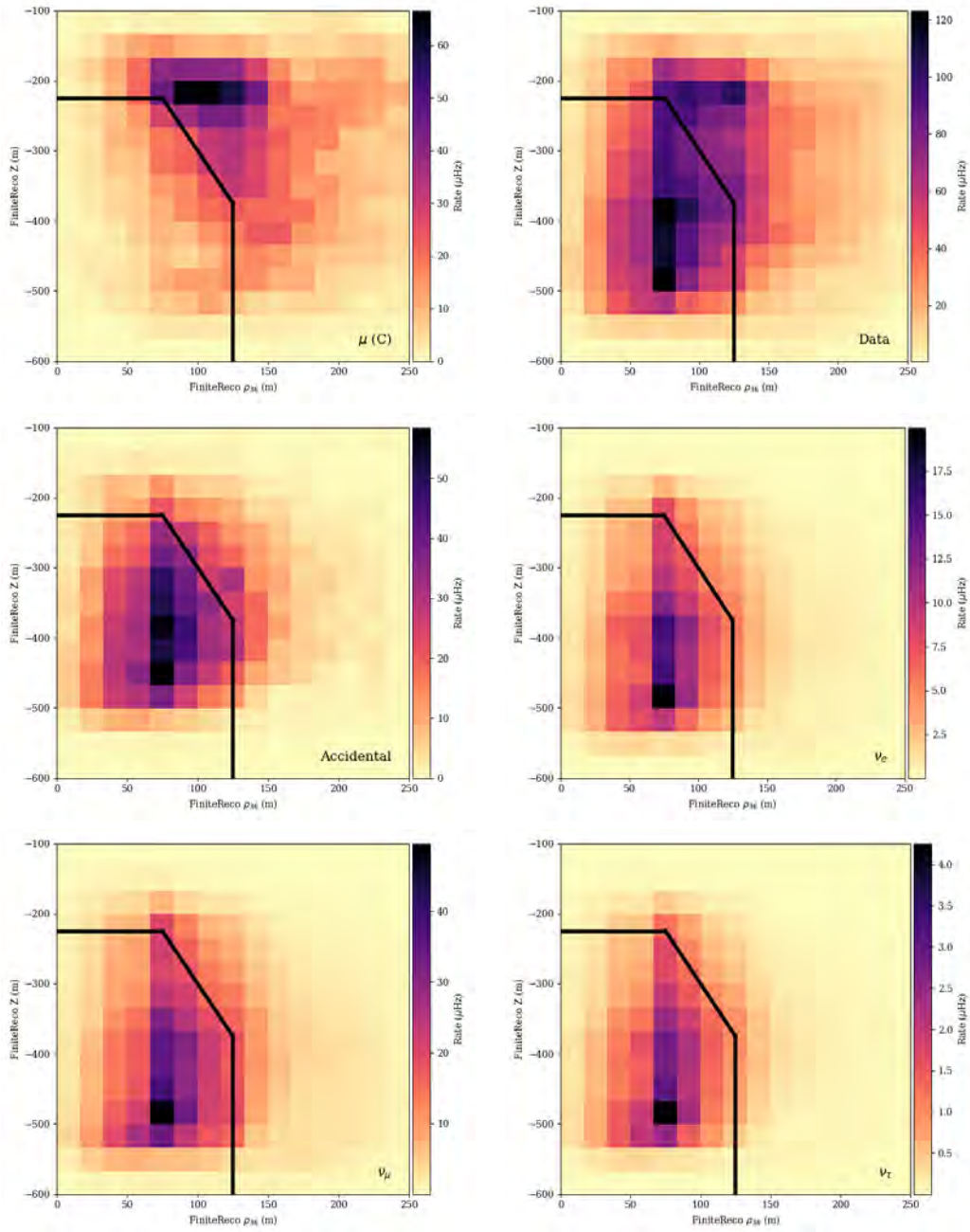


Figure 7.23 – The FiniteReco containment cut for each of the channels. The cut itself is shown with the black line. The atmospheric muons, modeled with the CORSIKA generator, are reconstructed at the top of the DeepCore volume.

The algorithm requires seeds for each of the particle parameters and a collection of hits over which to run. Pegleg also requires a set of splines describing the expected charge as a function of distance from the emission point. These splines are created using the CLSim module (see Section 4.2.2) to directly account for the the scattering and absorption properties of the bulk ice model.

For each particle hypothesis, the event is broken into time steps based on the observed pulses in the event. At each time step, the expected charge at each DOM is calculated based on the energy and position of the particle hypothesis. The charge expectation is evaluated for all DOMs, regardless of whether a hit is observed or not. The total likelihood of the hypothesis is then the product of the likelihoods at each DOM.

The likelihood space itself typically possesses multiple local minima due to the small number of hits. The fit is performed using the MultiNest minimizer package [118] in order to handle the complex likelihood space. The likelihood at each point is used to estimate the underlying likelihood space and produces new hypotheses for testing using importance nested sampling [119].

Given the large dimensionality of the 8D parameter space, significant computational power is required for the fit. Simplifications are introduced to reduce the computational requirements of the Pegleg reconstruction. Track lengths are limited to integer multiples of the track length used to produce the ice model spline functions. While this requirement is lifted in newer versions of the software [108], that change has not yet propagated to the current GRECO events. In addition, only DOMs within 150 m of the current particle position are evaluated to find the expected charge. All other DOMs are assumed to have an expected charge consistent with noise rates. This assumption allows the minimizer to avoid costly calculations of expected charge for distant DOMs at the expense of higher energy event resolutions.

In early versions of the Pegleg fit, the charge of individual pulses is used directly in the likelihood calculations [120]. Following the discoveries discussed in 7.8.2, however, the use of the charge was removed [108]. In the version of Pegleg used in the final version of this analysis, a deadtime window of 45 ns is introduced for each DOM directly following a pulse. During this window, the DOM may not contribute any further information to the fit. This changes the reconstruction likelihood from being on the observed charge to being sensitive only to the observation or absence of charge. Using this modification, disagreements between the data and simulated pulses resulting from mismodeling are be minimized.

### 7.7.2 Containment with Pegleg

With a more refined reconstruction, additional constraints on the containment of the starting vertices are possible. Similar to the work done with FiniteReco at Level 6, the reconstructed  $Z$  and  $\rho_{36}$  receive three cuts as shown in 7.24.

Once again, events at the top of and near the edge of DeepCore are more likely to be muons. An additional cut is applied at the bottom of the detector in order to limit the effect of observed discrepancies between data and simulation. Removing these events results in a 75% reduction of the atmospheric muon background at a cost of approximately 10% of the overall neutrino rate.

### 7.7.3 Other Cuts at L7

Cuts are also applied to the average reconstructed energy per hit DOM and the scatter in the timing distribution of hits, shown together in Figure 7.25. The former is expected to yields high values for events dominated by flaring DOMs (Section 7.8) or events where a particle interaction occurs very close to the face of a DOM. A cut

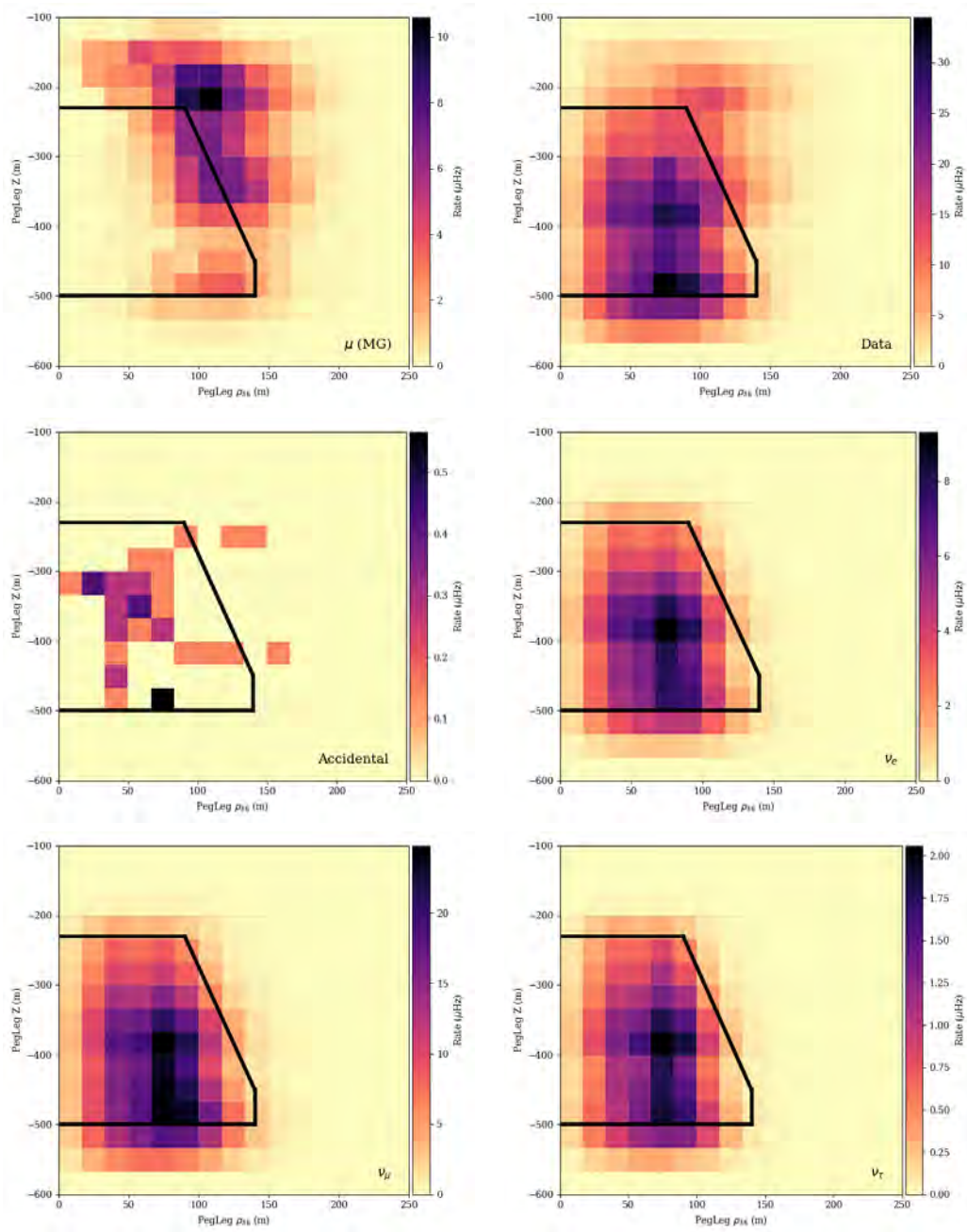


Figure 7.24 – The Pegleg L7 containment cut for each of the channels. The cut is shown with the black line. Note that the atmospheric muons are here represented by the higher-statistics MuonGun sample.

removing events with more than 3 GeV/DOM is applied only to events with fewer than 14 hits, limiting the impact on the neutrino signal events.

The scatter in the hit times is used to identify accidental events, which are not expected to produce hits correlated across DOMs. The cut, which removes events where the standard deviation of the hit times is larger than 800 ns, is also only applied for events with fewer than 14 hits. This limits the loss of neutrino events while removing a fraction of the remaining accidental triggers.

## 7.8 Calibration Discoveries with GRECO

Checks with the GRECO selection during the search for appearance uncovered disagreements between data and simulation. Five discoveries made with the selection are discussed here.

### 7.8.1 The Simulation SPE Templates

During the development of the GRECO selection, new calibration measurements showed that the SPE peak in data was misaligned. This SPE peak, a part of the SPE template described for simulation in Section 4.3.2, is used to convert between the pulses of the waveform, in units of millivolts, and the charge units in IceCube, in units of photoelectrons (*PEs*). The peak is intended to correspond to a value of 1 PE, indicating a single photon interacting at the photocathode of the PMT. While previous measurements had measured an average SPE template for the detector data, the new calibrations were used to measure the templates for individual DOMs.

The updated calibration measurements showed that the SPE peak used in data was not at 1 PE, but was, on average, at 1.045 PE. The IceCube collaboration subsequently corrected the SPE templates for data beginning in the IC86-5 (2015-2016) season, shifting the location of the extracted SPE peak in data from 1.045 PE to 1 PE. The correction is believed to result in a more accurate extraction of the charge in data. The simulation SPE template, shown in Figure 4.3, peaked at 1 PE by definition and was not changed. This shift mirrors effects observed during the fitting of the Vuvuzela V2 model in which a charge scaling variable was introduced to improve agreement with data and simulation (see Section 5.4).

After the correction, analyses searching for high energy neutrinos in the IceCube detector showed improved agreement between data and simulation. Previous analyses searching for oscillations in DeepCore had observed good agreement between data and Monte Carlo simulations prior to the correction to the SPE template in data [79, 80, 81]. In order to evaluate the effect of the correction, the IC86-5 data was processed using the standard GRECO processing scripts.

At low energies, most observed hits are due to single photons reaching the PMT. The average charge per DOM is therefore expected to approximately follow the SPE template. This variable was used to evaluate the effects of the correction at Level 7 of the GRECO selection.

The result is shown in Figure 7.26. As expected, the 2015 data shows a shift downward, with a peak closer to 1 PE. Unexpectedly, however, the corrected dataset shows substantial disagreement with simulated events.

Investigations of the disagreement showed that the data and simulation disagreed at all cut levels, including low cut levels unrelated to the GRECO selection. The issue has been identified to be the SPE templates used in the simulation. The template used is calculated as the average of 118 DOMs measured in the lab prior to deployment [104].

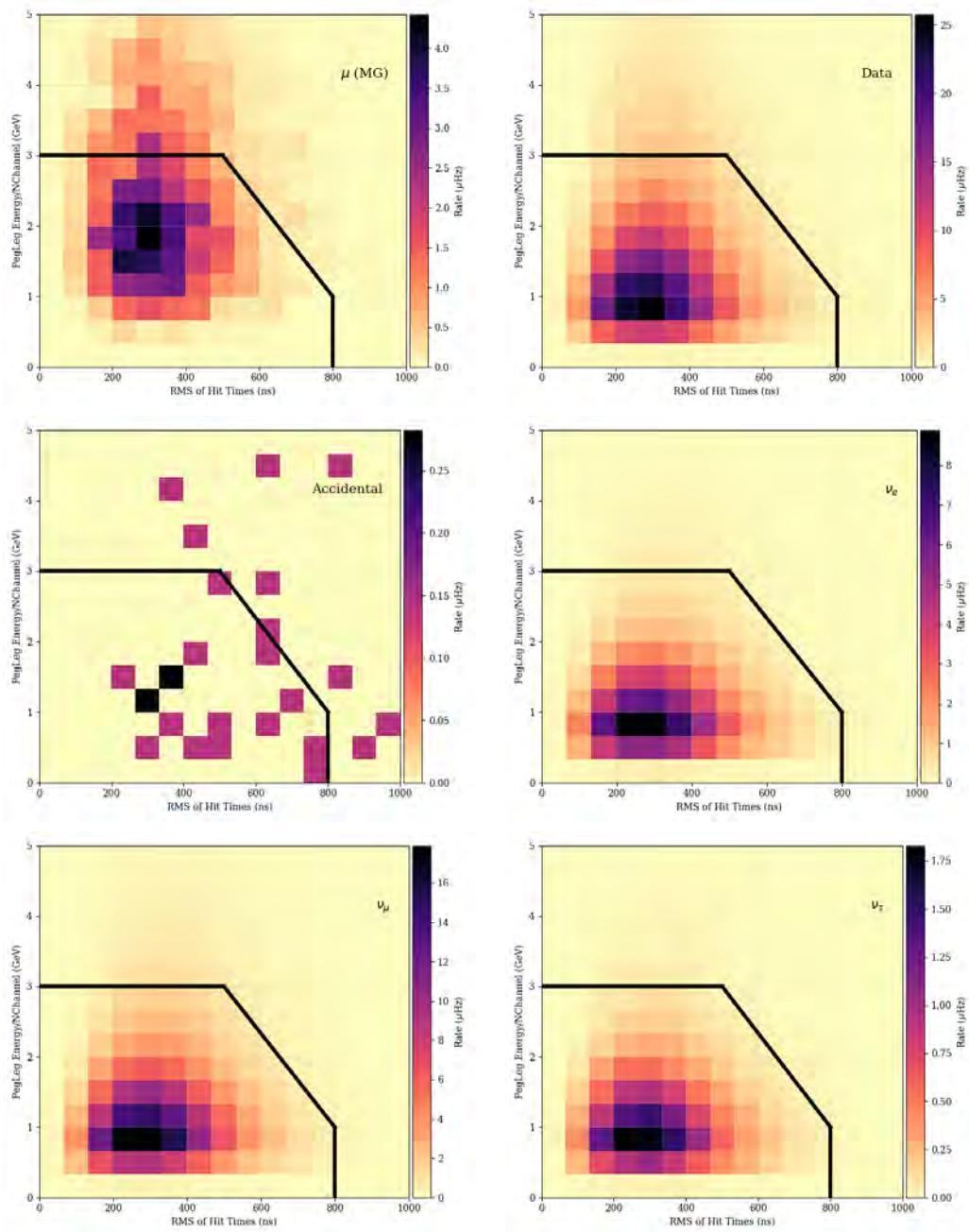


**Figure 7.25** – The cuts applied to the reconstructed energy per hit DOM and the standard deviation in the hit times. The cuts are designed to remove atmospheric muons and highly scattered events from the selection. The 2D cut shown here is applied only to events with fewer than 14 hit DOMs.

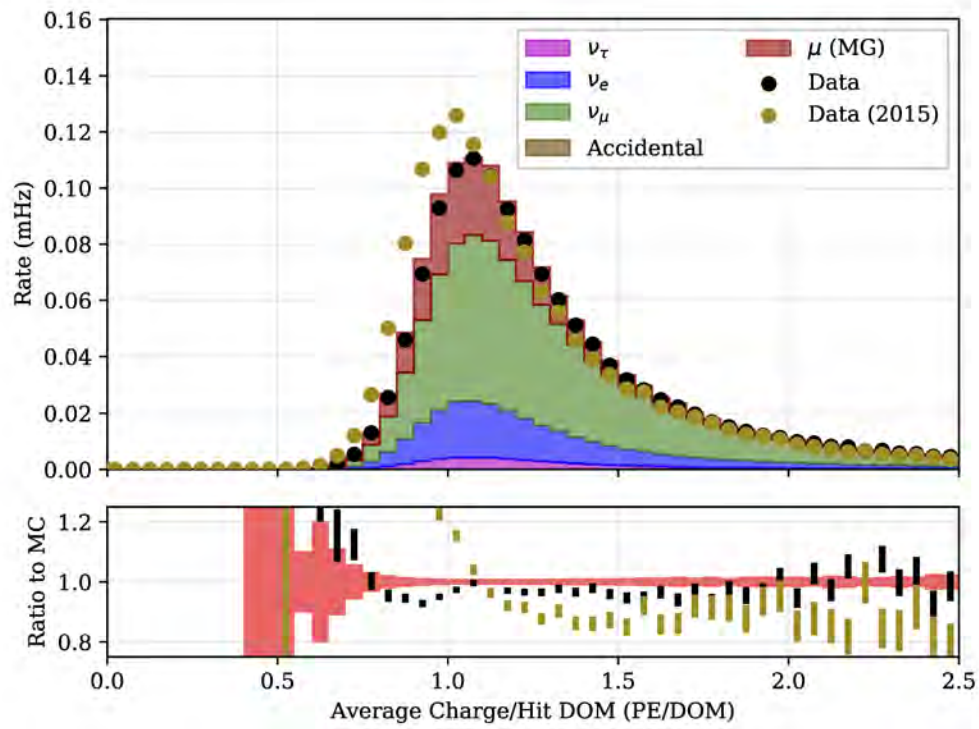


**Figure 7.26** – The effects of the SPE correction applied to data in 2015. As expected, the peak of the distribution is closer to 1 PE in the corrected 2015 data (gold circles) than in previous years (black circles). While the simulation showed good agreement with the data taken prior to the recalibration of the SPE peak, the recalibrated data shows marked disagreement. Investigations into this anomaly showed that the SPE templated used in simulation does not accurately model our data.

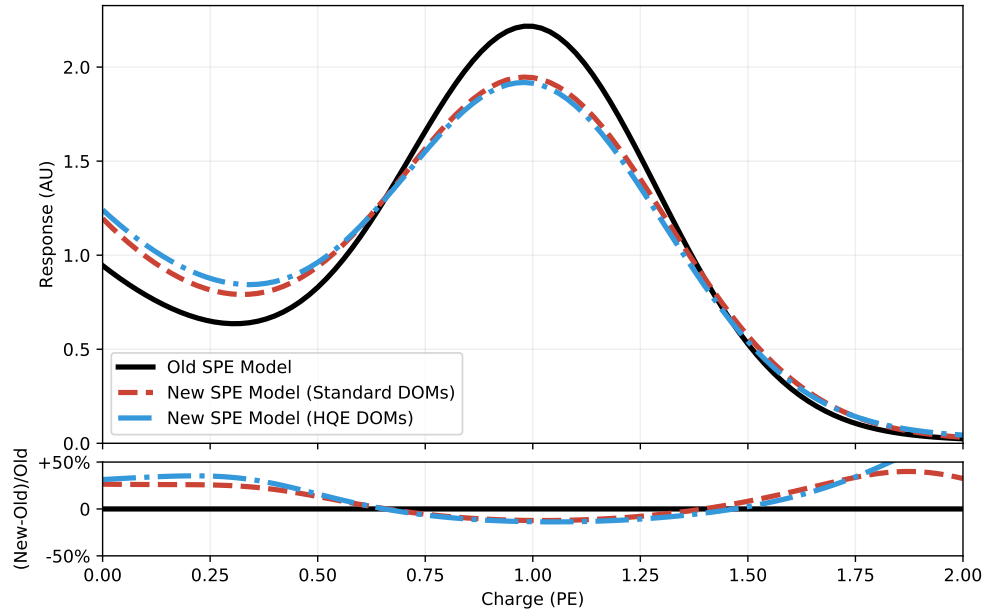


**Figure 7.27** – A comparison of the old SPE template previously used in the simulation of events to the new average templates for the high quantum efficiency DOMs and the standard IceCube DOMs. The new models predict a higher number of pulses with low charge, consistent with the excess observed from the corrected 2015 data in Figure 7.26.

New work has been performed to apply the SPE templates measured in the data calibrations to the Monte Carlo simulation for all DOMs in the detector. The new templates, shown in Figure 7.27, predict more hits with low charges, as observed in the 2015 data of Figure 7.26.

Due to time constraints, the updated simulation has not been evaluated in the GRECO sample. In order to reduce the potential disagreement arising between data and simulation due to mismodeled low charges, both the data and simulation have been processed with a version of the Pegleg reconstruction designed to limit the dependence on charge information.

### 7.8.2 Disagreement in PMT Simulation

While investigating charge variables related to the SPE template, additional disagreements were discovered in the PMT simulation. The first suspected cause of charge disagreements was erroneous splitting of the waveform during charge extraction.

The SPE template is used to convert the digitized waveforms from the FADC and ATWD into reconstructed photoelectrons consisting of charge and timing information. While the simulated response is known exactly when extracting pulses, the associated charge response of the DOM in data requires calibration. Using a mismodeled charge response to extract pulses in the data can result in single photoelectrons being erroneously split into multiple smaller reconstructed pulses.

Potential mismodeling effects of the charge extraction were checked in Figure 7.28. In these figures, the charge of each pulse is shown as a function of the measured time of the pulse, which is normalized to the time of the largest extracted pulse in the DOM for each event.

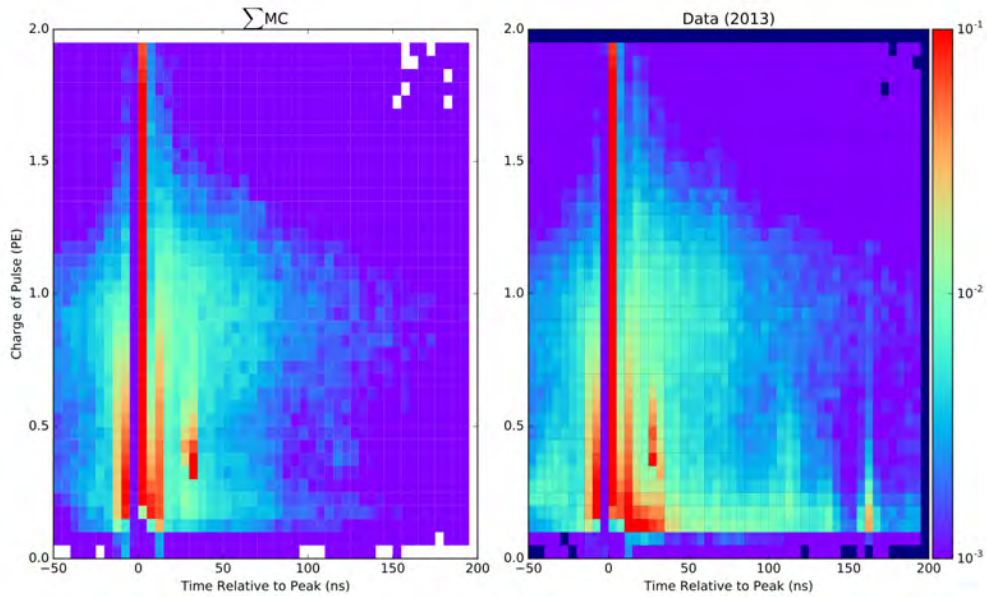


**Figure 7.28** – A comparison of the charge extraction in data and simulation at GRECO L7. Both the time and charge are shown for individual pulses on all DOMs. The time is measured relative to the largest pulse observed on each DOM during an event. The data and simulation histograms are independently normalized to 1.0. While the two show broad agreement, notable differences occur at low charge.

The erroneously split pulses are visible in data as a low-charge tail from  $t=0$  ns until  $t=50$  ns. In addition to this effect, however, many other regions of disagreement are visible. In data, there appear to be a significant number of prepulses not visible in the simulation occurring between  $t=-50$  ns and  $t=-20$  ns. The structure of the late pulses, appearing with approximately 0.4 PE of charge and at time  $t=30$  ns also appears notably different between the data and simulation. A final set of pulses, occurring at 160 ns, also appears to be unsimulated. All of the unsimulated features occur with charges less than 0.5 PE, a region strongly affected by the recalibration of the SPE templates.

These features remain unexplained. These may be the result of improper calibration of the PMTs, an incorrect SPE template used for charge extraction, or completely unknown effects.

It is currently unclear of the impact of the unsimulated features in analyses. Each feature occurs at low charge and is not expected to contribute a significant fraction of the total charge of an event. This timing structure requires additional calibration resources to identify and better simulate, the scope of which is beyond this work. Regardless, the presence of unsimulated features indicates that at least some charge information in the simulation is an unreliable model of the data.

Charge information is used at many levels of the GRECO selection. In order to excise charge from the selection, more than half of the variables used in the selection would need to be updated. Each of these charge-related variables individually shows reasonable agreement between data and simulation.

In light of the existing agreement between data and simulation, and without a firm timescale for the correction and reproduction of new Monte Carlo sets, the decision was made to move forward with the GRECO analysis without changes to earlier cuts. At

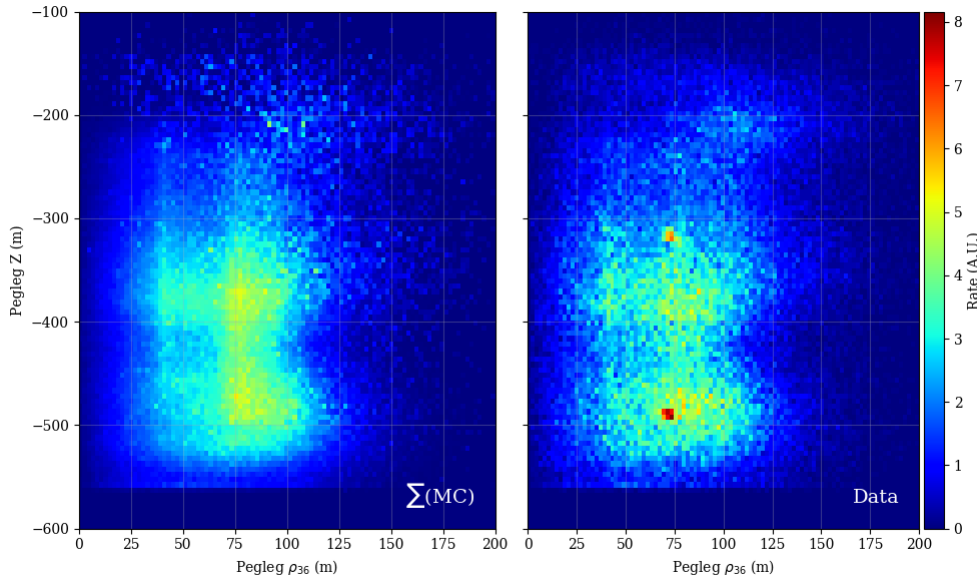


**Figure 7.29** – The reconstructed Z position plotted against the reconstructed distance from string 36. The L7 cuts from GRECO have been removed for this plot. The colorbars in both plots have been normalized to be identical. The data and simulation show good agreement except for two points in the data, near  $\rho_{36} = 75$  at depths of -310 and -490.

Level 7, the observed disagreements in the pulses and the SPE templates led to the removal of charge information from the Pegleg reconstruction.

### 7.8.3 Discovery of Flaring DOMs

Uncertainties in the ice model can lead to significant disagreements between data and simulation. The existing uncertainties on the bulk ice assume that the coefficients for all ice layers are fully correlated. However, it is possible that the ice model coefficients in parts of the detector are more poorly modeled than others. By looking at the event rate in data and simulation as a function of the depth and position in the detector, discrepancies in the ice model may be identified.

Two-dimensional histograms of the depth and radial distance also show systematic disagreement in some regions, as shown in Figure 7.29. These excess events appear to occur on a single string, string 83, shown in Figure 7.30, indicating an effect occurring due to the DOM hardware in the detector.

Follow-up work has shown that these DOMs, known here as *flaring DOMs*, appear to spontaneously emit light for unknown reasons. The light output is identifiable both based on the position of the hits and the amount of charge observed in nearby DOMs. These spurious events, first discovered in the GRECO selection, have since spawned dedicated searches to better understand spontaneous light emission from the DOMs. A small handful of DOMs have been identified by these searches with emission times as frequent as 1 Hz.

The affected events may be identified based on the charge profiles. DOMs directly adjacent to the emitting DOM observe a significant fraction of the total charge of the event. This may be characterized using the 'charge RMS' of the event

$$q_{RMS} = \frac{\sigma_q}{\sum_{hits} q_i} \quad (7.16)$$

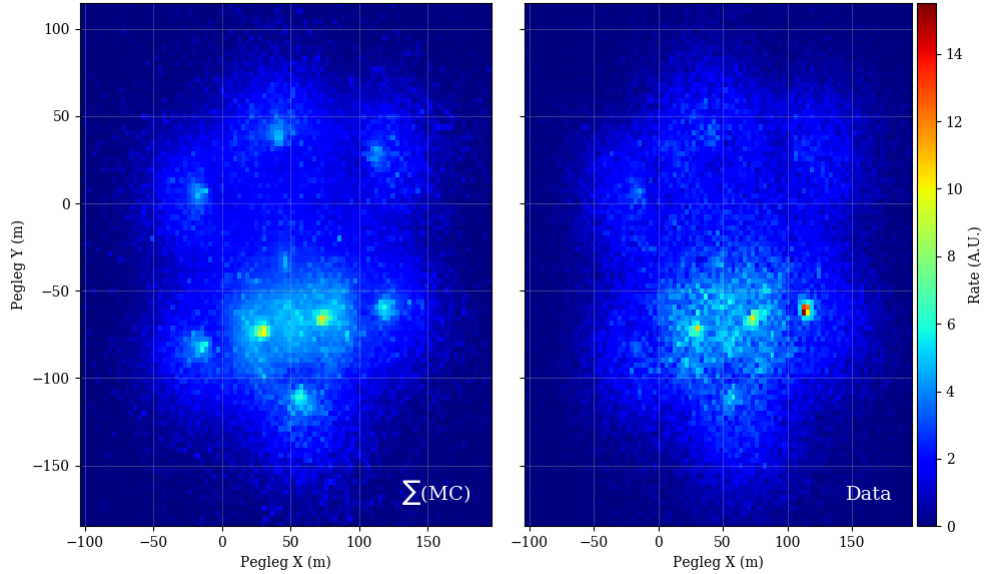


**Figure 7.30** – The reconstructed X position and Y position of events in the detector. The L7 cuts from GRECO have been removed for this plot. The colorbars in both plots have been normalized to be identical. Once again, reasonable agreement is observed in most regions, although data events have a clear excess near  $x=110$  m,  $y=-60$  m. This position corresponds to string 83.

This is shown in Figure 7.31. Events with a  $q_{RMS} > 0.85$  are cut from the analysis, removing the most obvious spurious events. A total of 975 events are removed from the GRECO data, resulting in a total reduction of 1.3% of the event sample. The removal of these events in data and simulation does not significantly impact the sample due to the low event rates involved.

#### 7.8.4 Simulation of Bedrock

Further investigations of the reconstructed Z position from Pegleg uncovered disagreements, shown in Figure 7.32. A small deficit of events in data is observed at  $Z \approx -450$ . Checks performed with other samples have shown similar disagreements at these depths, indicating disagreement in the ice model. Previously unblinded oscillation samples showing this issue have not observed significant issues in the goodness-of-fit. New ice models are underway with dedicated work to fix this region is underway.

Near the bottom of the detector, a clear excess of events in data indicated a mismodeling in the simulation. Events which interact below the detector typically require higher energies than those inside the fiducial volume in order to trigger DeepCore.

In the GRECO selection, events with energies above 1 TeV are modeled using NuGen simulation in order to account for events not properly simulated in the GENIE generator. Previous investigations have shown that the two generators use similar models of the cross-section and return similar event rates at low levels. The events from the NuGen generator were shown to make up a significant fraction of the high energy tail in the GRECO sample. These events were therefore checked for potential issues.

The NuGen and GENIE simulated event samples are merged in the GRECO analyses after removing NuGen events in overlapping energy ranges. The generated samples do include these overlapping regions, however. For the purposes of testing, the full sample of GENIE and NuGen events were compared in true and reconstructed energy and Z position.

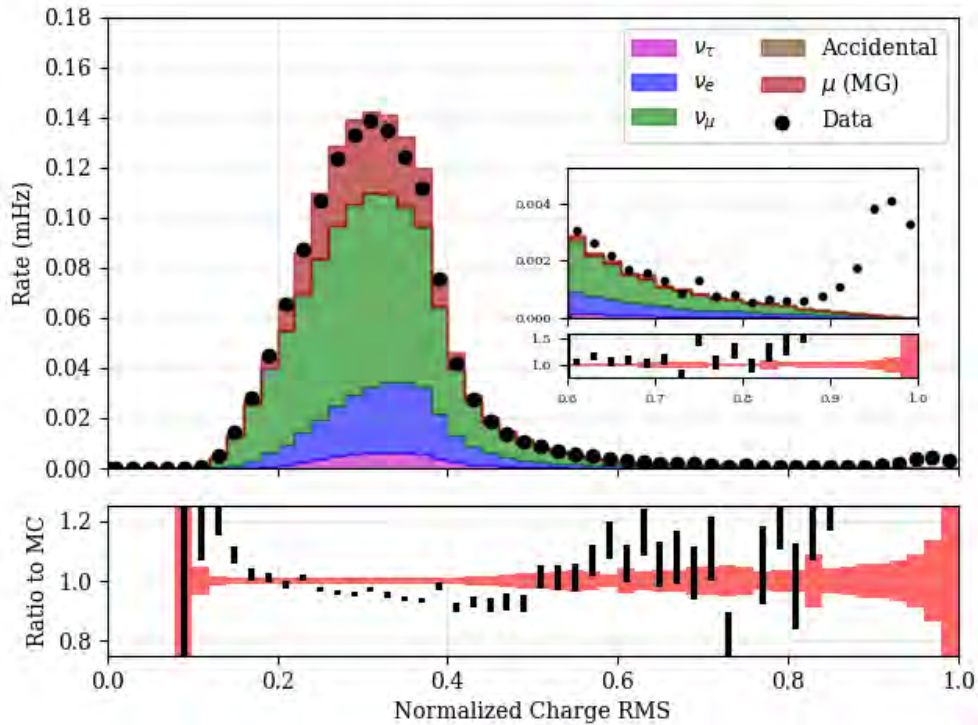


**Figure 7.31** – The RMS of the charges within each event at Final Level. The value of the RMS is normalized using the total charge observed. The events with flaring DOMs cluster at high values of the charge RMS, visible in the inset.

A comparison of the overlapping energy range of NuGen and GENIE events contained within the DeepCore fiducial volume showed some disagreement in the muon neutrino event sample. Figure 7.33 shows no disagreement in the neutral current and electron neutrino charged current events, indicating an effect specific to the muon neutrinos.

Limiting the energy range of both samples to the overlapping region 100-1000 GeV, other distributions may be checked. The cause of the discrepancy between the generators is shown in Figure 7.34. The two generators show broad agreement until a depth of approximately -830 m, corresponding to the interface between the Antarctic glacier and the underlying bedrock. In the GRECO selection, only events with an outgoing muon have the range necessary to reach DeepCore from the bedrock.

Further checks discovered the issue in IceCube’s implementation of the GENIE generator. When calculating the interaction probability for the neutrino interactions, the density of material is included. In the implementation of GENIE previously used by the IceCube collaboration, events were assumed to occur solely within or near the fiducial volume of DeepCore due to the low energies involved. The bedrock was therefore deemed unnecessary and not implemented in favor of assuming a uniform density of ice throughout the simulation volume. During initial implementation, the GENIE generator was planned for use up to 100 GeV due to technical limitations. Later work expanded this range up to 1 TeV with future work ongoing to push toward 10 TeV. The problems with the bedrock were mistakenly overlooked during the upgrades of the generator, leading to the systematic disagreement shown in Figure 7.32.

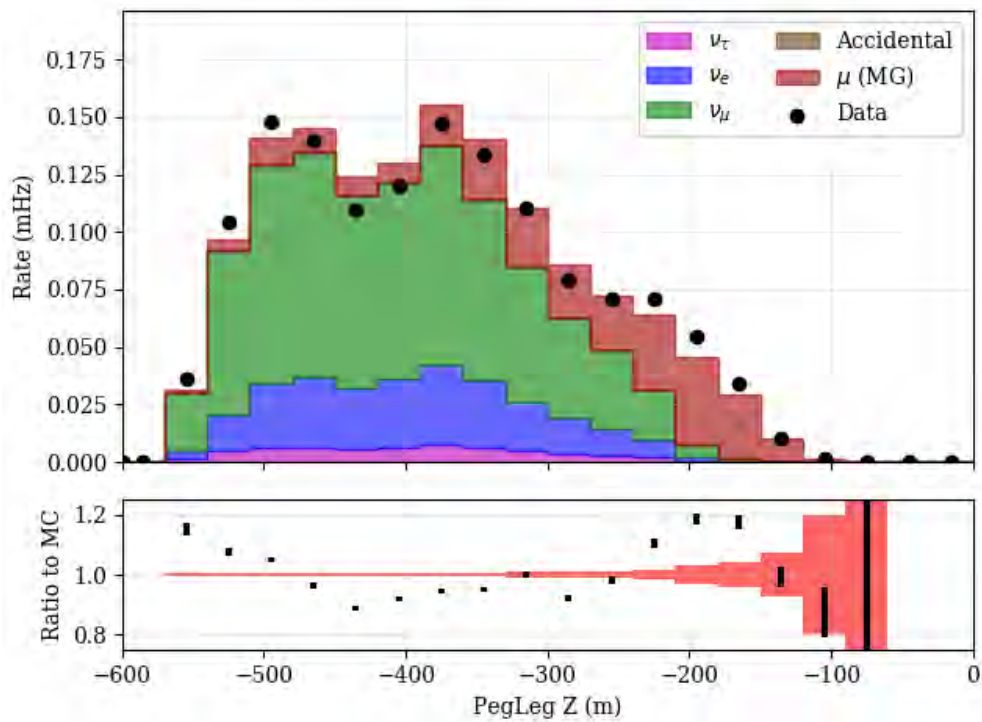


**Figure 7.32** – The reconstructed Z position using Pegleg. The GRECO L7 cuts have not been applied in order to show discrepancies below the detector. Noticeable disagreement is seen below the detector at a depth of -500 m. Additional disagreements are also visible at the top of DeepCore, a region dominated by atmospheric muons.

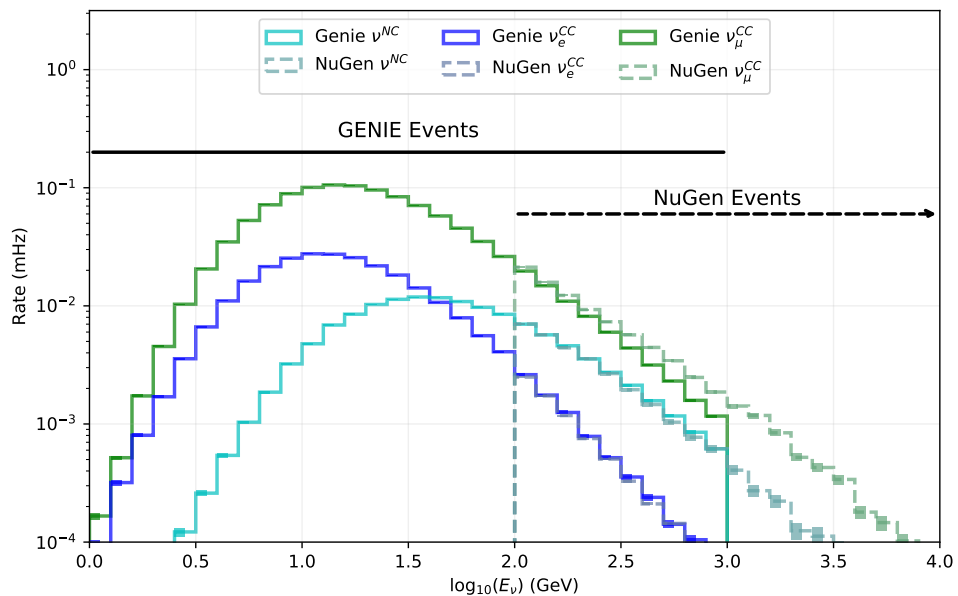


**Figure 7.33** – The NuGen and GENIE true energy spectra at Final Level. The neutrinos are shown without oscillations applied. The overlapping energy range, 100-1000 GeV, show good agreement between the two generators for neutral current and electron neutrino charged current interactions. The muon neutrinos disagree in the overlapping energy range.

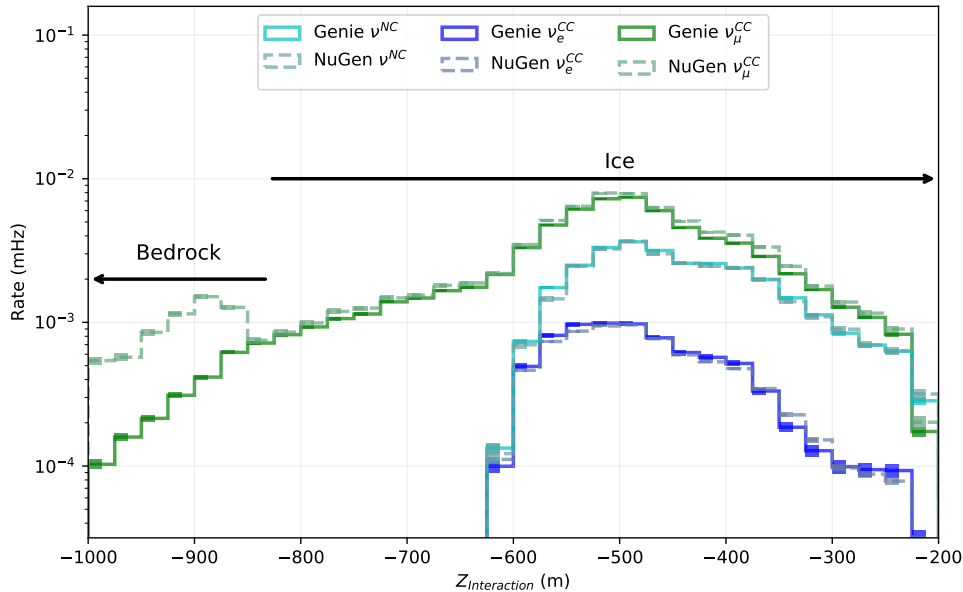


**Figure 7.34** – The NuGen and GENIE interaction depths at Final Level. Only events from the overlapping region of 100 GeV to 1 TeV are included. NuGen and GENIE agree above -830 m. The implementation of the GENIE generator in IceCube does not correctly model the bedrock at  $Z < -830$  m.

The bedrock has been properly included in both the NuGen generator as well as the PROPOSAL module for propagating the charged leptons. GENIE events therefore suffer solely from an incorrect interaction probability due to the discovered bug.

In order to limit other potential issues from the bedrock, the analysis space was restricted, removing events below the bottom of the detector ( $Z_{reco} \leq -500$ ). This cut significantly reduces the size of the sample by reducing the high energy events included at Final Level. The additional cut has some impact on the expected sensitivity, but was deemed necessary to minimize the potential impact of systematics issues associated with the bedrock events.

### 7.8.5 Anisotropy of DeepCore

The reconstructed zenith and energy are used in the search for appearance. The azimuthal direction is not used for oscillation searches, but was checked for agreement.

As described in Section 3.4, the anisotropy of the ice model can bias the propagation of light in the detector in the azimuthal direction. This can result in azimuthally biased reconstructions. The anisotropy is simulated using a direction and magnitude, both of which are used to model the effect throughout the detector. The IceCube simulation assumes that the anisotropy is independent of depth.

The reconstructed azimuthal directions from Pegleg in the GRECO sample is shown in Figure 7.35. Both data and the simulated events show sinusoidal variation as a function of azimuthal direction, a result of the anisotropy in the ice. The effect in data is stronger than in simulation, indicating that the average anisotropy of the DeepCore fiducial region is stronger than assumed for DeepCore.

The observed azimuthal disagreement of GRECO are the first hint that the anisotropy of the ice may not be uniform throughout the detector volume. New calibration measurements to incorporate these new properties into the simulation are underway. Because

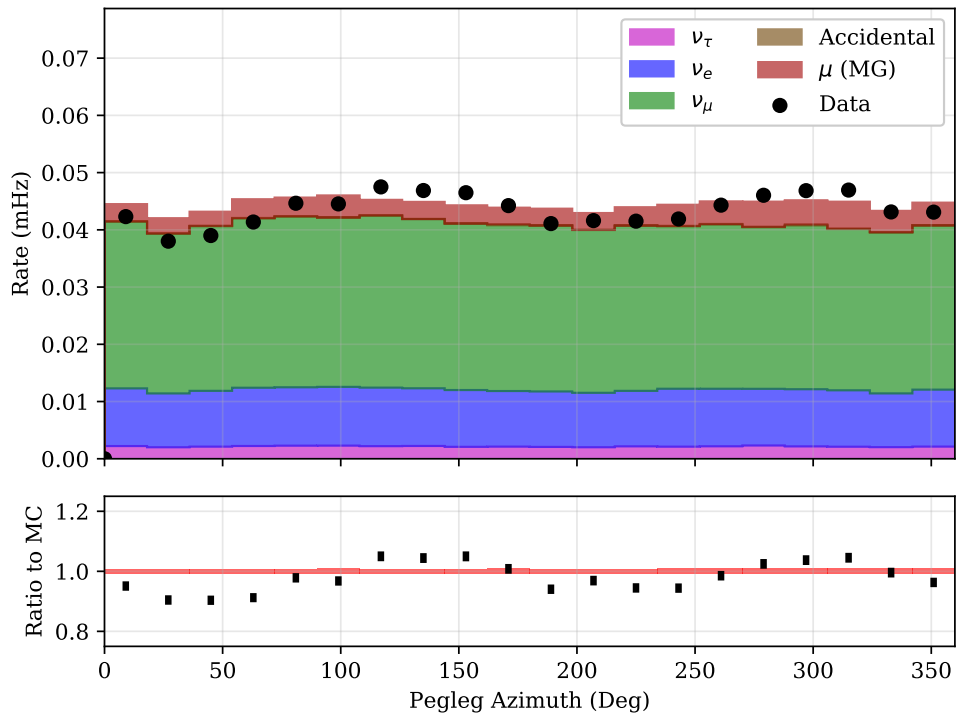


**Figure 7.35** – The reconstructed azimuthal direction from the Pegleg reconstruction at GRECO Level 7. The data and simulation have been scaled to the same rate. A variation as a function of azimuthal angle is seen in both the simulated events and data, although the effect is stronger in data.

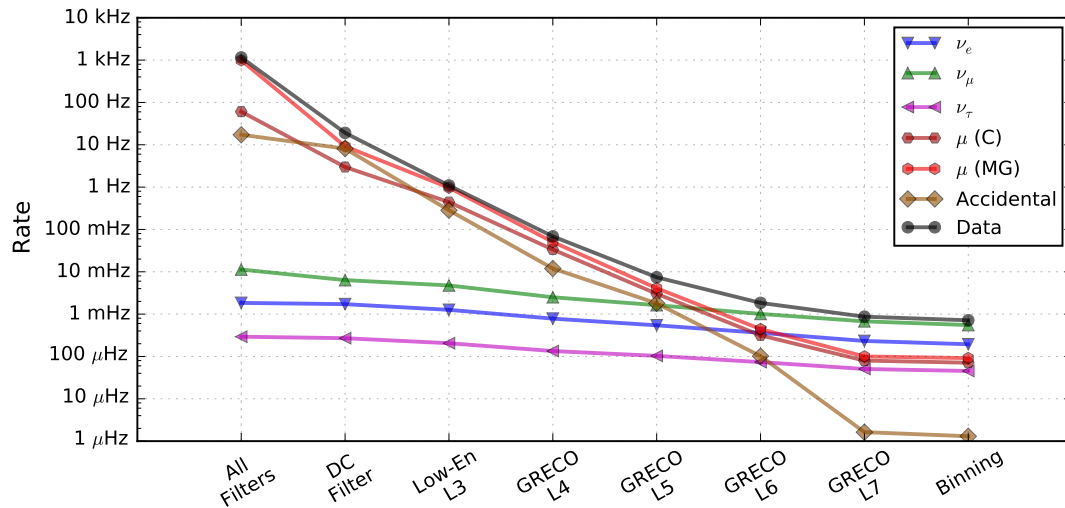


**Figure 7.36** – The rates at each cut level. The muon and accidental trigger rate drops from around 18 Hz after the DeepCoreFilter to less than 1 mHz at Final Level.

the anisotropy is not expected to directly impact the oscillation analysis, no additional cuts are introduced to the sample.

## 7.9 The Properties of the GRECO Event Selection

The completion of cuts yields the completed GRECO event selection. The rates of each simulation sample and of data are shown numerically in Table 7.5 or graphically in Figure 7.36. Also included is the analysis binning as described in Section ?? for reference.

The sample is dominated by atmospheric muon neutrinos. The major source of statistical uncertainty, shown in Table 7.6, is the atmospheric muons.

### 7.9.1 Selecting Runs from Data

Runs were selected from data to be used in the search for tau neutrino appearance based on four criteria:

**Inlce OK** Runs must not contain light from LEDs or other calibration devices

**All Strings** All 86 strings must have been taking data

**All DOMs** At least 5030 DOMs must be active during the entire run

**Full Runs** The run must be between 7 and 9 hours long.

These conditions were used to identify "good" runs between May 2012 and April of 2015. A total of 968 days of detector data were selected resulting in 62406 events.

### 7.9.2 Energy and Zenith Reach

The GRECO sample covers a wide range of energies, with some Final Level events possessing energies as low as 2 GeV or as high as 1 TeV. The bulk of the neutrino sample, shown in 7.37, occurs at the expected oscillation minimum near 25 GeV. Most neutrino events originate at the horizon, as expected from the atmospheric neutrino flux, although there exists an asymmetry between the upward- and downward-going events.

Type	IceCube Processing				GRECO			Analysis Binning
	Any Filter	DC Filter	Low-en L3	L4	L5	L6	L7	
CORSIKA	990598	9178	969.818	50.511	4.100	0.443	0.100	0.092
MuonGun	60669	2982	442.493	33.562	3.022	0.315	0.080	0.07
Accidentals	35855	8117	283.559	11.963	1.799	0.102	0.002	0.001
$\nu_e$	1.842	1.721	1.262	0.783	0.544	0.362	0.325	0.194
$\nu_\mu$	11.317	6.360	4.758	2.503	1.629	1.011	0.676	0.552
$\nu_\tau$	0.293	0.270	0.206	0.134	0.103	0.074	0.051	0.045
MC Total*	1026466	17303	1260	65.893	8.176	1.991	1.153	0.884
Data	1154426	19092	1092	68.592	7.422	1.841	0.871	0.715

**Table 7.5** – The event rates at each cut level in the GRECO selection. Note that the MuonGun events are included in this table, but do not contribute to the total Monte Carlo expectation to prevent double-counting of muon events from the CORSIKA sample. All rates are given in millihertz.

	Simulated Events	Weighted Rate (Events)	Uncertainty (Events)
$\nu_e$	333892	12708	26
$\nu_\mu$	842386	36134	45
$\nu_\tau$	122765	2970	13
MuonGun	2486	4651	102
Accidentals	12	85	25

**Table 7.6** – The statistical uncertainties at GRECO Final Level. The sample is dominated by neutrinos, but the largest contributions to the statistical uncertainty are due to limited statistics in MuonGun and accidental triggers. The event rates are scaled to the approximate number of events in data with an effective livetime of 2.3 years.

This asymmetry originates from the event selection, which selects against downward-going events in order to minimize the atmospheric muon background.

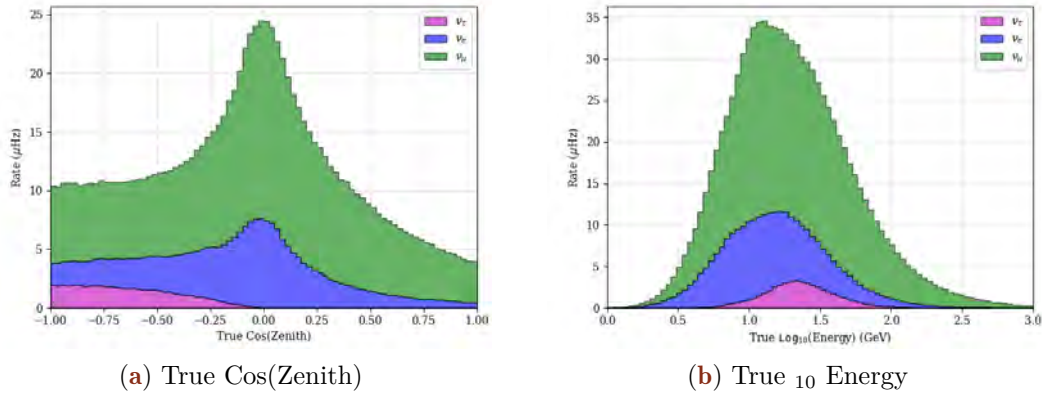


**Figure 7.37** – The true neutrino energy and zenith of the GRECO sample at Final Level. The sample shows an asymmetry between upgoing ( $\cos(\theta) < 0$ ) and downgoing ( $\cos(\theta) > 0$ ) event rates in the neutrinos due to selection bias. The sample has a long tail of events at both high and low energies. Using the NuFit 2.2 oscillation parameters and the flux model from Honda, the  $\nu_\tau$  events are observed in the very upgoing region around  $10^{1.4} = 25$  GeV.

### 7.9.3 Reconstructed Variables

The true variables of the neutrino distributions are not observables in most GRECO analyses. All events are described using the reconstructed energies and zenith angles from the Pegleg reconstruction, shown in Figure 7.38. The  $\nu_\tau$  sample reconstructs to slightly lower energies due to the loss in energy from the outgoing neutrino. The sample, when compared to data, shows reasonable shape agreement in both energy and zenith, although systematic disagreements occur above 100 GeV.

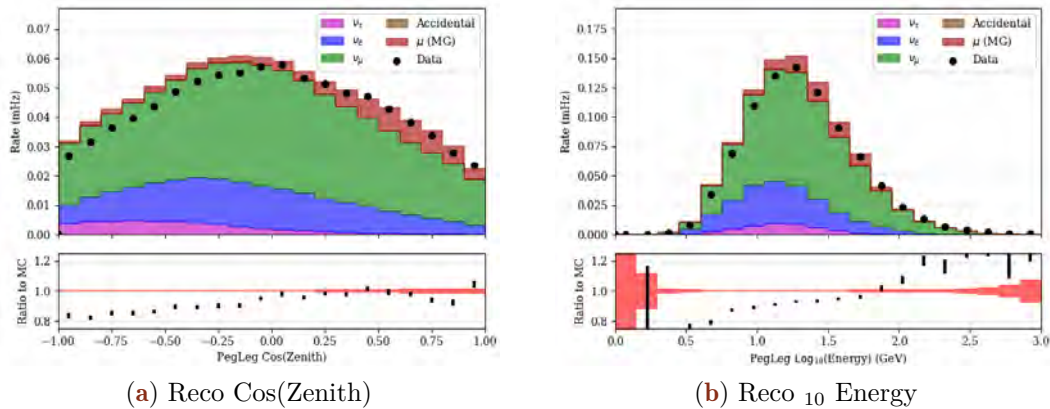


**Figure 7.38** – The reconstructed energy and zenith of the GRECO sample at Final Level. Events in data reconstruct to both relatively high energies ( $E_R > 100$  GeV) and very low energies ( $E_R \approx 2$  GeV). Using the NuFit 2.2 oscillation parameters and the flux model from Honda, the  $\nu_\tau$  events are observed in the very upgoing region around  $10^{1.4} = 25$  GeV.

The resolutions of the sample in energy and zenith are shown in Figures 7.39 and 7.40. The energy is well-reconstructed using Pegleg. The neutral current and tau neutrino

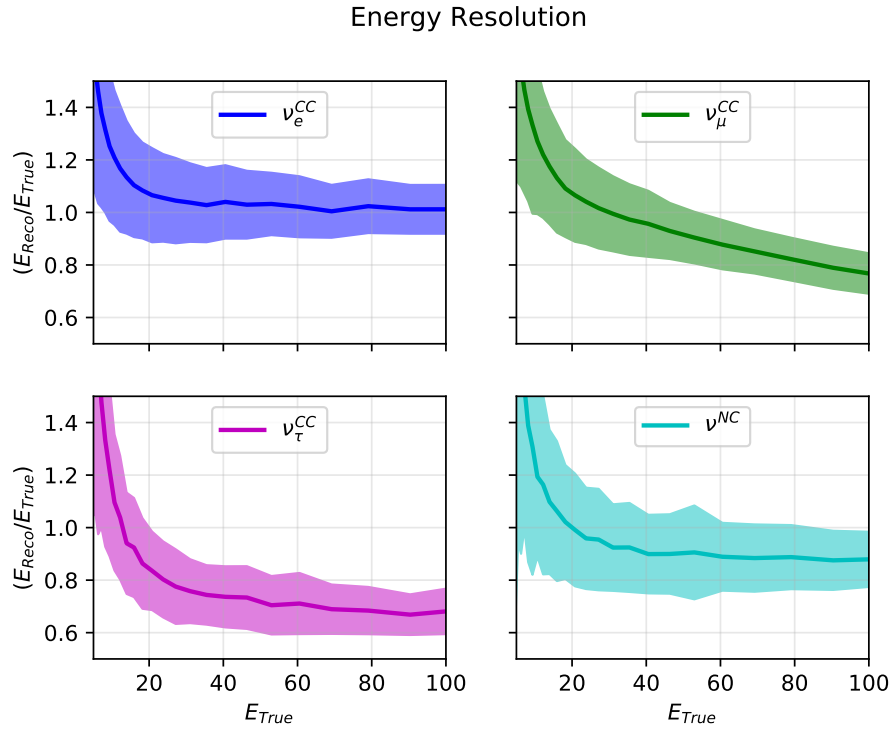


**Figure 7.39** – The resolution of the Pegleg reconstructed zenith of the GRECO sample at Final Level. The shaded band of each plot shows the  $1\sigma$  range for each plot. The Pegleg reconstruction energy resolution as a function of true energy. Cascade energies are well-reconstructed by Pegleg in the energy range of GRECO. The muon track is assumed to be minimum ionizing when calculating the associated energy. This assumption does not hold at higher energies.

events lose energy to outgoing neutrinos, resulting in less light deposition and lower reconstructed energies.

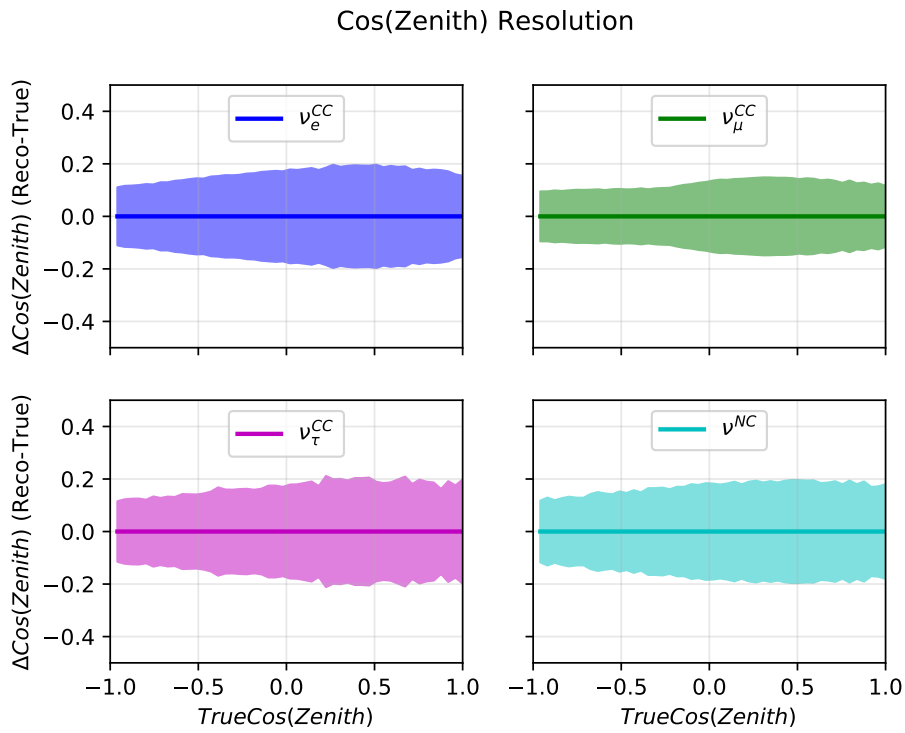


**Figure 7.40** – The resolution of the Pegleg reconstructed zenith of the GRECO sample at Final Level. The shaded band of each plot shows the  $1\sigma$  range for each plot. The reconstruction fits to within  $\Delta \cos\theta=0.15$  on average with better reconstruction resolution in the track-like muon neutrino charged current interactions.

# A Search for Tau Neutrinos from Oscillations

# 8

The GRECO event selection expects tau neutrinos with a rate of  $45 \mu\text{Hz}$ , corresponding to an expectation about 3000 events over the course of three years. These events will be used to search for tau neutrino appearance in DeepCore.

The tau neutrino appearance measurement is described in this chapter. The chapter begins in Section 8 with a discussion of how to parametrize the tau neutrino appearance as well as a review of the two previous tau neutrino appearance measurements performed by the OPERA and Super-Kamiokande experiments.

A description of the fitting process follows with descriptions of the systematic uncertainty parametrizations used in Section 8.3.1. The sensitivity of the measurement is given in Section 8.5.4. The impact of systematic uncertainties on the expected confidence interval is described in Section 8.7.

Finally, the results of the analysis are presented in Section 8.9.2 before a discussion of complementary oscillation results performed with the GRECO sample. A short conclusion follows to highlight some possible improvements for future analyses.

## 8.1 Parametrizing the Tau Neutrino Appearance

In order to measure the appearance of tau neutrino events, a choice of "appearance parameter" must be selected. Previous analyses have characterized the appearance using a normalization term [121, 122, 123]. This approach elegantly encapsulates many possible sources of uncertainty in the tau neutrino sector into a single, measurable value, including non-unitarity, uncertainties in the tau cross section,

### 8.1.1 CC vs CC+NC

As described in 1.5, neutrinos may interact via the charged current and neutral current interactions. These interactions provide separate windows into the measurement of tau neutrino appearance. Tau neutrino events may interact in either of these channels depending on the neutrino energy.

With a mass of  $1776.82 \pm 0.16 \text{ MeV}$  and a lifetime of  $290.3 \pm 0.5 \text{ femtoseconds}$  [10], tau leptons from tau neutrino charged current interactions in DeepCore at energies less than 100 GeV travel distances  $O(1 \text{ mm})$  before decaying. The charged current interactions of the tau result in a variety of signatures due to the unique decay behavior of the tau lepton.

$$\tau^- \rightarrow \begin{cases} \mu^- \bar{\nu}_\mu \nu_\tau & 17.41 \pm 0.04\% \\ e^- \bar{\nu}_e \nu_\tau & 17.83 \pm 0.04\% \\ \text{Hadrons} & \text{Otherwise} \end{cases} \quad (8.1)$$

In either the muonic or the electronic decay modes, a fraction of the energy is lost to outgoing neutrinos, resulting in a smaller observed charge than would be associated with a corresponding interaction of another neutrino type. Furthermore, the muonic decay mode may lead to a visible muon track for the tau neutrino interaction. These muon tracks associated with the appearance of tau neutrino would appear at lower energies than the tracks corresponding to the muon neutrino disappearance, allowing both the

appearance of tau neutrinos and the disappearance of muon neutrinos to be observed simultaneously.

Unlike charged current interactions, neutral current interactions of neutrinos have identical coupling to the Z boson regardless of flavor and, therefore, undergo no observable change due to unitary oscillations. Because of this, studies of the standard unitary PMNS matrix treat neutral current events as non-oscillating [121, 122, 123, 81]. In contrast, searches for new physics and sterile neutrinos measure deviations from the expected number of neutral current interactions in the detector [63].

For this analysis, both channels are used to measure the appearance of tau neutrinos.

### 8.1.2 The $\nu_\tau$ Normalization

In the atmospheric neutrino flux, tau neutrinos are only produced directly above energies of a few TeV through the decay of charmed mesons. Because effectively all tau neutrino events observable in DeepCore are the result of neutrino oscillations, the total number of observed tau neutrino interactions is a direct measure of the appearance.

Following the definition of analyses performed by other experiments [121, 122, 123], the tau neutrino normalization,  $N_{\nu_\tau}$ , is adopted as the primary physics parameter in the search for tau neutrino appearance. The normalization is defined to be a scaling of the number of expected tau neutrino events after the effects of all systematic uncertainties are applied. The parameter modifies the number of events expected in each bin

$$f'_{ijk} = \left( \sum_{m \neq \nu_\tau} f_{ijk}^m(\theta_{23}, \Delta m_{32}^2, \dots) \right) + N_{\nu_\tau} f_{ijk}^{\nu_\tau}(\theta_{23}, \Delta m_{32}^2, \dots) \quad (8.2)$$

where  $f_{ijk}^m$  is the expected rate in bin  $ijk$  from a particle type

$$m = (\nu_e^{CC}, \nu_\mu^{CC}, \nu_\tau^{CC}, \nu^{NC}, \mu_{Atm}, Accidental). \quad (8.3)$$

A value of  $N_{\nu_\tau} = 1.0$  indicates that the number of events is consistent with the number expected assuming unitary oscillations and the GRV98NLO cross section model in the GENIE generator. If the value differs significantly from 1.0, it may be indicative of either mismodeled cross-sections [124, 122] or of novel physics [125]. Due to the large existing uncertainties in the PMNS matrix described in 2.4.3, either situation is likely to yield valuable information.

### 8.1.3 Limits on the Tau Neutrino Normalization

This analysis is not the first to search for tau neutrino appearance. Two other experiments, OPERA and Super-Kamiokande, have reported previous measurements parametrized in the same way.

#### The OPERA Limit

The *Oscillation Project with Emulsion-tRacking Apparatus*, better known by the acronym *OPERA*, is an experiment designed to search for tau neutrino appearance [23]. Unlike IceCube's use of atmospheric neutrinos, OPERA uses muon neutrinos produced in the CERN Neutrinos to Gran Sasso (CNGS) beamline. OPERA uses bricks of emulsion cloud chambers in order to accurately track and reconstruct neutrino interactions in the fiducial volume. This technique allows analyzers to identify not only the initial neutrino interaction vertex, but also the decay products along the path of the charged lepton produced in charged current interactions. An example of one tau neutrino event observed is shown in Figure 8.1. In OPERA, the tau lepton produced during a tau

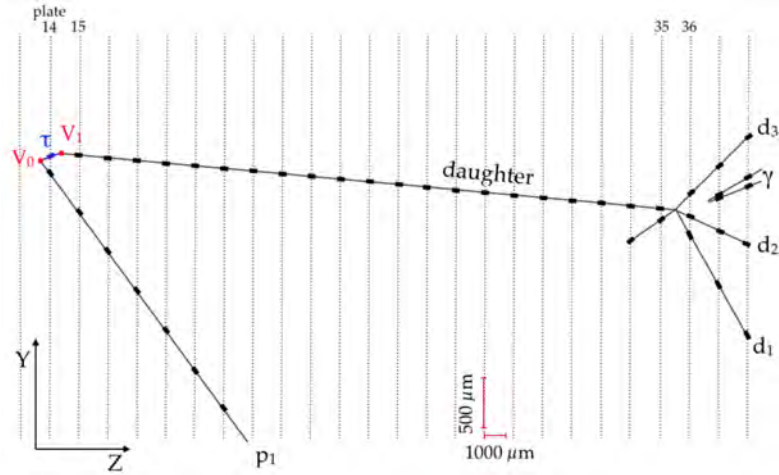


**Figure 8.1** – An event display of the reconstructed interaction of a tau neutrino in the OPERA detector. The initial interaction vertex,  $V_0$ , produces a tau lepton, shown in blue. The OPERA detector’s micrometer spatial resolution enables the identification of individual tau neutrino interactions. Figure from [123].

neutrino charged current interaction decays, producing a characteristic kink visible in the detector that can be used to identify tau neutrino candidate events. The ability to identify the particle dynamics is balanced by the small fiducial volume of the experiment, yielding only 5408 useful events for analysis from five years of data-taking [123].

In 2015, OPERA Collaboration released the final result in their search for tau neutrino appearance using charged current interactions. Five candidate events were identified in the data sample with a signal expectation of  $2.64 \pm 0.53$  and a background expectation of  $0.25 \pm 0.05$ . The data unambiguously rules out the no-appearance hypothesis, with a rejection at  $5.1\sigma$ .

OPERA reported a final value of  $N_\tau^{CC} = 1.8_{-1.1}^{+1.8}$  at the 90% confidence level. This value is consistent with the standard unitary oscillation scheme, but with large errors.

### The Super-Kamiokande Limit

Super-Kamiokande, described in Section 2.2, also has reported results in searches for tau neutrino appearance. The Super-Kamiokande collaboration developed an event selection in the search for tau neutrino events, including the implementation of a neural network trained to identify tau-like and non-tau-like events [121, 122]. Events are analyzed in terms of the zenith angle and the neural network output variable.

The background and signal event distributions, shown in Figure 8.2 are fit to 5326 days of atmospheric neutrino data with an unbinned likelihood with 28 systematic uncertainties included in the analysis.

The expected rates of the Super-Kamiokande analysis are shown in Table 8.1. The Super-Kamiokande measurement yields an expectation of 185.2 tau neutrino events in 5326 days or approximately 12.7 events per year. After fitting, the final rejection of the no-appearance hypothesis,  $N_\tau^{CC}=0$ , is found to be  $4.6\sigma$ . Like OPERA, Super-Kamiokande finds more tau neutrino candidate events than expected, with a best-fit normalization of  $N_\tau^{CC} = 1.47 \pm 0.32$  at the 68% level.

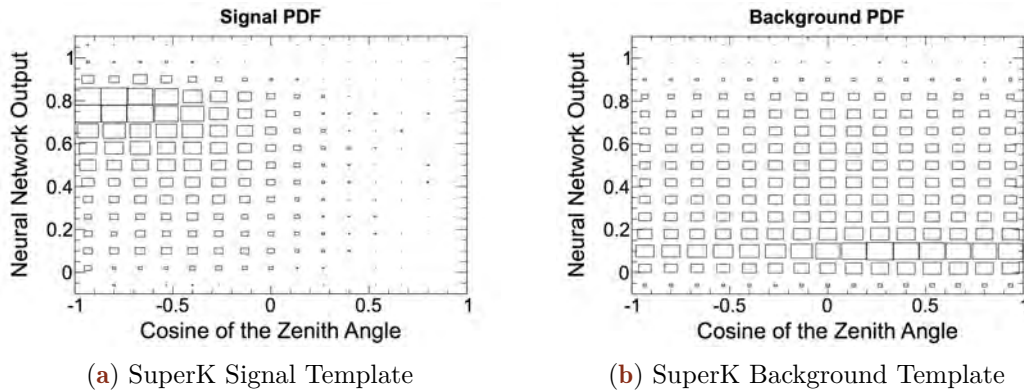


**Figure 8.2** – The signal (a) and background (b) histograms used in the Super-Kamiokande search for tau neutrino appearance. The data is binned to show the location of events, although the fit is performed using an unbinned likelihood. The signal tau neutrino events appear in the upgoing region. Image from [122].

Interaction Mode	Non-tau-like	tau-like	All
CC nue	3071.0	1399.2	4470.2
CC numu	4231.9	783.4	5015.3
CC nutau	49.1	136.1	185.2
NC	291.8	548.3	840.1

**Table 8.1** – The rates expected for each of the neutrino types in the Super-Kamiokande search for tau neutrino appearance. Reproduced from [122].

## 8.2 Binning of the Appearance Analysis

The signature of tau neutrino appearance in DeepCore is an energy and zenith angle dependent excess of cascade-like events. To measure the appearance signature, a binned likelihood, described in 8.4.5, is used to fit the simulation to the data. The analysis uses two variables to describe the oscillations: the reconstructed energy and zenith angle.

The choice of binning for zenith angles is selected to be similar, but somewhat finer than previous work and uses the full sky [79, 80, 81]. The upgoing events ( $\cos(\phi) = -1$ ) pass through the full diameter of the Earth where we expect the strongest oscillation effects while the downgoing events ( $\cos(\phi) = 1$ ) originate in showers above the Antarctic. The energy binning is identical to previous oscillation analyses from DeepCore and consists of 8 bins logarithmically spaced from 5.6 GeV to 56 GeV, avoiding potential problems due to disagreements at high energies discussed in Section 7.8.4.

### 8.2.1 Particle ID Variables

Separating the sample into cascade-like and track-like events provides better sensitivity than using solely track-like events [80, 81, 67, 122]. A separation of this type, referred to as a *particle identification* variable (*PID*), allows the disappearance and appearance effects to be observed independently and provides a stronger limit on uncertainties from systematic effects. Two such variables are available in the GRECO sample, shown in Figure 8.3.

The first PID candidate variable, the reconstructed length of a muon track, provides separation between events with a clear muon track from those without one. This leads to reasonable separation between the  $\nu_\mu$  events undergoing disappearance and  $\nu_\tau$  events

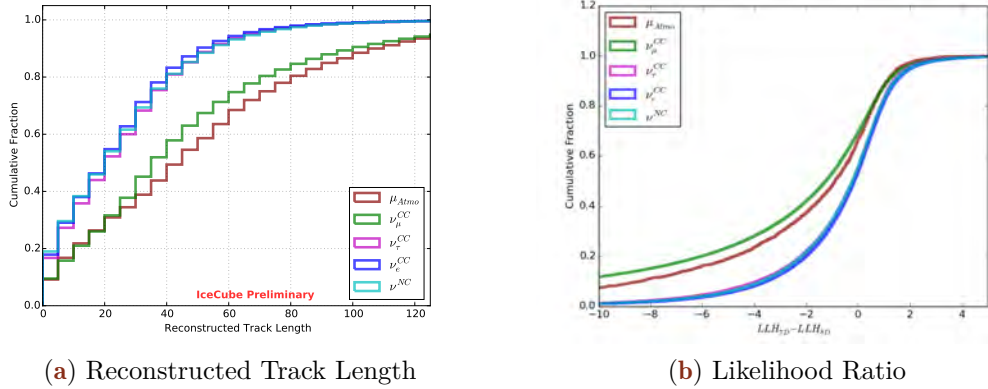


**Figure 8.3** – The cumulative distributions of two variables to separate track-like events (muon neutrino charged current, atmospheric muons) from the cascade-like events (neutral current, electron neutrinos, and tau neutrinos). Larger distances between the muon neutrino charged current and the tau neutrino charged current curves indicates better separating power.

undergoing appearance. This may be seen in Figure 8.3a, where the cumulative distribution of the various simulation components are shown as a function of the reconstructed track length. The optimal separation between the  $\nu_{\mu}$  and  $\nu_{\tau}$  charged current samples occurs between 30-50 meters. By separating the sample into cascade-like events (eg.  $L < 50$  m) and track-like events ( $L \geq 50$  m), the disappearance and appearance may be partially disentangled.

The second potential PID variable is the likelihood ratio between PegLeg’s mixed cascade+track reconstruction and an analogous cascade-only reconstruction performed using the same tools. A higher likelihood (lower log-likelihood) in the cascade fit implies that the event is more likely intrinsically cascade-like while the reverse is true for intrinsically track-like events. The information contained in the likelihoods of both fits may be combined to form a likelihood ratio, typically expressed in terms of the log-likelihoods.

$$\Delta LLH = \text{Log}_{10} R_L = \text{Log}(L_{\text{Cascade}}) - \text{Log}(L_{\text{Pegleg}}) \quad (8.4)$$

The cumulative plot of the likelihood ratio is shown in Figure 8.3b. There exists a broad choice of values with similar separation properties from approximately  $-4 < \Delta LLH < -2$ . Once again, separating events into two samples using the likelihood ratio may improve the ability of the analysis to disentangle the disappearance and appearance effects.

An event with a longer reconstructed muon track should be expected to prefer the PegLeg reconstruction over a cascade-only reconstruction. In order to choose between the parameters, the efficacy of separating each of the simulation samples from the tau neutrino charged current signal was evaluated. The results are shown in Figure 8.4, which give the fraction muon neutrino events rejected and the number of tau neutrino events accepted into the "cascade-like" sample for various choices of the PID values. Values further from a diagonal indicate better separation between the muon and tau neutrino events. The track length performs uniformly better than the likelihood ratio in separating the disappearing muon neutrino charged current and appearing tau neutrino charged

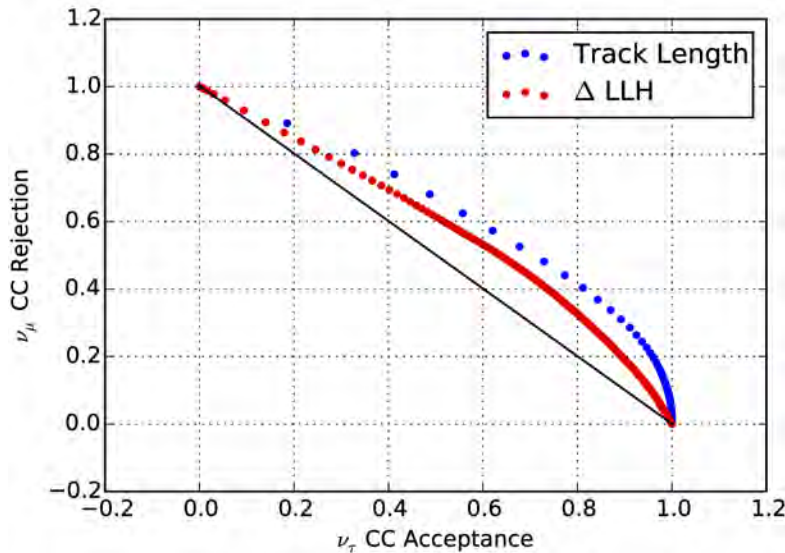


**Figure 8.4** – A comparison of the separating power between the reconstructed track length and the likelihood ratio. Each point represents one possible choice of separation value from Figure 8.3. Points further from the black line indicate stronger separating power between the muon neutrino and tau neutrino charged current events.

current events. The reconstructed track length is therefore selected as the PID variable for this analysis.

A choice of 50 meters of reconstructed track length is selected to separate the GRECO events into track-like ( $L \geq 50$  m) and cascade-like ( $L < 50$  m) event samples. Because the PegLeg reconstructed energy includes a contribution from the muon track, the division of the sample has an effect on the minimum energy of track-like events. Using Equation 7.15, the minimum energy of track-like events with no cascade energy and  $L \geq 50$  m is 11 GeV. Track-like events are kinematically limited from reconstructing with energies below this threshold. Both track- and cascade-like events may reconstruct with higher energies than 10 GeV.

## 8.2.2 The MC Fit Templates

The binned expectations used in the fit for tau neutrino appearance are shown in Figures 8.5 and 8.6. Neutrino histograms assume the oscillation parameters given by the Nu-Fit global fits in Section 2.3.4 [58].

Muon neutrino charged current events are the dominant component of both the track-like and the cascade-like histograms. The track-like muon neutrino charged current histogram shows a deficit of events in the upgoing region at an energy of  $10^{1.3} = 20$  GeV due to muon neutrino disappearance. The disappearance of muon neutrino events is visible in the track-like channel of both the muon neutrino charged current and the data histograms.

The tau neutrino events appear primarily in the cascade-like histogram. The signal  $\nu_\tau$  events occur in the very upgoing cascade channel and make up, at most, approximately 10% of the events in those bins.

Figure 8.6 includes histograms of both the simulated muons, produced using the DeepCore MuonGun generation scheme developed in Section 6.2, and the accidental triggers, produced using the Vuvuzela V2 model described in Chapter 5. Both samples are limited by the available simulation statistics. In the case of the accidental triggers,

the severely limited statistics available at the Final Level of the analysis precludes the direct use of the remaining events. Instead, the accidental trigger simulation is modeled assuming a uniform distribution in energy, zenith, and track length with a total event rate equal to the expected rate from the remaining simulation sample.

The muon background histogram contains approximately 2400 simulated events spread over 140 bins in energy, zenith, and track length. The atmospheric muon background events reconstruct as downgoing events visible in the track-like channel. Significant statistical uncertainties in the region of expected appearance limit the reach of the analysis. While additional simulated statistics would be beneficial, potentially following the scheme introduced in Section 6.3, the production of new sets has not been completed due to time constraints.

## 8.3 Parametrization of Systematic Uncertainties

The tau neutrino component of the GRECO selection makes up only 5% of the expected event rate at Final Level. The measurement is sensitive to a number of *systematic uncertainties*, including the neutrino oscillation parameters, the neutrino and muon fluxes, neutrino cross sections, and various detector systematic uncertainties. These uncertainties may be divided into two broad categories related to the method in which they are applied.

The first, the *analytic systematic uncertainties (ASU)*, have an analytic form that may be used to modify the weight of each event. Analytic uncertainties are calculated as modifications to the energy- and zenith-dependent flux weights of the event,  $f(E_i, \theta_i)$  to get the final event weight,  $w_i$ .

$$w_i = \left( \prod_m^{ASU} \delta w_{im} \right) f(E_i, \theta_i) \quad (8.5)$$

*Non-analytic systematic uncertainties (NSU)* require dedicated Monte Carlo simulations to parametrize the effects at Final Level. Properties which affect the trigger conditions or change the properties of photon propagation are examples of non-analytic uncertainties. These uncertainties cannot be evaluated at a per-event level and are instead applied as changes to the binned analysis histogram in energy, zenith, and track length.

Parametrizing non-analytic uncertainties requires dedicated simulation sets, known as *systematics sets*, such as those in Tables 8.2 and 8.3. Each systematic set must be processed through the GRECO processing stream and reconstructed with the Pegleg reconstruction. The histograms associated with each systematic set are compared to the *baseline set* to identify the effects of the systematic uncertainty in the reconstructed histogram. The systematic sets each provide a discrete point describing the change in the analysis histogram due to the selected non-analytic systematic uncertainty.

### 8.3.1 Parametrizing with Hyperplanes

For the GRECO tau neutrino appearance, a continuous parametrization of the discrete systematics sets is used to model the uncertainties. The parametrization method can be described by beginning with a simpler model in one dimension.

A simple linear parametrization of one non-analytic systematic uncertainty in a single bin is a linear model of the form

$$f' = (a(x - x_0) + b) f \quad (8.6)$$

where  $x$  and  $x_0$  are the current value and the baseline value of the systematic parameter and  $f$  and  $f'$  are the expected rate in the bin before and after applying the effect of the systematic uncertainty. The constants,  $a$  and  $b$ , are fit to the expected rates from the systematic sets  $\vec{f}_{SystSets}$  as a function of the systematic values  $\vec{x}_{SystSets}$  using the linear least squares method. This linear model provides a continuous parametrization from the discrete set of points and is used to describe the effect of the systematic parameter in the analysis histogram.

The model can be trivially extended to include multiple systematic uncertainties using a similar form.

$$f' = \left( \sum_m^{NSU} (a_m(x_m - x_{m0})) + b \right) f \quad (8.7)$$

All systematic effects  $m$  are described by independent linear models with a common constant  $b$ . The constants  $[a_0, a_1, \dots]$  and  $b$  are once again fit using the linear least squares method.

This model, referred to as a *hyperplane*, is used to describe the non-analytic systematics for each bin for the neutrinos. For atmospheric muons, the form is slightly modified to account for large changes in rate due to DOM efficiency and absorption uncertainties. In these two cases, an exponential model is selected to better describe the observed effects in simulation.

$$f' = \left( \sum_{m \neq DE, Abs}^{NSU} (a_m(x_m - x_{m0})) + \sum_k^{DE, Abs} (a_k e^{b_k(x_k - x_{k0})} - 1) + c \right) f \quad (8.8)$$

Separate hyperplanes are created for each bin in energy, zenith, and track length as well as for each simulated event type ( $\nu_e^{CC}$ ,  $\nu_\mu^{CC}$ ,  $\nu_\tau^{CC}$ ,  $\nu^{NC}$ ,  $\mu$ ). These parametrizations allow the evaluation of the effect of any combination of the six non-analytic systematics.

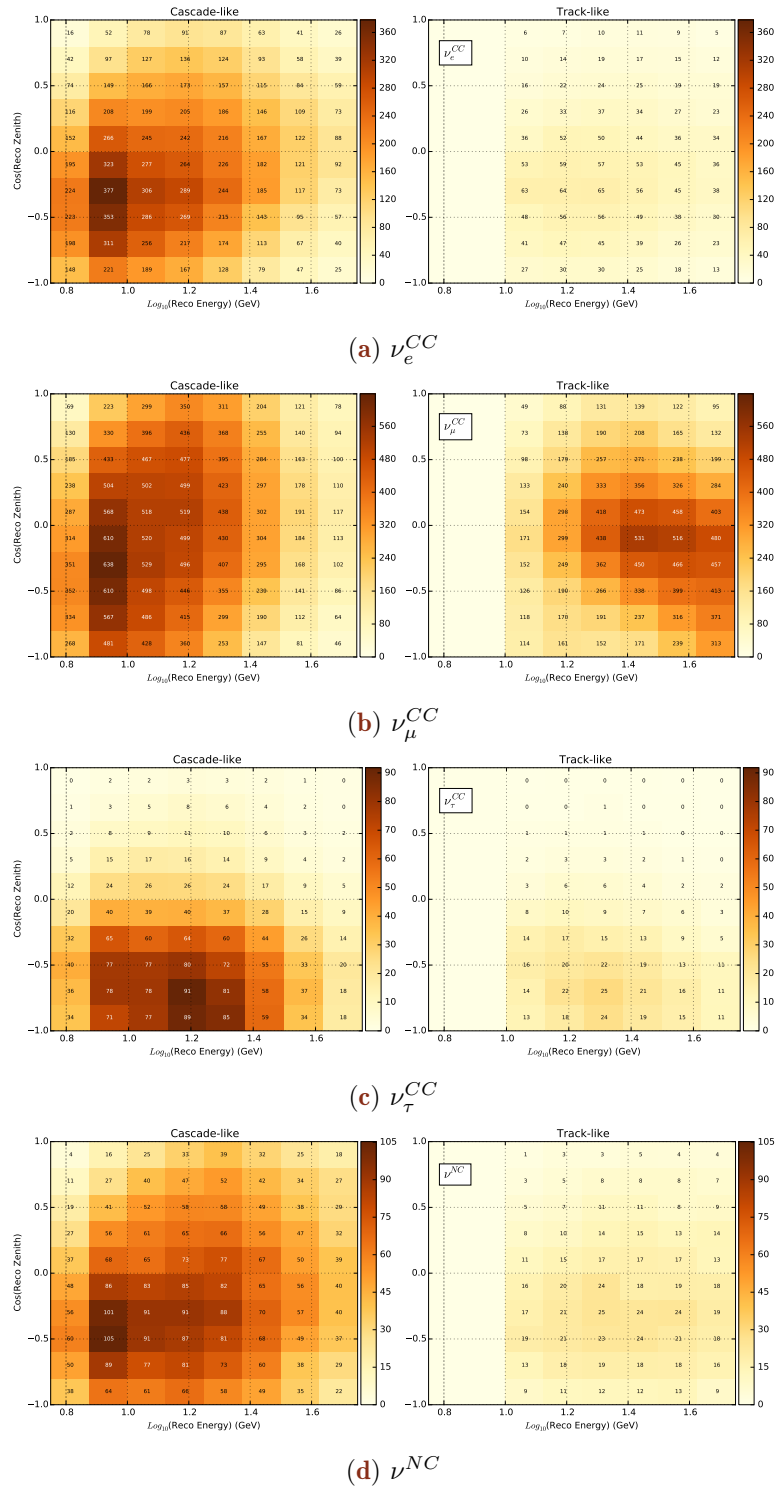


**Figure 8.5** – The neutrino histograms used in the fit for appearance. The colorbar shows the expected rate from the 3 year sample used in this thesis. The disappearance in the muon neutrino events is visible in the upgoing ( $\cos(\theta)=-1$ ) track-like histogram around an energy of  $10^{1.3}=20$  GeV. The appearance of tau neutrinos is primarily concentrated in the cascade-like histogram.

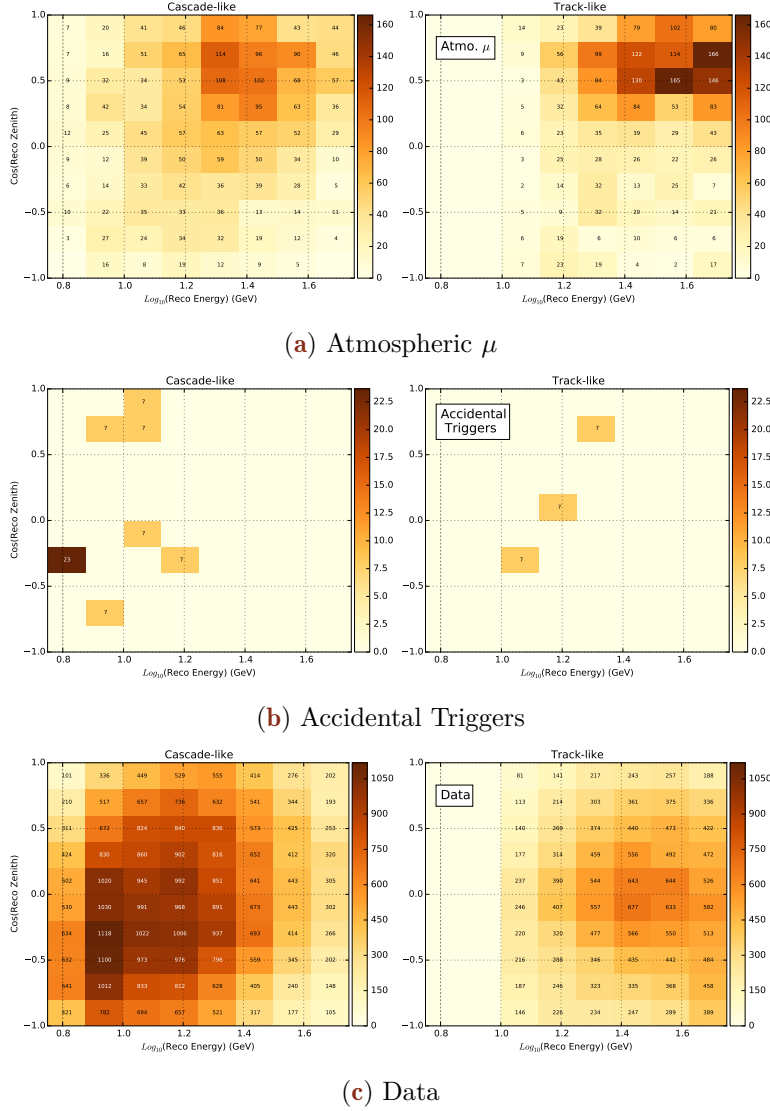


**Figure 8.6** – The background (a, b) and data (c) histograms used in the fit for appearance. The NuFit oscillation parameters are assumed [58]. The colorbar shows the expected rate in each bin from the 3 year sample used in this thesis. The numbers in the bins give the expected rate numerically. The disappearance of muon neutrinos is visible in data histogram in the upgoing ( $\cos(\theta)=-1$ ) track-like histogram around an energy of  $10^{1.3}=20$  GeV. Both the muon and accidental trigger histograms are limited by the simulations statistics.

Set Number	Coincident Fraction	DOM Eff	Hole Ice	Forward Coeff	Absorption	Scattering	Processed Livetime
Baseline	0%	100%	25	0	100%	100%	30 years
640C	100%	100%	25	0	100%	100%	30 years
641	0%	88%	25	0	100%	100%	30 years
643		94%					
644		97%					10 years
645		103%					
646		106%					
648		112%					
660	0%	100%	15	0	100%	100%	10 years
661			20				
662			30				
663			35				
670	0%	100%	25	2.0	100%	100%	10 years
671				-5.0			
672				-3.0			
673				1.0			
674				-1.0			
681	0%	100%	25	0.0	92.9%	92.9%	30 years
682					110%	100%	
683					100%	110%	

**Table 8.2** – Simulation sets used to describe non-analytic uncertainties of the signal neutrino events. The sets are divided into categories in which only one parameter is changed. Only parameters which are varied are shown for each row. While all listed sets have up to 30 years of effective livetime available, not all events are processed in each set due to the computational constraints of the Pegleg reconstruction.

Set Number	Oversizing	DOM Eff	Hole Ice	Forward Coeff	Absorption	Scattering	Comments
Baseline	1.0	99%	25	0	100%	100%	1 year DeepCore MuonGun
A	1.0	69.3%	30	0	100%	100%	
B		79.2%					
C	1.0	99%	15	0	100%	100%	
D			30				
E	1.0	99%	30	-2	100%	100%	
F				-4			
G	3.0	99%	25	0	100%	100%	1 year KDE Prescale
H					110%		
I					80%		
J					100%	80%	
K						110%	
L						120%	
M					92.9%	92.9%	
N					114.2%	114.2%	

**Table 8.3** – Simulation sets used to describe non-analytic uncertainties of the atmospheric muon events. The sets are divided into categories in which only one parameter is changed. Only parameters which are varied are shown for each row. Note that the bulk ice systematics sets use the KDE prescale simulation scheme introduced in Section 6.3.

Parameter	Baseline	Tested Shift	$\sum_{bins} \chi^2$
$\Delta m_{31}^2$	$2.2526 \times 10^{-3}$	$+0.10 \times 10^{-3}$	2.776
$\Delta m_{21}^2$	$7.49 \times 10^{-5}$	$+0.19 \times 10^{-5}$	$5.392 \times 10^{-4}$
$\theta_{23}$	0.72431	+0.02094	1.262
$\theta_{13}$	0.14765	+0.00262	$1.802 \times 10^{-3}$
$\theta_{12}$	0.58853	+0.01379	$2.978 \times 10^{-4}$
$\delta_{CP}$	0.0	$+\frac{\pi}{2}$	$2.407 \times 10^{-2}$

**Table 8.4** – Total  $\chi^2$  impact of each of the oscillation parameters. A  $\sum \chi^2 \approx 1$  corresponds to a  $1\sigma$  effect in the histogram. The atmospheric mixing parameters,  $\Delta m_{31}^2$  and  $\theta_{23}$  are the most important oscillation parameters for the GRECO selection. Of the remaining parameters, the CP-violating phase is the next most important.

## 8.4 Effects of Systematic Uncertainties

A set of 18 systematic uncertainties were used in the search for tau neutrino appearance. These parameters consist of the muon neutrino disappearance parameters as well as uncertainties in the flux, the cross sections, and the detector modeling. Each systematic will be briefly discussed and the effect on the analysis histogram will be shown.

### 8.4.1 Oscillation Parameters

The GRECO selection is sensitive to atmospheric neutrinos from 5 GeV to 60 GeV with a peak energy around 20 GeV. These neutrinos travel distances from approximately 20 km (directly downgoing) to 12700 km (directly upgoing), giving a range of  $0.35 \leq L/E \leq 2540$ . At these energies and baselines, the solar mass splitting  $\Delta m_{21}^2 = 7.49 \times 10^{-5} eV^2$  is too small to be important. This also limits the sensitivity of the GRECO events to the solar mixing angle  $\theta_{12}$ .

Only the atmospheric parameters,  $\Delta m_{31}^2$  and  $\theta_{23}$ , and the reactor angle,  $\theta_{13}$  may contribute. The reactor mixing angle affects the oscillation probability to electron neutrinos through the MSW effect at the GeV scale. Measurement constraints on  $\theta_{13}$  limit the uncertainty on this parameter.

This has been tested with the GRECO sample by changing each parameter by the  $1\sigma$  range given in [58]. The total value of the  $\chi^2$ , defined as in Section 8.5, was used to select the most important parameters for this fit.

The results are shown in Table 8.4. The atmospheric mixing parameters,  $\Delta m_{31}^2$  and  $\theta_{23}$ , have significantly larger impacts on the analysis histogram than the other parameters. For the purposes of GRECO analyses, only these parameters are therefore considered.

The effect of each is shown in Figures 8.7 and 8.8. Of the two, the mass splitting term has strong correlations expected with tau neutrino normalization  $N_{\nu_\tau}$ , changing both the location as well as the strength of the observed appearance.

The track-like and cascade-like histograms are both dominated by muon neutrino charged current interactions. Both the track-like and cascade-like events see strong effects from the uncertainties on the atmospheric mixing parameters.

### 8.4.2 Neutrino Flux Uncertainties

The underlying flux models of the atmospheric neutrinos and background muons contain significant uncertainties relevant to the search for tau neutrino appearance. The implementation of the flux used in IceCube is produced using a computationally expensive Monte Carlo simulation of the Earth [19]. Four analytic systematic uncertainties used

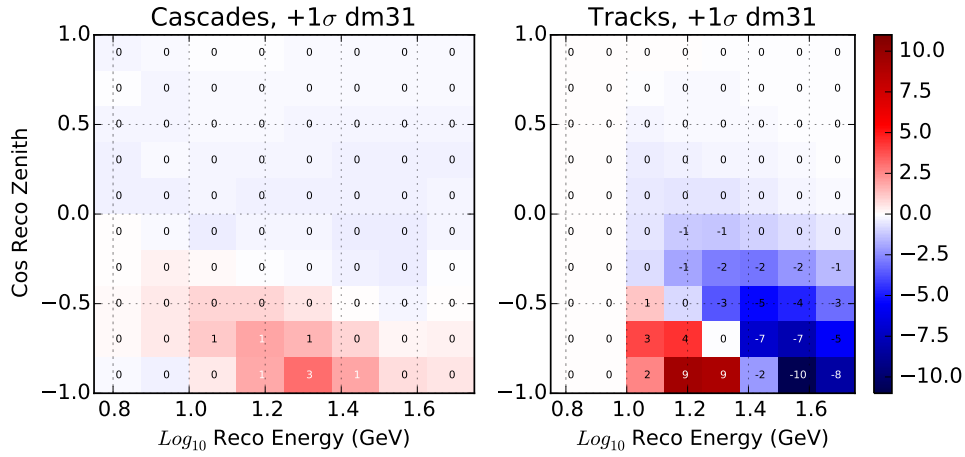


**Figure 8.7** – The effect of  $\Delta m_{31}^2$  in the analysis histogram. The colorbar shows the percent change in rate per bin for a shift of 10% in the mass splitting from the baseline value,  $2.526 \cdot 10^{-3} eV^2$ , to  $2.779 \cdot 10^{-3} eV^2$ . A strong disappearance effect is observed in the track-like events while the number of events in the appearance signal region of the cascade-like histogram is increased. Of the systematic uncertainties included in the tau neutrino appearance analysis, the mass splitting shows the strongest correlation with the value of  $N_{\nu_\tau}$ .

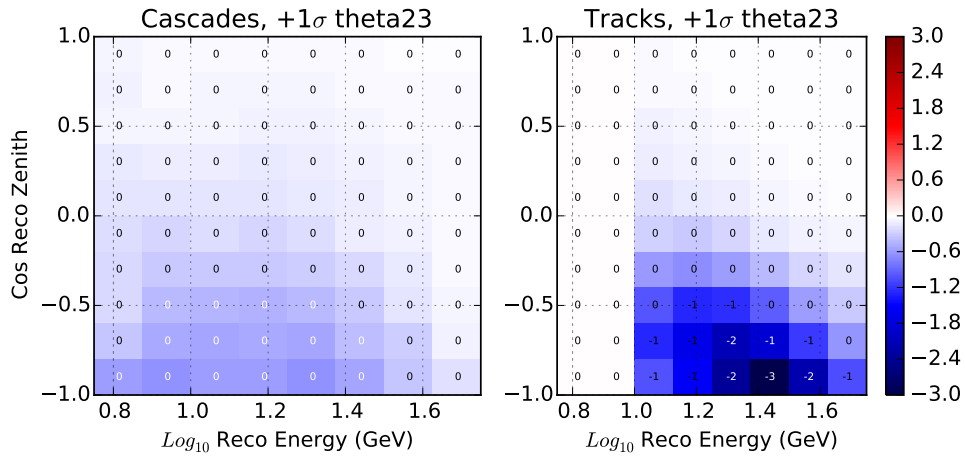


**Figure 8.8** – The effect of  $\theta_{23}$  in the analysis histogram. The colorbar shows the percent change in rate per bin for a shift of 10% from the baseline value,  $\sin^2\theta_{23} = 0.440$ , to  $\sin^2\theta_{23} = 0.50$ . As expected, the appearance modulates the strength of the muon neutrino disappearance. Because both the cascade-like and track-like sample are dominated by muon neutrino charged current events, this change results in a net disappearance in both histograms.

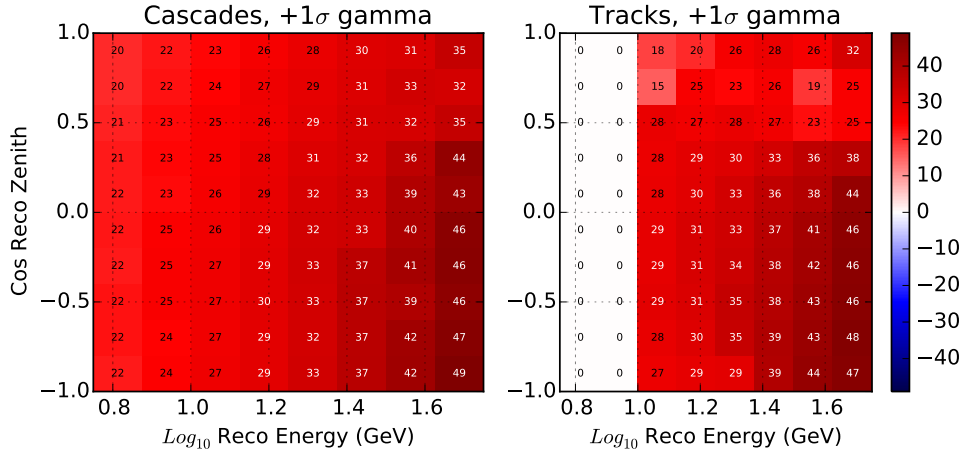


**Figure 8.9** – The effect of  $\delta\gamma_\nu$  in the analysis histogram. The colorbar shows the percent change in rate per bin for a shift of 10% from the baseline value. The spectral index has a strong effect on both histograms as a function of energy.

in this analysis modify the neutrinos flux. A fifth systematic uncertainty scales the total neutrino flux to account for uncertainties in the total event rate. This neutrino normalization is allowed to float freely with a constraint that the value be larger than 0.

### Neutrino Spectral Index

The spectral index of the neutrino flux is related to the cosmic ray spectrum. The change in the neutrino flux,  $\delta\gamma_\nu$  is implemented by modifying the neutrino event weight,  $w_i$  based on the energy of the event.

$$w'_i = \left( \frac{E_i}{1 \text{ GeV}} \right)^{\delta\gamma_\nu} w_i \quad (8.9)$$

For IceCube, a gaussian prior of  $0 \pm 0.1$  is used for the uncertainty in the spectral index. The effect is shown in Figure 8.9.

### $\nu_e/\nu_\mu$ Ratio

The number of electron and muon neutrinos produced during air showers depends on the dynamics of the shower and the hadronization model used in the prediction. For IceCube, the ratio of the electron and muon fluxes is used as a systematic by scaling the normalization of the two fluxes. The scaling factor,  $N_{\nu_e}$  is applied to the electron neutrino flux as a flat scale factor with a conservative prior of  $1.0 \pm 0.05$  derived from [126]. The effect on the histogram is shown in Figure 8.10.

### $\nu/\bar{\nu}$ and Upward/Horizontal Ratios

The shape of the neutrino spectrum is derived from Monte Carlo simulations that modify the kaon and pion branching ratios used to calculate the neutrino flux prediction [126, 127]. In order to utilize these uncertainties in the appearance analysis, parametrizations of the effects, shown in Figure 8.11, are included in the analysis [80, 81]. The effects of

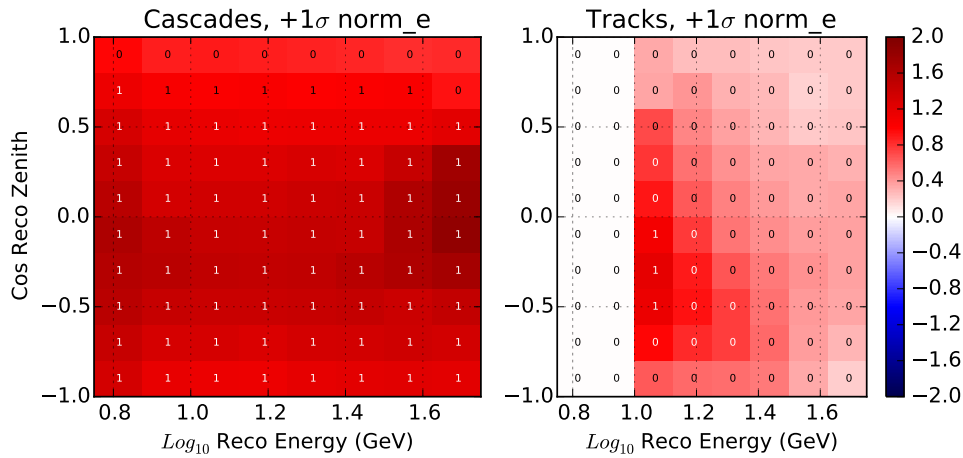


**Figure 8.10** – The effect of  $N_{\nu_e}$  in the analysis histogram. The colorbar shows the percent change in rate per bin for a shift of 5% from the baseline value. The strongest impact occurs in the cascade-like events near the horizon.

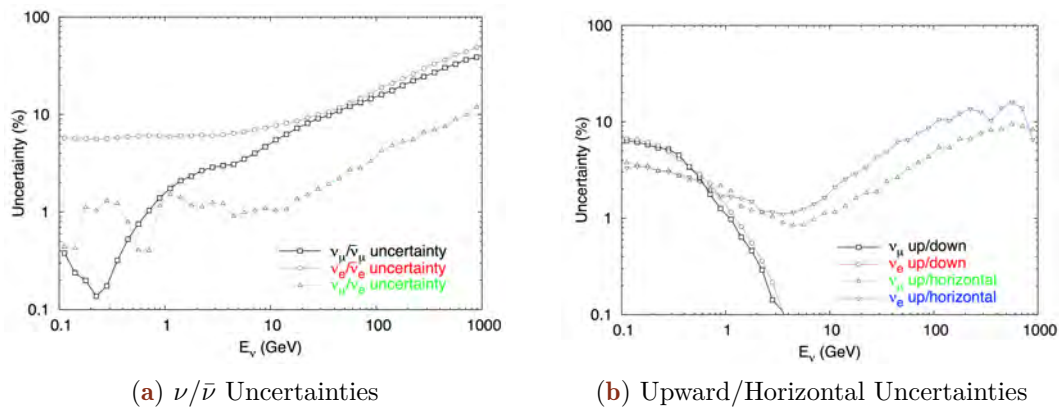


**Figure 8.11** – The neutrino flux uncertainties calculated in [126]. (a) The ratio of the muon to electron neutrino fluxes is shown in green. The effect is applied as an energy-independent scale factor with a conservative prior of 5% adopted in this analysis. The uncertainty of the neutrino to antineutrino flux, shown in black and red for muon neutrinos and electron neutrinos respectively, is parametrized as a function of energy and zenith for inclusion in the appearance analysis. (b) The ratio of the upward flux to the horizontal flux in the atmospheric neutrinos. The ratio changes due to uncertainties in the pion and kaon decays in cosmic ray air showers. The shape of the uncertainty is parametrized in energy and zenith for inclusion in this analysis.

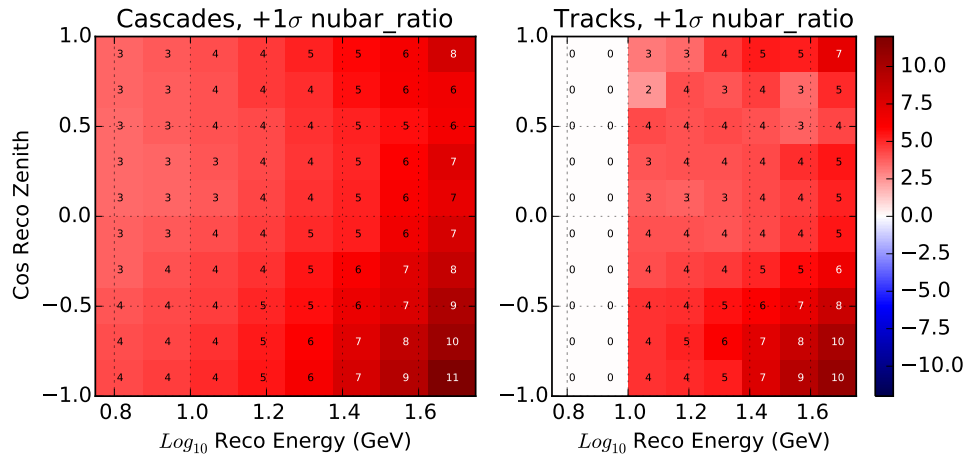


**Figure 8.12** – The effect of the  $\nu/\bar{\nu}$  uncertainty in the analysis histogram. The colorbar shows the percent change in rate per bin for a shift of  $1\sigma$  from the baseline value where  $1\sigma$  corresponds to the uncertainties of Figure 8.11a. Changing the ratio affects both histograms with the strongest effect occurring at the highest energies as expected from [126].

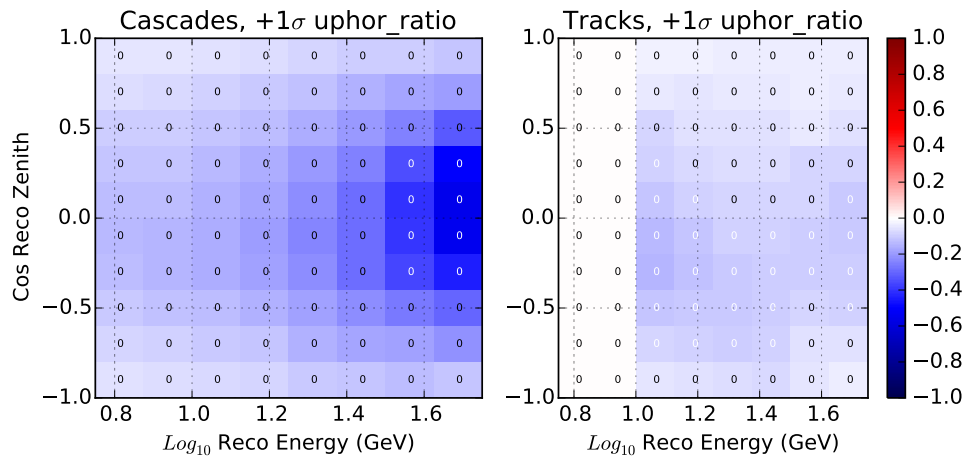


**Figure 8.13** – The effect of the upward/horizontal uncertainty in the analysis histogram. The colorbar shows the percent change in rate per bin for a shift of  $1\sigma$  from the baseline value where  $1\sigma$  corresponds to the uncertainties of Figure 8.11b. The uncertainty of the up/horizontal ratio has a small impact in the analysis space.

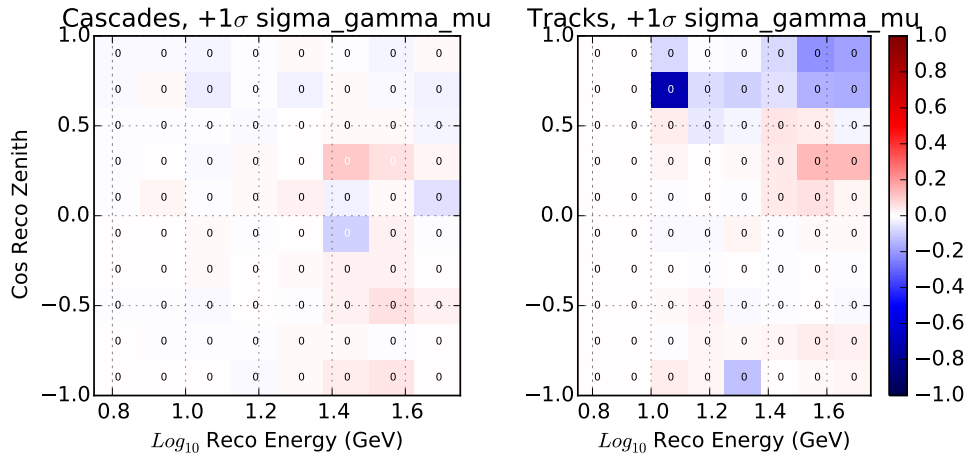


**Figure 8.14** – The effect of the  $\delta\gamma_{CR}$  uncertainty in the analysis histogram. The colorbar shows the percent change in rate per bin for a shift of  $1\sigma$  from the baseline value where  $1\sigma$  corresponds to the uncertainties of [128].

the  $\nu/\bar{\nu}$  uncertainty and the upward/horizontal uncertainty are shown in Figures 8.12 and 8.13 respectively.

### 8.4.3 Atmospheric Muon Flux

The appearance analysis includes two systematics on the atmospheric muon flux. The first is a normalization factor that scales the total number muons in the detector. This normalization is constrained to be positive, but otherwise includes a flat prior.

The second is an uncertainty on the cosmic ray spectral index,  $\gamma_{\mu}^p = .71 \pm 0.01$  for hydrogen nuclei and  $\gamma_{\mu}^{He} = .60 \pm 0.01$  for helium nuclei, derived from [127]. The uncertainty was evaluated by reweighting events based on the cosmic ray primary energies of CORSIKA simulation processed to GRECO Level 5. The resulting uncertainties were parametrized in terms of the energy at the MuonGun generation cylinder (see Section 6.2) and the direction of the muon [128].

The change in the analysis histograms due to the uncertainty in the spectral index of the cosmic ray spectrum is shown in Figure 8.14. The effect is small, resulting in less than a 0.1% shift in most bins. Despite the small effect, the parameter is included in the fit in order to account for uncertainties in the cosmic ray muons.

### 8.4.4 Cross-section Uncertainties

Uncertainties on the neutrino cross section can affect the rates of events in the final sample. Parametrizations of the QE, RES, and DIS interaction cross section uncertainties were tested for inclusion in this analysis.

### Axial Masses

The axial mass terms, described briefly in Section 1.4.1, control the cross section for the resonant and quasielastic interactions. Uncertainties are defined conservatively, following the default uncertainties available in the GENIE generator [94].

The GENIE generator provides tools to recalculate event weights for changes in the axial masses. The axial masses and their uncertainties from GENIE are  $M_a^{QE} = 0.99_{-0.15}^{+0.25}$  GeV and  $M_a^{RES} = (1.12 \pm 0.22)$  GeV.

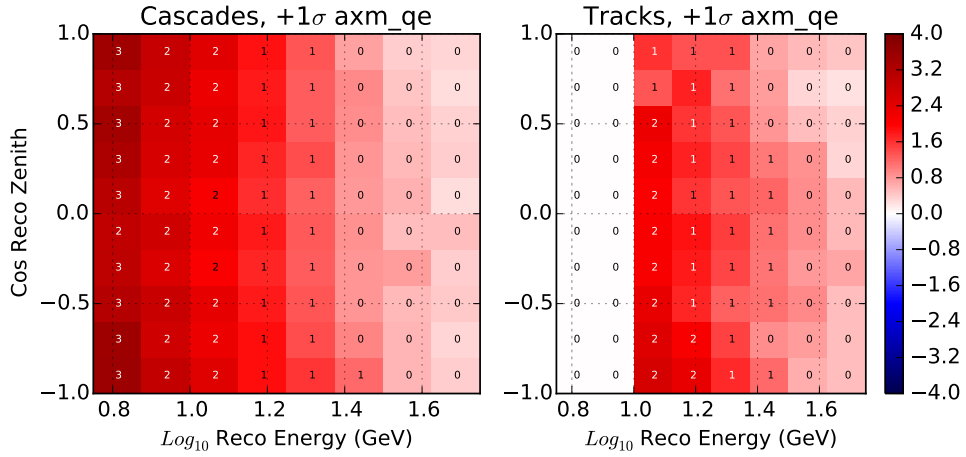


**Figure 8.15** – The effect of the axial mass  $M_a^{QE}$  uncertainty in the analysis histogram. The colorbar shows the percent change in rate per bin for a shift of  $1\sigma$  from the baseline value using the GENIE reweighting code.

For each QE and RES event, GENIE functions are used to find reweighting factors for 5 discrete points of the axial masses ( $-2\sigma$ ,  $-1\sigma$ ,  $0$ ,  $+1\sigma$ ,  $+2\sigma$ ). These weights are fit to a second order polynomial for each event to produce a smooth parametrization for the weight as a function of axial mass value.

The QE and RES events occur at low energies, as expected from Figure 1.7. The uncertainties reflect this, with the largest impact occurring at low reconstructed energy, as shown in Figures 8.15 and 8.16.

## DIS Cross Sections

Unlike the QE and RES interactions, the uncertainty of the deep inelastic cross section cannot be modeled using an axial mass term. Work by IceCube collaborators [129] have instead parametrized the uncertainty in the DIS events using comparisons between GENIE events and data from the NuTeV experiment [130]. The parametrization uses the Bjorken scaling factor,

$$x = \frac{Q^2}{2M\nu}, \quad (8.10)$$

where  $Q^2 = -q^2$  is the 4-momentum transfer,  $M$  is the nucleon mass, and  $\nu = E_{had}$  is the energy of the hadronic system [21]. The GENIE event rate can be corrected to match the NuTeV data using an empirical power law [129]:

$$w'_i = \begin{cases} (1 - 1.65125a)x^{-a}w_i & \nu \\ (1 - 1.8073a)x^{-a}w_i & \bar{\nu} \end{cases} \quad (8.11)$$

where  $a$  is  $0 \pm 0.0757$  for neutrinos and  $0 \pm 0.1008$  for antineutrinos. This method has been tested with the GRECO Level 7 dataset. The resulting uncertainties, shown in Figures 8.17 and 8.18, are small and have large degeneracies with other parameters. Because of the small size and degeneracy, these systematic uncertainties are not used in the fit.

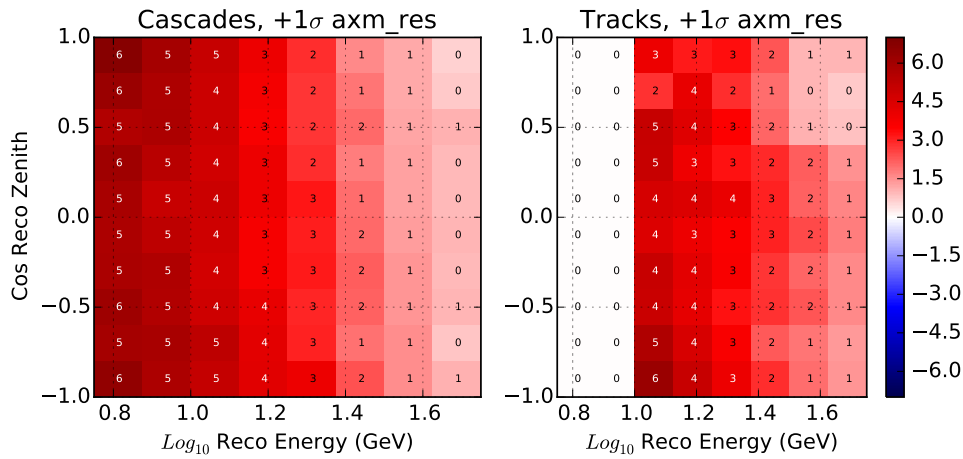


**Figure 8.16** – The effect of the axial mass  $M_a^{RES}$  uncertainty in the analysis histogram. The colorbar shows the percent change in rate per bin for a shift of  $1\sigma$  from the baseline value using the GENIE reweighting code.

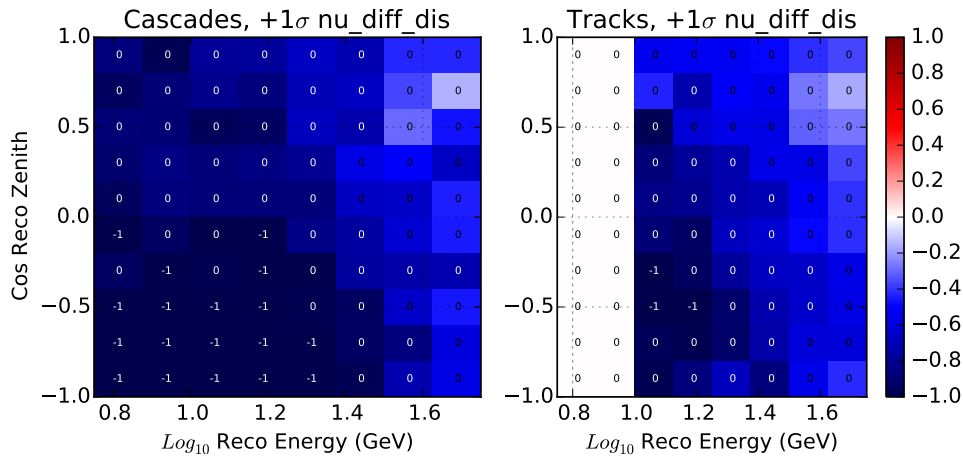


**Figure 8.17** – The effect of the DIS uncertainty for neutrinos in the analysis histogram. The colorbar shows the percent change in rate per bin for a shift of  $1\sigma$ . The effect is small and largely degenerate with other parameters.

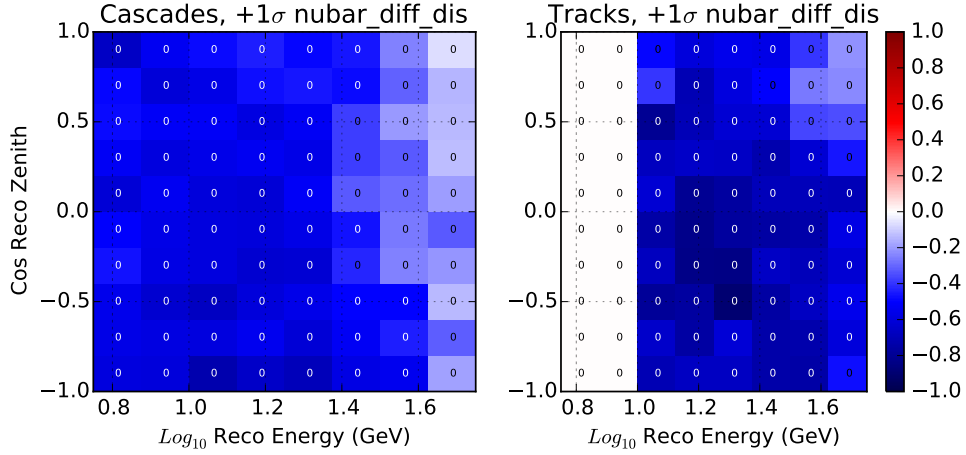


**Figure 8.18** – The effect of the DIS uncertainty for neutrinos in the analysis histogram. The colorbar shows the percent change in rate per bin for a shift of  $1\sigma$ . The effect is small and largely degenerate with other parameters.

### NC/CC Cross Section Ratio

IceCube is sensitive to both neutral current and charged current interactions. The uncertainty in the interaction cross section for the charged current is handled with the QE, RES, DIS uncertainties. To handle the uncertainty in the neutral current cross section, the normalization of neutral current interactions is fit in the tau appearance analysis. This normalization is measured relative to the charged current rates.

$$f'_{NC} = N_{NC} \cdot \frac{\sigma_{NC}}{\sigma_{CC}} \quad (8.12)$$

As in previous IceCube analyses, the neutral current normalization is fit with a prior of  $1.0 \pm 0.2$  [80, 81]. The effects are shown in Figure 8.19.

### 8.4.5 Detector Uncertainties

While the previous systematics uncertainties have been related to global physics parameters, the remainder are dedicated to understanding the uncertainties associated with the IceCube detector itself, such as the properties of the PMTs and the ice. These parameters, collectively referred to as the *detector uncertainties*, do not have analytic forms, but may affect the rate of events, the reconstruction properties of a given event, or both. The effect of these uncertainties is evaluated using dedicated Monte Carlo simulations.

The GRECO event selection uses a number of simulation sets, shown in Table 8.2 for signal and Table 8.3 for background, to characterize the effects of these Detector Uncertainties. Each set contains at least one simulation parameter changed from the baseline set and are run through the full GRECO processing.

### Coincident Fraction

The GENIE simulation sets are produced with exactly one neutrino interaction per event. In the actual detector, a fraction of triggered events will consist of a temporally coincident muon and neutrino pair which may be from the same air shower or from independent showers. These events are known as *coincident events*. In order to account for this

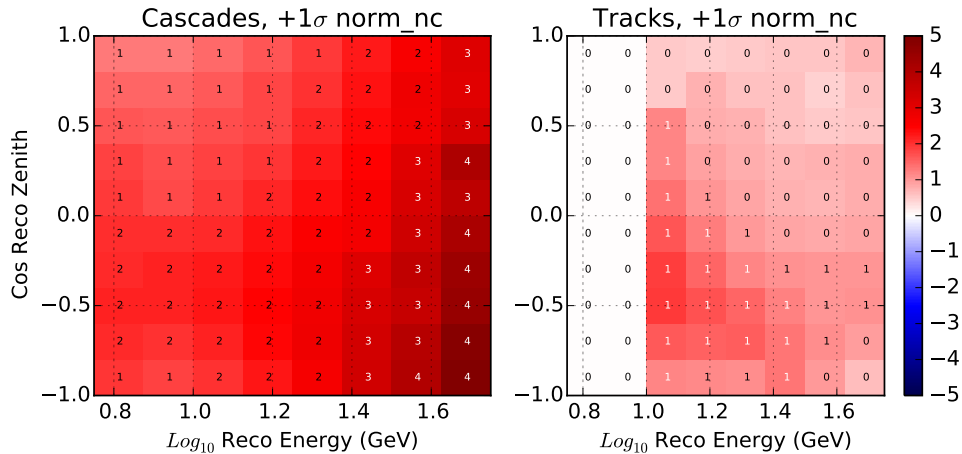


**Figure 8.19** – The effect of the neutral current normalization in the analysis histogram. The colorbar shows the percent change in rate per bin for a shift of 20%. The effect appears most strongly in the cascade-like sample.

possibility, a sample of such events were simulated with independent neutrino and muon generation. Every produced event contains at least one atmospheric muon in addition to exactly one neutrino interaction. By interpolating between this "100% coincident" sample and the standard "0% coincident" sets, the effect of the coincidences is included in the final analysis.

The GRECO event selection is designed to reject atmospheric muon-like events. Increasing the coincident event fraction leads to a lower total event rate, as events with muons are removed from the selection. In order to distinguish a change in the analysis histogram due to coincident events from a global normalization factor, the coincident event fraction is implemented to preserve the total number of events of each neutrino type. The effect of this systematic uncertainty on the binwise event rates in the final analysis is shown in Figure 8.20.

At Final Level, the true fraction of coincident events is unknown, but previous oscillation analyses have found no clear issues using the standard simulation sets assuming no coincident events. A derivation of the expected coincident event fraction using the atmospheric muon and neutrino rates and assuming the events are produced in independent air showers gives a coincident fraction of 10%. A prior is therefore implemented with a one-sided Gaussian distribution centered at 0% with a 10% width.

## DOM Efficiency

The *DOM efficiency* is a measure of the total uncertainty in the photon detection probability of IceCube DOMs relative to the expected PMT efficiency. Prior to deployment, measurements performed with 16 DOMs found an relative uncertainty of 7.7% on the efficiency of the IceCube DOMs [38]. DOMs measured in-situo using minimum ionizing muons in order to better account for local effects like cable shadowing and the glass-ice interface have found similar uncertainties for the PMT efficiency [131]. In this analysis, a conservative estimate of the uncertainty for the DOM efficiency,  $99\% \pm 10\%$ , is adopted. The difference between the two uncertainties has been tested and no impact on the tau neutrino appearance measurement was observed.

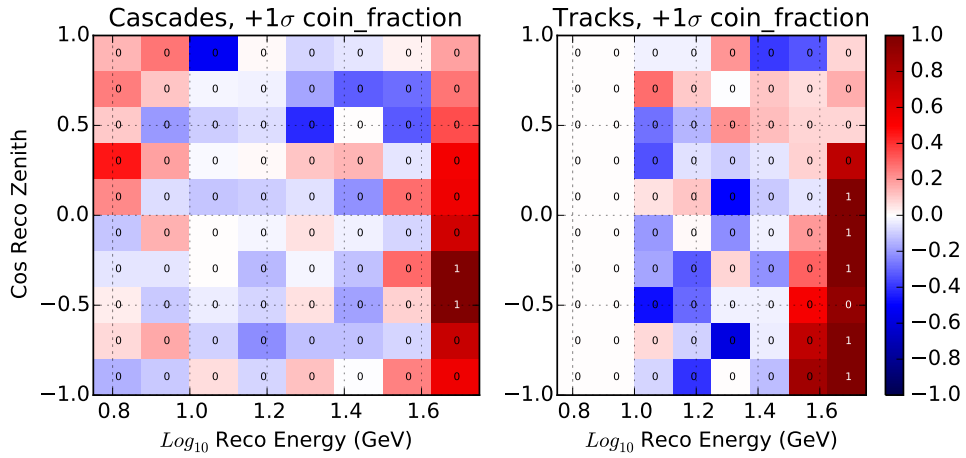


**Figure 8.20** – The effect of the coincident event rate in the analysis histogram. The colorbar shows the percent change in rate per bin for a shift of 10%. The parameter is implemented to be independently rate-preserving for each type of neutrino. The coincident event rate induces a small change in the rate of events at high energies.

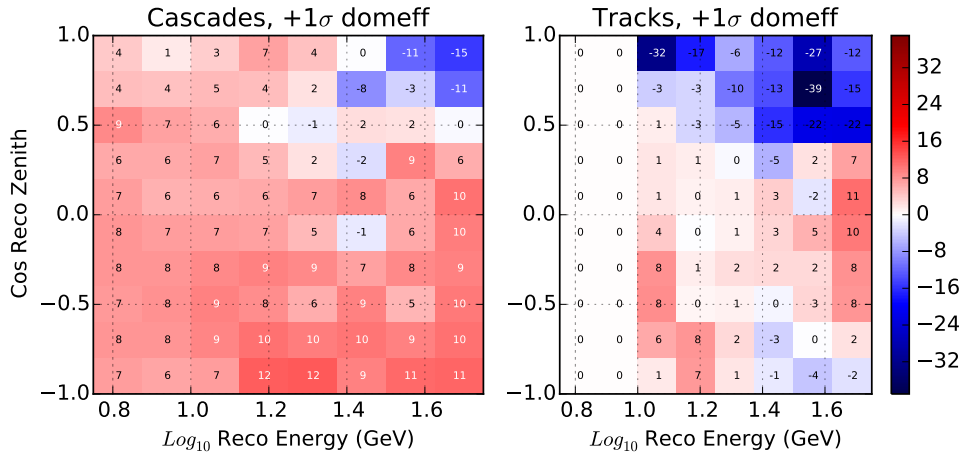


**Figure 8.21** – The effect of the DOM efficiency in the analysis histogram. The colorbar shows the percent change in rate per bin for a shift of 10%. The DOM efficiency increases the number of photons observed, improving both the reconstruction resolution and veto efficiency.

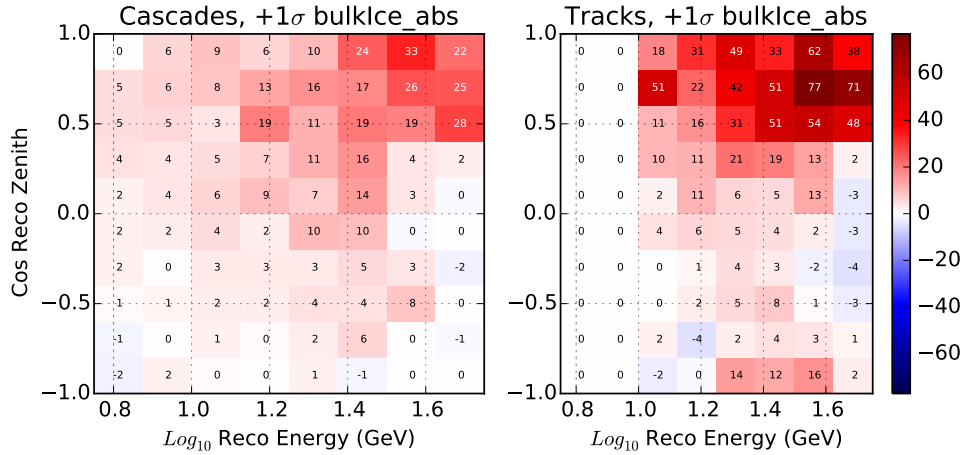


**Figure 8.22** – The effect of the absorption in the analysis histogram. The colorbar shows the percent change in rate per bin for a shift of 10%. The absorption stops photons before they reach DOMs and has similar effects as the DOM efficiency.

The DOM efficiency scales the quantum efficiency of observing photons incident at the DOM. A higher DOM efficiency leads to an increase in the number of observed photons at each DOM, granting more information about particle interactions in the ice. The improved knowledge of interactions improves the reconstruction of events, increasing neutrino event rates at Final Level and resulting in well-defined oscillation features in the reconstructed energy, zenith, and track length histograms used for oscillation measurements. In addition, higher DOM efficiency increases the number of hits observed along atmospheric muon tracks, yielding improved veto efficiency. The net effect of changing the DOM efficiency by 10% in the binwise expected event rates is shown in Figure 8.21.

### Bulk Absorption and Scattering

As described in Section 3.4, the bulk ice model used in IceCube is fit in-situ using data from the deployment and detector operation in a process similar to the one described in Section 5.4. The model consists of scattering and absorption coefficients fit as a function of depth within the detector. Uncertainties for these scattering and absorption coefficients, shown in Figure 3.10, provide a significant source of uncertainty for physics measurements in IceCube.

To handle these uncertainties at the analysis level, global scale factors are used to modify all scattering or absorption coefficients in the bulk ice model simultaneously. Using the most recent published uncertainties on our ice model, a total uncertainty of 10% is assumed for these global scale factors [87]. Three systematics sets of scaled scattering and absorption coefficients are used in the GRECO measurement of tau neutrino appearance, corresponding to sets with 10% larger absorption coefficients, 10% larger scattering coefficients, and a 7.1% reduction to both sets of coefficients.

The bulk ice uncertainties have not been tested in previous oscillation analyses [79, 80, 81]. but both parameters have significant impacts in the appearance analysis.

The absorption, shown in Figure 8.22, is dominated by effects due to atmospheric muons. This is due to the event selection: with weaker absorption (smaller coefficients), photons travel further in the ice and are more likely to be detected. The observation

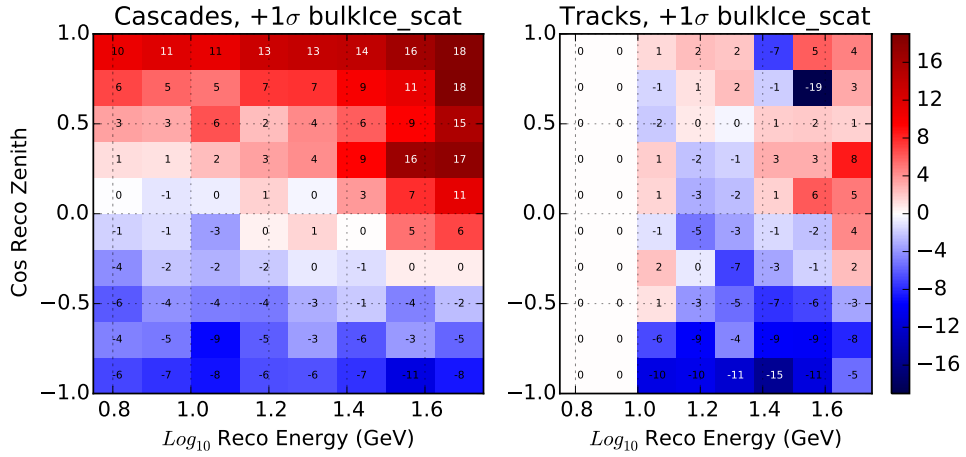


**Figure 8.23** – The effect of the scattering in the analysis histogram. The colorbar shows the percent change in rate per bin for a shift of 10%. The scattering changes the directions of photons as they propagate through the ice. Photons which scatter lose information about the source direction, leading to worse reconstructions.

of additional photons from the muon track improves the veto efficiency, leading to a significant decrease in the number of muons at Final Level.

The effect of the scattering is shown in Figure 8.23. A few bins in the downgoing track-like histogram show strong effects inconsistent with nearby bins. These bins arise due to statistical uncertainty in the parametrizations of the low statistics atmospheric muons sets. Other than these bins, the scattering does not appear to strongly affect the atmospheric muons.

In the neutrinos, the effects of the scattering are more important. In particular, stronger scattering (larger coefficients) lead to a reconstruction bias, with more events reconstructing as downgoing. This is a known effect of the reconstruction, where we use a version of the ice model which interprets off-time hits as being due to backscattered photons in a downgoing event.

### Hole Ice and Forward Scattering

While the bulk ice refers to the scattering and absorption properties of the entire interaction volume, additional care must be taken for the hole ice described in Sections 3.5 and 4.2.3.

The uncertainties associated with the hole ice are some of the most important systematic uncertainties in previous IceCube oscillation analyses [81]. The simulation of the hole ice model used here, discussed briefly in 4.2.3, requires two free parameters which will be referred to as the *hole ice* ( $p_1$  in Figure 4.2) and *forward scattering* ( $p_2$  in Figure 4.2) parameters.

The models of the angular acceptance were shown previously in Figure 4.2). The hole ice parameter, shown in Figure 8.24, modifies the efficiency of accepting photons incident from the horizon at each DOM while the forward scattering, shown in Figure 8.25, modifies only the acceptance of the very-forward region.

The effects of the two hole ice parameters show similar behavior to that of the scattering uncertainty in the bulk ice, as all three coefficients are modeling the scattering

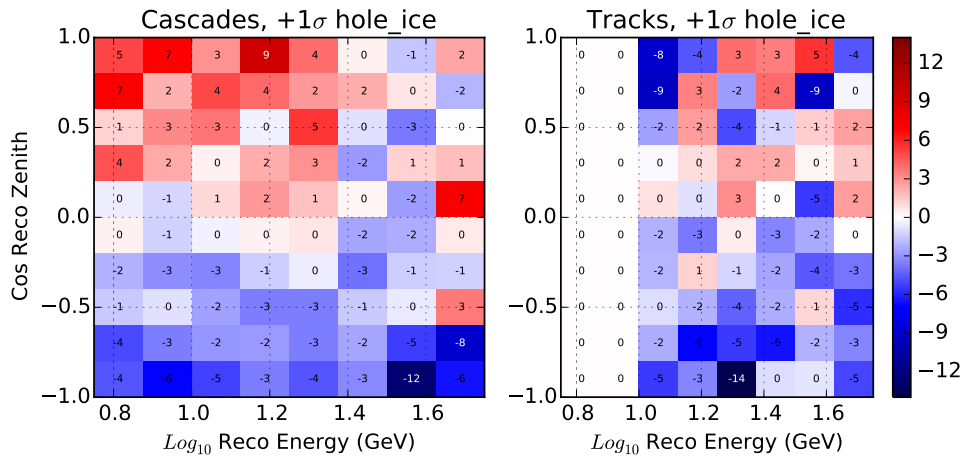


**Figure 8.24** – The effect of the hole ice systematic uncertainty in the analysis histogram. The colorbar shows the percent change in rate per bin for a shift of  $1\sigma$ . The hole ice parameter affects the efficiency of detecting photons at the side of the DOM. This parameter changes the angular distribution of photons at the DOM, leading to differences in the resolution of events.

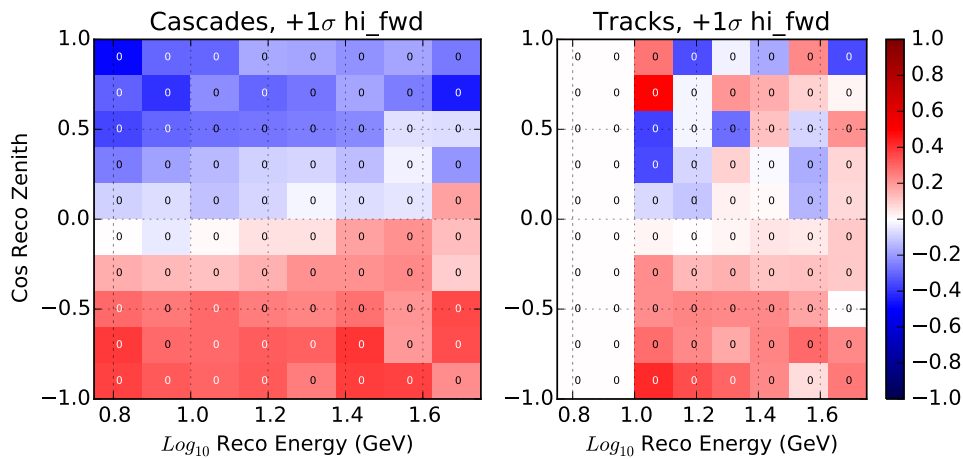


**Figure 8.25** – The effect of the forward scattering parameter in the analysis histogram. The colorbar shows the percent change in rate per bin for a shift of 10%. The forward scattering value affects the efficiency of detecting photons at the front of the DOM. This parameter changes the angular distribution of photons at the DOM, leading to differences in the resolution of events.

properties of different locations in the ice. Tests performed using the GRECO sample have shown that the three parameters are sufficiently distinct to include all three.

## 8.5 The Test Statistic for the Analysis

The measurement of tau appearance includes many systematic parameters. To obtain the best fit set of values, a minimization is performed using a  $\chi^2$  test statistic. The form of the  $\chi^2$ , which includes terms related to the limited simulation statistics available, is described here.

### 8.5.1 The $\chi^2$ Fit

The  $\chi^2$  is a test statistic used to describe the agreement between two binned histograms. In defining the  $\chi^2$ , the observed number of events in each bin of the histogram is assumed to be independently gaussian distributed with mean  $\mu = \sum_j^{Evs} w_j$  equal to the expected number of events in simulation.

$$P(x|\mu) = Ne^{-\frac{\left(x - \sum_j^{Evs} w_j\right)^2}{\sigma^2}} \quad (8.13)$$

where  $N$  is a normalization constant and  $x$  is the number of events observed in data. The variance within the bin is described by the Poisson uncertainty in the bin calculated as the sum of the weights

$$\sigma_P^2 = \mu = \sum_j^{Evs} w_j \quad (8.14)$$

The  $\chi^2$  may be defined by calculating the log-likelihood of the gaussian distribution.

$$\log(L(\mu|x)) = \log(N) + \frac{\left(x - \sum_j^{Evs} w_j\right)^2}{\sigma_P^2} \quad (8.15)$$

The first term is a constant and can be dropped. The remainder gives the definition of the standard  $\chi^2$  test statistic used for minimization. This is summed over all bins  $i$  to obtain a single value describing the agreement between the data and expectation. The standard  $\chi^2$  calculation is then

$$\chi^2 = \sum_i^{bins} \frac{\left(x_i - \sum_j^{Evs} w_{ij}\right)^2}{\sum_j^{Evs} w_{ij}}. \quad (8.16)$$

### 8.5.2 Finite Statistics

The  $\chi^2$  distribution implicitly assumes that the dominant source of uncertainty at the best-fit point comes from the statistical fluctuations of the data around the true distribution represented by the Monte Carlo simulation. The statistical properties of the background simulation sets cannot be ignored for the tau neutrino appearance analysis, however.

The statistical fluctuations of the simulation are negligible when the simulated livetime provides at least an order of magnitude larger simulation statistics than expected from the data itself. Additional simulated statistics may be produced to reduce fluctuations in the Monte Carlo histograms. In the situation where this is infeasible, modifications to the likelihood space itself can be used to account for the additional uncertainties. For this

analysis, the statistical uncertainty due to finite simulation statistics,  $\sigma_{FS}^2 = \sum_j^{Evs} w_j^2$ , is added to the weighted uncertainties in quadrature. This results in a modification of Equation 8.14.

$$\sigma^2 = \sigma_P^2 + \sigma_{FS}^2 = \sum_j^{Evs} w_j + w_j^2 \quad (8.17)$$

This changes the definition of the  $\chi^2$  to

$$\chi_{FS}^2 = \sum_i^{bins} \frac{\left(x_i - \sum_j^{Evs} w_{ij}\right)^2}{\sum_j^{Evs} w_{ij} + \sum_j^{Evs} w_{ij}^2} \quad (8.18)$$

where "finite statistics" subscript  $FS$  has been introduced to distinguish this value from the standard  $\chi^2$ . This can be rewritten explicitly in terms of the atmospheric muon and neutrino samples

$$\chi_{FS}^2 = \sum_i^{bins} \frac{\left(x_i - \sum_j^{Evs} \left((w_{ij})_\nu - (w_{ij})_\mu\right)\right)^2}{\sum_j^{Evs} (w_{ij})_\nu + (w_{ij})_\mu + \left(w_{ij}^2\right)_\nu + \left(w_{ij}^2\right)_\mu} \quad (8.19)$$

Test minimizations performed with the  $\chi^2$  form of Equation 8.18 presented a unique problem. Because the muon statistical uncertainty is large, fit parameters which increase the weight of muon events increase the denominator of the  $\chi^2$ . This was found to occur with the DOM efficiency and absorption systematic parameters, leading to a runaway minimization in Monte Carlo trials where the DOM efficiency was shifted by more than  $5\sigma$  and the  $N_{\nu_\tau}$  was biased by more than 40%.

In order to prevent this runaway effect, a further modification of the  $\chi^2$  is required. For this analysis, the total scale of the statistical uncertainty due to atmospheric muons,  $\sigma_{FS,\mu}^2$ , is fixed the seed values of the fit.

$$N_i^\mu = \frac{\left(\sum_j^{Evs} w_{ij}^2\right)_{Seed}}{\sum_j^{Evs} w_{ij}^2} \quad (8.20)$$

Inserting this term into the denominator, one obtains the form of the  $\chi_{FS}^2$

$$\chi_{FS}^2 = \sum_i^{bins} \frac{\left(x_i - \sum_j^{Evs} w_{ij}\right)^2}{\sum_j^{Evs} w_j + \left(\sum_j^{Evs} w_{ij}^2\right)_\nu + N_i^\mu \left(\sum_j^{Evs} w_{ij}^2\right)_\mu} \quad (8.21)$$

With this modification, the  $\chi^2$  minimization is well-behaved.

### 8.5.3 Fit Priors

Prior knowledge of some systematics parameters can be included in the fit using a *prior*. Priors are additional terms included multiplicatively (additively) in the likelihood (log-likelihood) calculation that represent one's belief about the likely value of the systematics. These often take the form of a gaussian distribution with mean  $\mu$  and variance  $\sigma^2$  given by external measurements. In the search for appearance, most priors

are handled assuming a standard gaussian form. For a systematic  $m$  with value  $x_m$ , these additional terms take the form

$$\chi_m^2 = \frac{(x_m - \mu)^2}{\sigma_m^2} \quad (8.22)$$

These additional terms are added to Equation 8.21 in order to calculate the final  $\chi_{FS}^2$  used in the minimization for this analysis.

$$\chi_{Total}^2 = \sum_i^{bins} (\chi_{FS}^2)_i + \sum_m^{syst} \chi_m^2 \quad (8.23)$$

A list of priors is shown in Table 8.5. Note that the coincident event fraction is effectively a one-sided Gaussian due to physical constraints on the value.

Systematic	Unit	Type	Baseline/Seed Value	Prior	Allowed Range	Reference
Physics Parameter	$N_{\nu\tau}$	Analytic	1.0	-	0.0 - 2.0	-
Oscillations	$\Delta m_{3j}^2$	Analytic	2.526	-	2.0 - 3.0	[58]
	$\text{Sin}^2\theta_{23}$	Analytic	0.440 (NO), 0.66 (IO)	-	0.0 - 1.0	[58]
Total Rates	$N_\nu, N_\mu$	Analytic	2.25	-	0.0 - 10.0	-
Cross-section	Axial Mass (QE)	Analytic	0.0	$0.0 \pm 1.0$	-5.0 - 5.0	[94]
	Axial Mass (RES)	Analytic	0.0	$0.0 \pm 1.0$	-5.0 - 5.0	[94]
	$N_{\nu NC}$	Analytic	1.0	$1.0 \pm 0.2$	0.0 - 2.0	[81]
Flux	$\gamma_\nu$	Analytic	0.0	$0.0 \pm 0.10$	-0.50 - 0.50	[19]
	$\gamma_\mu$	Analytic	0.0	$0.0 \pm 1.0$	-5.0 - 5.0	[127]
	Up/Horizontal Ratio	Analytic	0.0	$0.0 \pm 1.0$	-5.0 - 5.0	[126]
	$\nu/\bar{\nu}$ Ratio	Analytic	0.0	$0.0 \pm 1.0$	-5.0 - 5.0	[126]
	$\Phi_{\nu_e}$	Analytic	1.0	$1.0 \pm 0.05$	0.8 - 1.2	[126]
	Coincident Fraction	Non-analytic	0.0	$0.0 + 0.10$	0.0 - 1.0	-
Detector	DOM Efficiency	Non-analytic	1.0	$1.0 \pm 0.1$	0.7 - 1.3	[73, 131]
	Hole Ice	Non-analytic	0.25	$0.25 \pm 0.10$	0.0 - 0.5	[81]
	Forward Scattering	Non-analytic	0.0	-	-5.0 - 5.0	[81]
	Absorption	Non-analytic	1.0	$1.0 \pm 0.1$	0.5 - 1.5	[73]
	Scattering	Non-analytic	1.0	$1.0 \pm 0.1$	0.5 - 1.5	[73]

**Table 8.5** – Priors and allowed ranges for each systematic included in this analysis.

### 8.5.4 Fitting Code

In order to understand the expected sensitivity of this analysis, a software fitting package previously used to fit the  $\nu_\mu$  disappearance is used [79, 80, 81].

The code, known as *OscFit*, works in multiple stages. After separating the simulation into separate channels consisting of  $\nu_e^{CC}$ ,  $\nu_\mu^{CC}$ ,  $\nu_\tau^{CC}$ ,  $\nu^{NC}$ ,  $\mu_{atm}$ , and accidental triggers, the analytic systematics are applied. These systematics solely rely on information about the particle interaction in order to calculate correction factors to the event weights and are not sensitive to the order of application. The oscillation calculations are performed as analytic systematics based on the Prob3++ code [56] to calculate the full three-flavor unitary oscillations including matter effects within the Earth using a reference model of the Earth [99].

When including the neutral current interactions from tau neutrino events in the signal definition and fitting  $N_\tau^{NC+CC}$ , the neutral current events are reweighted for oscillations at this stage. The *OscFit* code assumes the neutral current interaction rate is unaffected by oscillations and instead models neutral current interactions using only muon neutrino and electron neutrino simulated neutral current events. Because no charged leptons are produced in the neutral current interactions, no differences in event topology are expected based on flavor of neutrino interaction.

For the purposes of this analysis, the neutral current interactions from electron neutrino and muon neutrino events are used to model the effect of the tau neutrino neutral current events. The Prob3++ code calculates oscillation probabilities for the muon and electron neutrino events to oscillate to tau neutrinos. These probabilities are used to identify a sample of neutral current events used to model the tau neutrino neutral current interactions.

The modification to the muon neutrino neutral current event weight given the tau neutrino normalization,  $N_{\nu_\tau}$ , is then given by

$$\begin{aligned}
 w'_{i,\nu_\mu^{NC}} &= w_{i,\nu_\mu^{NC}} \\
 &\quad - w_{i,\nu_\mu^{NC}} P_{\nu_\mu \rightarrow \nu_\tau} \left( E_i, \cos(\theta_i) | \Delta m_{3j}^2, \theta_{23} \right) \\
 &\quad + N_{\nu_\tau}^{NC+CC} w_{i,\nu_\mu^{NC}} P_{\nu_\mu \rightarrow \nu_\tau} \left( E_i, \cos(\theta_i) | \Delta m_{3j}^2, \theta_{23} \right)
 \end{aligned} \tag{8.24}$$

where  $w_{i,\nu_\mu^{NC}}$  and  $w'_{i,\nu_\mu^{NC}}$  are event weights before and after application of the neutral current oscillations,  $E_i$  and  $\cos(\theta_i)$  are the energy and zenith angle of the event, and  $\Delta m_{3j}^2$  and  $\theta_{23}$  are the atmospheric mass splitting and mixing angle respectively. The first term corresponds to the unoscillated muon neutrino neutral current weight. The second and third terms correspond to the muon neutrino disappearance and tau neutrino appearance in the neutral current channel respectively. The oscillation weighting of the neutral current electron neutrinos events follows the same form.

After oscillations and other analytic systematic uncertainties are applied, the events are binned in energy, zenith, and track length with one histogram per simulated channel type. The non-analytic systematic uncertainties are applied to the each of the binned templates bin-by-bin using hyperplanes calculated as described in Section 8.3.

Once all systematic uncertainties have been applied, the normalization terms representing the overall scale factors for the neutrino rate,  $N_\nu$ , the muon rate,  $N_\mu$ , and the accidental rate,  $N_{noise}$ , are multiplied to the respective histograms. The final histograms are summed together to form the final simulation expectation to be compared to the data using the  $\chi_{FS}^2$  described in Equation 8.21.

The value of the  $\chi_{FS}^2$  is minimized as a function of the various systematics using the iMinuit2 package [106, 105]. The minimization continues until the requested tolerance,  $10^{-16}$ , is reached by the minimizer, after which the best fit histogram and systematics values are returned to the user.

## 8.6 Expected Sensitivity to Appearance

With the full set of systematics included, the *sensitivity* of the analysis is calculated. The sensitivity is a measure of the expected result and can be performed with simulated events prior to the final fit to data.

To evaluate the expected sensitivity of this analysis, the OscFit code is used to find the best-fit value of the  $\chi_{FS}^2$ . Multiple methods are used to evaluate both the average expected sensitivity and range of variation of the sensitivity due to both the data and simulation statistics. A summary of the results using all methods is shown in Figure 8.26. Each component will be described in turn.

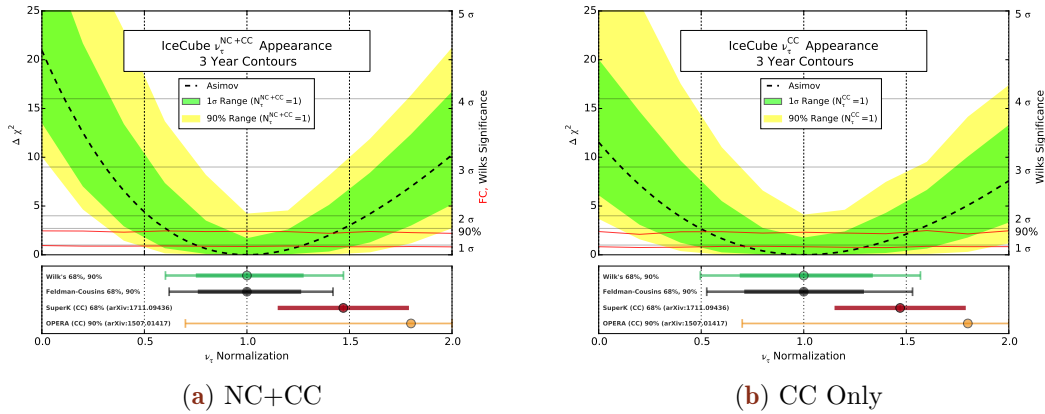


**Figure 8.26** – The sensitivity of this analysis in the (a) NC+CC and (b) CC-only channel. The top plot shows the Asimov expectation (black dotted line) and the Brazilian flag (green, yellow bands). The significances assuming Wilk’s theorem (gray horizontal lines) and Feldman-Cousins (red horizontal lines) are also shown. The bottom plot shows the expected 1 $\sigma$  and 90% ranges for Wilks theorem and Feldman-Cousins compared to the most recent results from the OPERA and Super-Kamiokande analyses.

### 8.6.1 The Asimov Dataset

The first method, known as the *Asimov* expectation [132], begins by creating the expected histogram using baseline values of the systematics and oscillations. The produced histogram, representing an exact PDF of the expected events, is then used as an estimate of the data. A scan is performed over values of  $N_{\nu_\tau}$ , minimizing the  $\chi_{FS}^2$  at each point to produce a contour. A final minimization is performed allowing the minimizer to identify the global best-fit value of  $N_{\nu_\tau}$ .

The final expected sensitivity in the Asimov approach is given by calculating the  $\Delta\chi^2$  between the values of the  $\chi_{FS}^2$  at each point and the global best fit.

$$\Delta\chi^2(N_{\nu_\tau}) = \chi_{FS}^2(N_{\nu_\tau}) - \chi_{FS}^2(N_{\nu_\tau}^{Global}) \quad (8.25)$$

The value of  $\Delta\chi_{FS}^2$  as a function of  $N_{\nu_\tau}$  is shown by the dotted black line in Figure 8.26. These values may be converted into expected significance levels using the procedure described in Section 8.6.2.

### 8.6.2 The Brazilian Flag

The second method, producing what is known as a *Brazilian flag* plot due to the color scheme, provides an estimate of the statistical uncertainty on the Asimov sensitivity. The production of a Brazilian flag begins with the production of a pseudo-data histogram from the Asimov histogram.

Because the simulation sets used here have significant uncertainties due to limited simulation statistics in the background samples, the first step is to vary the event rate in each bin within the statistical uncertainties of the Monte Carlo.

A new realization of the simulation histogram is produced by sampling new rates in each bin using a gaussian distribution with mean  $\mu_i = \sum_j^{Evs} w_{ij}$  and variance  $\sigma_i^{MC}$  given by

$$\sigma_i^2 = \sqrt{\sum_j^{Evs} w_{ij}^2}. \quad (8.26)$$

The new histograms are then summed together and a final rate in each bin is sampled from a Poisson distribution with mean equal to the new expectation, creating a representation of one possible realization of the data in the analysis. The OscFit minimization then proceeds as described in the Asimov case for each of 500 realizations of pseudo-data, with the calculation of the  $\Delta\chi^2$  as described in Equation 8.25. The Brazilian flag shows the  $1\sigma$  and 90% range of  $\Delta\chi^2$  values at each value of  $N_{\nu_\tau}$ . This provides a graphical representation, shown in the colored bands of Figure 8.26, of the expected range of variation of the sensitivity given solely statistical uncertainties.

## 8.7 Feldman-Cousins vs Wilk's Theorem

Estimates of the sensitivity of the analysis were performed using a theorem by Samuel S. Wilks [133]. The theorem describes the distribution of the log-likelihood ratio when fits form a "nested model" where fit parameters used in one fit hypothesis,  $H_0$ , form a complete subset of those used in another fit hypothesis,  $H$ . If the two likelihoods used in the log-likelihood ratio differ by  $N$  parameters, Wilk's theorem states that the distribution of the test statistic  $\Delta\chi^2$  will asymptotically approach a chi-squared distribution with  $N$  degrees of freedom.

In the case of the measurement of tau neutrino appearance, fits are performed twice in order to obtain the log-likelihood ratio: once with the value of  $N_{\nu_\tau}$  fixed to various points and once with  $N_{\nu_\tau}$  freely floating. The  $\Delta\chi^2$  is calculated at each fit point relative to the overall best-fit likelihood using Equation 8.25. These two fits form a nested model with  $N=1$ , allowing the application of Wilk's theorem to estimate significances.

Wilk's theorem gives a useful estimate of the significance and requires negligible additional computational power. However, the theorem states only an asymptotic limit and assumes that the nested hypotheses are from boundaries and have no discrete steps. Evaluation of the applicability of Wilk's theorem requires a more robust analysis using Monte Carlo trials.

A procedure, introduced by Gary Feldman and Robert Cousins [134], can be applied instead. Instead of assuming a number of degrees of freedom, the Feldman-Cousins procedure requires directly using the distribution of the  $\Delta\chi_{FS}^2$  test statistic in order

to evaluate the significance. For IceCube oscillation results, a method similar to the procedure by Feldman and Cousins is used [81].

To begin, a value of  $N_{\nu_\tau}^{True}$  is selected. Monte Carlo trials are produced with this true value and the  $\Delta\chi^2$  between the best-fit value of  $N_{\nu_\tau}$  and  $N_{\nu_\tau}^{True}$  for each trial is calculated. The distribution of the  $\Delta\chi_{FS}^2$  values is used to identify the value of  $\Delta\chi_{FS}^2$  below which  $P_{i=1\sigma}(\Delta\chi_{FS}^2) \approx 68.27\%$  of trials lie. This value is the  $1\sigma$  level for the chosen value of  $N_{\nu_\tau}^{True}$ . The procedure is repeated for each required value of  $N_{\nu_\tau}^{True}$  and different significance levels  $i$ .

Examples of the likelihood ratio distribution for various values of  $N_{\nu_\tau}^{True}$  are shown in Figure 8.27. A  $\chi^2$  distribution with 1 degree of freedom is overlaid, showing the expected distribution assuming Wilk's theorem. The difference in location of the 90% level from Wilks (green) and Feldman-Cousins (red) is also shown. The distributions show a preference for a slightly narrower distribution than expected from Wilk's theorem. The difference indicates that the Feldman-Cousins procedure is necessary to correctly characterize the final result.

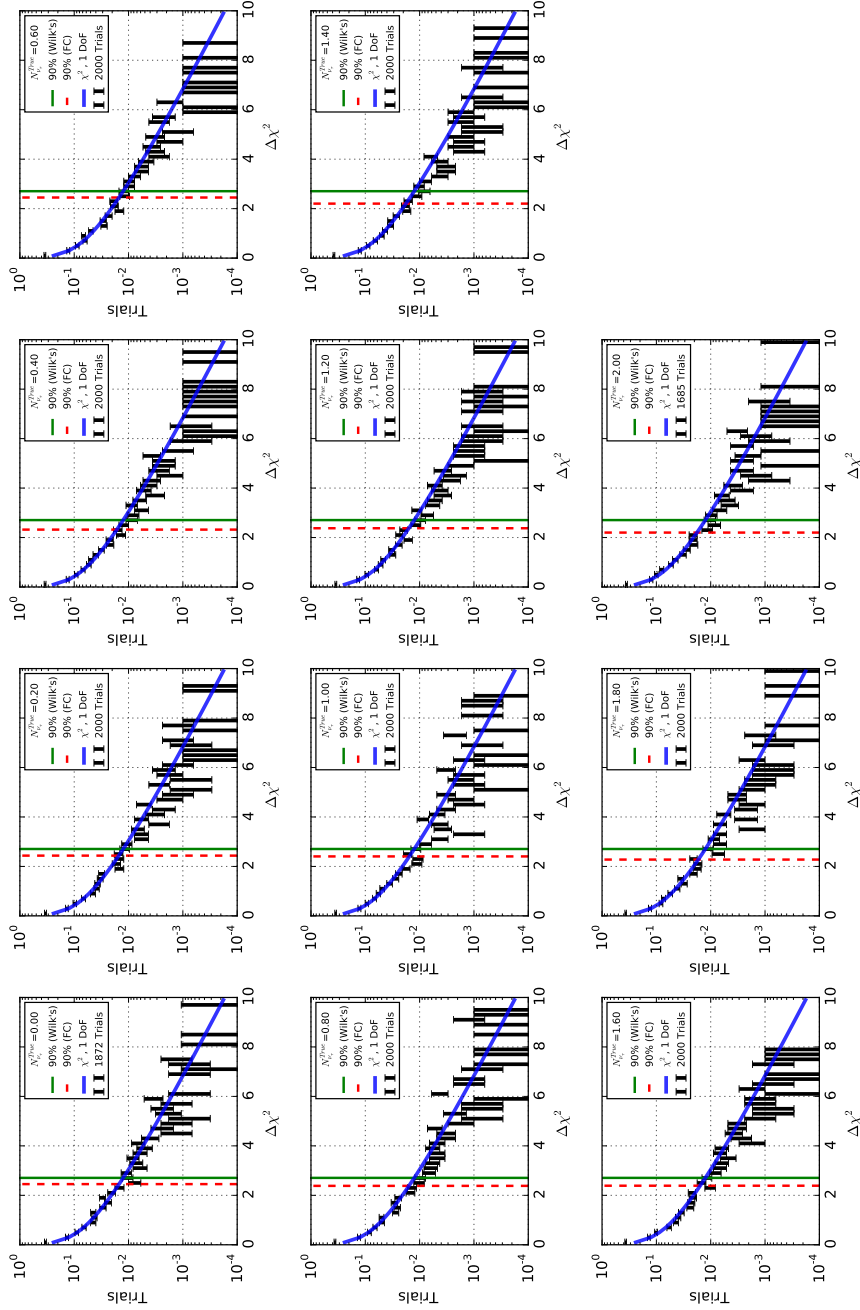


**Figure 8.27** – The distributions the  $\Delta\chi_{FS}^2$  for 11 points in  $N_{\nu\tau}^{True}$  in the NC+CC fit. The assumption of 1 degree of freedom from Wilk's theorem is tested at the location of  $(\Delta\chi_{FS}^2)_{90\%}$  for each point. The distribution calculated from Monte Carlo trials is narrower than that predicted by Wilk's theorem, indicating that a more complete treatment with the Feldman-Cousins procedure is necessary.

The evaluated  $(\Delta\chi_{FS}^2)_i$  are limited to the discrete values chosen in  $N_{\nu\tau}^{True}$ . In order to obtain a continuous model, a cubic spline is used to interpolate the values of  $(\Delta\chi_{FS}^2)_i$  as a function of  $N_{\nu\tau}^{True}$ . Similarly, the contour from data fit to a cubic spline for interpolation. The crossing points of the two splines is the best estimate for the uncertainty of the final result.

The procedure does not rely on assumptions about the distribution of the  $\Delta\chi_{FS}^2$  values and works in cases where the likelihood ratio distribution is not chi-squared distributed. The number of trials required to reduce the effect of statistical fluctuations in the evaluation, however, can make such evaluations prohibitively expensive.

A total of 1000 trials at each point are evaluated for the fits to both  $N_{\nu\tau}^{CC}$  and  $N_{\nu\tau}^{NC+CC}$ . All trials were produced assuming the baseline values of each systematic and with  $N_{\nu\tau} = 1$ . The resulting values of  $(\Delta\chi_{FS}^2)_{FC}^i$  are shown in the red lines in Figure 8.26.

## 8.8 Impact of Systematic Uncertainties

There are various ways to measure the impact of the included systematics in this analysis. Described here are methods to evaluate, in order of increasing importance, the total systematics impact, the impact of each systematic individually, the correlation between systematics, and the effect of non-baseline values. Each of these test different aspects of the sensitivity and all are included for completeness.

### Total Impact of Systematic Uncertainties

The total impact of the systematics on the sensitivity is measured by comparing the total Asimov sensitivity to an Asimov sensitivity calculated using no systematic uncertainties. This is shown at the bottom of Figure 8.28. It is clear from the comparison that the analysis is very sensitive to the included systematics set.

### N+1 Tests: Sensitivity of Analysis to Systematic

A different test is also possible: Instead of calculating likelihoods with no systematic uncertainties included, a single systematic uncertainty is used at a time. This test, called an N+1 test for the addition of one uncertainty at a time, yields useful information on a sample's sensitivity to single systematic parameters. The results of the N+1 tests are shown in Figure 8.28.

A small change in sensitivity between the "no systematic uncertainties" case above and an N+1 Asimov sensitivity may have two possible explanations. The first that the current analysis is unaffected by changes in the systematic parameter, implying that the systematic uncertainty should be investigated for removal in the analysis. The second possibility is that the systematic may have correlations with other parameters in order to produce an effect. The second case is more difficult to diagnose, but further tests are possible.

### N-1 Tests: Redundancy Between Systematics

In contrast to the N+1 tests, N-1 tests start with the full suite of systematics included. One systematic parameter is fixed to the baseline value and removed from the fit prior to minimization of the  $\Delta\chi^2$ . The change in the expected result, shown in Figure 8.29, allows the investigation of redundancy between systematic uncertainties. If, for example,

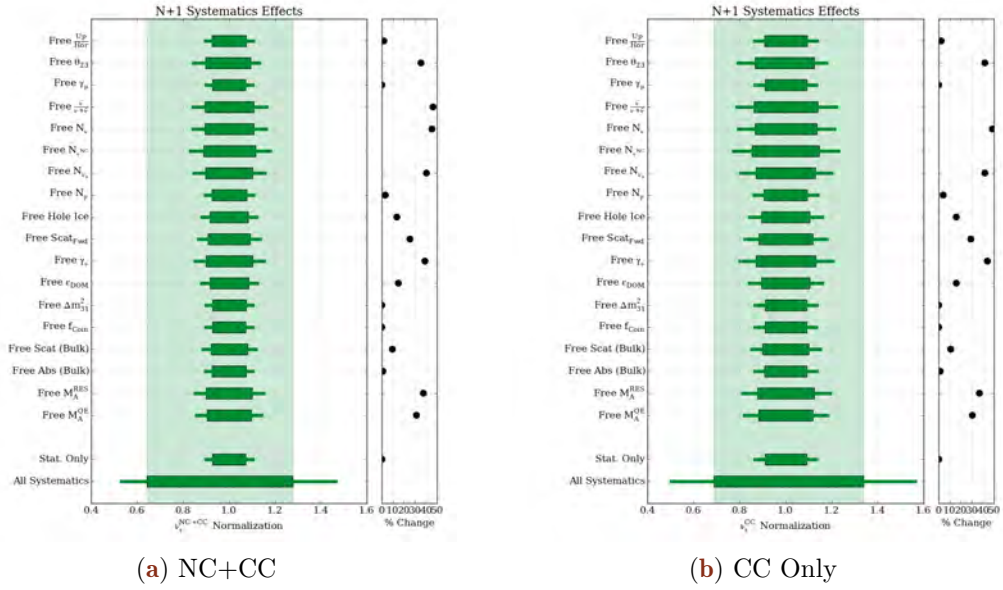


**Figure 8.28** – The N+1 parameter tests for (a) the NC+CC fit and (b) the CC-only fit. Only one parameter is allowed to move at a time. The change in the  $1\sigma$  and 90% expected confidence intervals give an indication of the strength of each systematic parameter in isolation.

two systematic parameters have similar effects in the final histogram, then the N-1 test will show no change in sensitivity due to the removal of one.

The redundancy tests show that the analysis is most strongly affected by the mass splitting  $\Delta m_{31}^2$ , the  $\nu/\bar{\nu}$  ratio, and the forward scattering in the hole ice model. The up/horizontal ratio, electron neutrino flux normalization, and muon spectral index all have negligible impact in the analysis according to the redundancy tests.

It is also possible that the analysis is strongly sensitive to the value of the systematic and is unlikely to move from the baseline value. These tests can be useful in identifying redundant parameters for removal, although with the caveat that combinations of parameters are not tested. After removal of multiple redundant parameters, the updated Asimov sensitivity should be tested once again to verify that the combination of removed parameters remains irrelevant for the fit. This procedure was used to remove the effects of the DIS uncertainties discussed in Sections 8.4.3. No further parameters have been removed from the tau neutrino appearance fit.

### "Hidden Potential" Tests: Non-Baseline Values

Both the N+1 and N-1 test suffer from a particular flaw. Both fail to test the analysis for exceptionally strong sensitivity to particular systematic uncertainties. In order to identify these parameters, the "hidden potential" test has been proposed. In this test, the Asimov sensitivity of the full analysis containing all proposed systematics is used as a baseline. Each systematic is then fixed, one at a time, off of the baseline value before rerunning the minimization. The parameters with priors are fixed to one standard deviation from the prior mean. The change in the sensitivity gives an indirect measure of the strength of the systematic effect in the analysis. If no change is observed, the parameter is likely to be redundant and may be investigated for removal from the analysis.

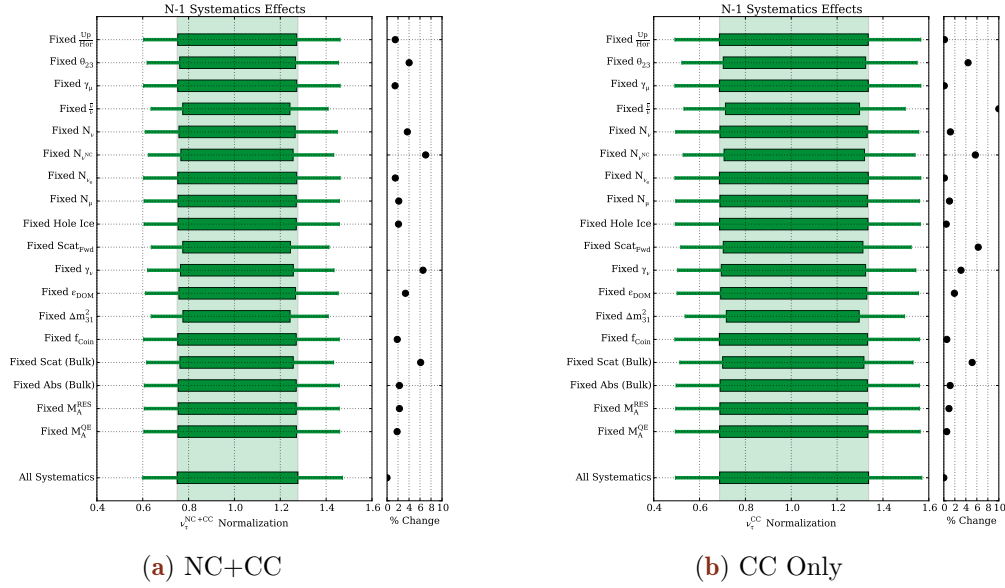


**Figure 8.29** – The N-1 redundancy tests for (a) the NC+CC fit and (b) the CC-only fit. Each parameter is held fixed at the baseline value and the change in the  $1\sigma$  and 90% expected confidence intervals are tested to identify the most important systematic parameters.

## 8.9 Fitting Data

Icecube analyses are developed *blindly* in order to minimize bias. A blind analysis limits potential bias in a measurement by either obfuscating the final measurement parameters or limiting the sensitivity of tests including data. Oscillation analyses using DeepCore use a staged blind analysis approach.

The initial stage, testing with a small sample of the data to detect software issues, is referred to as a *burn sample* test. The remaining stages in an IceCube oscillation analysis consist of *blind fits*, where the full dataset is fit while physics parameters are blinded, and the final *unblinding*, in which the best fit parameters are revealed. These stages will be discussed in turn.

### 8.9.1 Burn Sample Fits

The burn sample used in the search for appearance consisted of 8.7 days of livetime. A total of 1000 events were found in this burn sample, which was created and tested before the GRECO Level 7 cuts were finalized.

The best fit value of the burn sample was  $N_{\nu_\tau}^{CC} = 0$ . When the normalization was allowed to move into unphysical values of the normalization, the best fit moved to  $N_{\nu_\tau}^{CC} = 1.23$ . One thousand Monte Carlo trials were produced to evaluate the probability of seeing a result more extreme than the unphysical result in the burn sample. Of the 1000 trials, 14.8% had a value more negative than -1.23, indicating that this is a common occurrence with so little livetime.

Most systematics implemented at the time of the blind fits returned reasonable values. There was one notable exception: the mass splitting  $\Delta m_{31}^2$  returned a value of  $3.19 \cdot 10^{-3} eV^2$ . This value was well inside the expected range for the burn sample fits. At a value of  $N_{\nu_\tau}^{CC} = 1.0$ , the mass splitting fit to  $\Delta m_{31}^2 = 2.4 \cdot 10^{-3} eV^2$ , in good agreement with the global best fit value,  $2.526 \cdot 10^{-3} eV^2$ .

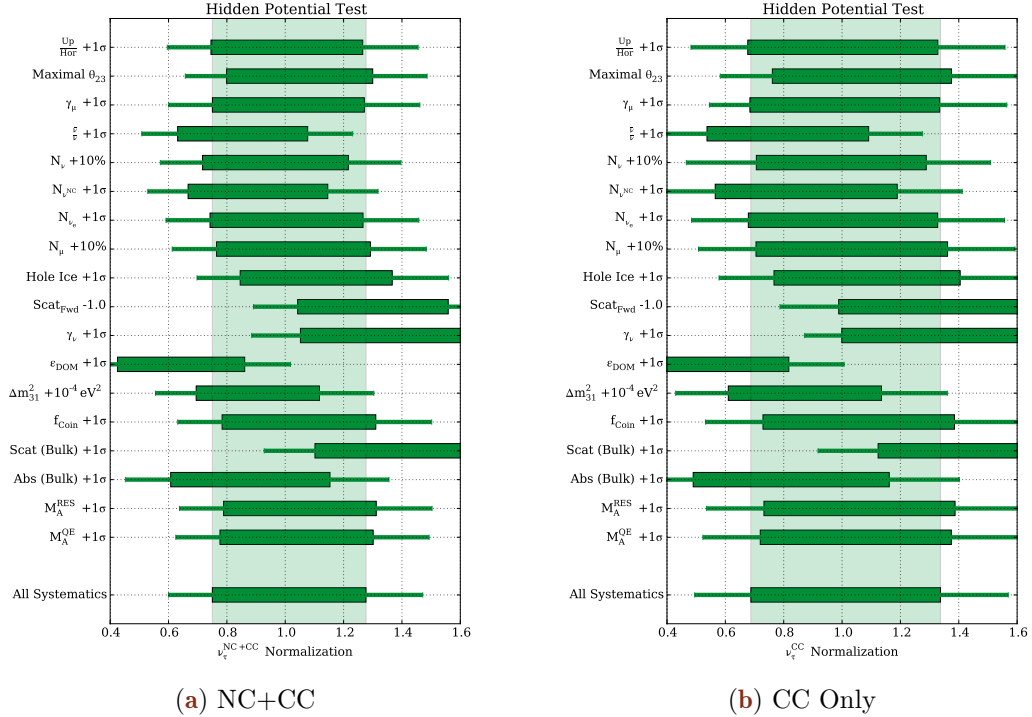


**Figure 8.30** – The hidden potential tests for (a) the NC+CC fit and (b) the CC-only fit. Each parameter is held fixed off the baseline value and the change in the  $1\sigma$  and 90% expected confidence intervals are tested to identify the most important systematics parameters. If this test shows no impact, mismodeling of the systematic uncertainty has negligible impact on the final analysis.

### 8.9.2 Blind Fits: Checking the Goodness-of-Fit

Once the burn sample tests are complete, the next stage is to perform what is known as a *blind fit*. The concept, developed for oscillation analyses in IceCube, exists as an intermediate stage between the low-sensitivity burn sample tests and the final fit.

Unlike the burn sample fits, the blind fit uses the full data sample for testing. All systematics are included in the fit. The final physics parameters, in this case the oscillation parameters,  $\Delta m_{31}^2$  and  $\theta_{23}$ , and the value of  $N_{\nu\tau}$ , are allowed to fit freely, but the final results are restricted and cannot be viewed. The goodness-of-fit and systematics values are free for investigation.

The blind fit exists in order to identify systematic disagreements between data and simulation. Investigations of poor agreement are performed blindly without knowledge of the impact on the physics parameters.

Analyzers are free to move onto a request for full unblinding if the goodness-of-fit exceeds 5%. If the goodness-of-fit is significantly lower than this limit, the sample and fit must be investigated further to identify any potential issues or oversights. If no issues are discovered, analyzers can move to a full unblinding request.

The goodness-of-fit, known more informally as the *p-value* associated with the fit, is calculated from an ensemble of Monte Carlo trials. The fraction of trials with  $\chi_{FS}^2$  larger than that observed in data gives the first p-value.

If the fit is particularly poor, a large number of trials may be necessary in order to calculate an accurate p-value. In these cases, the a  $\chi^2$  distribution can be fit to the trials distribution to provide an estimate of the p-value of the fit.

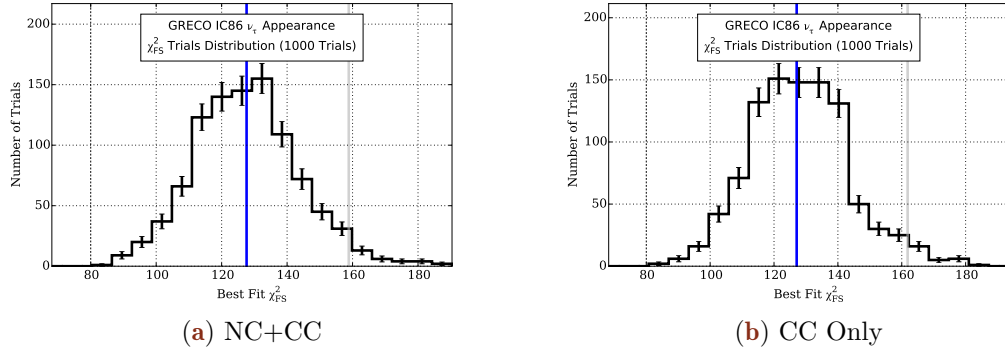


**Figure 8.31** – Goodness of fit in the appearance search. The trials distribution, shown in black, is used to calculate the pvalue. The grey line shows the location corresponding to a 5% p-value. The blue line shows the value of  $\chi^2_{FS}$  found from data. Both fits show good agreement with data and simulation.

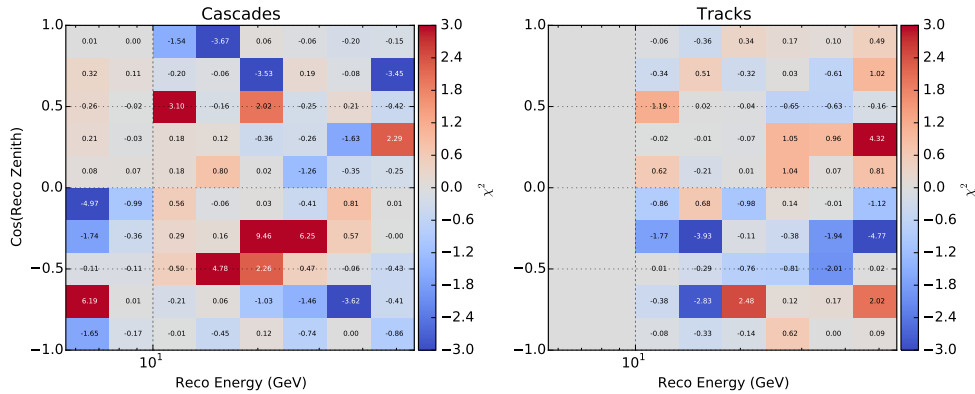


**Figure 8.32** – A map of the "signed"  $\chi^2_{FS}$  values for the CC-only fit.

During the first work with blind fits, this analysis used a wide range of reconstructed energies, including events up to 800 GeV in order to better constrain systematic terms from the non-oscillating higher energy regions. Blind fits in the GRECO analysis initially showed significant disagreement between the data and simulation, with a goodness-of-fit of  $10^{-7}$ . Investigations yielded new discoveries, discussed in Section 7.8, about the calibration of both Monte Carlo simulation and data.

After the removal of the flaring DOM events, the correction of bedrock events, and the elimination of the charge in the Pegleg fit, a new blind fit was performed and the goodness-of-fit was again tested. The resulting  $\chi^2_{FS}$  for the charged current only and neutral current + charged current fits were 127.095 and 127.623 respectively. One thousand trials were run for each fit using the updated sample, yielding estimates of the test statistic distributions. The p-values, shown in Figure 8.31, were  $p=52.8\%$  and  $p=49.8\%$  calculated from trials respectively. The full map of the  $\chi^2_{FS}$  values is shown in Figures 8.32 and 8.33 in terms of the "signed"  $\chi^2$

$$\chi^2_{Sign} = (d - f) \chi^2_{FS} \quad (8.27)$$

where  $d$  is the data rate and  $f$  is the total simulated rate at the best-fit point.

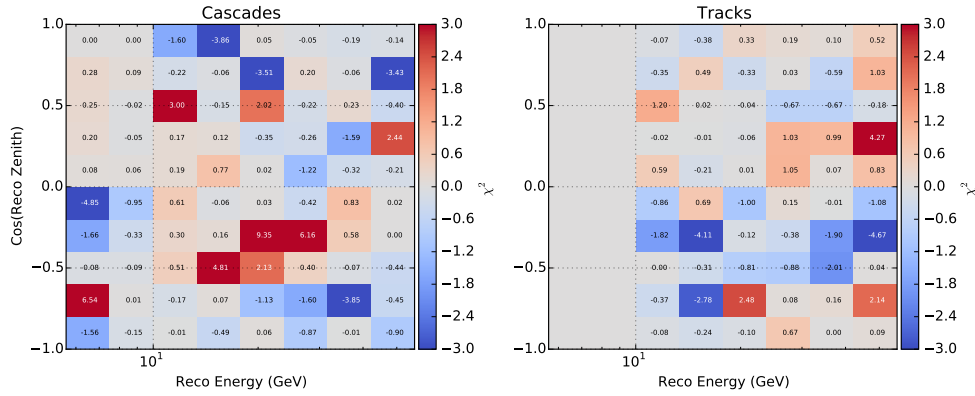


**Figure 8.33** – A map of the "signed"  $\chi^2_{FS}$  values for the NC+CC fit.

## 8.10 Results from the Search for Appearance

With good agreement between data and simulation in the CC-only and CC+NC fits, the appearance measurement with GRECO was granted unblinding approval. For the fit using only charged current tau neutrino events, the best fit value is  $N_{\nu_\tau}^{CC} = 0.566^{+0.356}_{-0.303}$  (syst+stat). For the fit including both neutral and charged tau neutrinos, the best fit is  $N_{\nu_\tau}^{NC+CC} = 0.733^{+0.305}_{-0.243}$  (syst+stat). The intervals are given at the  $1\sigma$  level and include the effects of the Feldman-Cousins procedure. Both results, shown in Figure 8.10 and Figure 8.35, fit lower than expected from unitary 3-flavor oscillations, although both are consistent with such a model.

The final value of the systematics, shown numerically in Table 8.6 and graphically in Figure 8.36, are within  $1\sigma$  of the expectation at the best-fit points. Many systematics were expected to be determined primarily from the data instead of from priors. Figures 8.37 and 8.38 shows the expected values of each systematic parameter measured in 1000 trials. The shaded band shows the  $1\sigma$  prior range for each of the parameters, if present. Not only are all systematics within the relevant priors, but most systematic parameters fit within the expected posteriors as well.

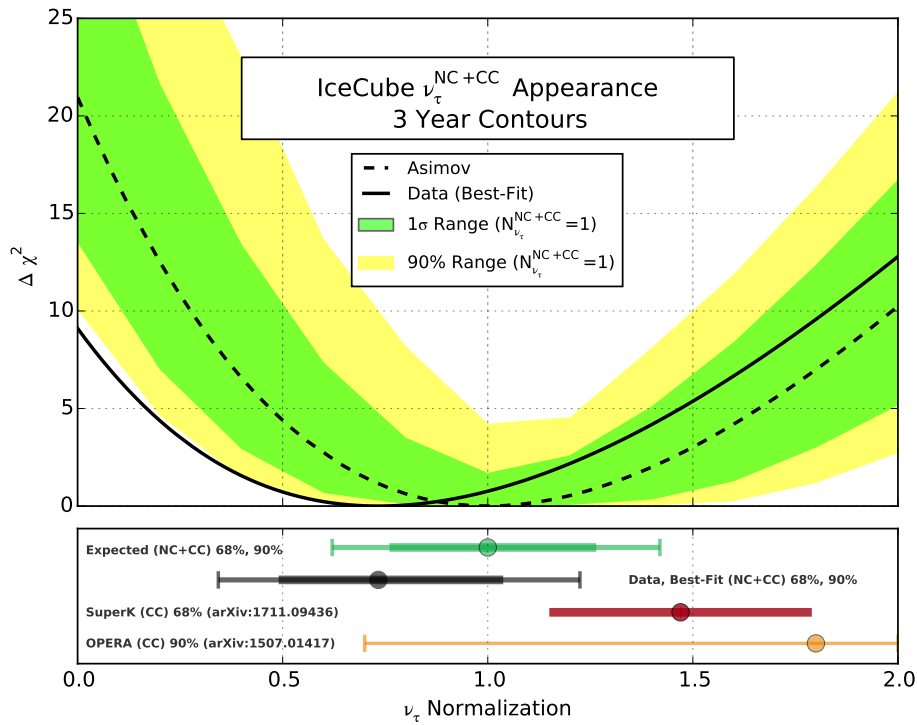


**Figure 8.34** – The final result of the CC-only fit. The best fit is lower than 1.0, at  $N_{\nu_\tau}^{CC} = 0.566^{+0.356}_{-0.303}$  (syst+stat).

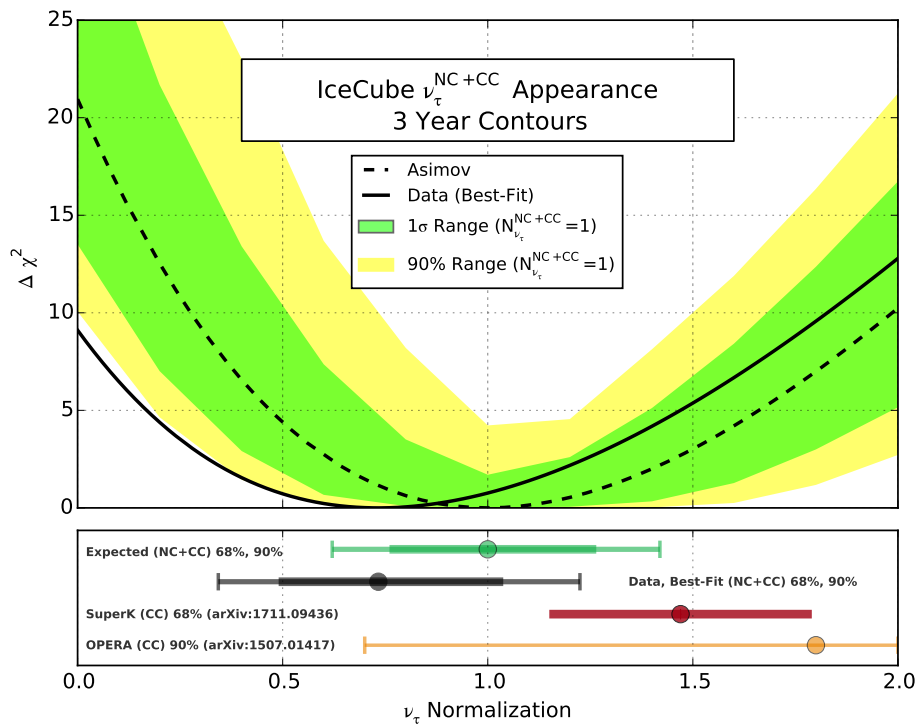


**Figure 8.35** – The final result of the NC+CC fit. The best fit is lower than 1.0, at  $N_{\nu_\tau}^{NC+CC} = 0.733^{+0.305}_{-0.243}$  (syst+stat).

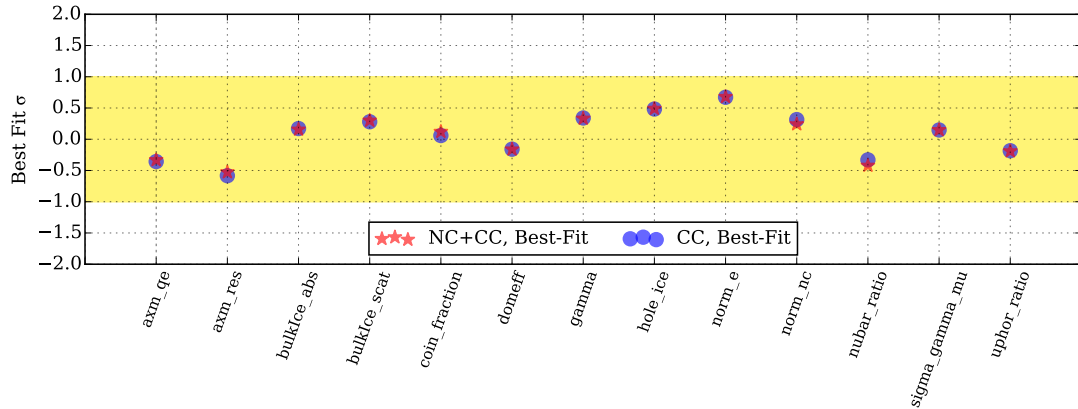


**Figure 8.36** – The value of each systematic with priors. The best-fit values are shown for each while the priors are shown by the yellow band. The CC and NC+CC fits are highly correlated, as expected, with very little difference in the systematics best-fit values. All values fit well within the expected  $1\sigma$  ranges.

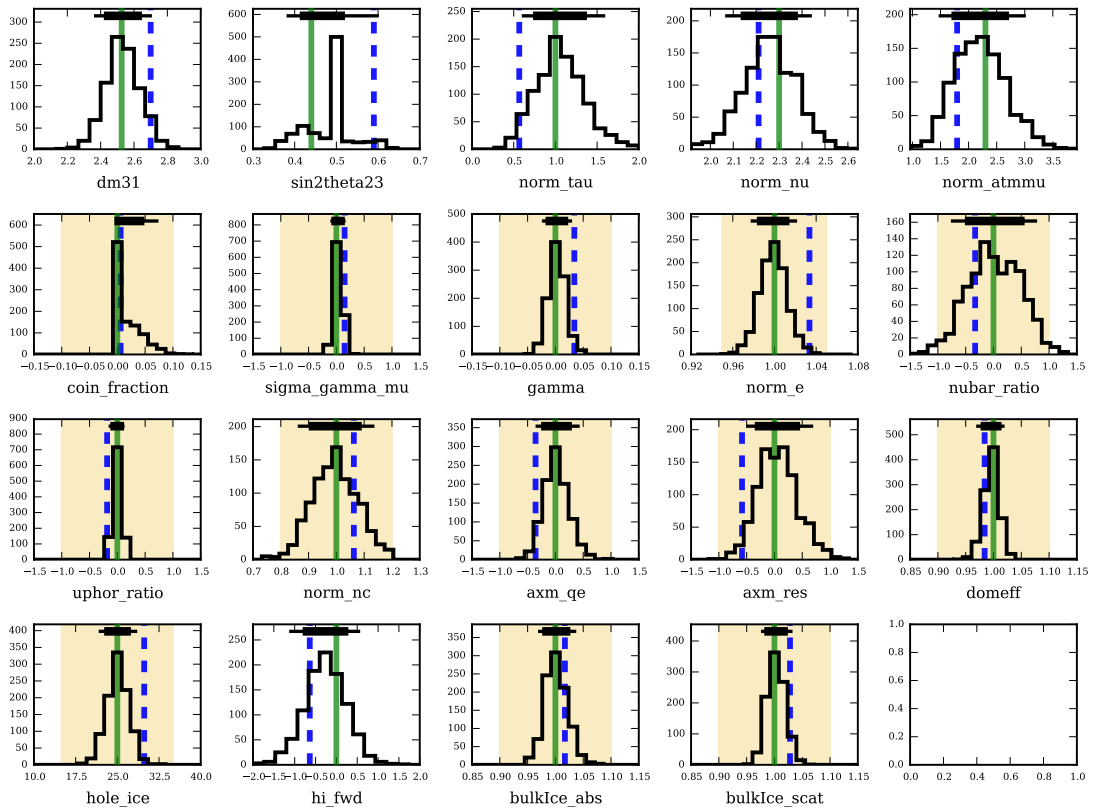


**Figure 8.37** – A comparison of the posterior expected from trials to the final data fit value for each parameter for the CC-only fit. The trials used to build the posterior distribution in each parameter assume baseline values for systematics,  $N_{\nu\tau}^{CC} = 1$ , and Nu-Fit 2.2 values [57]. The green vertical line shows the true injected value. The blue dotted line shows the best-fit value from data. The black bar shows the  $1\sigma$  and 90% ranges calculated from the posterior distribution.

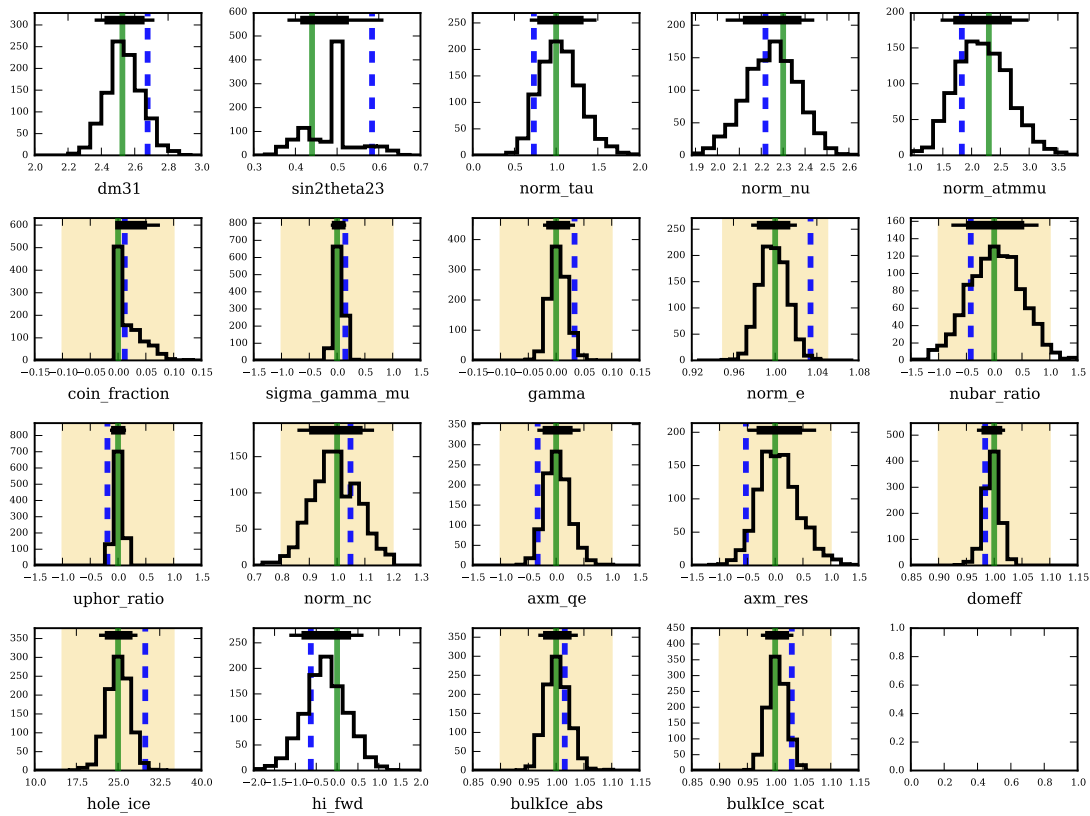


**Figure 8.38** – A comparison of the posterior expected from trials to the final data fit value for each parameter for the NC+CC fit. The trials used to build the posterior distribution in each parameter assume baseline values for systematics,  $N_{\nu_\tau}^{NC+CC} = 1$ , and Nu-Fit 2.2 values [57]

Parameter Type	Fit Parameter	Units	Prior	Disappearance	Appearance	
					CC-Only	NC+CC
Oscillations	$\Delta m_{32}^2$	$10^{-3} \text{ eV}^2$	-	2.548	2.625	2.602
	$\sin^2(\theta_{23})$	-	-	0.576	0.590	0.584
	$N_{\nu_\tau}$	-	-	1.0 (Fixed)	0.566	0.733
Cross-section	Axial Mass (QE)	$\sigma$	$0 \pm 1.0$	-0.250	-0.357	-0.332
	Axial Mass (RES)	$\sigma$	$0 \pm 1.0$	-0.3737	-0.583	-0.526
	$N_{NC}$	-	$1 \pm 0.2$	1.016	1.063	1.048
Neutrino Flux	$\nu_\mu$ Norm	Years	-	2.151	2.210	2.219
	$\nu_e/\nu_\mu$	-	$1 \pm 0.05$	1.031	1.034	1.033
	$\gamma_\nu$	-	$0 \pm 0.10$	0.045	0.034	0.033
	$\nu/\bar{\nu}$	$\sigma$	$0 \pm 1.0$	-0.700	-0.330	-0.422
	Up/Hor	$\sigma$	$0 \pm 1.0$	-0.207	-0.184	-0.191
	$f_{Coincident}$	%	$0 + 0.1$	0.027	0.006	0.012
Muon Flux	$\mu$ Norm	Years	-	1.845	1.795	1.830
	$\gamma_{CR}$	$\sigma$	$0 \pm 1.0$	0.113	0.148	0.148
Detector	DOM Efficiency	-	$1.0 \pm 0.1$	0.980	0.984	0.984
	Hole Ice	-	$25 \pm 10$	30.526	29.833	29.894
	Forward Scattering	-	-	-0.839	-0.638	-0.630
	Absorption	%	$1.0 \pm 0.1$	1.014	1.017	1.016
	Scattering	%	$1.0 \pm 0.1$	1.033	1.028	1.030

**Table 8.6** – The best-fit systematics values for each systematic parameter in the fit. The corresponding parameters for  $N_{\nu_\tau} = 1$  (ie, the muon neutrino disappearance fit) are included for reference. The CC-only and NC+CC fits are highly correlated, as expected.

The DeepCore results are the first to fit a value lower than expected, with both OPERA and Super-Kamiokande experiments returning results larger than  $N_{\nu_\tau}^{CC} = 1$ . The results are consistent with unitary oscillations.

## 8.11 Complementary Measurements from This Analysis

### 8.11.1 Oscillation Parameters

Thanks to significant contributions from others [108, 135], dedicated measurements of the atmospheric mixing parameters have also been performed using the GRECO selection. In these measurements, the value of  $N_{\nu_\tau}$  remains fixed to unity. The derived results are therefore directly comparable to results from other oscillation experiments.

#### $\nu_\mu$ Disappearance Results

Using similar tools as the appearance analysis, a complementary search for  $\nu_\mu$  disappearance was performed [135]. The measurement of the disappearance parameters,  $\Delta m_{3j}^2$  and  $\theta_{23}$ , used an identical choice of binning and systematics set as the appearance search described above. The  $\chi_{FS}^2$  statistic was found by minimization with the iMinit package [105, 106] across a grid of values arranged linearly in  $\Delta m_{3j}^2$  and  $\sin^2\theta_{23}$  covering both octants. At each point, the disappearance parameters were fixed during minimization. Both the normal and inverted ordering were tested separately.

The result is shown in Figure 8.39 compared to previous atmospheric oscillation measurements by IceCube [81], Super-Kamiokande [136] and the MINOS experiment [137]. Results from accelerator measurements are shown from the *NO $\nu$ A* [138] and T2K [139] experiments. All results show the 90% contour around the best-fit point. The GRECO result mildly prefers the normal ordering and the second octant, although maximal mixing ( $\sin^2\theta_{23} = 0.5$ ) is well within the best-fit contours.

The GRECO result and previous IceCube results are statistically consistent with one another, although the GRECO result prefers a larger mass splitting. Global fits, which prefer a value of the mass splitting of  $2.494_{-0.031}^{+0.033}$  as of the time of this writing [58], favor the new GRECO result over the previous IceCube result.

#### Mass Ordering

In order to quantify the preference for the mass ordering, a dedicated measurement using the GRECO sample was performed [108]. This measurement included differences relative to the appearance and disappearance measurements. Only upgoing reconstructed GRECO events were included, although the energy range was extended to 3-100 GeV. All simulation templates were smoothed during the analysis using a dedicated implementation of the kernel density estimation technique implemented in the C++ programming language [109]. This code, unlike the SciPy KDE implementation used in 6.3, includes functionality for weighted event samples and variable bandwidth estimation.

The systematics set used in the mass ordering analysis was identical to that of the disappearance measurement, with the value of  $N_{\nu_\tau}$  fixed to unity. Systematics included in the mass ordering measurement were applied using a parallel branch of the OscFit code used in the appearance measurement.

Statistical uncertainties arising from the simulation statistics were estimated using a bootstrapping technique included in the KDE implementation. The test statistic used in

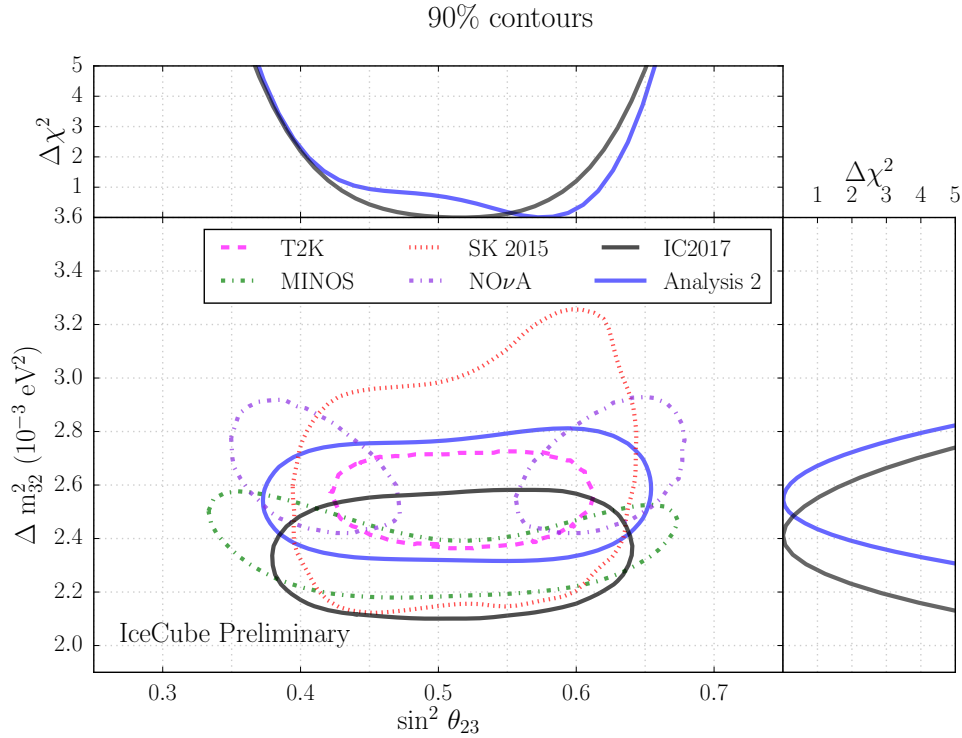


**Figure 8.39** – The results of a muon neutrino disappearance measurement with the GRECO event selection. The new result, shown in blue, fits a larger value of the mass splitting than the most recent published IceCube results [81], shown in black. The GRECO dataset also prefers a value away from maximal mixing,  $\sin^2\theta_{23} = 0.5$ , a first for a DeepCore measurement. The GRECO results are competitive with dedicated oscillation measurements from other experiments.

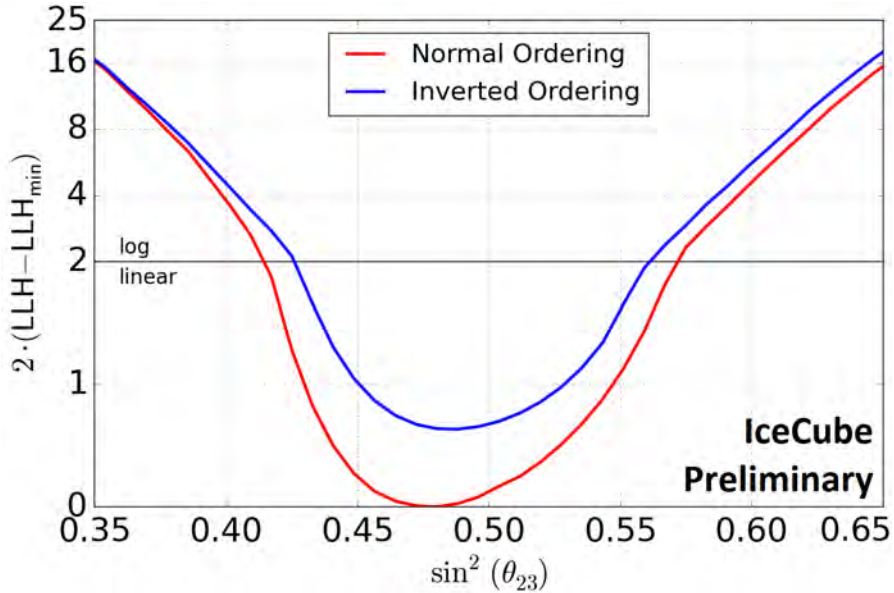


**Figure 8.40** – The measurement of the neutrino mass ordering with the GRECO event selection. The fit is performed only on upgoing events, but includes contributions from a wider energy range than the measurement of tau neutrino appearance. A weak preference for normal ordering is observed.

the mass ordering measurement was the numerical convolution between the Poissonian uncertainty due to the expected event count and a Gaussian model of the bootstrapped Monte Carlo statistical uncertainty.

Unlike the appearance and disappearance measurements, the neutrino mass ordering is not a continuous parameter. The calculation of a final significance proceeds following the method described in [128], a full description of which is beyond the scope of this work. Using GRECO events, a good fit is obtained at the best-fit point with a p-value of approximately 80%. A weak preference for the normal mass ordering is found at approximately  $0.3\sigma$  [108].

### 8.11.2 Implications and Future Work

There exist various ways to interpret the value of  $N_{\nu_\tau}$ . The value of the tau neutrino normalizations in the CC-only and NC+CC channels are both consistent with the expected value of 1.0. The standard 3-flavor oscillation model is not strongly disfavored from the GRECO oscillation result. The current result does, however, provide some tension with the most recent exclusive result from Super-Kamiokande [122], which reported  $1.47 \pm 0.32$ . The GRECO and Super-Kamiokande inclusive results differ by approximately  $1.8\sigma$ , assuming the total uncertainties are added in quadrature. In practice, various systematics, including the atmospheric mixing angle and mass splitting, are likely correlated between the analyses, implying approximately  $2\sigma$  of tension between the two results.

This analysis, like previous oscillation analyses produced by IceCube, has known limitations. The GRECO selection includes only three years of detector data. The data from those three years are selected using strict criteria that explicitly excludes non-standard runs, including those that are ended prematurely. These short runs are often otherwise unremarkable, but make up a significant fraction of the uptime of the detector in these years and are potentially useful for analysis. The addition of these runs would increase the total number of events in the GRECO sample by up to 15%. The addition of these events presents a simple way to improve the existing result on relatively short timescales.

The three years of data may also be extended in other ways. The data was originally collected between April 2012 and May 2015. Since the beginning of this work, additional years of detector data have been collected. These additional years of data were not included due to calibration changes in the IC86-5 season, discussed in Section 7.8.1, which may lead to disagreement between years. These updated calibrations have since been applied to the earlier years of detector data as well, leading to a self-consistent dataset of approximately 7 years.

The analysis of these events requires a number of upgrades to the simulation which are ongoing at the time of this work. New efforts are underway updating the simulated SPE templates to better describe the charge profile observed in the detector. These new templates are fit to detector data for each DOM and are updated for each year, although the year-to-year variations have proven to be small. New signal and background simulation is therefore necessary to incorporate these upgrades. The new simulations are underway, with completion and verification expected within the coming year. If the new sets show good agreement with data, charge information may be reintroduced to the reconstruction, potentially leading to improvements in the reconstructed resolution of events.

The current GRECO selection was the first oscillation selection in IceCube to successfully use simulated atmospheric muon background events at analysis level. The

simulated livetime is too limited, at 10 months, to allow for precision measurements using the additional years of data. While the GRECO selection is efficient at rejecting these simulated muons, additional simulation efforts require vast computational resources. Future analyses will require significantly larger muon datasets in order to adequately describe backgrounds.

The production of additional events for these analyses will require nearly a factor of 9 more events to reach parity between the expected number of muon events in 7 years of data and the raw Monte Carlo statistics. If only the standard simulation methods are used, this will require about 1.5 years worth of production time. While the new sets would include muon bundles, a feature not present during production of this work, the sets may still be limited outside of the DeepCore fiducial volume.

The production of new MuonGun simulation is ongoing with efforts to further develop the KDE prescale simulation methods described in Section 6.3. The KDE prescale method yields significant reductions to the production time of MuonGun simulation for the GRECO selection when using no DOM oversizing. This can improve by another 8x further if using a DOM oversizing factor of 3. This may be a viable option for the production of various systematics sets in order to speed the production of background events. Additional improvements to the simulation efficiency are possible and will undoubtedly be investigated in the near future. Even using the improvements described here, however, large muon sets are, for the first time, viable as background models in IceCube oscillation analyses.

Improvements are not only possible in the background simulation, however. Investigations described in Section 7.8 have spawned discussions of the limitations of the current GENIE generator production scheme. While GENIE was originally planned to be used solely for very low energy oscillation analyses, the dawn of new event selections such as GRECO spanning wider energy ranges can lead to notable disagreement due to the generation scheme. To better describe the detector, GENIE generation must be examined to identify unsimulated phase space necessary for further analyses. The simulation of events below the detector, in both the GENIE generator as well as in future MuonGun background simulations, must be given priority in order to explain the events occurring at the bottom or below the IceCube detector.

Future measurements of the tau neutrino appearance are already underway. Software updates to the GRECO selection are continuing, with new analyses planned for appearance, disappearance, and other searches for low energy neutrinos.

Future measurements may incorporate an planned detector upgrade. The measurements and techniques for simulated backgrounds presented here will form an integral part of upgrade efforts. The GRECO selection may also provide a template for selections using the upgraded detector, significantly improving the sensitivity to future oscillation measurements.

# Bibliography

- [1] H. Becquerel. “Sur les radiations émises par phosphorescence”. In: *Comptes Rendus* 122 (1896) (cit. on p. 1).
- [2] J Chadwick. “Intensitätsverteilung im magnetischen Spectrum der  $\beta$ -Strahlen von radium B + C”. In: *Verhandl. Dtsc. Phys. Ges.* 16 (1914), p. 383 (cit. on p. 1).
- [3] W. Pauli. *Offener Brief an die Gruppe der Radioaktiven bei der Gauvereins-Tagung zu Tübingen*. ETH Zürich, 1930 (cit. on p. 1).
- [4] E. Fermi. “Versuch einer Theorie der  $\beta$ -Strahlen. I”. In: *Zeitschrift für Physik* 88.3 (1934), pp. 161–177 (cit. on p. 1).
- [5] C. L. Cowan Jr., F. Reines, F. B. Harrison, H. W. Kruse, and A. D. McGuire. “Detection of the Free Neutrino: A Confirmation”. In: *Science* 124 (July 1956), pp. 103–104 (cit. on p. 1).
- [6] Nobel Foundation. *Nobel Prize in Physics*. 1995 (cit. on p. 2).
- [7] G. Danby, J-M. Gaillard, K. Goulianos, et al. “Observation of High-Energy Neutrino Reactions and the Existence of Two Kinds of Neutrinos”. In: *Phys. Rev. Lett.* 9 (1 1962), pp. 36–44 (cit. on p. 2).
- [8] DONUT Collaboration, K. Kodama, N. Ushida, et al. “Observation of tau neutrino interactions”. In: *Physics Letters B* 504 (Apr. 2001), pp. 218–224. eprint: [hep-ex/0012035](#) (cit. on pp. 2, 10, 25).
- [9] K. Kodama, N. Ushida, C. Andreopoulos, et al. “Final tau-neutrino results from the DONuT experiment”. In: *Phys. Rev. D* 78.5, 052002 (Sept. 2008), p. 052002. arXiv: 0711.0728 [[hep-ex](#)] (cit. on p. 2).
- [10] K. A. Olive et al. “Review of Particle Physics”. In: *Chin. Phys.* C38 (2014), p. 090001 (cit. on pp. 2–4, 9, 10, 16, 44, 106).
- [11] The ALEPH Collaboration, the DELPHI Collaboration, the L3 Collaboration, et al. “Precision Electroweak Measurements on the Z Resonance”. In: *ArXiv High Energy Physics - Experiment e-prints* (Sept. 2005). eprint: [hep-ex/0509008](#) (cit. on pp. 2, 17).
- [12] A. De Angelis. “Domenico Pacini, uncredited pioneer of the discovery of cosmic rays”. In: *ArXiv e-prints* (Mar. 2011). arXiv: 1103.4392 (cit. on p. 3).
- [13] J. R. Hoerandel. “Early cosmic-ray work published in German”. In: *American Institute of Physics Conference Series*. Ed. by J. F. Ormes. Vol. 1516. American Institute of Physics Conference Series. Feb. 2013, pp. 52–60. arXiv: 1212.0706 (cit. on pp. 3, 4).
- [14] Arthur H. Compton. “A Geographic Study of Cosmic Rays”. In: *Phys. Rev.* 43 (6 1933), pp. 387–403 (cit. on p. 3).

- [15] Nobel Foundation. *Nobel Prize in Physics*. 1936 (cit. on p. 3).
- [16] M Blau and H Wambacher. “Disintegration Processes by Cosmic Rays with the Simultaneous Emission of Several Heavy Particles”. In: 140 (Jan. 1937), pp. 585–585 (cit. on p. 4).
- [17] W. Bothe and W. Kolhoferster. “Das Wesen der Hoehenstrahlung”. In: *Zeitschrift fur Physik* 56 (Nov. 1929), pp. 751–777 (cit. on p. 4).
- [18] G. W. Clark, J. Earl, W. L. Kraushaar, et al. “Cosmic-Ray Air Showers at Sea Level”. In: *Phys. Rev.* 122 (2 1961), pp. 637–654 (cit. on p. 4).
- [19] M. Honda, M. S. Athar, T. Kajita, K. Kasahara, and S. Midorikawa. “Atmospheric neutrino flux calculation using the NRLMSISE-00 atmospheric model”. In: *Phys. Rev. D* 92.2, 023004 (July 2015), p. 023004. arXiv: 1502.03916 [astro-ph.HE] (cit. on pp. 4, 5, 118, 135).
- [20] Wikimedia Commons. *File:Standard Model of Elementary Particles.svg* — *Wikimedia Commons, the free media repository*. [Online; accessed 23-February-2018]. 2017 (cit. on p. 6).
- [21] J. A. Formaggio and G. P. Zeller. “From eV to EeV: Neutrino cross sections across energy scales”. In: *Reviews of Modern Physics* 84 (July 2012), pp. 1307–1341. arXiv: 1305.7513 [hep-ex] (cit. on pp. 7, 8, 39, 124).
- [22] D. Chirkin and W. Rhode. “Propagating leptons through matter with Muon Monte Carlo (MMC)”. In: *ArXiv High Energy Physics - Phenomenology e-prints* (July 2004). eprint: hep-ph/0407075 (cit. on pp. 9, 40).
- [23] H. Pessard. “The Opera Experiment”. In: *High Energy Physics, ICHEP 2004*. Ed. by H. Chen, D. Du, W. Li, and C. Lu. Apr. 2005, pp. 299–303. eprint: hep-ex/0504033 (cit. on pp. 10, 25, 107).
- [24] Minos Collaboration, D. G. Michael, P. Adamson, et al. “The magnetized steel and scintillator calorimeters of the MINOS experiment”. In: *Nuclear Instruments and Methods in Physics Research A* 596 (Nov. 2008), pp. 190–228. arXiv: 0805.3170 [physics.ins-det] (cit. on p. 10).
- [25] S. Mufson, B. Baugh, C. Bower, et al. “Liquid scintillator production for the NOvA experiment”. In: *Nuclear Instruments and Methods in Physics Research A* 799 (Nov. 2015), pp. 1–9. arXiv: 1504.04035 [physics.ins-det] (cit. on p. 10).
- [26] L. Aliaga and et al. “Design, calibration, and performance of the MINERvA detector”. In: *Nuclear Instruments and Methods in Physics Research A* 743 (Apr. 2014), pp. 130–159. arXiv: 1305.5199 [physics.ins-det] (cit. on p. 10).
- [27] Y. Kudenko and T2K Collaboration. “The near neutrino detector for the T2K experiment”. In: *Nuclear Instruments and Methods in Physics Research A* 598 (Jan. 2009), pp. 289–295. arXiv: 0805.0411 [physics.ins-det] (cit. on p. 10).
- [28] M. Antonello, B. Baibussinov, V. Bellini, et al. “ICARUS at FNAL”. In: *ArXiv e-prints* (Dec. 2013). arXiv: 1312.7252 [physics.ins-det] (cit. on p. 10).
- [29] P. A. Čerenkov. “Visible Radiation Produced by Electrons Moving in a Medium with Velocities Exceeding that of Light”. In: *Physical Review* 52 (Aug. 1937), pp. 378–379 (cit. on p. 10).
- [30] P. A. Cherenkov. “Visible luminescence of pure liquids under the influence of  $\gamma$ -radiation”. In: *Dokl. Akad. Nauk SSSR* 2.8 (1934). [Usp. Fiz. Nauk93,no.2,385(1967)], pp. 451–454 (cit. on p. 10).

- [31] I. M. Frank and I. E. Tamm. “Coherent visible radiation of fast electrons passing through matter”. In: *Compt. Rend. Acad. Sci. URSS* 14.3 (1937). [Usp. Fiz. Nauk93,no.2,388(1967)], pp. 109–114 (cit. on pp. 10, 11).
- [32] D.J. Griffiths. *Introduction to Electrodynamics*. Ed. by Pearson Education Limited. Fourth. 2013 (cit. on p. 10).
- [33] S. Tavernier. *Experimental Techniques in Nuclear and Particle Physics*. Ed. by Springer-Verlag. 2010 (cit. on p. 11).
- [34] K.A. Olive and Particle Data Group. “Review of Particle Physics”. In: *Chinese Physics C* 38.9 (2014), p. 090001 (cit. on p. 11).
- [35] B. Aharmim, S. N. Ahmed, A. E. Anthony, et al. “Combined analysis of all three phases of solar neutrino data from the Sudbury Neutrino Observatory”. In: *Phys. Rev. C* 88.2, 025501 (Aug. 2013), p. 025501. arXiv: 1109.0763 [nucl-ex] (cit. on pp. 11, 12).
- [36] C. W. Walter. “The Super-Kamiokande Experiment”. In: *Neutrino Oscillations: Present Status and Future Plans*. Ed. by J. A. Thomas and P. L. Vahle. World Scientific Publishing Co, 2008, pp. 19–43 (cit. on p. 11).
- [37] F. Montanet. “Design and expected performance of the ANTARES neutrino telescope”. In: *Nuclear Physics B Proceedings Supplements* 87 (June 2000), pp. 436–438. eprint: astro-ph/0001380 (cit. on p. 11).
- [38] M. G. Aartsen, M. Ackermann, J. Adams, et al. “The IceCube Neutrino Observatory: instrumentation and online systems”. In: *Journal of Instrumentation* 12 (Mar. 2017), P03012. arXiv: 1612.05093 [astro-ph.IM] (cit. on pp. 11, 25, 27–29, 31–33, 42, 64, 127).
- [39] John N. Bahcall. “Solar Neutrinos. I. Theoretical”. In: *Phys. Rev. Lett.* 12 (11 1964), pp. 300–302 (cit. on p. 12).
- [40] Raymond Davis. “Solar Neutrinos. II. Experimental”. In: *Phys. Rev. Lett.* 12 (11 1964), pp. 303–305 (cit. on p. 12).
- [41] Bruce T. Cleveland, Timothy Daily, Jr. Raymond Davis, et al. “Measurement of the Solar Electron Neutrino Flux with the Homestake Chlorine Detector”. In: *The Astrophysical Journal* 496.1 (1998), p. 505 (cit. on p. 12).
- [42] J. N. Abdurashitov, V. N. Gavrin, V. V. Gorbachev, et al. “Measurement of the solar neutrino capture rate with gallium metal. III. Results for the 2002-2007 data-taking period”. In: *Phys. Rev. C* 80.1, 015807 (July 2009), p. 015807. arXiv: 0901.2200 [nucl-ex] (cit. on p. 12).
- [43] W. Hampel, J. Handt, G. Heusser, et al. “GALLEX solar neutrino observations: results for GALLEX IV”. In: *Physics Letters B* 447.1 (1999), pp. 127–133 (cit. on p. 12).
- [44] M. Altmann, M. Balata, P. Belli, et al. “Complete results for five years of GNO solar neutrino observations”. In: *Physics Letters B* 616.3 (2005), pp. 174–190 (cit. on p. 12).
- [45] Herbert H. Chen. “Direct Approach to Resolve the Solar-Neutrino Problem”. In: *Phys. Rev. Lett.* 55 (14 1985), pp. 1534–1536 (cit. on p. 13).
- [46] Nobel Foundation. *Nobel Prize in Physics*. 2015 (cit. on p. 13).

- [47] Y. Fukuda, T. Hayakawa, E. Ichihara, et al. “Evidence for Oscillation of Atmospheric Neutrinos”. In: *Phys. Rev. Lett.* 81 (8 1998), pp. 1562–1567 (cit. on pp. 13, 14).
- [48] B. Pontecorvo. “Neutrino Experiments and the Problem of Conservation of Leptonic Charge”. In: *Sov. Phys. JETP* 26 (1968). [*Zh. Eksp. Teor. Fiz.*53,1717(1967)], pp. 984–988 (cit. on p. 14).
- [49] Z. Maki, M. Nakagawa, and S. Sakata. “Remarks on the Unified Model of Elementary Particles”. In: *Progress of Theoretical Physics* 28 (Nov. 1962), pp. 870–880 (cit. on p. 14).
- [50] C. Giganti, S. Lavignac, and M. Zito. “Neutrino oscillations: The rise of the PMNS paradigm”. In: *Progress in Particle and Nuclear Physics* 98 (Jan. 2018), pp. 1–54. arXiv: 1710.00715 [[hep-ex](#)] (cit. on pp. 15, 17, 18).
- [51] S. T. Petcov. “The Nature of Massive Neutrinos”. In: *Adv. High Energy Phys.* 2013 (2013), p. 852987. arXiv: 1303.5819 [[hep-ph](#)] (cit. on p. 15).
- [52] E. K. Akhmedov and A. Y. Smirnov. “Paradoxes of neutrino oscillations”. In: *Physics of Atomic Nuclei* 72 (Aug. 2009), pp. 1363–1381. arXiv: 0905.1903 [[hep-ph](#)] (cit. on p. 15).
- [53] A. Y. Smirnov. “The MSW Effect and Matter Effects in Neutrino Oscillations”. In: *Physica Scripta Volume T* 121 (Jan. 2005), pp. 57–64. eprint: [hep-ph/0412391](#) (cit. on p. 17).
- [54] S. M. Bilenky. “Neutrino oscillations: brief history and present status”. In: *ArXiv e-prints* (Aug. 2014). arXiv: 1408.2864 [[hep-ph](#)] (cit. on p. 17).
- [55] V. Barger, K. Whisnant, S. Pakvasa, and R. J. N. Phillips. “Matter effects on three-neutrino oscillations”. In: *Phys. Rev. D* 22 (11 1980), pp. 2718–2726 (cit. on p. 17).
- [56] Super-Kamiokande Collaboration. *Prob3++*. 2012 (cit. on pp. 17, 136).
- [57] J. Bergström, M. C. Gonzalez-Garcia, M. Maltoni, and T. Schwetz. “Bayesian global analysis of neutrino oscillation data”. In: *Journal of High Energy Physics* 9, 200 (Sept. 2015), p. 200. arXiv: 1507.04366 [[hep-ph](#)] (cit. on pp. 17, 148, 149).
- [58] I. Esteban, M. C. Gonzalez-Garcia, M. Maltoni, I. Martinez-Soler, and T. Schwetz (cit. on pp. 17, 18, 111, 115, 118, 135, 151).
- [59] S. Gariazzo, C. Giunti, M. Laveder, Y. F. Li, and E. M. Zavanin. “Light sterile neutrinos”. In: *Journal of Physics G Nuclear Physics* 43.3, 033001 (Mar. 2015), p. 033001. arXiv: 1507.08204 [[hep-ph](#)] (cit. on pp. 17, 18, 20).
- [60] J. M. Conrad, C. M. Ignarra, G. Karagiorgi, M. H. Shaevitz, and J. Spitz. “Sterile Neutrino Fits to Short Baseline Neutrino Oscillation Measurements”. In: *ArXiv e-prints* (July 2012). arXiv: 1207.4765 [[hep-ex](#)] (cit. on p. 18).
- [61] S. Gariazzo, C. Giunti, M. Laveder, and Y. F. Li. “Updated global 3+1 analysis of short-baseline neutrino oscillations”. In: *Journal of High Energy Physics* 6, 135 (June 2017), p. 135. arXiv: 1703.00860 [[hep-ph](#)] (cit. on pp. 18, 20).
- [62] M. G. Aartsen, K. Abraham, M. Ackermann, et al. “Searches for Sterile Neutrinos with the IceCube Detector”. In: *Physical Review Letters* 117.7, 071801 (Aug. 2016), p. 071801. arXiv: 1605.01990 [[hep-ex](#)] (cit. on pp. 18, 20, 31).

- [63] P. Adamson, D. J. Auty, D. S. Ayres, et al. “Active to Sterile Neutrino Mixing Limits from Neutral-Current Interactions in MINOS”. In: *Physical Review Letters* 107.1, 011802 (July 2011), p. 011802. arXiv: 1104.3922 [hep-ex] (cit. on pp. 20, 107).
- [64] P. Adamson, I. Anghel, A. Aurisano, et al. “Search for Sterile Neutrinos Mixing with Muon Neutrinos in MINOS”. In: *Physical Review Letters* 117.15, 151803 (Oct. 2016), p. 151803. arXiv: 1607.01176 [hep-ex] (cit. on p. 20).
- [65] P. Adamson, L. Aliaga, D. Ambrose, et al. “Search for active-sterile neutrino mixing using neutral-current interactions in NOvA”. In: *Phys. Rev. D* 96.7, 072006 (Oct. 2017), p. 072006. arXiv: 1706.04592 [hep-ex] (cit. on p. 20).
- [66] K. Abe, Y. Haga, Y. Hayato, et al. “Limits on sterile neutrino mixing using atmospheric neutrinos in Super-Kamiokande”. In: *Phys. Rev. D* 91 (5 2015), p. 052019 (cit. on p. 20).
- [67] IceCube Collaboration, M. G. Aartsen, M. Ackermann, et al. “Search for sterile neutrino mixing using three years of IceCube DeepCore data”. In: *ArXiv e-prints* (Feb. 2017). arXiv: 1702.05160 [hep-ex] (cit. on pp. 20, 57, 109).
- [68] Stephen Parke and Mark Ross-Lonegan. “Unitarity and the three flavor neutrino mixing matrix”. In: *Phys. Rev. D* 93 (11 2016), p. 113009 (cit. on pp. 20–23).
- [69] M. G. Aartsen, M. Ackermann, J. Adams, et al. “Calibration and characterization of the IceCube photomultiplier tube”. In: *Nuclear Instruments and Methods in Physics Research Section A: Accelerators, Spectrometers, Detectors and Associated Equipment* 618.1 (2010), pp. 139–152 (cit. on pp. 25, 26, 30, 42).
- [70] Hammamatsu Photonics. *PHOTOMULTIPLIER TUBE DATA SHEET R7081-02 for ICECUBE Experiment*. 2003 (cit. on p. 25).
- [71] M. J. Larson. “Simulation and identification of non-Poissonian noise triggers in the IceCube neutrino detector”. M.Sc. Alabama U., 2013 (cit. on pp. 27, 28, 42, 44–46, 66–68).
- [72] R. Abbasi, Y. Abdou, T. Abu-Zayyad, et al. “The design and performance of IceCube DeepCore”. In: *Astroparticle Physics* 35 (May 2012), pp. 615–624. arXiv: 1109.6096 [astro-ph.IM] (cit. on pp. 30, 31, 66, 67).
- [73] M. G. Aartsen, R. Abbasi, Y. Abdou, et al. “Measurement of South Pole ice transparency with the IceCube LED calibration system”. In: *Nuclear Instruments and Methods in Physics Research A* 711 (May 2013), pp. 73–89. arXiv: 1301.5361 [astro-ph.IM] (cit. on pp. 30, 32, 135).
- [74] The HAWC Collaboration and The IceCube Collaboration. “Combined Analysis of Cosmic-Ray Anisotropy with IceCube and HAWC”. In: *ArXiv e-prints* (Aug. 2017). arXiv: 1708.03005 [astro-ph.HE] (cit. on p. 31).
- [75] M. G. Aartsen, G. C. Hill, A. Kyriacou, et al. “Measurement of the multi-TeV neutrino interaction cross-section with IceCube using Earth absorption”. In: *Nature* 551 (Nov. 2017), pp. 596–600. arXiv: 1711.08119 [hep-ex] (cit. on p. 31).
- [76] M. G. Aartsen, K. Abraham, M. Ackermann, et al. “Observation and Characterization of a Cosmic Muon Neutrino Flux from the Northern Hemisphere Using Six Years of IceCube Data”. In: *Ap.J.* 833, 3 (Dec. 2016), p. 3. arXiv: 1607.08006 [astro-ph.HE] (cit. on p. 31).

- [77] IceCube Collaboration. “Evidence for High-Energy Extraterrestrial Neutrinos at the IceCube Detector”. In: *Science* 342, 1242856 (Nov. 2013), p. 1242856. arXiv: 1311.5238 [astro-ph.HE] (cit. on p. 31).
- [78] S. Euler. “Observations of Oscillations of Atmospheric Neutrinos with the IceCube Neutrino Observatory”. Ph.D. Rheinisch-Westfälische Technische Hochschule (RWTH), 2013 (cit. on pp. 31, 32, 67, 75, 84, 86).
- [79] M. G. Aartsen, R. Abbasi, Y. Abdou, et al. “Measurement of Atmospheric Neutrino Oscillations with IceCube”. In: *Physical Review Letters* 111.8, 081801 (Aug. 2013), p. 081801. arXiv: 1305.3909 [hep-ex] (cit. on pp. 32, 57, 67, 90, 109, 129, 136).
- [80] M. G. Aartsen et al. “Determining neutrino oscillation parameters from atmospheric muon neutrino disappearance with three years of IceCube DeepCore data”. In: *Phys. Rev. D* 91.7 (2015), p. 072004. arXiv: 1410.7227 [hep-ex] (cit. on pp. 32, 57, 67, 90, 109, 120, 126, 129, 136).
- [81] M. G. Aartsen et al. “Determining neutrino oscillation parameters from atmospheric muon neutrino disappearance with three years of IceCube DeepCore data”. In: *Phys. Rev. D* 91.7 (2015), p. 072004. arXiv: 1410.7227 [hep-ex] (cit. on pp. 32, 34, 57, 67, 90, 107, 109, 120, 126, 129, 130, 135, 136, 139, 151, 152).
- [82] M. G. Aartsen, M. Ackermann, J. Adams, et al. “Search for annihilating dark matter in the Sun with 3 years of IceCube data”. In: *European Physical Journal C* 77, 146 (Mar. 2017), p. 146. arXiv: 1612.05949 [astro-ph.HE] (cit. on p. 32).
- [83] M. G. Aartsen, K. Abraham, M. Ackermann, et al. “All-flavour search for neutrinos from dark matter annihilations in the Milky Way with IceCube/DeepCore”. In: *European Physical Journal C* 76, 531 (Oct. 2016), p. 531. arXiv: 1606.00209 [astro-ph.HE] (cit. on p. 32).
- [84] N. E. Bramall, R. C. Bay, K. Woschnagg, R. A. Rohde, and P. B. Price. “A deep high-resolution optical log of dust, ash, and stratigraphy in South Pole glacial ice”. In: *Geophys. Res. Lett.* 32, L21815 (Nov. 2005), p. L21815 (cit. on p. 32).
- [85] M. Ackermann, J. Ahrens, X. Bai, et al. “Optical properties of deep glacial ice at the South Pole”. In: *Journal of Geophysical Research (Atmospheres)* 111, D13203 (July 2006), p. D13203 (cit. on p. 32).
- [86] IceCube Collaboration. *IceCube Dust Map*. 2011. URL: <http://icecube.berkeley.edu/~bay/dustmap/> (cit. on p. 33).
- [87] IceCube Collaboration, M. G. Aartsen, R. Abbasi, et al. “The IceCube Neutrino Observatory Part VI: Ice Properties, Reconstruction and Future Developments”. In: *ArXiv e-prints* (Sept. 2013). arXiv: 1309.7010 [astro-ph.HE] (cit. on pp. 32–34, 52, 129).
- [88] M. Rongen. “Measuring the optical properties of IceCube drill holes”. In: *European Physical Journal Web of Conferences*. Vol. 116. European Physical Journal Web of Conferences. Apr. 2016, p. 06011 (cit. on p. 33).
- [89] D. Heck, G. Schatz, T. Thouw, J. Knapp, and J. N. Capdevielle. “CORSIKA: A Monte Carlo code to simulate extensive air showers”. In: (1998) (cit. on p. 36).
- [90] E.-J. Ahn, R. Engel, T. K. Gaisser, P. Lipari, and T. Stanev. “Cosmic ray interaction event generator SIBYLL 2.1”. In: *Phys. Rev. D* 80.9, 094003 (Nov. 2009), p. 094003. arXiv: 0906.4113 [hep-ph] (cit. on p. 36).

- [91] Joerg R. Hoerandel. “On the knee in the energy spectrum of cosmic rays”. In: *Astropart. Phys.* 19 (2003), pp. 193–220. arXiv: astro-ph/0210453 [astro-ph] (cit. on pp. 36, 38, 52).
- [92] T. K. Gaisser, T. Stanev, and S. Tilav. “Cosmic ray energy spectrum from measurements of air showers”. In: *Frontiers of Physics* 8 (Dec. 2013), pp. 748–758. arXiv: 1303.3565 [astro-ph.HE] (cit. on pp. 37, 38).
- [93] J. van Santen. “Neutrino Interactions in IceCube above 1 TeV: Constraints on Atmospheric Charmed-Meson Production and Investigation of the Astrophysical Neutrino Flux with 2 Years of IceCube Data taken 2010–2012”. PhD thesis. U. Wisconsin, Madison (main), 2014 (cit. on pp. 37, 58, 78).
- [94] C. Andreopoulos, C. Barry, S. Dytman, et al. “The GENIE Neutrino Monte Carlo Generator: Physics and User Manual”. In: *ArXiv e-prints* (Oct. 2015). arXiv: 1510.05494 [hep-ph] (cit. on pp. 39, 123, 135).
- [95] M. Gluck, E. Reya, and A. Vogt. “Dynamical parton distributions revisited”. In: *European Physical Journal C* 5 (Sept. 1998), pp. 461–470. eprint: hep-ph/9806404 (cit. on p. 39).
- [96] S. Agostinelli et al. “GEANT4: A Simulation toolkit”. In: *Nucl. Instrum. Meth.* A506 (2003), pp. 250–303 (cit. on p. 39).
- [97] Makoto Asai, Andrea Dotti, Marc Verderi, and Dennis H. Wright. “Recent developments in Geant4”. In: *Annals Nucl. Energy* 82 (2015), pp. 19–28 (cit. on p. 39).
- [98] A. Gazizov and M. Kowalski. “ANIS: High energy neutrino generator for neutrino telescopes”. In: *Computer Physics Communications* 172 (Nov. 2005), pp. 203–213. eprint: astro-ph/0406439 (cit. on p. 40).
- [99] Adam M. Dziewonski and Don L. Anderson. “Preliminary reference Earth model”. In: *Physics of the Earth and Planetary Interiors* 25.4 (1981), pp. 297–356 (cit. on pp. 40, 136).
- [100] A. Cooper-Sarkar, P. Mertsch, and S. Sarkar. “The high energy neutrino cross-section in the Standard Model and its uncertainty”. In: *Journal of High Energy Physics* 8, 42 (Aug. 2011), p. 42. arXiv: 1106.3723 [hep-ph] (cit. on p. 40).
- [101] J. H. Koehne, K. Frantzen, M. Schmitz, et al. “PROPOSAL: A tool for propagation of charged leptons”. In: *Comput. Phys. Commun.* 184 (2013), pp. 2070–2090 (cit. on p. 40).
- [102] Dmitry Chirkin. “Photon tracking with GPUs in IceCube”. In: *Nucl. Instrum. Meth.* A725 (2013), pp. 141–143 (cit. on p. 41).
- [103] John E. Stone, David Gohara, and Guochun Shi. “OpenCL: A Parallel Programming Standard for Heterogeneous Computing Systems”. In: *IEEE Des. Test* 12.3 (May 2010), pp. 66–73 (cit. on p. 41).
- [104] Y. Hasegawa. *Analysis of Charge Response functions of the IceCube PMTs*. Chiba University. 2007. URL: <http://www.pp1.phys.chiba-u.jp/research/IceCube/pmt/SPE/CRAnalysis.html> (cit. on pp. 43, 90).
- [105] iminuit team. *iminuit – A Python interface to Minuit* (cit. on pp. 50, 137, 151).
- [106] F. James and M. Roos. “Minuit – a system for function minimization and analysis of the parameter errors and correlations”. In: *Computer Physics Communications* 10 (Dec. 1975), pp. 343–367 (cit. on pp. 50, 137, 151).

- [107] Eric Jones, Travis Oliphant, Pearu Peterson, et al. *SciPy: Open source scientific tools for Python*. [Online; accessed <today>]. 2001– (cit. on p. 61).
- [108] M. Leuermann. “Testing the Neutrino Mass Ordering with Three Years of IceCube/DeepCore Data”. Pending. Ph.D. Rheinisch-Westfälische Technische Hochschule (RWTH) Aachen, 2018 (cit. on pp. 63, 86, 88, 151, 153).
- [109] S. Schoenen. “Discovery and characterization of a diffuse astrophysical muon neutrino flux with the iceCube neutrino observatory”. Ph.D. Rheinisch-Westfälische Technische Hochschule (RWTH), 2017 (cit. on pp. 63, 151).
- [110] Andreas Hocker et al. “TMVA - Toolkit for Multivariate Data Analysis”. In: *PoS ACAT (2007)*, p. 040. arXiv: physics/0703039 [PHYSICS] (cit. on pp. 70, 73).
- [111] AMANDA Collaboration. “Muon track reconstruction and data selection techniques in AMANDA”. In: *Nuclear Instruments and Methods in Physics Research Section A: Accelerators, Spectrometers, Detectors and Associated Equipment* 524.1 (2004), pp. 169–194 (cit. on p. 72).
- [112] D. Pandel. “Bestimmung von Wasser- und Detektorparametern und Rekonstruktion von Myonen bis 100 TeV mit dem Baikal Neutrino teleskop NT-72”. PhD thesis. Humboldt-Universität, 1996 (cit. on p. 78).
- [113] AMANDA Collaboration. “Muon track reconstruction and data selection techniques in AMANDA”. In: *Nuclear Instruments and Methods in Physics Research A* 524 (May 2004), pp. 169–194. eprint: astro-ph/0407044 (cit. on p. 78).
- [114] J. A. Nelder and R. Mead. “A Simplex Method for Function Minimization”. In: *The Computer Journal* 7.4 (1965), pp. 308–313. eprint: /oup/backfile/content\_public/journal/comjnl/7/4/10.1093/comjnl/7.4.308/2/7-4-308.pdf (cit. on p. 79).
- [115] M. G. Aartsen et al. “The IceCube Neutrino Observatory Part II: Atmospheric and Diffuse UHE Neutrino Searches of All Flavors”. In: (2013). arXiv: 1309.7003 [astro-ph.HE] (cit. on p. 81).
- [116] J. Kiryluk and for the IceCube Collaboration. “First search for extraterrestrial neutrino-induced cascades with IceCube”. In: *ArXiv e-prints* (Sept. 2009). arXiv: 0909.0989 [astro-ph.HE] (cit. on p. 81).
- [117] M. Dunkman. “Measurement of Atmospheric Muon Neutrino Disappearance with IceCube-DeepCore”. Ph.D. The Pennsylvania State University, 2015 (cit. on pp. 85, 86).
- [118] F. Feroz, M. P. Hobson, and M. Bridges. “MultiNest: an efficient and robust Bayesian inference tool for cosmology and particle physics”. In: *Monthly Notices of the Royal Astronomical Society* 398.4 (2009), pp. 1601–1614. eprint: /oup/backfile/content\_public/journal/mnras/398/4/10.1111/j.1365-2966.2009.14548.x/2/mnras0398-1601.pdf (cit. on p. 88).
- [119] F. Feroz, M. P. Hobson, E. Cameron, and A. N. Pettitt. “Importance Nested Sampling and the MultiNest Algorithm”. In: *ArXiv e-prints* (June 2013). arXiv: 1306.2144 [astro-ph.IM] (cit. on p. 88).
- [120] M. G. Aartsen, R. Abbasi, M. Ackermann, et al. “Energy reconstruction methods in the IceCube neutrino telescope”. In: *Journal of Instrumentation* 9, P03009 (Mar. 2014), P03009. arXiv: 1311.4767 [physics.ins-det] (cit. on p. 88).

- [121] K. Abe, Y. Hayato, T. Iida, et al. “Evidence for the Appearance of Atmospheric Tau Neutrinos in Super-Kamiokande”. In: *Physical Review Letters* 110.18, 181802 (May 2013), p. 181802. arXiv: 1206.0328 [hep-ex] (cit. on pp. 106–108).
- [122] Super-Kamiokande Collaboration, : Z. Li, et al. “A Measurement of the Tau Neutrino Cross Section in Atmospheric Neutrino Oscillations with Super-Kamiokande”. In: *ArXiv e-prints* (Nov. 2017). arXiv: 1711.09436 [hep-ex] (cit. on pp. 106–109, 153).
- [123] N. Agafonova, A. Aleksandrov, A. Anokhina, et al. “Discovery of  $\tau$  Neutrino Appearance in the CNGS Neutrino Beam with the OPERA Experiment”. In: *Physical Review Letters* 115.12, 121802 (Sept. 2015), p. 121802. arXiv: 1507.01417 [hep-ex] (cit. on pp. 106–108).
- [124] S. Aoki, A. Ariga, T. Ariga, et al. “Study of tau-neutrino production at the CERN SPS”. In: *ArXiv e-prints* (Aug. 2017). arXiv: 1708.08700 [hep-ex] (cit. on p. 107).
- [125] G. Pagliaroli, N. Di Marco, and M. Mannarelli. “Enhanced tau neutrino appearance through invisible decay”. In: *Phys. Rev. D* 93.11, 113011 (June 2016), p. 113011. arXiv: 1603.08696 [hep-ph] (cit. on p. 107).
- [126] G. D. Barr, S. Robbins, T. K. Gaisser, and T. Stanev. “Uncertainties in atmospheric neutrino fluxes”. In: *Phys. Rev. D* 74.9, 094009 (Nov. 2006), p. 094009. eprint: astro-ph/0611266 (cit. on pp. 120–122, 135).
- [127] J. Evans, D. Garcia Gamez, S. D. Porzio, S. Söldner-Rembold, and S. Wren. “Uncertainties in atmospheric muon-neutrino fluxes arising from cosmic-ray primaries”. In: *Phys. Rev. D* 95.2, 023012 (Jan. 2017), p. 023012. arXiv: 1612.03219 [astro-ph.HE] (cit. on pp. 120, 123, 135).
- [128] S. Wren. “Neutrino Mass Ordering Studies with IceCube-DeepCore”. Ph.D. The University of Manchester, 2017 (cit. on pp. 123, 153).
- [129] S. Mandalia. *Update on the differential DIS cross-section error*. Internal Presentation. 2016 (cit. on p. 124).
- [130] M. Tzanov, D. Naples, S. Boyd, et al. “Precise measurement of neutrino and antineutrino differential cross sections”. In: *Phys. Rev. D* 74.1, 012008 (July 2006), p. 012008. eprint: hep-ex/0509010 (cit. on p. 124).
- [131] J. Feintzeig. “Searches for Point-like Sources of Astrophysical Neutrinos with the IceCube Neutrino Observatory”. Ph.D. University of Wisconsin, 2014 (cit. on pp. 127, 135).
- [132] G. Cowan, K. Cranmer, E. Gross, and O. Vitells. “Asymptotic formulae for likelihood-based tests of new physics”. In: *European Physical Journal C* 71, 1554 (Feb. 2011), p. 1554. arXiv: 1007.1727 [physics.data-an] (cit. on p. 137).
- [133] S. S. Wilks. “The Large-Sample Distribution of the Likelihood Ratio for Testing Composite Hypotheses”. In: *Ann. Math. Statist.* 9.1 (Mar. 1938), pp. 60–62 (cit. on p. 138).
- [134] G. J. Feldman and R. D. Cousins. “Unified approach to the classical statistical analysis of small signals”. In: *Phys. Rev. D* 57 (Apr. 1998), pp. 3873–3889. eprint: physics/9711021 (cit. on p. 138).

- [135] E. Cheung. “Measurements of Atmospheric Neutrino Oscillation Parameters Using Three Years of IceCube Data”. Pending. Ph.D. University of Maryland, 2018 (cit. on p. 151).
- [136] R. Wendell. “Atmospheric results from Super-Kamiokande”. In: *American Institute of Physics Conference Series*. Vol. 1666. American Institute of Physics Conference Series. July 2015, p. 100001. arXiv: 1412.5234 [hep-ex] (cit. on p. 151).
- [137] P. Adamson et al. “Combined analysis of  $\nu_\mu$  disappearance and  $\nu_\mu \rightarrow \nu_e$  appearance in MINOS using accelerator and atmospheric neutrinos”. In: *Phys. Rev. Lett.* 112 (2014), p. 191801. arXiv: 1403.0867 [hep-ex] (cit. on p. 151).
- [138] The NOvA Collaboration, P. Adamson, L. Aliaga, et al. “Measurement of the neutrino mixing angle  $\theta_{23}$  in NOvA”. In: *ArXiv e-prints* (Jan. 2017). arXiv: 1701.05891 [hep-ex] (cit. on p. 151).
- [139] T2K Collaboration, K. Abe, J. Amey, et al. “First combined analysis of neutrino and antineutrino oscillations at T2K”. In: *ArXiv e-prints* (Jan. 2017). arXiv: 1701.00432 [hep-ex] (cit. on p. 151).